Evaluation of Nondestructive Testing Methods to Assess the Condition of Concrete Bridge Decks

by

Christian Mikael Jetzel

A thesis submitted to the Graduate Faculty of
Auburn University
in partial fulfillment of the
requirements for the Degree of
Master of Science

Auburn, Alabama
August 7, 2021

Keywords: nondestructive testing, concrete testing, impact-echo, half-cell potential, surface resistivity

Approved by

Anton K. Schindler, Chair, Professor and HRC Director, Department of Civil and Environmental Engineering
James S. Davidson, Professor, Department of Civil and Environmental Engineering
Mary L. Hughes, Lecturer, Department of Civil and Environmental Engineering

ABSTRACT

Bridges are critical parts of the transportation infrastructure in the United States and throughout the world. During their lifecycle, reinforced-concrete bridge decks can experience distresses and defects in the form of corrosion of reinforcing steel, delaminations, vertical cracking, honeycombing, and concrete degradation, all of which can compromise a bridge's structural integrity if not monitored and addressed. Nondestructive testing (NDT) provides a method for surveying reinforced-concrete bridge decks without causing damage to the structure (i.e. coring), and can provide means to track the deterioration of the bridge decks. Developments in technology throughout recent decades have made NDT methods more reliable, time-efficient, and cost-efficient, driving departments of transportation to consider using NDT methods for surveying and monitoring bridges under their jurisdictions.

Five NDT methods were assessed in this project for use by the Alabama Department of Transportation (ALDOT): impact-echo, ground penetrating radar (GPR), half-cell potential, surface resistivity, and infrared thermography. Through research and testing of each method, it was determined that the impact-echo method was most effective and most suitable for use by ALDOT, as it proved to be the most precise, accurate, and time-efficient during testing in the laboratory at Auburn University's Department of Civil and Environmental Engineering.

A full-scale bridge deck NDT site was constructed for ALDOT at the National Geotechnical Experimentation Site in Opelika, Alabama. In order to determine which defects to include in the full-scale test site, research was performed to determine the most suitable method for replicating common types of defects that occur in reinforced-concrete bridge decks. Methods that accurately represented defects in the laboratory experimental program were used to create defects within the full-scale bridge deck NDT site. This full-scale NDT test site can be used to conduct NDT training, calibrate equipment, and evaluate new NDT methods.

ACKNOWLEDGMENTS

First, I would like to thank my God, who has blessed me immeasurably. Without His blessings of grace and mercy, I would not be where I am today, nor would I have the hope of eternal life. If you are reading this and do not know Jesus, I encourage you now to consider following and establishing a personal relationship with Him. He is worthy.

I would like to thank Rob Crosby for his help throughout the course of this research project. From aiding in the early stages of casting specimens in the laboratory, to spurring me on during the testing of the laboratory specimens, to helping design and construct the full-scale testing site, your hard work and insight was greatly appreciated. I can definitively say that this project would not be complete without your help, my friend. My thanks also goes out to William Bloodworth for the important role he played in construction process of the full-scale NDT site.

Credit goes to Zack Coleman for his work with the GPR and infrared thermography methods of nondestructive testing, as well as his work to extract cores from all laboratory test specimens. I would like to thank Grant Cooper, Matt Scales, Hongyang Wu, Anna Quinn, Daniel Richey, Elliott Burrow, David Whitmore, and others for their help during the times we cast concrete in the laboratory throughout this project.

I would like to thank Dr. Anton Schindler for giving me the opportunity to work on this project, and for his advice and guidance throughout the course of my research. I also want to thank Dr. Mary Hughes and Dr. James Davidson for their willingness to serve on my committee, and for the aid they gave in completing this report.

Last, but certainly not least, I would like to thank those near and dear to me: my family (Mom, Dad, Andrew, Mimi, and Papa, as well as all of my extended family) and my girlfriend, Morgan. Your unwavering love and support for me has been second to none, and I would not be writing this today were it not for the tremendous role each of you have played in my life.

Thank you again to all who helped me reach this milestone in my education.

TABLE OF CONTENTS

LIST OF TABLES

Appendices

LIST OF FIGURES

Appendices

CHAPTER 1

INTRODUCTION

1.1 BACKGROUND

Throughout the world, society is largely reliant on transportation for nearly all aspects of life. In the United States, much of the economy is based on the infrastructure of the highway system. Because society is so reliant upon this highway system, it is one of the most worn pieces of American infrastructure, yet one of the most difficult to maintain or replace.

Every four years, the American Society of Civil Engineers releases a report outlining the state of America's infrastructure. In the 2017 Infrastructure Report Card, America's bridges were given an overall grade of C+ (ASCE 2017). Eleven percent of bridges were designated structurally deficient, while 39 percent of bridges were found to be over 50 years old (ASCE 2017). A structurally deficient bridge is one that requires significant maintenance, rehabilitation or replacement (ASCE 2017). With the rise in age of America's bridge infrastructure, there is an increased likelihood of deterioration and defects within bridge structural elements, particularly concrete bridge decks. An example of degradation that is clearly visible on the underside of a concrete bridge deck is shown in Figure 1-1.

Figure 1-1: Degradation on the underside of a bridge deck due to corrosion (Afshinnia 2020)

In order to optimize time and resources for maintenance, repair, and replacement, highway departments need to have an awareness of the condition of all of their bridges, both on the surface as well as within the structural elements. For concrete structural elements, such as bridge decks, standard testing of the in situ concrete can result in lane closures or total bridge closure, as well as localized damage to the concrete. These can prove to be both time-consuming and harmful to the bridges themselves, and still may not provide adequate insight into interior defects of the concrete. Nondestructive testing (NDT) methods provide highway agencies with an ability to test public bridges relatively quickly and, more importantly, without damaging the structure. These NDT methods are used to determine concrete properties and evaluate the structure (ACI 228 2013). NDT methods are usually noninvasive, meaning that structural elements generally do not sustain damage in preparation for testing, nor during testing. Among other motivations, nondestructive testing may be applied to a bridge for quality control or assurance, location and determination of the extent of deterioration within the structure, or determining the concrete's overall uniformity (International Atomic Energy Agency 2002). Additionally, NDT can increase the confidence level of a smaller number of destructive tests, saving time and money in addition to limiting damage to the structure (International Atomic Energy Agency 2002).

Early forms of nondestructive testing consisted of hammer sounding, chain dragging and visual inspection. Those forms of testing, though reliable, were time-consuming and results were subjective based upon visual and audible assessment. As time progressed, new and more standard tests, such as the rebound hammer, impact echo, and ground penetrating radar, were developed to replace these early forms of testing. Advances in technology, such as handheld devices with the ability to automatically process and plot data for user interpretation, have allowed NDT methods to become a more accepted and necessary form of structural evaluation (Lim and Honggang 2011). An example of a modern nondestructive testing equipment and testing output are shown in Figure 1-2 and Figure 1-3, respectively.

Figure 1-2: Using ground-penetrating radar to survey a bridge deck (Gucunski, et al. 2013)

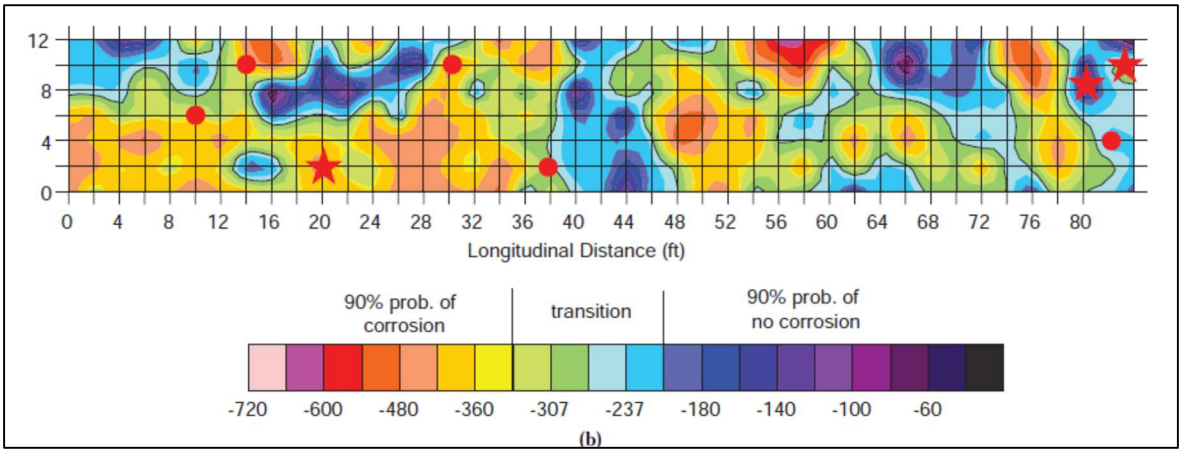

Figure 1-3: Sample results from a half-cell potential survey (Gucunski, et al. 2013)

1.2 RESEARCH OBJECTIVES

The primary objective of the work documented in this thesis was to develop a full-scale test site where Alabama Department of Transportation (ALDOT) personnel can conduct NDT training, calibrate equipment, and evaluate new NDT methods. Typical defects that occur in concrete structures, such as voids, delaminations, cracks, corrosion, and deterioration, were cast into the bridge deck at varying locations throughout the bridge.

In addition to this main objective, the following secondary objectives are part of this project:

- Evaluate methods for replicating the aforementioned defects in a controlled manner and identify successful methods to use in construction of the full-scale test site,
- Identify NDT methods that can accurately detect and characterize the in-place condition (e.g., voids, delaminations, cracks, corrosion, etc.) of concrete structures,
- Evaluate the strengths and limitations of various NDT methods by considering accuracy, precision, speed, cost and ease of use, and
- Assess the ability of the selected NDT methods to detect defects in concrete structures and provide recommendations on which NDT methods ALDOT should implement.

1.3 RESEARCH METHODOLOGY

This study was conducted to analyze various nondestructive testing techniques for the Alabama Department of Transportation, and to eventually construct a full-scale testing site for state department of transportation personnel to perform training, calibration, evaluation of new NDT methods. In order to complete the project objectives, twenty bridge deck specimens, measuring 3 × 7 ft, were constructed in the laboratory at Auburn University's Department of Civil Engineering. Various artificial defects were cast into these specimens for the purpose of determining artificial defect construction methods that accurately simulated defective or distressed concrete. Candidate nondestructive testing methods were used to survey these laboratory specimens; those methods were evaluated for their respective strengths and limitations in surveying for defects within reinforced concrete bridge decks.

Once the survey of laboratory specimens was complete, and all data was analyzed, the full-scale bridge deck NDT site was designed and constructed. Defect construction methods that accurately replicated defective and distressed concrete were selected for use in the full-scale test site.

1.4 THESIS OUTLINE

The existing research and literature related to all aspects of this project are presented in Chapter 2. First, traditional condition assessments used to evaluate concrete bridge decks are discussed. Next, common types of defects and distresses occurring in concrete bridge decks are detailed, as well as an overview of literature describing the manufacture of artificial defects in

concrete elements. Lastly, an overview of nondestructive testing methods that covers the principles, procedures, advantages and limitations of each process is included.

In Chapter 3, the experimental plan developed for this research study is presented. First, the NDT methods that were evaluated over the course of this project are discussed, as well as a description of how the different testing methods were performed. Next, an overview of the design of the test specimens is presented. Finally, details of the construction of all test specimens are described.

The results obtained during this research study are presented in Chapter 4. First, an evaluation of the NDT methods used by the research team are discussed. Next, results of testing the laboratory specimens are presented, followed by an evaluation of the methods used to create defects within the laboratory specimens. Finally, a summary of results obtained is offered.

In Chapter 5, the design and construction of the full-scale NDT testing site is outlined. First, a design of the full-scale bridge deck NDT site is detailed. Next, construction of the full-scale bridge deck NDT site is described. Finally, a summary of the layout of defects within the full-scale bridge deck NDT site is presented.

A summary of the research project is presented in Chapter 6. This chapter also describes the conclusions drawn from the study, as well as recommendations made from this research.

In Appendix A, raw concrete sampling data are presented, including fresh properties of concrete cast during laboratory experimentation, as well as raw compressive strength data of NDT bridge elements. Appendix B contains design drawings of NDT bridge elements.

CHAPTER 2

LITERATURE REVIEW

2.1 INTRODUCTION

In this chapter, a literature review of nondestructive testing methods is presented. An overview of the traditional forms of concrete bridge deck assessment is detailed in Section 2.2. In Section 2.3.1, the types of distresses that commonly occur in reinforced-concrete bridge decks are presented, followed by methods for manufacturing artificial defects in Section 2.3.2. Concluding the literature review is Section 2.4, where a background of the nondestructive tests evaluated in this project is provided.

2.2 OVERVIEW OF TRADITIONAL CONDITION ASSESSMENT METHODS

Prior to societal advances in technology, nondestructive testing was limited to a basic form of human-structure interaction. The technology used to automate tests in present day had not been developed, therefore test performance and results were based upon operator observation and skill, often yielding subjective results. Traditional forms of assessment methods are visual condition assessments, as well as sounding methods.

2.2.1 Visual Condition Assessment

Visual inspection of bridge deck condition is the most commonly used assessment method for bridges and serves as a baseline from which other, more in-depth methods may be applied (Moore, et al. 2001). Because of its simplicity and variability compared to other methods, a visual assessment is typically one of the first methods employed during evaluation of a bridge. Inspectors may look for cracks, pop-outs, spalling, disintegration, color change, weathering, staining, surface blemishes and lack of uniformity (International Atomic Energy Agency 2002).

Initial elements of a visual inspection consist of a walk-through inspection to observe the structure and the collection of any background documents detailing design and construction of the bridge (ACI 228 2013). Any visible surface cracking may be observed, mapped, and documented. At particular areas of interest, optical magnification could be used to more closely observe the local areas of slab distress, and a crack comparator may be used to measure and

notate the width of cracks present (ACI 228 2013). In some cases, scoping technologies, such as fiberscopes, bore scopes or small video cameras, may be used to observe regions within the slab that are inaccessible to the naked eye (ACI 228 2013). Use of these tools requires drilling small holes into the regions of interest, if other access channels are not already present (ACI 228 2013).

While visual assessment is a necessary tool for monitoring health of bridges, it is limited by the skill of the inspector and results will likely be subjective. Additionally, a visual inspection does not reveal defects present within the slab that are not distinguishable from the surface. Visual assessments should be supplemented by a series of NDT methods to provide proper condition assessment of a bridge deck (ACI 228 2013).

2.2.2 Sounding Methods

Sounding methods are some of the earliest forms of nondestructive testing where a user applies a stimulus to the concrete structure and observes a reaction. The two most common forms of sounding methods used are chain dragging and hammer sounding. The objective of these sounding methods is to detect regions of the deck where the sound created by either striking the surface with a hammer or dragging the chain changes from a clear ringing sound, which indicates a sound deck, to a somewhat mute and hollow sound, which indicates a delaminated deck (Gucunski, et al. 2013). The presence of a delamination changes the frequency of oscillation of the concrete in the bridge deck and, subsequently, the audible response of the deck (Gucunski, et al. 2013).

Chain dragging is performed exactly as the name implies. The procedure consists of the user dragging a chain over the bridge deck surface and listening for any changes in sound, indicating a delaminated deck (ASTM D4580 2018). Performing a hammer sounding test consists of striking the surface of the slab with a metallic hammer and listening for any tonal differences indicating presence of a delamination (ASTM D4580 2018). The process of performing chain dragging and hammer sounding can be seen in Figure 2-1 and Figure 2-2, respectively. In either case, areas indicating a delamination within the bridge deck are then notated on the bridge deck surface, after which they are mapped for analysis. Chain dragging is a method better suited to quickly locate general regions of delamination when testing over a large area, whereas hammer sounding, because it is characterized by individual point testing, is

more applicable for accurately defining the boundaries of delaminated areas (Gucunski, et al. 2013).

Figure 2-1: Typical chain dragging method (Gucunski, et al. 2013)

Figure 2-2: Typical hammer sounding method (Gucunski, et al. 2013)

Chain dragging and hammer sounding are well-established methods. Even today, both are common inspection methods used by state departments to detect delaminated areas in bridge decks (Gucunski, et al. 2013). Both methods are advantageous in that they are relatively simple methods, requiring minimal training, accompanied by a simple mapping process. Contrary to the benefits, these methods have a number of limitations and disadvantages. The tests are largely subjective, as results are based on the operator's skill level and hearing ability (Gucunski, et al. 2013). Additionally, the methods struggle to reveal early-stage delaminations, as those delaminations produces oscillations outside the audible range and therefore cannot be detected

by the human ear (Gucunski, et al. 2013). Finally, these methods are labor intensive and require traffic control, preferably in the form of bridge closure to ensure worker safety and test accuracy. Any lane closure or bridge closure can become expensive for the bridge owner over long durations.

2.3 BRIDGE DECK DISTRESSES

During their life cycle, bridges experience many distresses, brought on by both human and natural causes. This section presents and discusses the most common and concerning forms of distress found in concrete bridge decks, as well as methods for manufacturing artificial defects in concrete elements for analysis in a controlled (e.g. laboratory) setting.

2.3.1 Types of Distresses and Defects

Reinforced-concrete bridge decks incur a loss of structural integrity over time due to causes such as poor construction, penetration of deicing salts, freeze-thaw cycling, overloading, fatigue, and corrosion of the reinforcing steel (Gucunski, et al. 2013). These developments of deterioration are complex in nature and often impact one another (Gucunski, et al. 2013). It is critical to monitor bridge decks, detect these distresses early in their development, and mitigate and address the damage in order to keep costs at a minimum. The common types of distresses and defects that plague reinforced-concrete bridge decks and pose the greatest concern to bridge engineers are corrosion of the reinforcing steel, horizontal delaminations, vertical cracking, honeycombing and concrete degradation (Gucunski, et al. 2013).

2.3.1.1 Corrosion

Concrete is a material with high alkalinity. Because of that high alkalinity, embedded reinforcing steel is protected with a passive film on the steel surface (Emmons 1994). When the protective oxide film is destroyed, an electric cell is formed at the reinforcing steel, and the electrochemical reaction commonly known as corrosion is allowed to take place (Gucunski, et al. 2013).

The American Concrete Institute (ACI) defines corrosion as “an electrochemical process that involves electron transfer between different species at the steel-concrete interface” (ACI 222 2019). When no external electrical source is present to drive the reaction, electron transfer occurs between two half-cell chemical reactions; one reaction is capable of producing electrons

while the other reaction is capable of consuming electrons (ACI 222 2019). Corrosion requires an anode, cathode and electrolyte; reinforcing steel provides both the anode and cathode required for the electrochemical reaction, while moisture entrained within the concrete matrix acts as an electrolyte (Emmons 1994). Some areas of the reinforcing steel become anodes, allowing iron ions to enter into solution with oxygen, while other areas of the reinforcing steel act as cathodes and receive current resulting in formation of hydroxide ions (Gucunski, et al. 2013). Corrosion rate depends on concrete cover, humidity, temperature, pH of water in the concrete, and exposure to pollution and salt, among other factors (Gucunski, et al. 2013). The two main forms of reinforcement corrosion are chloride-induced corrosion and carbonation (Gucunski, et al. 2013).

Chlorides become introduced to concrete in marine environments or cold environments where deicing salts are used on roadways. Chlorides on the surface of the concrete diffuse through the concrete matrix and eventually reach the reinforcing steel, and if the chlorides reach a critical threshold, then corrosion will begin (Emmons 1994). A representation of chloride-induced corrosion is shown in Figure 2-3. As rust builds up at the reinforcement layer, the section area of the steel expands due to the presence of oxides, resulting in tensile forces causing the adjacent concrete to crack (Emmons 1994). When cracking begins to occur, chlorides, oxygen and moisture are able to more easily penetrate the concrete, thereby accelerating the corrosion process (Emmons 1994). Eventually, concrete will delaminate and then begin to spall off, exposing the reinforcing steel.

The method of corrosion of reinforcing steel due to carbonation is relatively similar to that of chloride-induced corrosion. Carbon dioxide in the air, which is typically higher in industrial and urban atmospheres, diffuses into the pores of the concrete matrix and reacts with calcium hydroxide in the concrete (Emmons 1994). Subsequently, the alkalinity of the concrete is reduced, and the passive protection of the reinforcing steel is lost (Emmons 1994). In an acidic or mildly alkaline environment, where oxygen and moisture are present, corrosion takes place (Emmons 1994).

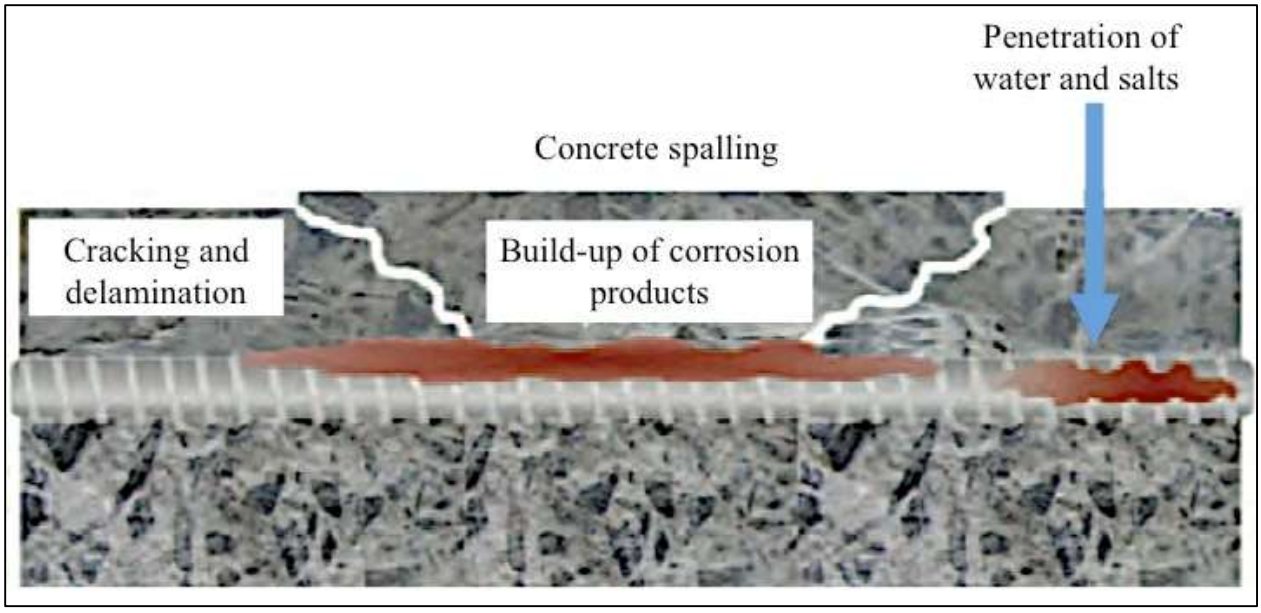

Figure 2-3: Method of chloride-induced corrosion (Adapted from Gucunski, et al. 2013)

In either case, unaddressed corrosion over a period of time can cause severe damage to reinforced-concrete bridge decks. Aggressive corrosion can cause a loss in bridge deck structural capacity due to both section loss of steel and cracking of surrounding concrete (Emmons 1994). Section loss of the reinforcing steel, like that shown in Figure 2-4 and Figure 2-5, results in a higher steel stress under the same loading due to reduced cross-sectional area. Additionally, the delamination of surrounding concrete reduces the concrete's contribution to load resistance as well as its protection of the reinforcing steel.

Figure 2-4: Reinforcing steel with severe corrosion (ACI 364 2017)

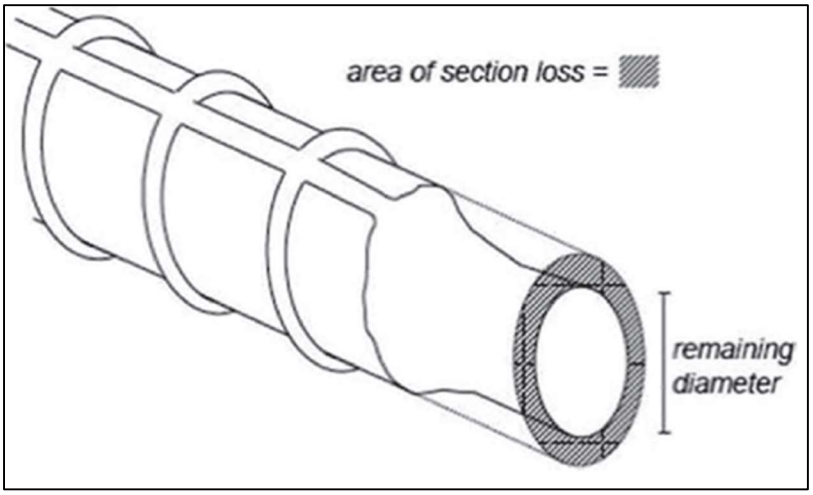

Figure 2-5: Diagram of section loss due to corrosion (ACI 364 2017)

2.3.1.2 Delaminations

ACI defines a delamination as "a planar separation in a material that is roughly parallel to the surface of the material" (American Concrete Institute 2018). These cracks are formed from the expansion of reinforcing steel brought on by corrosion (Gucunski, et al. 2013). These delaminations manifest themselves as cracks or as a larger fracture plane at the layer of the reinforcing steel, as shown in Figure 2-6 (Gucunski, et al. 2013). Excessive early-age temperature gradients and drying shrinkage gradients can also cause delaminations, as shown in Figure 2-7. During a concrete's curing process, heat is created as the cementitious materials within the mixture hydrate. As the reaction slows, the temperature of the concrete falls, causing a slight volumetric decrease within the concrete. Additionally, excess water within the concrete mixture may evaporate during the curing process, causing further decrease in concrete volume. If the concrete is restrained from expanding and contracting, as is the case with most bridge decks, tensile stresses beyond the strength of the concrete may develop, causing delaminations to occur within the concrete. Delaminations can occur in a single location or can manifest themselves over a large area, depending on the magnitude of stress applied to the concrete. Delaminations are subsurface cracks, meaning that they are not visible from the surface of the bridge deck, until corrosion becomes so severe that its expansive forces become greater than the concrete cover can resist (Emmons 1994).

Figure 2-6: Delaminated core (Gucunski, et al. 2013)

Figure 2-7: Delaminated core from the US 331 bridge deck (Schindler, et al. 2010)

2.3.1.3 Vertical Cracking

Vertically oriented cracks can be caused by a variety of different mechanisms, including shrinkage, thermal effects, and traffic loading, among others (Gucunski, et al. 2013). Shrinkage cracking can often occur in bridge decks because of their planar configuration. Over time, as

concrete loses water to the atmosphere, shrinkage occurs within the specimen (Emmons 1994). If the concrete specimen is unrestrained, then no cracking occurs; alternatively, if the specimen is restrained, as is the case with most bridge decks, the build-up of stresses may surpass the tensile strength of the concrete, causing cracking to occur (Emmons 1994).

Concrete can also undergo cracking due to thermal effects, whether from hydration heat or ambient temperature change (Gucunski, et al. 2013). During its curing process, concrete experiences heating as the cementitious materials hydrate. As the concrete hardens and its temperature decreases, the specimen experiences small volumetric changes due to the decrease in temperature. Depending on the early age strength of the concrete and the temperature change experienced by the concrete, cracking could result (Emmons 1994). Additionally, ambient temperature changes through different seasons can cause expansion and contraction of bridge decks, which can lead to cracking if the structure is restrained. The effect of vertical cracking due to high thermal stresses is shown in Figure 2-8 below.

Figure 2-8: Core displaying cracking due to restrained drying and thermal shrinkage (Schindler, et al. 2010)

Vertical cracking of the bridge deck could also occur due to traffic loading, both as transverse flexure of the slab between beams or longitudinal flexure of the composite system at

interior supports of continuous spans. As the structural members undergo flexural stress, cracks could form in the slab if the induced flexural stresses increase beyond the tensile strength of the concrete. Vertically oriented cracks, especially those due to loading, are largely the concern of validation and load testing (Gucunski, et al. 2013).

2.3.1.4 Honeycombing and Voids

When referring to concrete construction, a honeycomb can be defined as a void left in the concrete due to failure of the mortar to effectively fill the areas surrounding coarse aggregates (Emmons 1994). An example of honeycombed concrete can be seen in Figure 2-9. Honeycombing can occur due to many different causes. Improper design of members can yield honeycombing due to congestion of reinforcement, narrow section design, and a concrete mixture design with oversized coarse aggregate, insufficient fine aggregate, or low workability (Emmons 1994). Additionally, poor construction practices such as leaking forms, insufficient concrete cover, excessive free-fall, improper tremie, or inadequate consolidation can lead to the formation of honeycombs or rock pockets within the concrete structure (Emmons 1994). Honeycombed areas have low strength properties. Some may be seen from the surface, while others can occur subsurface and are only detectable through concrete assessment techniques.

Figure 2-9: Honeycombed concrete (Mishra n.d.)

2.3.1.5 Concrete Degradation

Concrete degradation is any form of reduction of strength or modulus of a concrete structure (Gucunski, et al. 2013). Concrete degradation can be a result of microcracking, delayed

ettringite formation (DEF), alkali-silica reaction (ASR), freeze-thaw cycles or plastic shrinkage (Gucunski, et al. 2013). DEF is a form of sulfate attack that is believed to mainly occur from a lack of heat control during the curing phase of concrete (Gucunski, et al. 2013). For DEF to occur, internal temperature of a plain portland cement specimen must be above approximately 160°F and the specimen must be kept moist almost permanently (Taylor, Famy and Scrivener 2000). Research suggests that monosulfate from clinker is intimately mixed with calcium-silicate hydrate (C-S-H) at the end of the heat treatment, and that if conditions are suitable for expansion, ettringite is then mixed with C-S-H (Taylor, Famy and Scrivener 2000). This formation of ettringite causes expansion within the concrete, resulting in empty cracks forming around the aggregates (Gucunski, et al. 2013). The effect of DEF can be observed in Figure 2-10.

Figure 2-10: Surface cracking due to DEF distress (Taylor, Famy and Scrivener 2000)

ASR occurs when aggregates, such as reactive forms of silica, react with potassium, sodium and calcium hydroxide from the cement and create a gel around the reacting aggregates (Emmons 1994). When that gel is exposed to moisture, it expands, causing both internal and external tension cracking in the concrete (Emmons 1994). This expansion and cracking can result in both structural deformation and the development of a network of cracking throughout

the structure, impairing the concrete strength (Gucunski, et al. 2013). An example of cracking due to ASR is shown in Figure 2-11.

Figure 2-11: ASR induced cracking and spalling (Afshinnia 2020)

Freeze-thaw disintegration occurs when pore water in the concrete structure freezes over and over due to exposure to low atmospheric temperatures over many years (Emmons 1994). That water expands as it freezes, causing local tension forces in the concrete that can lead to microcracking and macrocracking (Emmons 1994). Water can enter the system through concrete pores or vertical cracks brought on by a number of various mechanisms, including previous freeze-thaw cycles.

Plastic shrinkage can also cause concrete degradation by the same mechanism described in 2.3.1.3. Concrete loses water over time to the atmosphere, and shrinkage occurs within the specimen (Emmons 1994). Since bridge decks are restrained from freely shrinking, a build-up of tensile stresses are likely to occur, and if those stresses surpass the tensile strength of the concrete, cracking will occur (Emmons 1994).

2.3.2 Manufacturing of Artificial Defects in Concrete Elements

The manufacture of artificial defects is critical to the research documented in this report. Defects that occur naturally within concrete structures oftentimes occur over the course of a number of years and due to a number of different causes. The defects also occur in a variety of locations and can manifest themselves in different sizes based on the level of distress present.

Hence, artificial defects are needed in order to control the size and location of distresses within concrete so that accurate calibration and training on NDT equipment can be conducted. This section presents and discusses previous research performed to manufacture defects relating to corrosion, delaminations, vertical cracking, honeycombing and concrete degradation.

2.3.2.1 Corrosion

2.3.2.1.1 Almusallum, et al. (1996)

In 1996, Almusallum, et al. successfully performed accelerated corrosion techniques on reinforced-concrete slabs in order to test the effect of corrosion on slab flexural behavior. Reinforced-concrete slabs were constructed to be 12 × 28 × 2.5 in. (305 × 711 × 63.5 mm) using approximately 4,500 psi concrete and No. 2 (6 mm) Grade 60 reinforcing bars spaced at 2.25 in. (57 mm) (Almusallam, et al. 1996). The specimens were partially immersed into a five percent sodium chloride solution and connected to five stainless steel plates (Almusallam, et al. 1996). The system was then connected to a direct current rectifier, with the reinforcing steel serving as the anode and the stainless steel plates serving as the cathode, and 2 amps (A) of current was applied to the specimens, as shown in Figure 2-12 (Almusallam, et al. 1996). A calibration curve was developed, establishing a relationship between the duration of applied current and the resulting degree of steel corrosion, which allowed the researchers to gain the desired amount of corrosion (Almusallam, et al. 1996).

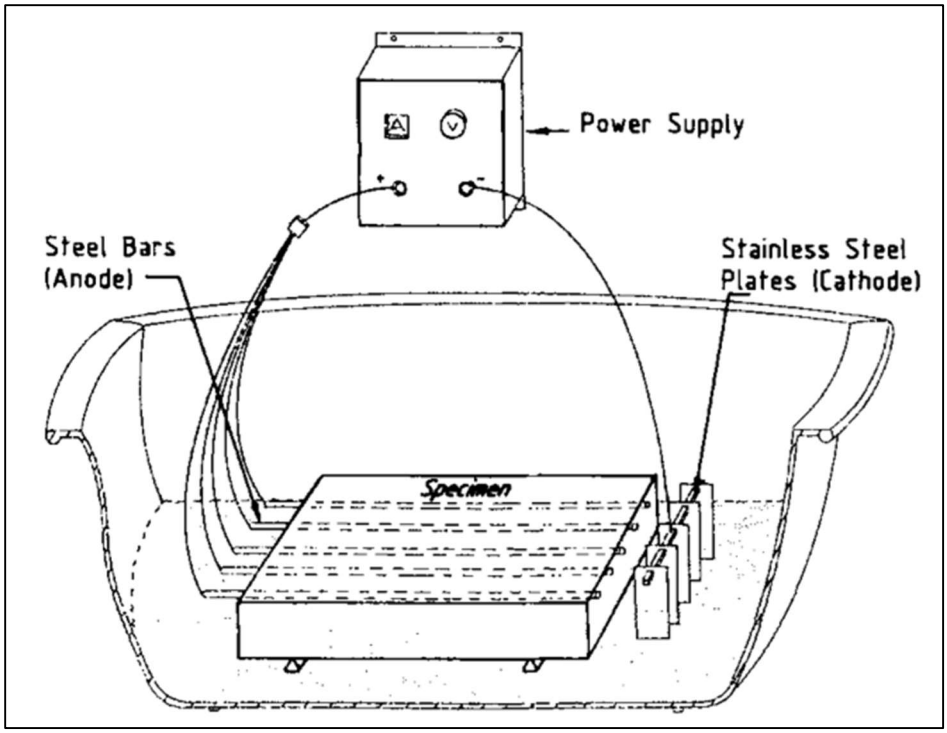

Figure 2-12: Accelerated corrosion setup (Almusallam, et al. 1996)

2.3.2.1.2 Jayaprakash, Pournasiri and De'nan (2012)

Jayaprakash, Pournasiri and De'nan successfully used accelerated corrosion techniques to test the effect of bond strength in concrete cylinders enveloped in fiber-reinforced polymer with reinforcing steel exposed to corrosion activity. Concrete cylinders measuring 4 × 8 in. (100 × 200 mm) were cast with 4,300 psi (30 MPa) concrete in a laboratory condition with a single piece of 0.79 in. (20 mm) diameter reinforcing steel embedded 5.9 in. (150 mm) from the top of the cylinder (Jayaprakash, Pournasiri and De'nan 2012). The cylinders were cured for 28 days, after which they were wrapped in various types of fiber-reinforced polymer (Jayaprakash, Pournasiri and De'nan 2012). Specimens were then immersed in a five percent sodium chloride solution for 6, 12 or 24 days; the level of solution was kept 1.6 in. (40 mm) below the top of the cylinders, as shown in Figure 2-13 (Jayaprakash, Pournasiri and De'nan 2012).

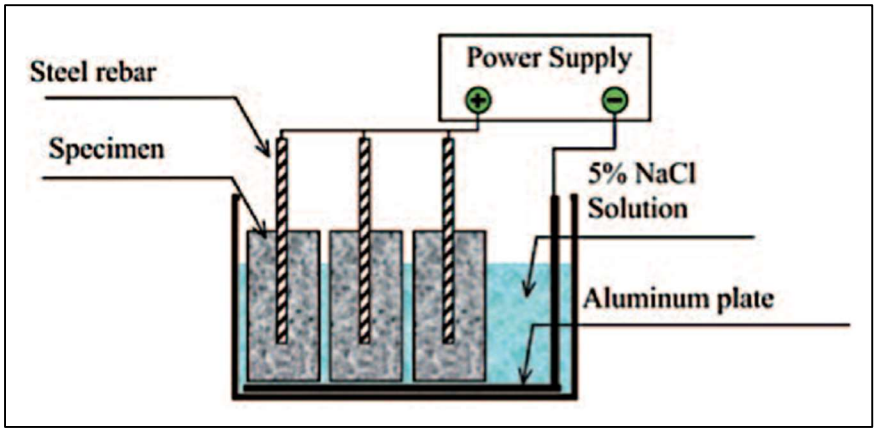

Figure 2-13: Accelerated corrosion setup (Jayaprakash, Pournasiri and De'nan 2012)

2.3.2.1.3 Guo, et al. (2015)

Guo, et al. (2015) successfully employed accelerated corrosion techniques on four single shaft piers in order to investigate the seismic capacity of corroded bridge piers. Four columns measuring 10.5 ft (3.2 m) in height, including footing thickness, with a cross sectional area of approximately 10 × 24 in. (0.25 × 0.6 m) were constructed with 6,300 psi (43 MPa) strength concrete (Guo, et al. 2015). Twelve steel bars measuring 0.63 in. (16 mm) in diameter served as the longitudinal reinforcement, while 0.31 in. (8 mm) diameter bars served as rectangular ties in the column (Guo, et al. 2015). The clear cover to the first layer of reinforcing steel was 1 in. (25 mm) (Guo, et al. 2015). The reinforcing steel, both longitudinal and transverse, was set as the anode in the electrochemical reaction, while a stainless steel mesh surrounding the columns functioned as the cathode (Guo, et al. 2015). The bottom of each specimen was enclosed by a tank filled with 3.5 percent sodium chloride solution (Guo, et al. 2015). Specimens were designed to have corrosion levels corresponding to five percent, ten percent and fifteen percent steel loss (Guo, et al. 2015). A diagram of the accelerated corrosion process is shown in Figure 2-14.

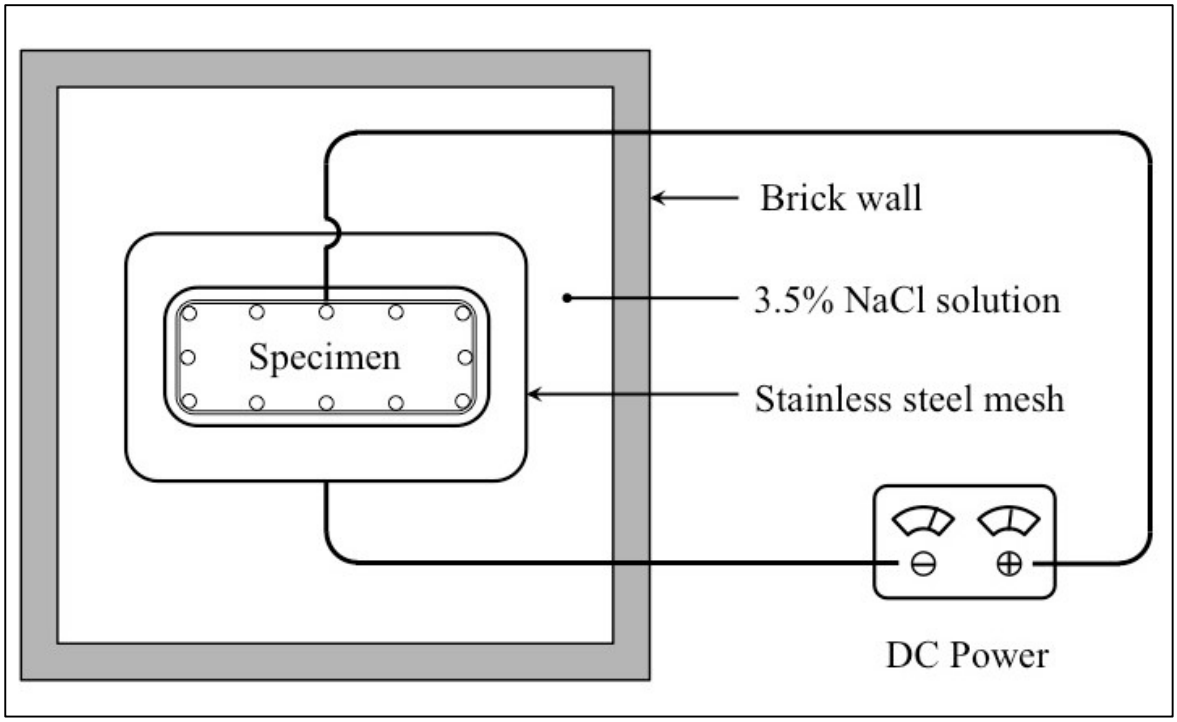

Figure 2-14: Accelerated corrosion setup (Adapted from Guo, et al. 2015)

Guo et al. also provides an equation for predicting steel mass loss by using Faraday's Law in the following formula:

$$\eta = \frac{\Delta m}{M} = \frac{M i_{cor} t}{F d \rho} \qquad \text{Equation 2.1}$$

where η is the corrosion rate (%); Δm is the mass loss (g); M is the molar mass of the iron atom (55.85 g/mol); i_{cor} is the corrosion current density (A/m^2); t is the accelerated corrosion time (s); F is the Faraday constant (96,485 C/mol); d is the radius of the steel bar (m); q is the density of the steel material (7.8×10^3 kg/m^3). This equation was used to determine the required applied current and current duration to reach the desired level of corrosion damage (Guo, et al. 2015).

2.3.2.1.4 BAM Division 8.2 (2018)

The Federal Institute for Materials Research and Testing in Germany used accelerated corrosion techniques in an experiment to create a reinforced-concrete specimen with deteriorated reinforcing steel with the goal being to control the corrosion rate and steel material loss through use of electric current over a set period of time (BAM Division 8.2 2018). The basic setup of the experiment showing the principle of the application was a single concrete block with two metal rods spaced approximately 2 in. (5 cm) apart, one serving as the anode and the other acting as the cathode (BAM Division 8.2 2018). When connected to an electrical source, current flows from

the negative rod to the adjacent rod, causing it to corrode so long as the bond between concrete and metal is sufficient (BAM Division 8.2 2018). A diagram of the accelerated corrosion principle is shown in Figure 2-15. The actual experiment was performed on a larger concrete specimen with dimensions of 37 × 17.5 in. (900 × 450 mm) (BAM Division 8.2 2018). Six pairs of 8 in. (200 mm) long steel rods, spaced at 2 in. (50 mm), were connected to independent electrical sources (BAM Division 8.2 2018). Cables separately connected each pair of steel bars to an external electrical source, which provided current for an allotted time period, as shown in Figure 2-16 (BAM Division 8.2 2018).

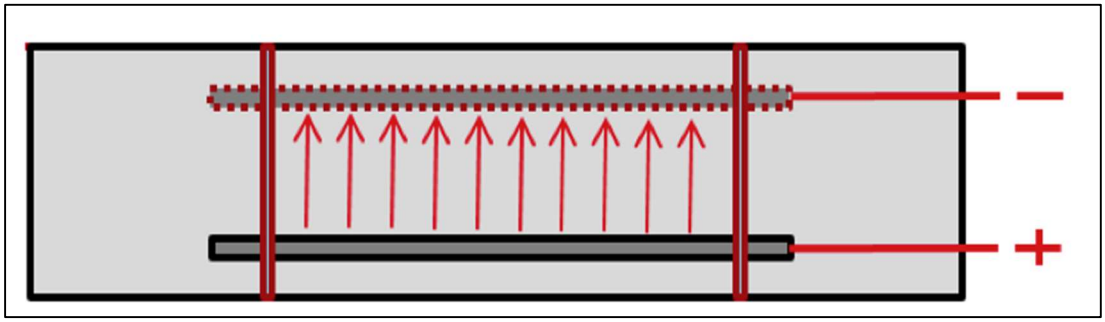

Figure 2-15: Accelerated corrosion principle (BAM Division 8.2 2018)

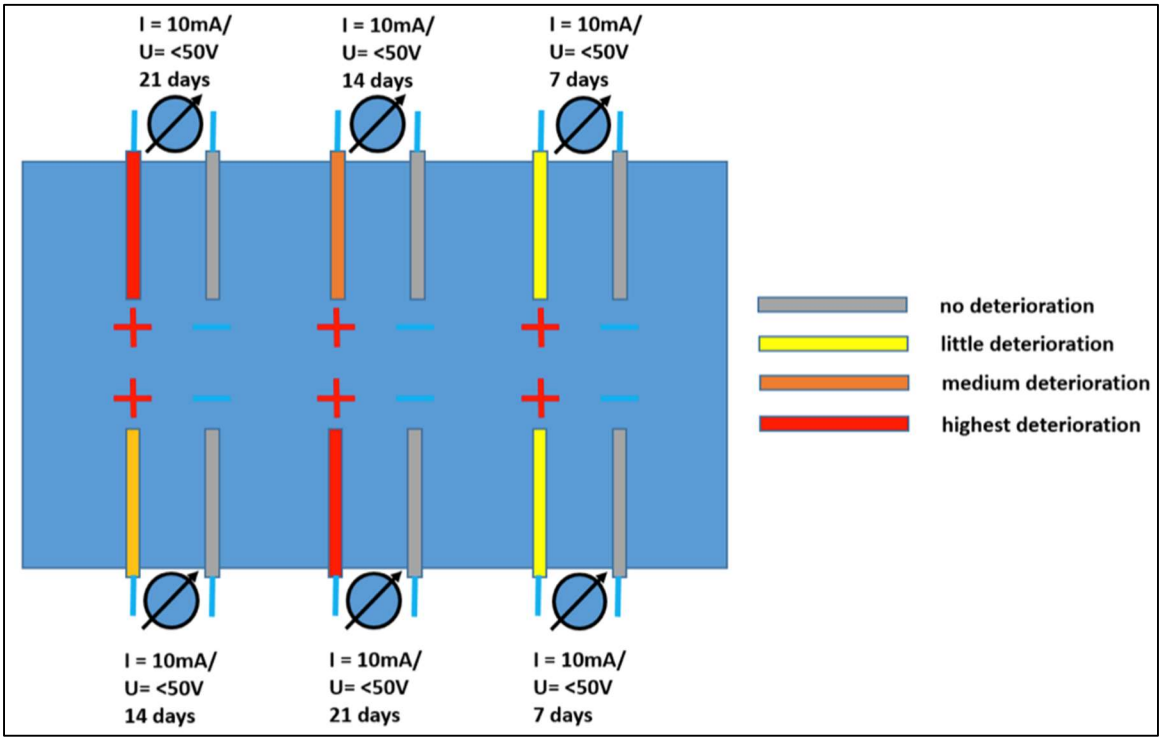

Figure 2-16: Accelerated corrosion setup (BAM Division 8.2 2018)

2.3.2.2 Delaminations

2.3.2.2.1 Sansalone and Carino (1989)

In 1989, Sansalone and Carino employed the use of artificial delaminations for the purpose of testing the reliability of the impact echo method in detecting delaminated areas in reinforced-concrete bridge decks with and without overlays. A 7.9 in. (200 mm) thick reinforced-concrete slab measuring 9.8 × 4.9 ft (3.0 × 1.5 m) was cast with a top and bottom layer of welded wire fabric reinforcement (Sansalone and Carino 1989). Thin sheets of plastic were embedded within the slab to simulate delaminations (Sansalone and Carino 1989). These thin plastic sheets were detectable using the impact-echo method (Sansalone and Carino 1989). A diagram of the slab specimen is provided in Figure 2-17.

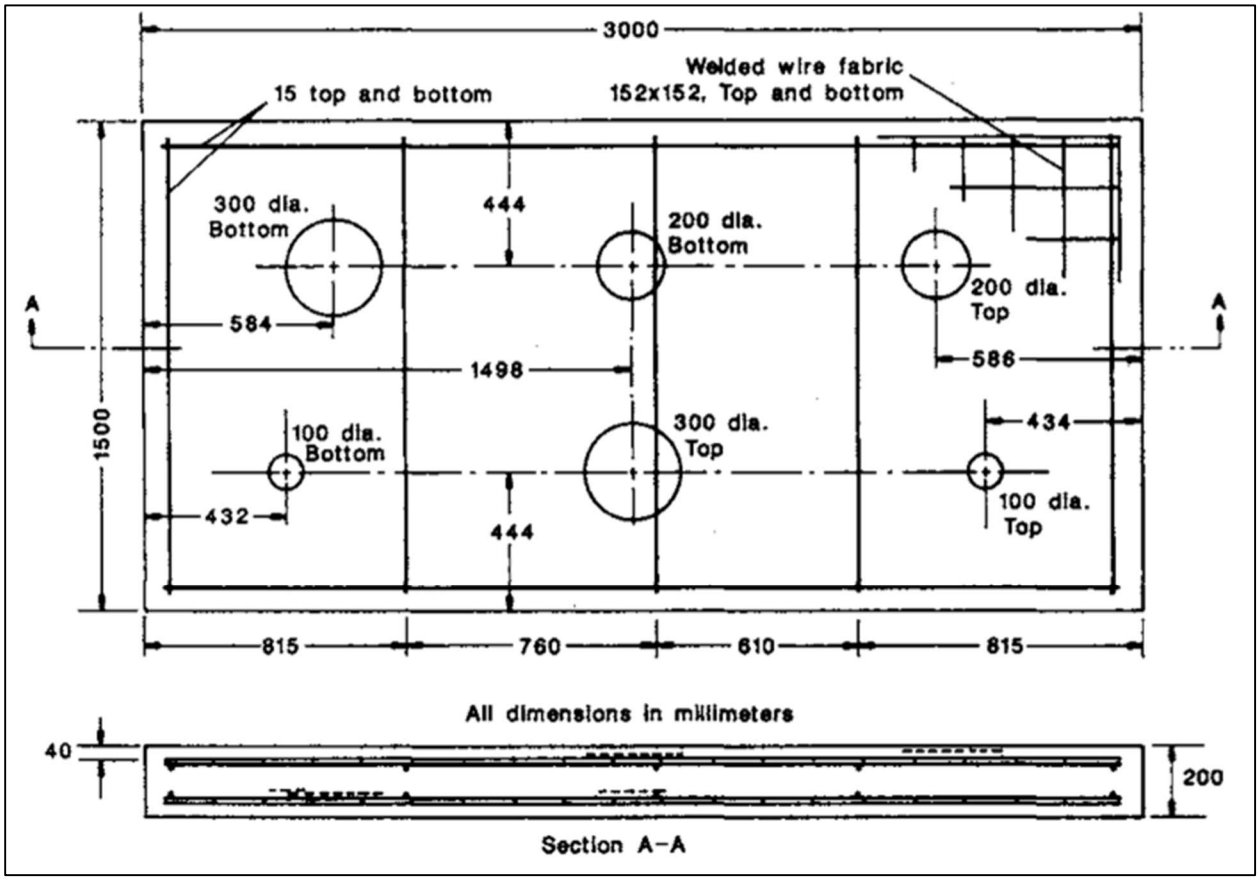

Figure 2-17: Plastic sheets used for delaminations (Sansalone and Carino 1989)

2.3.2.2.2 Cheng and Sansalone (1993)

Researchers at Cornell University used artificial delaminations in order to test the impact echo response of concrete plates containing delaminations. Controlled-flaw specimens consisted

of a 95 in. (2.4 m) long, 55 in. (1.4 m) wide, 8 in. (0.2 m) thick reinforced-concrete plate and a 120 in. (3 m) long, 60 in. (1.5 m) wide, 16 in. (0.4 m) thick plain concrete specimen (Cheng and Sansalone 1993). The reinforced-concrete plate was reinforced with 1 in. (25.4 mm) steel bars, with 1.5 in. (40 mm) cover to the top layer of reinforcement (Cheng and Sansalone 1993). Flexible foam sheets with a thickness of 0.2 in. (5 mm) replicated delaminations (Cheng and Sansalone 1993). Deep delaminations measured 16 in. (0.4 m) in diameter and were placed 12 in. (0.3 m) below the slab surface; shallow delaminations measured 8 in. (0.2 m) in diameter and were placed 4 in. (0.1 m) below the slab surface (Cheng and Sansalone 1993). These simulated delaminations were able to be detected and characterized using the impact-echo method (Cheng and Sansalone 1993). A diagram detailing the research setup is shown in Figure 2-18.

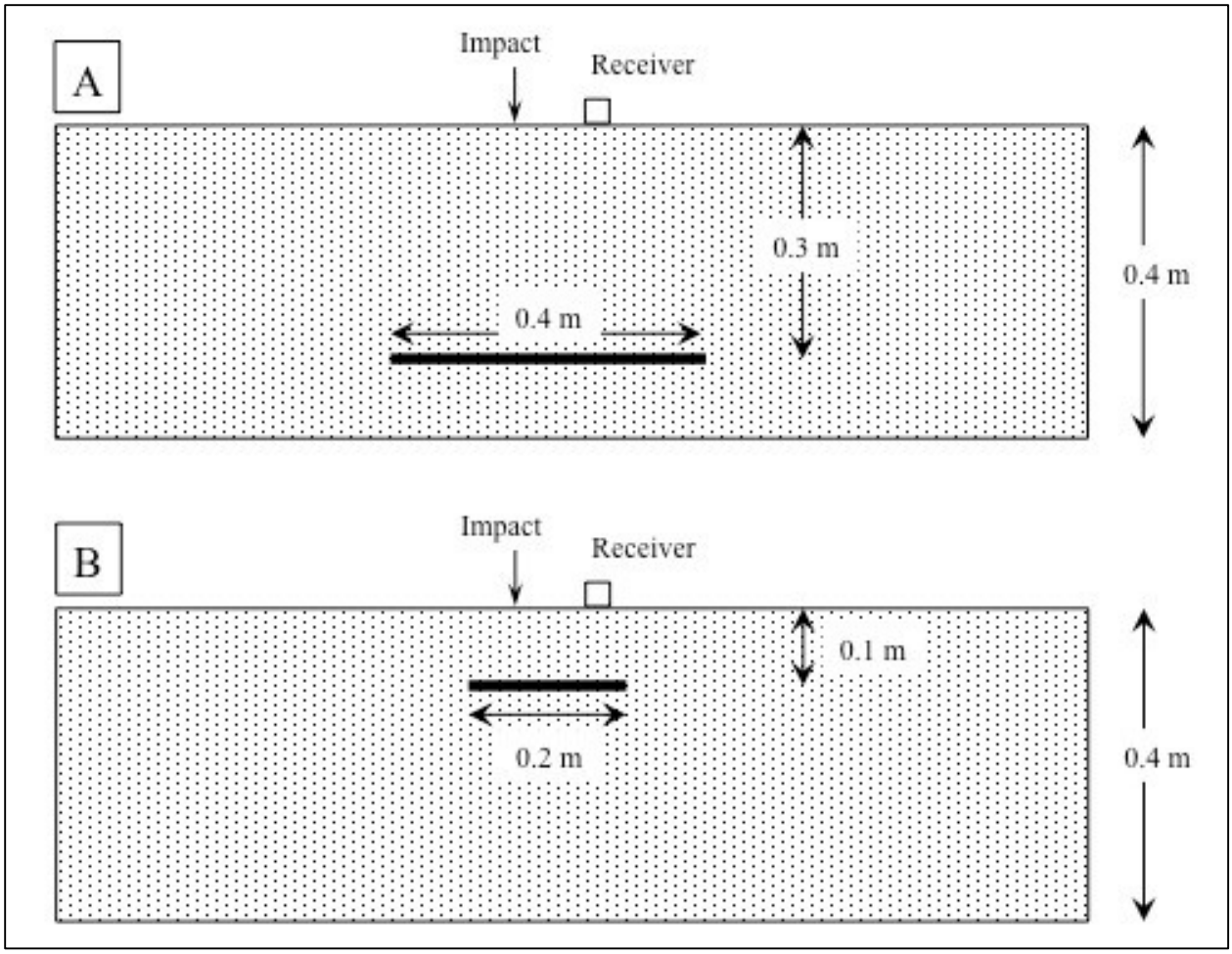

Figure 2-18: Foam sheets used as (A) deep and (B) shallow delaminations (Cheng and Sansalone 1993)

2.3.2.2.3 Cotič et al. (2015)

Cotič et al. (2015) employed the use of artificial delaminations in order to test the limits of infrared thermography to detect delaminations in concrete structures. Four test specimens were created using the same concrete mixture (Cotič, et al. 2015). Acrylic sheets that were 0.4 × 0.4 in. (10 × 10 cm) and were approximately 0.2 in. (5 mm) thick were placed into the specimens to act as delaminations (Cotič, et al. 2015). These simulated delaminations were able to be detected using the infrared thermography method (Cotič, et al. 2015).

2.3.2.2.4 Lin and Sansalone (1996)

Lin and Sansalone (1996) used artificial delaminations in order to study interface bond quality in concrete. The test specimens constructed as a portion of the laboratory experimental procedure measured 70 × 70 in. (1.8 × 1.8 m) in plan view, with a thickness of 12 in. (0.3 m) (Lin and Sansalone 1996). Delaminations were created using four thin Styrofoam sheets measuring 16 × 16 in. (0.4 × 0.4 m) in plan view, and placed 4 in. (0.1 m) below the surface of the concrete (Lin and Sansalone 1996). These foam sheets were cut into a checkerboard pattern to simulate unbonded area fractions valuing 0.2, 0.5, 0.8 and 1.0 (Lin and Sansalone 1996). These values represent the ratio of the amount of bonded area to the total area of the sheet. This study showed that the impact-echo method was able to detect interfaces with unbonded fractions greater than 0.2, or twenty percent (Lin and Sansalone 1996).

2.3.2.2.5 Lin, Sansalone and Poston (1996)

Lin, Sansalone and Poston (1996) employed the use of artificial delaminations in order to study interface bond quality in concrete. Test specimens constructed as part of the laboratory experimental investigation measured 60 × 70 in. (1.5 × 1.8 m) in plan view (Lin, Sansalone and Poston 1996). One specimen, which was constructed to examine the effects of a weak interface on impact-echo response, was delaminated using a layer of sand (Lin, Sansalone and Poston 1996).

2.3.2.3 Vertical Cracking

2.3.2.3.1 Lin, et al. (2018)

Lin, et al. (2018) implemented artificial vertical cracking in a reinforced-concrete bridge deck for the purpose of assessing nondestructive evaluation methods on bridge decks with overlays at the Turner-Fairbank Highway Research Center in Virginia. Concrete bridge specimens were constructed to be 120 × 40 × 8 in. with both transverse and longitudinal reinforcing steel spaced at 8 in. on center (Lin, et al. 2018). Each specimen had a variety of defects within. Artificial vertical cracks were simulated with corrugated plastic sheets having heights of 2.5 in. at the center and 6 in. near the edge, which simulated varying depths of open cracks (Lin, et al. 2018).

2.3.2.4 Honeycombing and Voids

2.3.2.4.1 Maierhofer (2003)

In 2003, a researcher at the Federal Institute for Materials Research and Testing in Germany used artificial voids in order to study the science behind ground penetrating radar. Eight polystyrene blocks, measuring either 8 × 8 × 4 in. (20 × 20 × 10 cm) or 4 × 4 × 4 in. (10 × 10 × 10 cm), were placed at varying positions within the concrete test specimen, which measured 60 × 60 × 20 in. (1.5 × 1.5 × 0.5 m) (Maierhofer 2003). Polyamide threads in the wooden formwork held the polystyrene blocks in place during casting (Maierhofer 2003).

2.3.2.4.2 Lin et al. (2018)

Lin et al. (2018) also implemented artificial honeycombing and voids in the reinforced-concrete bridge deck for the purpose of assessing nondestructive evaluation methods on bridge decks with overlays. Artificial honeycombing was replicated by a bag of loose aggregates covered by a thin layer of concrete (Lin, et al. 2018). This served to replicate concrete mixtures with a lack of integrity (Lin, et al. 2018). Artificial voids were created with a soft Styrofoam board, having dimensions of 12 × 8 × 2 in. (Lin, et al. 2018). The Styrofoam board was selected because it was a material with low wave impedance, comparable to that of air (Lin, et al. 2018).

2.3.2.4.3 BAM Division 8.2 (2018)

The Federal Institute for Materials Research and Testing in Germany also used artificial honeycombing in an experiment to create a reinforced-concrete specimen with honeycombed regions in order to test their suitability for NDT detection. A concrete specimen was constructed with dimensions of 48 × 48 × 16 in. (120 × 120 × 40 cm) (BAM Division 8.2 2018). The specimen was reinforced with a top and bottom layer of reinforcing steel, which consisted of 0.31 in. (8 mm) diameter steel bars spaced at 4 in. (10 cm) on center in both the longitudinal and transverse direction (BAM Division 8.2 2018). The clear cover from the surface to the first layer of reinforcing steel was 2 in. (5 cm) (BAM Division 8.2 2018). Nine honeycombs were comprised of a coarse-aggregate-rich concrete mixture (BAM Division 8.2 2018). The honeycombs were hemispherical in shape, each having a radius of 4 in. (100 mm) or 3 in. (75 mm) (BAM Division 8.2 2018). Photographs of some constructed artificial honeycombs are shown in Figure 2-19. All nine honeycombed regions could be detected using the ultrasound pulse-echo method.

Figure 2-19: Honeycombed implants (BAM Division 8.2 2018)

2.3.2.5 Concrete Degradation

2.3.2.5.1 Ham, et al. (2016)

In 2016, Ham, et al. employed the use of artificial concrete degradation in order to study the characterization of distributed cracking damage in concrete using a contactless surface wave method. In order to simulate artificial degradation and cracking damage within the concrete specimens, the researchers used polypropylene fibers measuring 0.04 in. (1 mm) in diameter and 2 in. (50 mm) in length (Ham, et al. 2016). The level of simulated damage was governed by the amount of polymer fibers added into the concrete mixture (Ham, et al. 2016). Three test specimens were created with fibers added at rates of 0.0 percent, 0.3 percent or 0.6 percent by volume (Ham, et al. 2016).

2.4 OVERVIEW OF NONDESTRUCTIVE TESTING METHODS

Advances in technology have allowed for tremendous progression in the field of nondestructive testing. Outlined in this section are the test principles, test procedures, applications and limitations of the various NDT methods employed throughout the course of this project. The following methods will be covered: impact echo, half-cell potential, surface resistivity, ground penetrating radar and infrared thermography.

2.4.1 Impact Echo

2.4.1.1 Test Principles

The impact echo method is a nondestructive testing method that was developed in the mid-1980s, with field instruments becoming commercially available in 1992 (Sansalone and Streett 1996). The method is based upon an impact-generated stress pulse that propagates throughout the structure. This pulse travels into the body of the concrete structure as dilatational (P-) and distortional (S-) waves and travels along its surface as a Rayleigh (R-) wave (Cheng and Sansalone 1993). P-waves and S-waves may also be described as compression and shear waves, respectively (Sansalone and Carino 1989). The P-and S-waves travel into the concrete along hemispherical wave fronts and are reflected by internal interfaces, such as cracks or voids, and by the external faces of the structure (Cheng and Sansalone 1993). These reflections are monitored by a receiver or transducer located adjacent to the impact location. A diagram showing a simplified version of the impact echo is displayed in Figure 2-20.

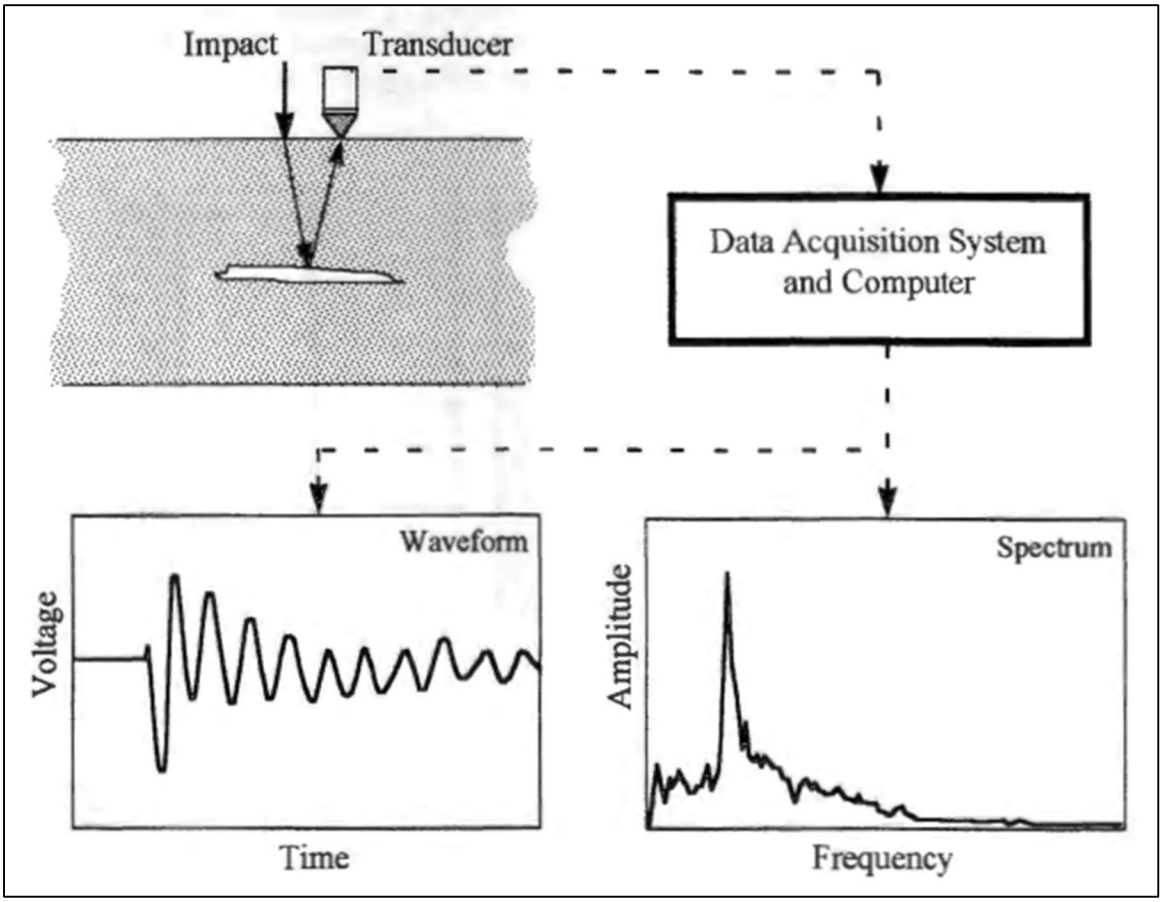

Figure 2-20: Simplified impact-echo method (Sansalone and Streett 1996)

When waves travel back to the surface, they are then reflected back in to the body of concrete, setting up a resonance condition between the internal defects and the external faces of the specimen (Cheng and Sansalone 1993). Because P-waves cause greater displacements near the point of impact than S-waves, the P-waves are of greater importance to the impact echo method (Cheng and Sansalone 1993). As P-waves arrive at the transducer, the time-domain signal is recorded by a data acquisition and analysis system connected to the transducer. From there, automated programs transform the time-domain signal into the frequency domain using the fast Fourier transform technique in order to determine the frequency of P-wave arrivals (Cheng and Sansalone 1993). Dominant frequencies are determined by peaks in the resulting amplitude spectrum (Cheng and Sansalone 1993). Once the dominant frequency for a point scan is determined, the depth to the reflection interface can be determined by the following equation:

$$d = \frac{C_p}{2f} \qquad \text{Equation 2.2}$$

where d is the depth to the reflection interface; C_p is the P-wave speed in the test object; f is the dominant frequency of P-wave reflections (Cheng and Sansalone 1993).

Additionally, delaminations can be characterized by wave response, as shown in Figure 2-21. Areas without delamination are characterized by a dominant frequency peak corresponding to the bottom of the bridge deck (Gucunski, et al. 2013). Delaminated areas will show dominant peaks corresponding to both the bottom of the deck and the delaminated interface, the latter becoming more prominent as the severity of delamination increases (Gucunski, et al. 2013). Shallow delaminations are characterized by a lower frequency response, which are a result of the slender, delaminated portion of the deck oscillating as a plate with restrained ends, exciting its flexural mode of response (Cheng and Sansalone 1993). This response will appear as a frequency lower than the return frequency of the bottom of the deck (Cheng and Sansalone 1993).

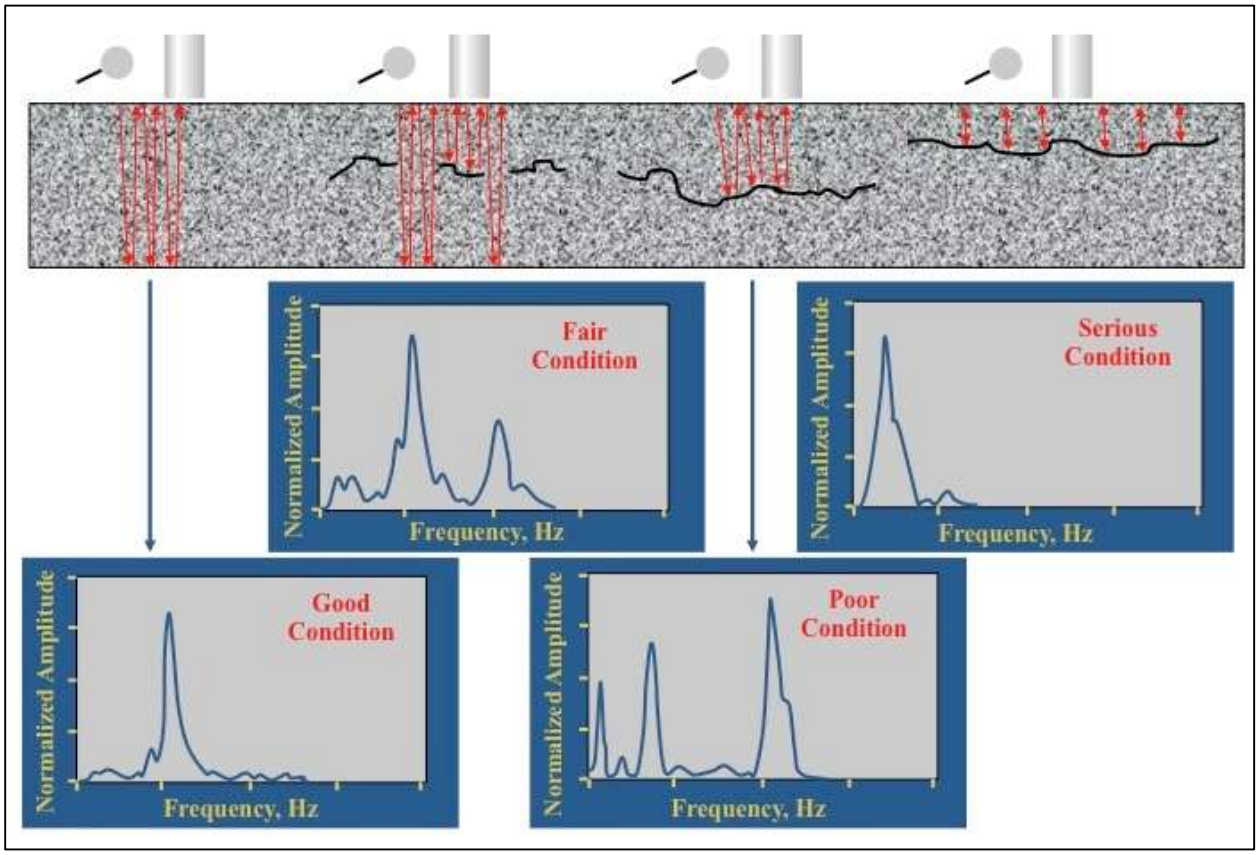

Figure 2-21: Impact-echo wave response (Adapted from Gucunski, et al. 2013)

2.4.1.2 Testing Procedure

Equipment needed to perform the impact echo method is a source of impact, a receiver, and a data acquisition and analysis system. The source of impact must be spherical and capable of producing an impact with duration of 30 ± 10 μs and adequate energy to produce surface displacements (ASTM C1383 2015). The receiver must be a broadband transducer capable of detecting the small, normal displacements corresponding to the arrival of the impact-driven P-waves (ASTM C1383 2015). The data acquisition system must be either a portable computer with two-channel data-acquisition capability or a two-channel waveform analyzer (ASTM C1383 2015). This system must be capable of sampling data at a frequency between 250 kHz and 500 kHz, with voltage range and resolution matched to the sensitivity of the transducer, and able to produce a readout of returning time and voltage (ASTM C1383 2015). Additionally, the system must operate from a power source, such as a battery, that does not produce electrical noise capable of interfering with data acquisition (ASTM C1383 2015).

Before beginning the impact echo testing procedure, all dirt and debris must be removed from the dry testing surface; if the surface is too rough to achieve adequate contact between the transducer tip and the concrete, it must be ground smooth (ASTM C1383 2015). The transducer is to be placed on the point at which the measurement is to take place, and the impactor shall be placed a distance less than 40 percent of the nominal deck thickness from the transducer (ASTM C1383 2015). The data acquisition system should be prepared with the adequate parameters, such as sample frequency, voltage range and trigger level (ASTM C1383 2015). The impact shall then be performed, after which the waveform shall be inspected to assure its validity by confirming that the wave follows the general correct shape of a typical valid impact echo test, similar to that shown in Figure 2-22 (ASTM C1383 2015). Once multiple valid tests have been accomplished, the testing for that particular point is complete and the user may move to another test point.

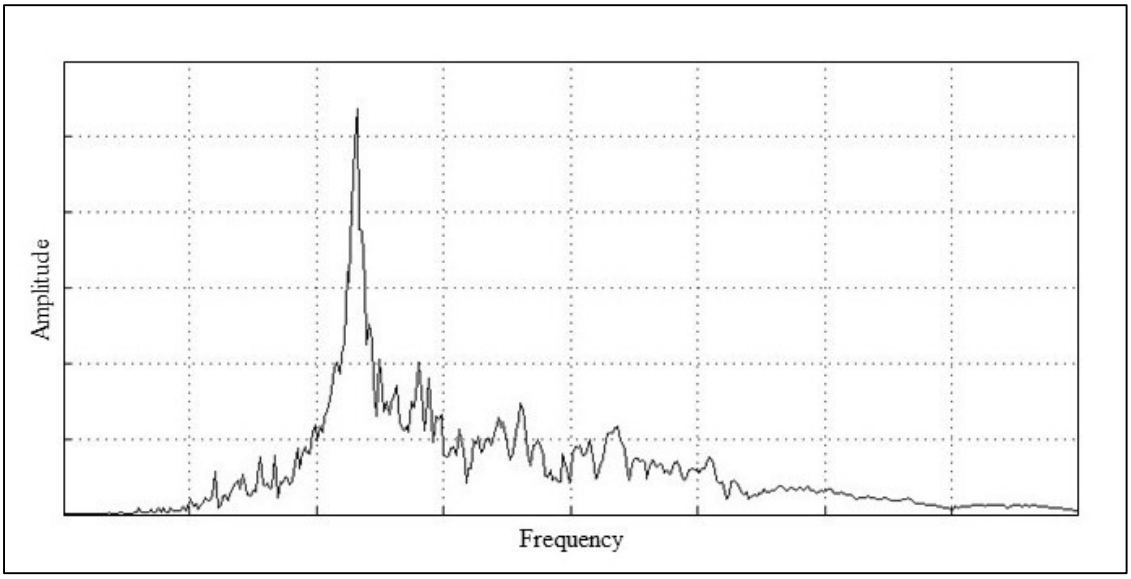

Figure 2-22: Example of an acceptable impact echo waveform in the frequency-amplitude domain

The NDT industry has seen the impact echo method develop from its origins, with manual impact via hardened steel balls and spring rods, to automated systems where impact, data reception and analysis, and even point location are streamlined and controlled by a program. Two different techniques of testing using the standard impact echo method can be found in Figure 2-23 and Figure 2-24.

Figure 2-23: Performing an impact-echo scan with the Olson Instruments IE Head

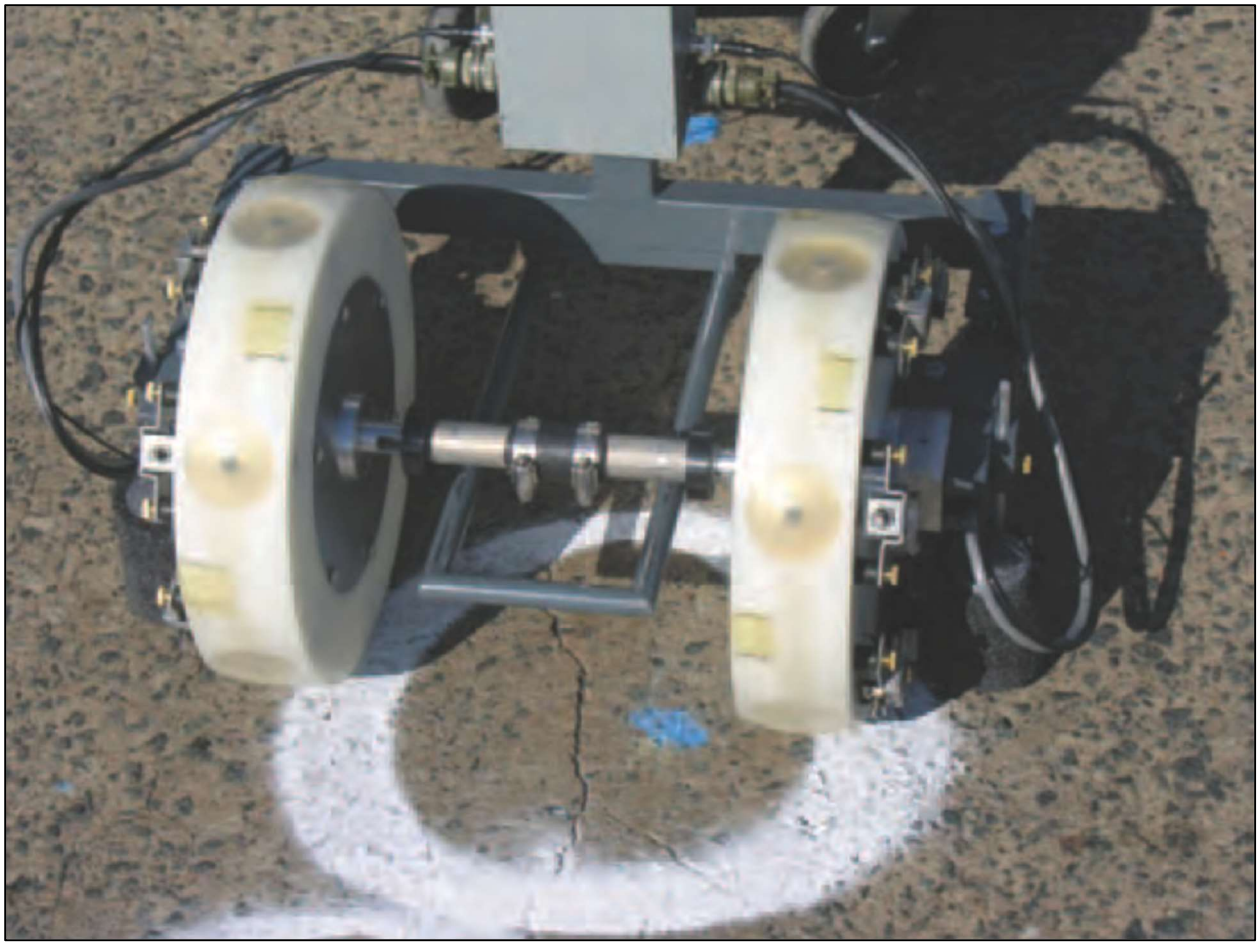

Figure 2-24: Impact-echo rolling bridge deck scanner (Gucunski, et al. 2013)

2.4.1.3 Applications

The impact echo method was principally developed to detect delaminations in reinforced-concrete structures (Sansalone and Carino 1989). However, it has a range of application including assessment of reinforced-concrete elements with delaminations, characterization of surface cracks, detection of voids, particularly related to post-tensioning ducts, and material characterization (Gucunski, et al. 2013). It allows for the condition of a delaminated area to be evaluated based on the wave frequency response. The method can provide measurements of concrete slab thickness to an accuracy of three percent (Sansalone and Streett 1996). Additionally, one of its greatest assets is that scans are not adversely affected by the presence of reinforcing steel (Sansalone and Streett 1996).

2.4.1.4 Limitations

One of the main limitations of the impact echo method is its ability to detect delaminations in reinforced-concrete elements with overlays (Gucunski, et al. 2013). While the method is successful in performing scans on slabs with portland cement concrete overlays, it can only detect delaminations in bridge decks with asphalt overlays at relatively low temperatures when the asphalt is more rigid (Gucunski, et al. 2013). Additionally, data collection must be performed on a dense grid in order to accurately define delaminated areas (Gucunski, et al. 2013). Lastly, boundary conditions, such as edges of concrete elements, affect impact echo results (Gucunski, et al. 2013). Though this is more applicable to reinforced-concrete girders and piers, it should also be taken into consideration when scanning near the edge of bridge decks.

2.4.2 Half-Cell Potential

2.4.2.1 Test Principles

The half-cell potential test is a common method for detection of the corrosion probability in reinforced-concrete structures. It is based upon the potential difference between two separate half-cell reactions. The corrosion electrochemical process creates an anodic reaction, otherwise known as a half-cell oxidation reaction (ACI 228 2013). In this reaction, iron atoms lose electrons and move into the nearby concrete as ferrous ions (ACI 228 2013). Those electrons flow to a cathodic site in the reinforcing steel, where they combine with oxygen and water in the concrete to form oxide ions (ACI 228 2013). Subsequently, the ferrous ions move through the concrete to the cathodic site, where they react to form hydrated iron oxide, otherwise known as rust (ACI 228 2013). This corrosion reaction creates one of the half-cells.

The other half-cell is obtained by providing a reference cell. A reference cell is typically a portable copper/copper sulfate half-cell, which is composed of a copper bar submerged in a saturated solution of copper sulfate, placed on the surface of the concrete (Gucunski, et al. 2013). Each of these half-cells creates an electric potential, or a flow of electrons. This reference cell acts as a standard for measuring potential of the reinforcement half-cell. With a voltmeter, one can measure the potential difference between the half-cells and collect data corresponding to the probability of corrosion over the area of a reinforced-concrete structure. A diagram of a simplified half-cell potential test method is shown in Figure 2-25. A general standard to determine corrosion probability is presented in Table 2-1.

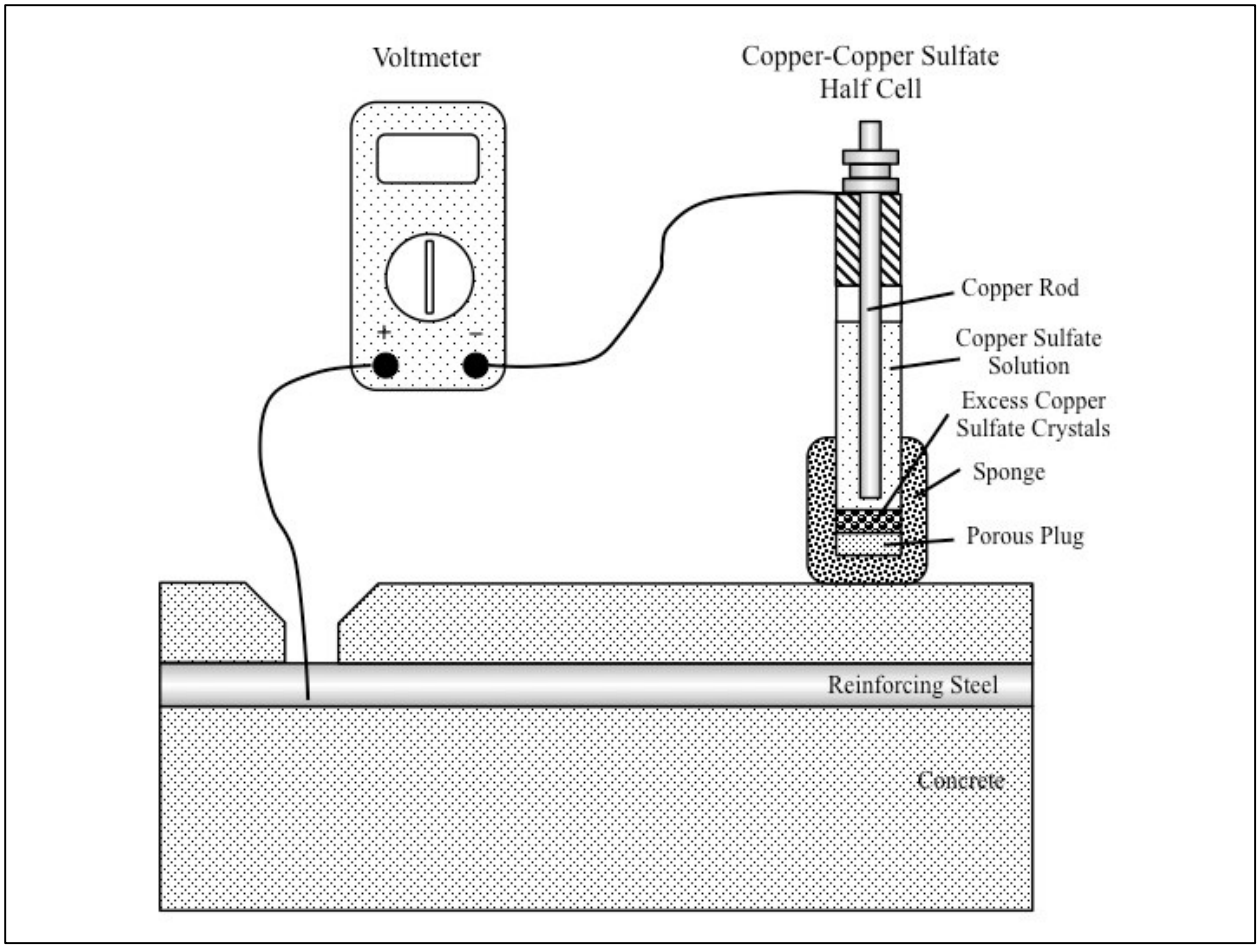

Figure 2-25: Simplified half-cell potential method (Adapted from ACI 228 2013)

Table 2-1: Corrosion probability from copper-copper sulfate half-cell potential measurements (Adapted from ASTM C876 2015)

Measured Potential (mV)	Probability of Corrosion
> -200	< 10%
-200 to -350	uncertain
< -350	> 90%

2.4.2.2 Testing Procedure

An ASTM acceptable reference electrode is needed to perform the standard half-cell potential test. Additionally, a voltmeter, lead wires, and a contact solution are needed, in accordance with ASTM C876 (2015). Before conducting a standard half-cell potential test, direct electrical connection to the reinforcing steel must be made. This connection should be in the form of a lead wire affixed to a compression type clamp, a welded or brazed protruding rod,

or a self-tapping screw connected to the reinforcing steel (ASTM C876 2015). In some cases where no reinforcement is exposed, this procedure requires the removal of a layer of concrete in order to uncover the steel (ASTM C876 2015). The lead wire joined to the reinforcing steel should be connected to the positive terminal of the voltmeter, and the lead wire for the reference electrode should be connected to the negative terminal of the voltmeter (ASTM C876 2015). If the voltage reading at a certain point changes with time, then the testing surface needs to be pre-wetted as described in ASTM C876 (2015).

Testing is performed at a certain point by notating and recording the potential difference displayed on the voltmeter. Testing may be performed on a grid or at random points (ASTM C876 2015). No minimum spacing requirement exists, though a spacing of 4 feet is sufficient for most large areas (ASTM C876 2015). When the potential difference becomes more negative than 50 mV, indicating some potential for corrosion activity, readings should be taken on a smaller grid (ASTM C876 2015). Resulting data may be compiled and presented as an equipotential contour map or a cumulative frequency distribution (ASTM C876 2015).

Some manufacturers produce streamlined half-cell potential tests, in which the reference electrode is in the form of a rolling wheel and the voltmeter is replaced by a data acquisition system. An example of these advanced forms of testing is shown in Figure 2-26. Performance of a half-cell potential test with these devices varies slightly from the standard half-cell potential test, but the basic principles and fundamentals of the method remain.

Figure 2-26: Rolling half-cell potential test (Gucunski, et al. 2013)

2.4.2.3 Applications

The main application of the half-cell potential test is to determine the probability of corrosion activity within a reinforced-concrete structure (Gucunski, et al. 2013). This method, either alone or combined with others, can accurately detect areas with high corrosion activity, which can lead to early detection of delaminations.

2.4.2.4 Limitations

The half-cell potential method requires an electrical connection to the reinforcing steel, and, in some cases, requires removal of some concrete to expose the reinforcement (ACI 228 2013). If conditions are not adequate, the surface of the concrete must be wetted (ACI 228 2013). Additionally, this test method is not applicable to coated reinforcement, as the coated layer impedes the electrical connection through the concrete (ACI 228 2013). The testing method does not quantify the rate of corrosion, only the probability or likelihood of corrosion activity at the time of the test (ACI 228 2013). Lastly, in order to obtain the most accurate interpretation of results, specifically the quantification of corrosion activity, this test should be run by an experienced individual (ACI 228 2013).

2.4.3 Surface Resistivity

2.4.3.1 Test Principles

The surface resistivity method, otherwise known as the electrical resistivity method, is a test developed to assess the corrosion rate in a reinforced-concrete structure by measuring the concrete's resistivity of electrical flow. As previously discussed, corrosion of reinforcing steel relies upon the flow of ferrous ions though the concrete matrix from the anode to the cathode of the electrochemical reaction. The electrical resistance of the concrete controls the ease with which those ions move through the concrete (ACI 228 2013). The concrete's electrical resistance depends on its microstructure and degree of saturation, as well as the conductivity of pore solution within the concrete (ACI 228 2013). A more porous microstructure will result in a lower resistivity and subsequently a higher potential rate of corrosion (ACI 228 2013).

The standard method for measuring the resistivity of a concrete structure is to perform a surface resistivity test on the in situ concrete. This process consists of applying a current to the concrete through electrodes and measuring the potential of the resulting electrical field from other electrodes (Gucunski, et al. 2013). The most common electrode configuration for a surface resistivity test for civil engineering applications is known as the Wenner setup, as shown in Figure 2-27 (Gucunski, et al. 2013).

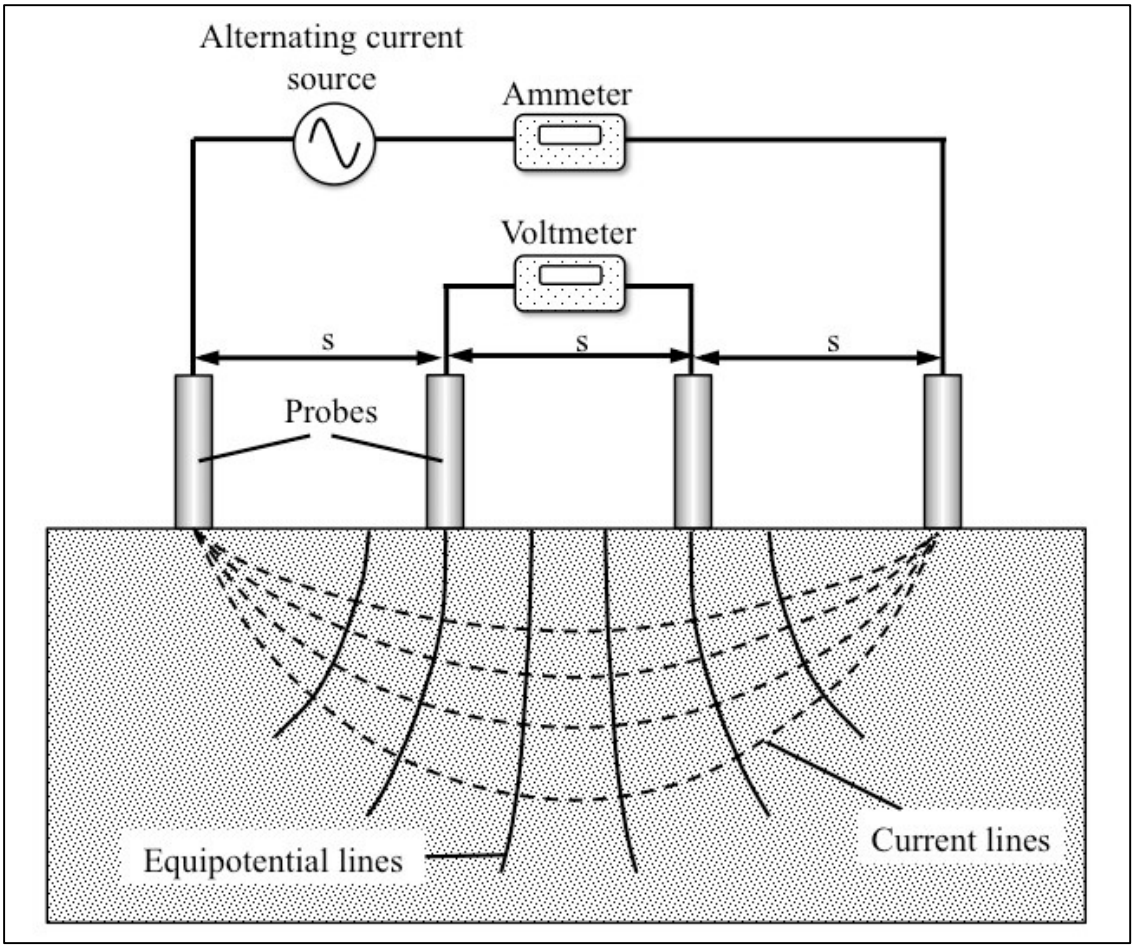

Figure 2-27: Surface resistivity principle (Adapted from ACI 228 2013)

The Wenner system, developed in 1916 by American physicist Frank Wenner, consists of four equally spaced probes configured along a single line (ACI 228 2013). The two outermost probes are connected to an alternating current source, while the two inner probes are connected to a voltmeter (ACI 228 2013). When current is applied to the outer probes, an electrical field is created between them, which is measured by the two inner probes (Gucunski, et al. 2013). The apparent resistivity can then be calculated according to the following equation (ACI 228 2013):

$$\rho = \frac{2\pi sV}{I} \qquad \text{Equation 2.3}$$

where ρ is the resistivity of the material (Ω-cm); s is the spacing between electrodes (cm); I is the amplitude of current (A); and V is the measured voltage (V). The resistivity is described as "apparent" because the above equation was derived assuming the measured material was homogeneous and semi-infinite, which is not the case for concrete structures (ACI 228 2013). Thus, measuring a non-homogeneous material, such as concrete, or measuring a specimen with

tight boundary conditions can yield discrepancies in the true resistivity of the specimen. With the relationship between electrical resistivity and the typical corrosion rate in reinforced-concrete presented in Table 2-2, one can determine the probable rate of corrosion within a reinforced-concrete structure.

Table 2-2: Predicted corrosion rates from surface resistivity readings (Gucunski, et al. 2013)

Resistivity (kΩ-cm)	Corrosion Rate
< 5	Very high
5-10	High
10-20	Moderate-low
> 20	Low

2.4.3.2 Testing Procedure

The procedure for a surface resistivity test is straightforward and simple. Technology available today combines the four probes of the Wenner system into a single unit, similar to that shown in Figure 2-28, that produces current, records the resulting potential, and often reports the calculated resistivity at the test location. On devices with adjustable spacing between probes, care should be taken to ensure the proper probe spacing. Probes that are spaced too closely can lead to scattered results due to the presence or absence of individual coarse aggregate particles, which have a very high resistivity (International Atomic Energy Agency 2002). Additionally, probes spaced too far apart can lead to inaccuracies due to the applied current field being constrained by specimen boundaries or being affected by reinforcing steel (International Atomic Energy Agency 2002). If possible, it is recommended to take readings between reinforcing steel bars (ACI 228 2013).

Figure 2-28: Compact surface resistivity test probe

To ensure the most accurate results, it is also important that the probes be adequately coupled to the concrete surface. Wetting of the concrete surface before testing is advised, sometimes paired with a conductive liquid or gel at test locations to improve overall probe conductivity (International Atomic Energy Agency 2002). To this date, there has been no standard test method for surface resistivity of reinforced-concrete developed or produced by ASTM; however, AASHTO T358 (2015) covers how to test the resistivity of standard concrete cylinders or cores.

2.4.3.3 Applications

The surface resistivity method is most often used to qualify a concrete's vulnerability to corrosion by characterizing its corrosive environment (Gucunski, et al. 2013). In conjunction with other methods, such as the half-cell potential test, a surface resistivity survey can be used to locate regions of probable corrosion in a concrete structure. The surface resistivity method can also aid in locating areas susceptible to chloride penetration (Gucunski, et al. 2013).

2.4.3.4 Limitations

Though it is a manual process that has yet to be commercially automated, the main disadvantage to the surface resistivity method lies in the interpretation of results (Gucunski, et al. 2013). Many properties, such as porosity, moisture, temperature and salt content, influence results of a surface resistivity test (Gucunski, et al. 2013). The contribution of each property to the total result is varying, delineated and uncertain (Gucunski, et al. 2013). In addition, the

presence of reinforcing steel in the potential field can result in an apparent resistivity value lower than the actual resistivity, and reinforcing steel should be avoided if possible (ACI 228 2013).

As previously discussed, Equation 2.3 was derived assuming a homogeneous material. Concrete is a nonhomogeneous material, and thus can yield slight inconsistencies in testing. Additionally, to obtain accurate and consistent results, the test probes require adequate galvanic coupling to the surface of the concrete, which demands that the concrete surface be wetted prior to testing (Gucunski, et al. 2013).

2.4.4 Ground-Penetrating Radar

2.4.4.1 Test Principles

Ground-penetrating radar (GPR) is a nondestructive testing method that relies upon the propagation of electromagnetic energy to locate subsurface objects and interfaces within a structure. The electromagnetic energy, characterized by short pulses in a specified frequency range, is delivered to the structure by way of an antenna (ACI 228 2013). As each pulse travels through the survey structure, a portion of the energy is reflected back to the surface every time the pulse crosses a boundary of materials with dissimilar dielectric properties (ACI 228 2013). Any energy not reflected at this interface continues to penetrate deeper into the structure, reflecting at other anomalies until the energy is fully attenuated, as shown in Figure 2-29 (Gucunski, et al. 2013). The reflections are absorbed by the antenna and processed for data such as distance to the reflector, pulse speed through the medium, and the amount of pulse attenuated (ACI 228 2013).

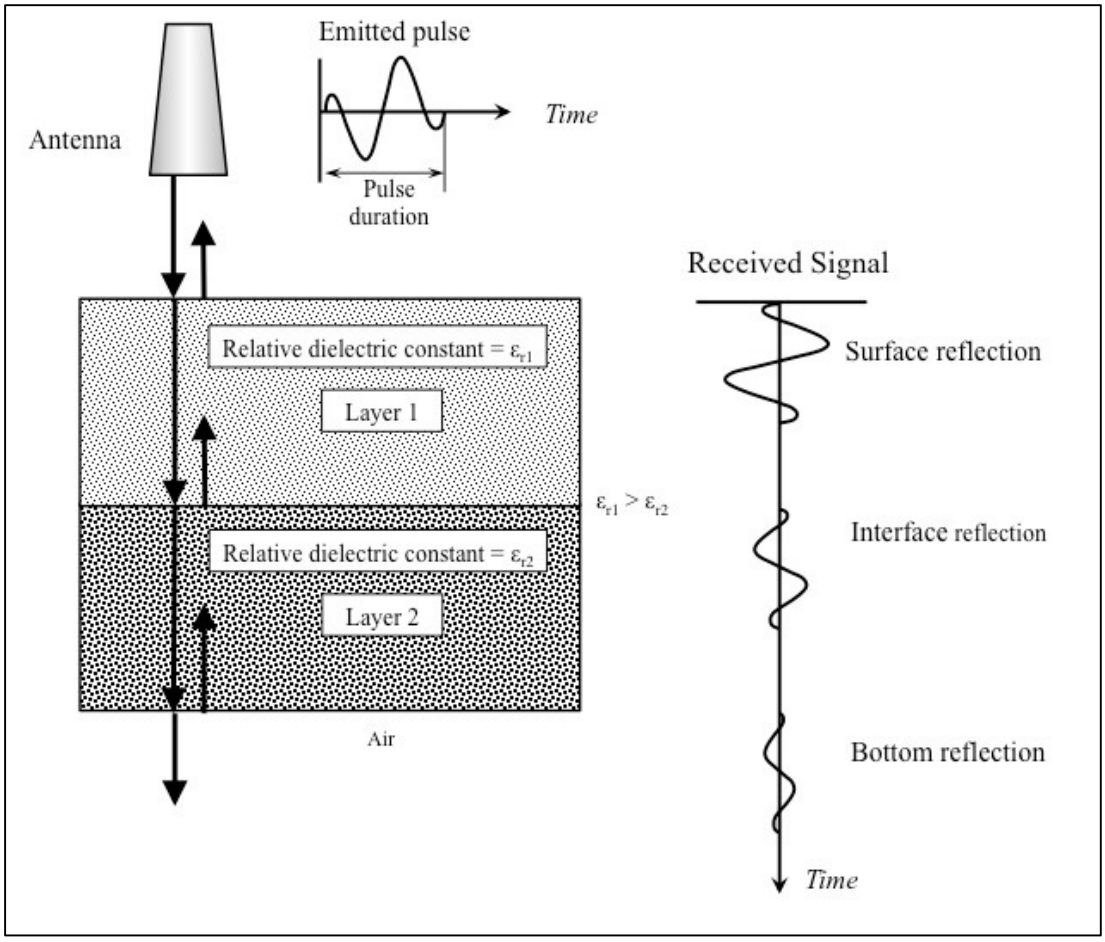

Figure 2-29: GPR signal propagation through a medium (Adapted from ACI 228 2013)

The most significant material properties affecting electromagnetic wave propagation are electrical conductivity and dielectric permittivity (Gucunski, et al. 2013). Electrical conductivity, which is the inverse of resistivity, governs the ability or ease of electromagnetic energy to travel through a particular medium (Gucunski, et al. 2013). Highly conductive materials absorb most of the applied energy, stopping wave penetration into the material, while lesser conductive materials allow for deeper wave and energy propagation. The dielectric permittivity, or the dielectric constant, of a material governs the speed at which electromagnetic energy propagates through a medium (Gucunski, et al. 2013). The relative dielectric constant (ε_r) of a material is defined as ratio of a material's dielectric constant to that of free space (ACI 228 2013). Typical relative dielectric constants for common construction materials are displayed in Table 2-3. The amount of signal or energy reflected from an interface within a low-loss dielectric medium is characterized by the reflection coefficient of the interface, which is calculated as follows (ACI 228 2013):

$$\rho_{1,2} = \frac{\sqrt{\varepsilon_{r1}} - \sqrt{\varepsilon_{r2}}}{\sqrt{\varepsilon_{r1}} + \sqrt{\varepsilon_{r2}}} \quad \text{Equation 2.4}$$

where $\rho_{1,2}$ is the reflection coefficient; ε_{r1} is the relative dielectric constant of Material 1; and ε_{r2} is the relative dielectric constant of Material 2. Equation 2.4 holds that if a wave encounters an interface where the second material has a higher dielectric constant than the first material, the reflected wave has a change in polarity (ACI 228 2013). Additionally, as the dissimilarity between dielectric constants increases, so does the reflection coefficient. This explains why the presence of moisture and reinforcing steel so greatly affect GPR scans.

Table 2-3: Relative dielectric constants for various construction materials (Adapted from Gucunski, et al. 2013)

Medium	Relative Dielectric Constant
Air	1
Water (fresh)	81
Concrete	8-10
Gravel	4-7
Sand	4-6
Clay	25-40
Silt	16-30
Steel	∞

Because of the stark dielectric contrast between steel and concrete, it is common to observe a series of sharp hyperbolae when scanning reinforced-concrete structures, particularly reinforced-concrete bridge decks. In Figure 2-30, an example diagram of a typical GPR scan is provided. All of the reinforcing steel bars on the top layer have distinct, pronounced hyperbolae, indicating sound reinforcing steel, while the leftmost bar corresponds to a somewhat fuzzy hyperbola, indicating some signal attenuation at that location (Gucunski, et al. 2013). In analyzing GPR scans of reinforced-concrete bridge decks, areas of high signal attenuation are often correlated to areas of high deterioration, as chlorides and moisture present in the concrete greatly affect signal penetration (Gucunski, et al. 2013). Significant cracking and delaminations within a bridge deck allow for a greater presence of moisture and chlorides.

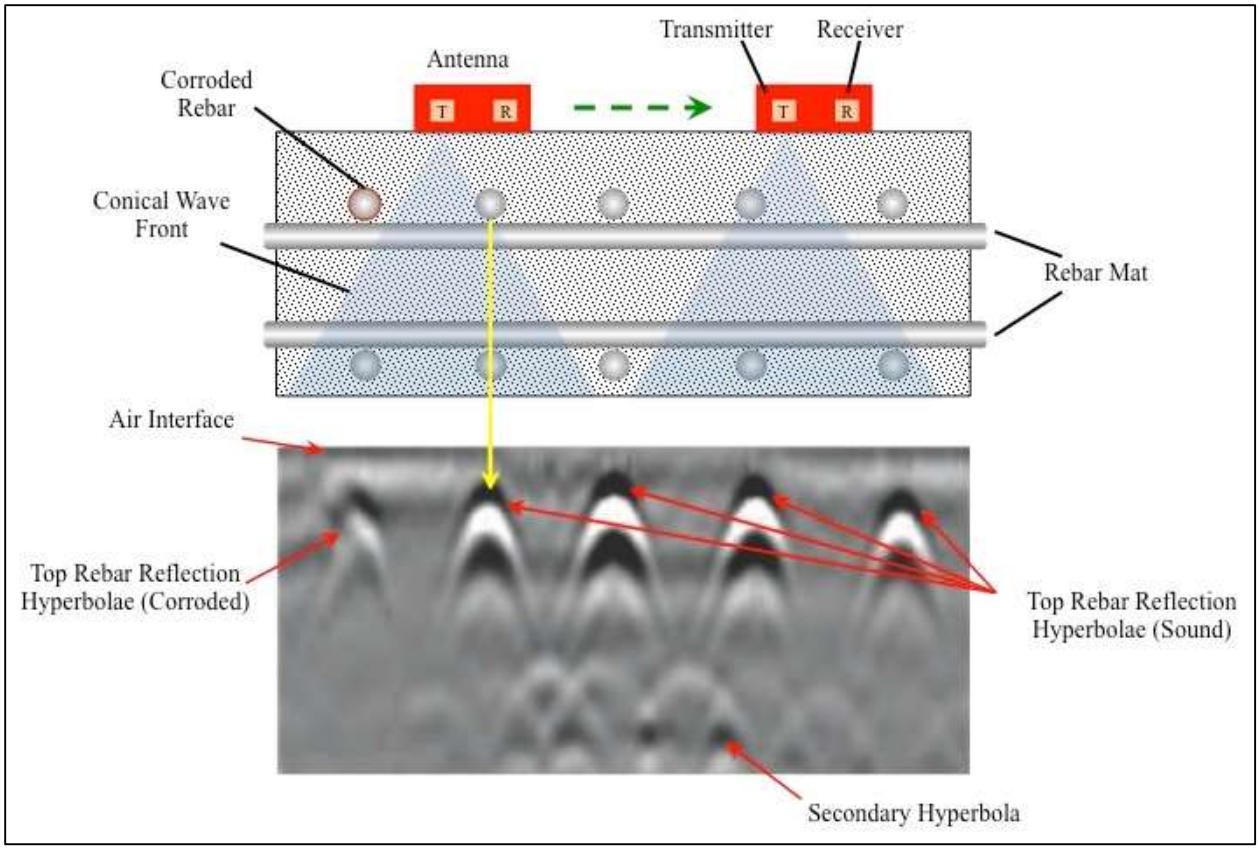

Figure 2-30: Interpreting GPR hyperbolae from reinforcing steel reflections (Adapted from Gucunski, et al. 2013)

2.4.4.2 Testing Procedure

Equipment necessary for the performance of a ground-penetrating radar test are a GPR system, data acquisition system and a distance-measuring system (ASTM D6087 2015). GPR systems are of two classes based upon the type of antenna employed by the system. Some systems use air-launched antennas while others use ground-coupled antennas, each available in a variety of frequency ranges (ASTM D6087 2015). Low-frequency antennas produce waves with significant penetration at a low resolution; high-frequency antennas produce waves that only penetrate to shallow depths yet produce high-resolution wave data (ACI 228 2013). High-frequency antennas are better suited for bridge decks, as shallow penetration is adequate.

The antenna, which may either be manually propelled or attached to a survey vehicle, is moved across the surface of the test specimen (ACI 228 2013). The process of manual GPR scanning using a cart to move the antenna and data acquisition system is shown in Figure 2-31. As the antenna is moved, it transmits short pulses of electromagnetic energy into the structure at

a high frequency and receives the return signals of wave reflection (ACI 228 2013). The returned waves, which contain information on distance to the reflector, pulse speed through the medium, and the amount of pulse attenuated, are then processed by the data acquisition system. Most current data acquisition systems will, with necessary user inputs, combine each individual signal and create a grayscale line scan, similar to that shown in the bottom part of Figure 2-30. This line scan, which plots the data as differing gray tones based on the amplitude of the return signal, represents a cross-sectional view of the test specimen (ACI 228 2013). With multiple line scans, one can gain insight into the structure along various cross-sectional planes throughout its body.

Figure 2-31: GPR scanning of a bridge deck with a cart (Gucunski, et al. 2013)

2.4.4.3 Applications

The ground-penetrating radar method of evaluation is advantageous because it permits high-speed scanning of structural elements and is able to penetrate across concrete-air interfaces (ACI 228 2013). GPR assessment serves a wide range of uses in scanning reinforced-concrete bridge decks. Applications of GPR assessment include measurement of deck thickness, concrete cover, rebar configuration, qualification of potential for delaminations, characterization of concrete deterioration, and estimation of concrete properties (Gucunski, et al. 2013).

Reinforcing steel is especially easy to detect, as the dielectric constant of steel is much greater than that of concrete materials.

2.4.4.4 Limitations

Despite a wide range of applications and advantages to the GPR method of evaluation, there are also many limitations. First, the method is highly sensitive to moisture, as water has a much greater dielectric constant than other concrete materials. As concrete saturation increases, the dielectric constant of the concrete will consequently increase (ACI 228 2013). Additionally, strong reflections from reinforcing steel can obscure weaker reflections from other reflecting interfaces that may be present, and multiple reflections from reinforcing bars may mask signals from greater depths (ACI 228 2013). This can make detection of delaminations at or below the level of reinforcing steel difficult, particularly when reinforcement is congested or tightly spaced. Cracks and delaminations at any level can be difficult to detect unless moisture is also present in the cracks or region of the delamination (ACI 228 2013). GPR is sensitive to corrosive environments and, to some extent, can be used to map areas of probable deterioration (Gucunski, et al. 2013). Despite this fact, GPR cannot definitively provide detailed information about the presence of corrosion, such as corrosion rate or section loss of the reinforcement (Gucunski, et al. 2013). Because of complexities in the GPR principle, especially relating to multi-layer materials such as reinforced-concrete slabs, an experienced operator is needed to produce accurate test results (ACI 228 2013).

2.4.5 Infrared Thermography

2.4.5.1 Test Principles

In the 1980's, infrared thermography (IR) began to be employed in the field of nondestructive testing for detecting subsurface anomalies within concrete structures (Gucunski, et al. 2013). The IR principle relies on emissions caused by thermal radiation of concrete to create a visual image of voids and anomalies within a structure (ACI 228 2013). This thermal radiation is applied to the surface, in most cases, by solar heating and cooling, though heat lamps are also occasionally used. Thermography does not directly measure the surface temperature; rather it relies on the variation of radiance along the surface (ACI 228 2013).

Two main principles govern IR testing for concrete, the first being that energy is emitted from a surface in the form of electromagnetic radiation (ACI 228 2013). The Stefan-Boltzmann law describes the unit rate of energy emitted in the following equation (ACI 228 2013):

$$R = e\sigma T^4 \qquad \text{Equation 2.5}$$

where R is the rate of energy radiation per unit area of surface, W/m^2; e is the surface emissivity; σ is the Stefan-Boltzmann constant, 5.67×10^{-8} (W/m^2·K^4); and T is the absolute temperature of the surface (K). Materials with greater emissivity values will emit energy at a higher unit rate than materials with a lower value of emissivity. The second principle is that anomalies beneath the concrete surface affect the radiant energy emitted from the concrete surface by interrupting heat transfer through the structure (ACI 228 2013). As ambient temperature increases throughout the daytime, concrete absorbs heat, subsequently causing it to emit radiant energy (Vaghefi, et al. 2015). Anomalies within the concrete, such as delaminations and air voids, have different thermal characteristics and are far less conductive than sound concrete and therefore heat at a quicker rate than surrounding areas of concrete (Vaghefi, et al. 2015). Hence, delaminated areas on in IR scan will appear with warmer temperatures than adjacent areas, as shown in Figure 2-32.

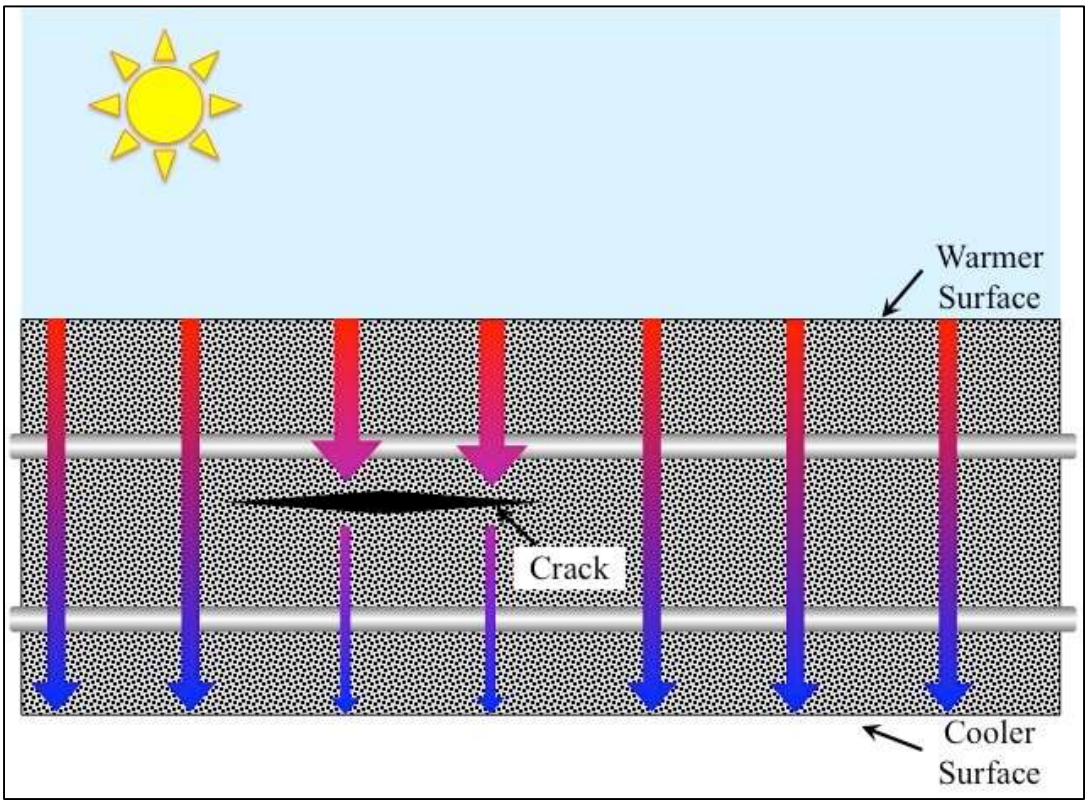

Figure 2-32: Infrared thermography principle (Adapted from Gucunski, et al. 2013)

2.4.5.2 Testing Procedure

Equipment necessary for the performance of infrared thermography testing is an infrared scanner, video or data recorder, distance measuring device, test vehicle and a contact thermometer (ASTM D4788 2013). In some cases, with modern technology, the infrared scanner, recorder and distance-measuring device may all be integral within one system. Prior to testing, any debris should be removed from the bridge deck surface, and the deck surface should have been dry for at least 24 hours (ASTM D4788 2013). Typically, 3 hours of direct sunlight is sufficient to create necessary thermal radiation differences for IR detection (ASTM D4788 2013). It is important that testing be done at a time when there is a large heating or cooling gradient, such as early in the morning or evening (ACI 228 2013). Such times allow for anomalies to be detected before ambient temperatures thermally saturate the concrete surfaces.

When performing an IR test, data should be collected in a continuous manner, from one end of the test zone to the other (ASTM D4788 2013). The test should be performed at speeds less than 10 mph, as to ensure adequate and complete data collection (ASTM D4788 2013). Survey equipment should be mounted such that the infrared scanner is able to detect a lateral range of at least 14 feet, allowing for a single lane to be scanned in one pass (ASTM D4788 2013). Each lane should be scanned. Caution should be taken to avoid processing or interpreting incorrect results in areas shaded by vegetation and other structures or areas adjacent to barrier walls where heat may become trapped, as these external sources can negatively influence the collected data (ASTM D4788 2013). In Figure 2-33 and Figure 2-34, examples of IR testing are shown. A program should be used to plot test results and the delaminations should be reported and expressed as a percent of the total deck area (ASTM D4788 2013).

Figure 2-33: Vehicle mounted IR technology (Gucunski, et al. 2013)

Figure 2-34: Manually operated IR technology (Gucunski, et al. 2013)

2.4.5.3 Applications

Infrared thermography is predominantly used to detect delaminations, voids and cracks in concrete structures, especially bridge decks (Gucunski, et al. 2013). It also finds use in detecting voids in shallow post-tension tendon ducts as well as delaminations and debonding in pavements (Gucunski, et al. 2013). IR testing is advantageous and cost-effective, particularly for testing of slabs and bridge decks, because an individual test iteration covers a much greater surface area than other NDT methods (ACI 228 2013). If testing is performed correctly, results are simple to process and interpret, yielding a percentage of deterioration within the tested area (ACI 228 2013).

2.4.5.4 Limitations

Despite its advantages, IR testing has many limitations that must be considered. The main limitation to IR testing is the extensive effect of environmental conditions, particularly cloud cover, wind, level of direct sunlight and presence of surface water (ACI 228 2013). All of these conditions affect the results of an IR test, and every one of the conditions is a variable controlled by nature, not by the operator. Additionally, as the depth of a defect increases, it becomes more difficult to detect because it provides less of a surface differential temperature than shallow anomalies (ACI 228 2013). Because of these limitations, an experienced individual is required to perform IR tests to ensure that boundary conditions and environmental conditions do not negatively influence the collected data (ACI 228 2013).

CHAPTER 3

LABORATORY EXPERIMENTAL PROGRAM

3.1 INTRODUCTION

The main objective of this research was to develop a full-scale test site where personnel from the Alabama Department of Transportation (ALDOT) will be able to conduct NDT training, perform equipment calibration, and evaluate new NDT methods. This test site, a full-scale reinforced-concrete bridge deck, contained controlled defects at known locations throughout its body. Achievement of this project objective required the formation and completion of several subtasks. First, it was necessary to identify which NDT methods can accurately detect and characterize the in-place condition of concrete structures, with additional consideration being placed on the advantages and disadvantages of the various NDT methods evaluated. It was also necessary to develop suitable methods of construction for replicating defects that occur naturally within concrete structures. With consideration being given to the previous research efforts and literature outlined in Chapter 2, an experimental plan was developed that most adequately accomplished the aforementioned objectives, given the resources available to the Auburn University research team. In Chapter 3 details of this experimental plan are discussed. Test equipment details and materials are presented in Section 3.2. The design of test specimens and methods that were used in construction of test specimens are discussed in Sections 3.3 and 3.4, respectively.

3.2 EVALUATION OF NDT METHODS

Based on a review of documented literature and a consideration of equipment available to the Auburn University research team, five candidate NDT methods were selected for use in this research. These five methods are the impact-echo, half-cell potential, surface resistivity, ground-penetrating radar (GPR), and infrared thermography methods. Each test method has its individual strengths that can be advantageous in determining the in-place condition of reinforced-concrete bridge decks. Equipment necessary for the performance of each test method was available to the research team, either through ownership by Auburn University's Highway Research Center or via loan from the Alabama Department of Transportation.

This report describes the use of the impact-echo, half-cell potential and surface resistivity methods. Evaluation of the latter two methods employed throughout this research project, GPR and infrared thermography, were the responsibility of another researcher on the team. Therefore, these two methods were excluded from this particular report, though consideration was given to development of artificial defects detectable by all five methods.

3.2.1 Impact-Echo Method

For impact-echo testing, the research team used the Impact-Echo system equipment manufactured by Olson Instruments. The Olson Instruments system consisted of a handheld probe unit, known as the IE Head, and the data processing system, known as the Freedom Data PC, as well as necessary cable connections, as shown in Figure 3-1. The IE Head functioned as both the impactor and receiver in the impact-echo method. The Freedom Data PC served as the data-acquisition system, compiling signals that were collected by the IE Head and providing post-processing and analysis of that data. The Freedom Data PC was equipped with WinIE software, which is a program developed by Olson Instruments for the purpose of collecting and analyzing impact-echo data. The Olson Instruments Impact-Echo system complies with ASTM C1383 specifications.

Figure 3-1: Olson Instruments Impact Echo system

The system employed by the research team performed the impact-echo test method at individual point locations along the surface of a test specimen. In order to form a complete yet non-excessive data set for each specimen, the impact-echo test method was performed at points corresponding to a 4 in. grid along the surface of each test specimen. In accordance with ASTM C1383 (2015), slab surfaces were ground smooth and swept clean prior to testing to ensure adequate contact between the transducer tip and the concrete surface. A single point scan was taken to calibrate the wave-speed within the system prior to testing of the slab. At each point, three individual scans were taken, with the average result being reported by the data-acquisition system. The operator inspected each individual scan for a valid waveform before continuing to the next scan.

3.2.2 Half-Cell Potential Method

For half-cell potential testing, the research team used the Profometer Corrosion wheel electrode from Proceq. Equipment for this setup consisted of the Profometer operating system and a rolling wheel electrode, in addition to necessary cables and connections, as shown in Figure 3-2. The Profometer operating system is a handheld device that was used to measure and, subsequently, record the potential difference between the corrosion half-cell and the rolling wheel reference electrode as the wheel was moved along a path. The rolling wheel electrode was a copper-copper sulfate half-cell. The Proceq Profometer Corrosion wheel electrode complies with ASTM C876.

The Proceq system for performing the half-cell potential test entailed rolling the wheel electrode along a line. The research team performed line-scans spaced at 6 in., which fell well within the limits for test spacing detailed in ASTM C876 (2015). Direct contact was made to the reinforcing steel by use of a bolt twisted into a threaded hole in the reinforcement. The concrete slabs returned relatively stable readings at a single location, but to ensure proper testing, the surfaces of the slabs were wetted. The distilled water compartment of the Proceq rolling wheel electrode, which applied water to the surface of the slab, allowed for water to be added to the surface as the test was performed. Data processing and reporting along each line-scan was performed within the software of the Proceq Profometer.

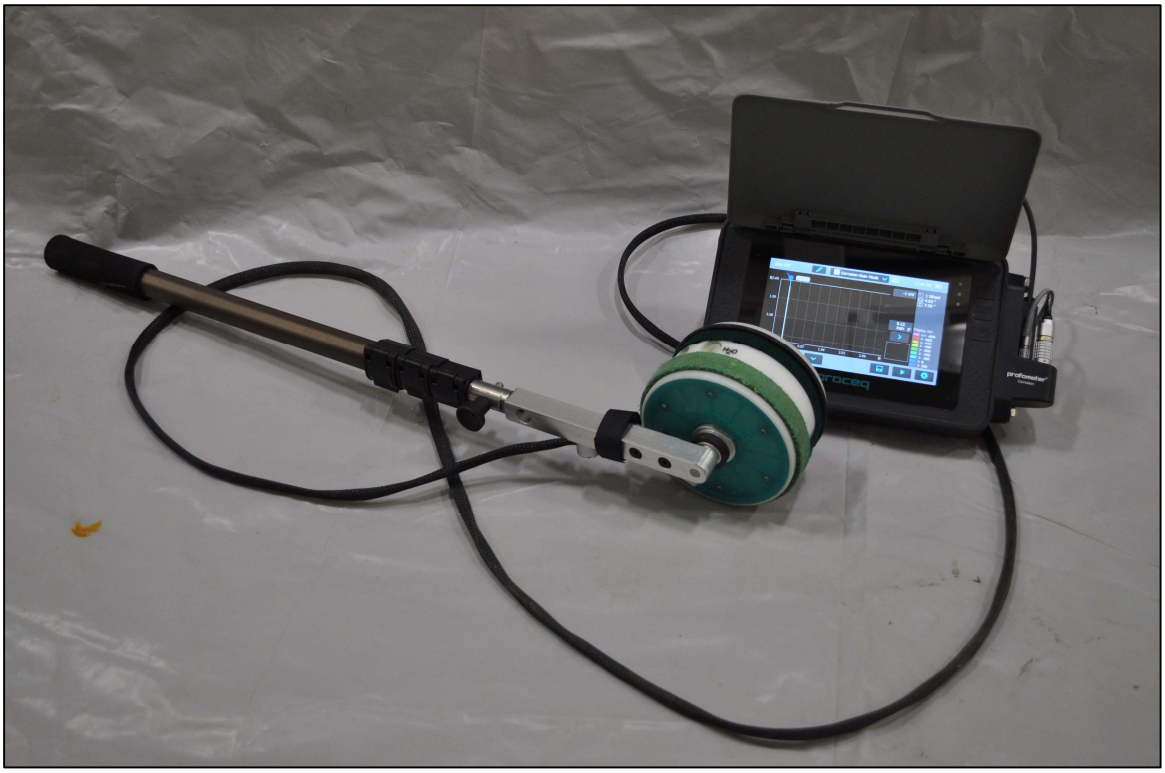

Figure 3-2: Proceq Profometer half-cell potential test equipment

3.2.3 Surface Resistivity Method

To perform surface resistivity testing, the research team employed the Proceq Resipod, which consisted of a four-probe Wenner system and a digital display at the top of the unit, as shown in Figure 3-3. The instrument used features probes spaced at 1.5 in. (38 mm), which conforms to AASTHO specifications. There is no ASTM standard for the surface resistivity test method, but researchers closely followed the procedures and recommendations outlined in the user manual for the Resipod.

Frequently during the testing process, the probes were dipped into distilled water in order to keep probe reservoirs full, as recommended by Proceq (2017). This helped to ensure good connection between the concrete surface and the instrument. Because reinforcing steel can have a substantial effect on resistivity readings, measurements were taken diagonally at each bar spacing, as shown in Figure 3-4. This orientation of testing is recommended by Proceq to avoid the presence of bars beneath the testing point, and to prevent bars running parallel to the probe (Proceq 2017). For every point tested, five readings were taken, and the median measurement was recorded. Readings were recorded by hand, in lieu of utilizing the Resipod's memory

feature, and were later manually entered into a post-processing software. Testing was performed in a laboratory setting, with temperatures around 70°F.

Figure 3-3: Proceq Resipod surface resistivity test equipment

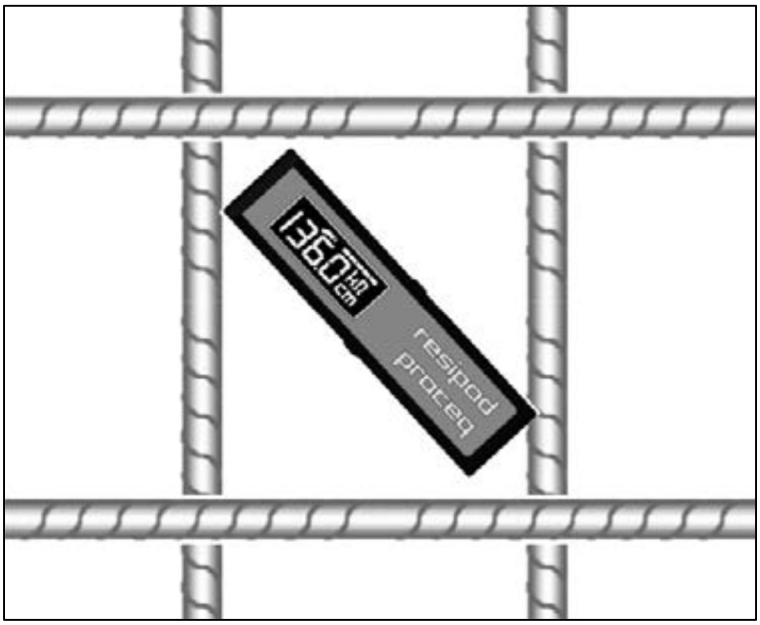

Figure 3-4: Optimal scanning orientation for the surface resistivity method (Proceq 2017)

3.3 DESIGN OF SPECIMENS TO EVALUATE DEFECTS AND NDT METHODS

After the candidate testing methods were researched and determined, the research team formulated a plan for the construction of specimens containing artificial defects to allow these

test methods to be assessed. This plan was based fundamentally upon the previous research efforts of peers in the field of nondestructive testing. A synopsis of the conclusions drawn from previous literature for the manufacture of artificial defects in reinforced-concrete bridge decks is presented in Table 3-1.

Table 3-1: Summary of the manufacture techniques of defects

Defect Category	Type(s)	Methods to Simulate in Test Slabs
Voids	• Internal	• Plastic bags filled with water, sand, clay • Polystyrene shapes
Delaminations	• At top steel • At bottom steel	• Embed plastic and/or foam sheets • Two-lift construction (sand, smooth surface, oil, etc.)
Cracking	• Vertical (transverse): • Partial depth • Full depth • Surface cracking (plastic shrinkage)	• Embed plastic and/or foam sheets • Evaluate different thicknesses • Two-stage construction on each side of cold joint to produce vertical crack
Corrosion	• Top Mat and/or • Bottom Mat	• Add chlorides to fresh concrete • Pond chlorides on specimen • Use very shallow top cover • Accelerate with impressed current
Deterioration	• Microcracking and macrocracking distress due to ASR, DEF, freeze-thaw cycles:	• Embed chunk of concrete that has been pre-distressed with freeze-thaw damage • Use poor quality concrete: • High air content • Lack of paste, with honeycombs
Poor Construction	• Low strength • Poor consolidation • Poor curing	• Use poor quality concrete • Low strength • Lack of vibration

As Gucunski, et al. (2013) described, the main forms of distress in reinforced-concrete bridge decks are voids, delaminations, vertical cracking, corrosion and degradation (or deterioration). Additionally, poor construction practices can lead to distress within concrete

structures. It was important to the research team that all forms of distress are represented within the final, full-scale test site. Therefore, it was imperative to determine suitable methods of constructing each type of defect, taking ideas from previous works and implementing and assessing them in a controlled laboratory setting.

Voids can be constructed using polystyrene shapes, as described by Maierhofer (2003), or by use of bags filled with different construction materials, as detailed by Lin et al. (2018). Sansalone and Carino (1989), as well as Cheng and Sansalone (1993), proved that delaminations, which typically occur at a layer of reinforcing steel, can be replicated by placing thin sheets of plastic or foam into concrete during the casting process. Lin and Sansalone (1996) displayed that partially delaminated sections could be created by using thin styrofoam sheets cut into checkerboard patterns. Lin, Sansalone and Poston (1996) showed that a thin layer of sand could create a delamination at a concrete interface. Vertical cracking can be replicated by using plastic sheets oriented vertically, as reported by Lin et al. (2018). Multiple researchers, including Almusallum et al. (1996), Jayaprakash, Pournasiri and De'nan (2012), and Guo et al. (2015), among others, found success in accelerated corrosion using chloride exposure and impressed current techniques. Uniformly distributed cracking, either macrocracking or microcracking, was replicated by Ham et al. (2016) by adding synthetic polymer fibers into the concrete mixture prior to casting.

In order to test the adequacy of these methods for replicating defects, it was determined that multiple reinforced-concrete slabs were to be cast at the Auburn University Structural Engineering Laboratory in the Harbert Engineering Center ("the laboratory"). The various methods for constructing artifical defects were used when casting the slabs and the slabs were subsequently tested with the candidate NDT methods upon the curing of the concrete. The specimens were coded and grouped based upon the defects within. In Table 3-2, a summary of the alphanumeric coding and grouping of the test specimens is presented.

Table 3-2: Alphanumeric coding and grouping of test specimens

Defect Type	Number of Slabs	Specimen ID
Voids	2	V1 to V2
Delaminations	8	DL1 to DL8
Cracking	1	CR1
Corrosion	2	C1 to C2
Deterioration	4	DE2 to DE5
Poor Construction	2	PC1 to PC2
No Defect - Control	1	CONTROL
Total Number	**20**	

3.4 DETAILS AND CONSTRUCTION OF TEST SPECIMENS

In total, twenty reinforced-concrete slabs were constructed to test the suitability of the defect replication methods. All specimens were constructed in the laboratory by the research team. Each slab measured 7 ft long and 3 ft wide. The research team selected these plan dimensions with constructability in mind; each slab was able to be cast on a single 4 × 8 ft sheet of plywood. This provided construction simplicity, and allowed the slabs to be easily moved and stacked in the laboratory. Fourteen of the specimens were constructed with a thickness of 7.25 in., while six specimens were constructed to have a thickness of 12 in. Standard dimensional lumber and plywood were used as formwork for the sides of the slabs during the casting process. A specimen thickness of 7.25 in. was used because it provided a depth near the common thickness for reinforced-concrete bridge decks while also allowing nominal 2 × 8 in. dimensional lumber to be used as formwork. A specimen thickness of 12 in. was used in cases to test the detectability of defects at deeper locations. The 12 in. thick specimens were constructed using built-up formwork consisting of nominal 2 × 12 in. dimensional lumber and a strip of 3/4 in. thick plywood to create the full 12-inch depth.

Each slab was reinforced with two layers of reinforcing steel, each comprised of No. 5, Grade 60 steel bars spaced at 8 in. on center in the both the transverse direction and longitudinal directions. Unless otherwise specified, the clear cover, which is the distance from the outermost layer of reinforcing steel to the nearest concrete face, was 2 in. to the top layer of reinforcing

steel, 1 inch to the bottom layer of reinforcing steel, and 2 in. on all sides. All reinforcing steel was cut to length and tied together in the laboratory.

Unless otherwise specified, a standard ALDOT bridge deck mixture of ready-mixed concrete, whose mixture proportions are detailed in Table 3-3, was used to construct all test specimens.

Table 3-3: ALDOT bridge deck mixture proportions

Item	Proportions	
#57 Limestone Coarse Aggregate	1,900	lb/yd^3
Fine Aggregate	1,285	lb/yd^3
Portland Cement	465	lb/yd^3
Class C Fly Ash	155	lb/yd^3
Water	275	lb/yd^3
Air Entraining Admixture	1.5	oz/yd^3
HRWR Admixture	25	oz/yd^3

This mixture requires a specified 28-day compressive strength of 4,000 psi, and is commonly used through the state of Alabama in reinforced-concrete bridge decks (ALDOT Bridge Bureau 2019). The concrete was delivered to the laboratory by a ready-mixed concrete truck, as shown in Figure 3-5. Concrete was dispensed from the mixer's chute into a concrete placement bucket, shown in Figure 3-6, where it was then moved to the casting location in the laboratory by an overhead crane. Before any concrete was placed into the specimen forms, a certified ACI technician tested the slump, air content and unit weight of the concrete mixture. Six standard 6 in. diameter by 12 in. tall cylinders were cast for each mixture. All fresh properties of the concrete mixtures are detailed in Appendix A.

Figure 3-5: Ready-mixed truck delivering concrete to the laboratory

Figure 3-6: Ready-mixed concrete being placed into the concrete placement bucket

Upon completion of fresh property testing and sampling, concrete was placed into the specimen formwork and consolidated using vibratory consolidation techniques, as shown in

Figure 3-7, unless otherwise specified. All specimens were leveled using a screeding process, after which they were trowel finished and subsequently broom finished for surface roughness. Specimens were moist-cured for seven days after casting, and formwork was removed following the curing process. Prior to testing with NDT equipment, the slab surfaces were smoothed using a water-fed grinding tool.

Figure 3-7: Vibratory consolidation of concrete

3.4.1 Void Specimens

3.4.1.1 Specimen V1

Specimen V1 was constructed with the following objectives in mind:

- Determine smallest detectable deep void,
- Determine effect of depth of void on void detection, and
- Determine suitability of using water-filled balloons to simulate voids.

In order to investigate the detectability of these defects at both deep and shallow locations, this slab was constructed to be 12 in. thick. The voids were created using water-filled balloons with diameters between 0.5 and 2.5 in. that were tied to the reinforcing steel at locations shown in Figure 3-8. Deionized water was used to fill the balloons. In Figure 3-9, Specimen V1 is shown prior to placement of ready-mixed concrete. During the concrete placement and consolidation process, care was taken to ensure that the locations of the water-filled balloons were not altered.

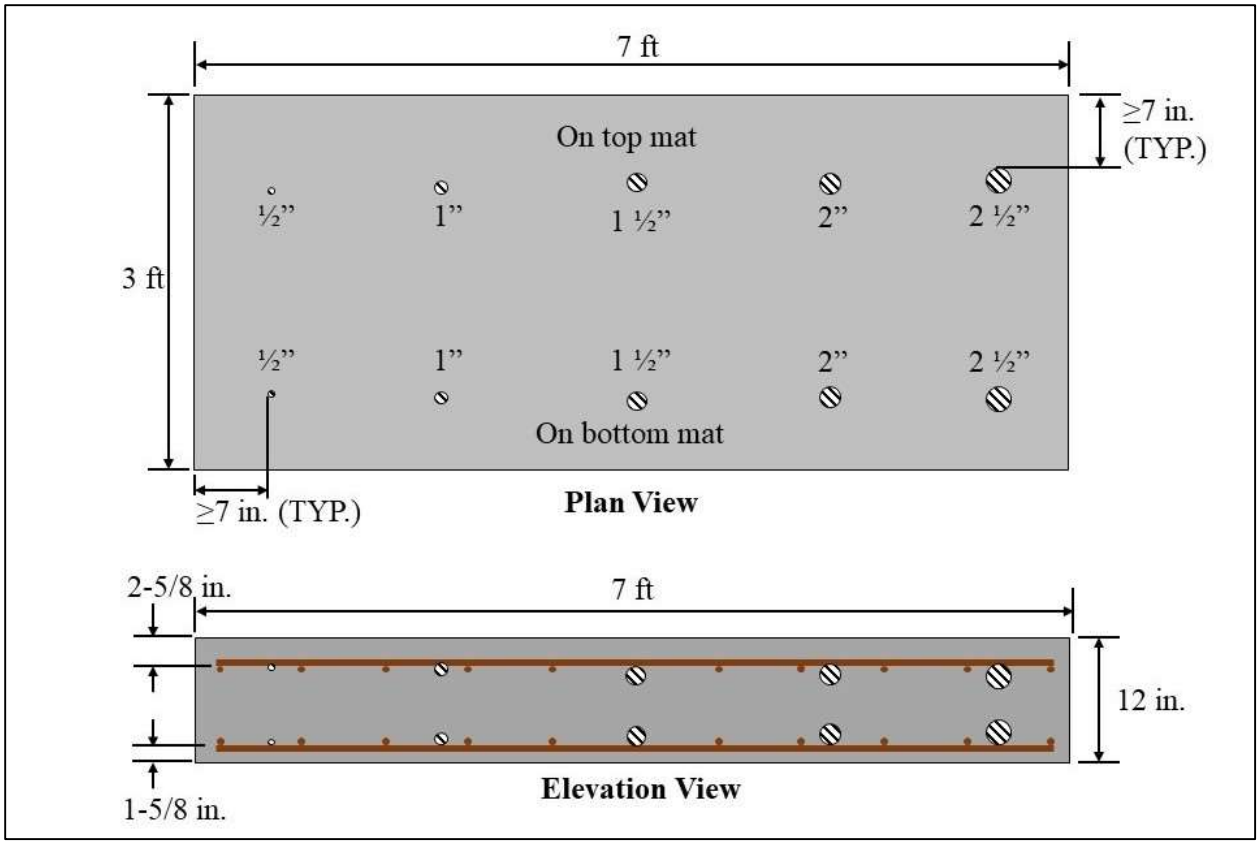

Figure 3-8: Diagram for Specimen V1

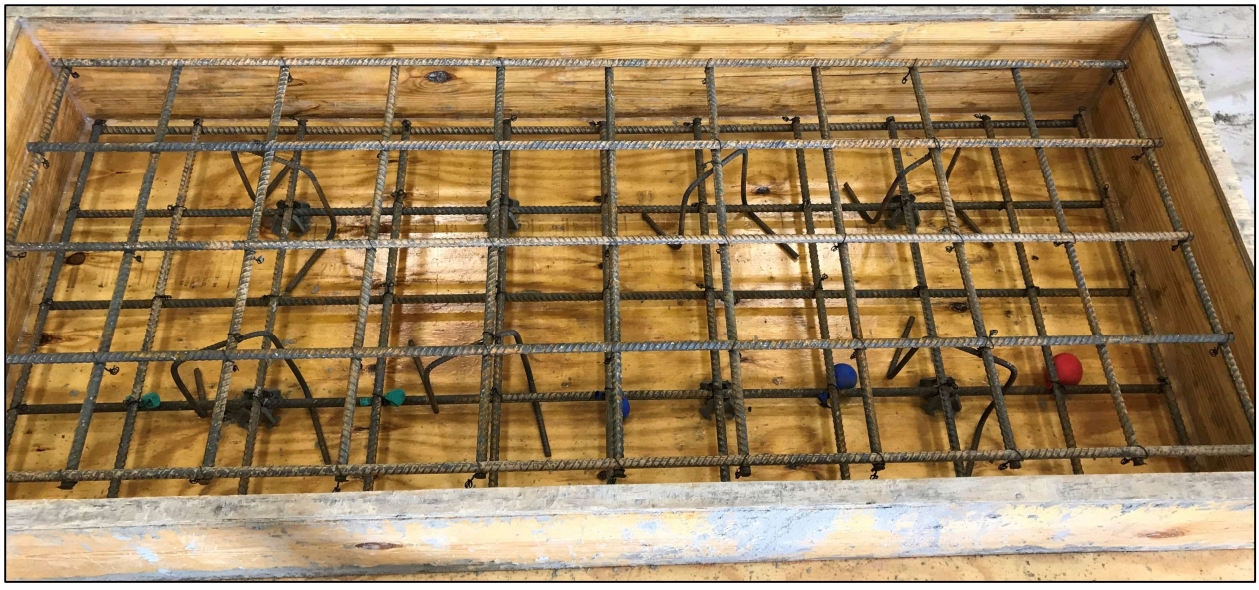

Figure 3-9: Specimen V1 prior to concrete placement

3.4.1.2 Specimen V2

Specimen V2 was constructed with the following objectives in mind:

- Determine smallest detectable deep void,
- Determine effect of depth of void on void detection, and
- Determine suitability of using clay-filled balloons to simulate voids.

In order to investigate the detectability of these defects at both deep and shallow locations, this slab was constructed to be 12 in. thick. The voids were created using clay-filled balloons with diameters between 0.5 and 2.5 in. that were tied to the reinforcing steel at locations shown in Figure 3-10. Clay was used to fill the balloons. In Figure 3-11, Specimen V2 is shown prior to placement of ready-mixed concrete. During the concrete placement and consolidation process, care was taken to ensure that the locations of the clay-filled balloons were not altered.

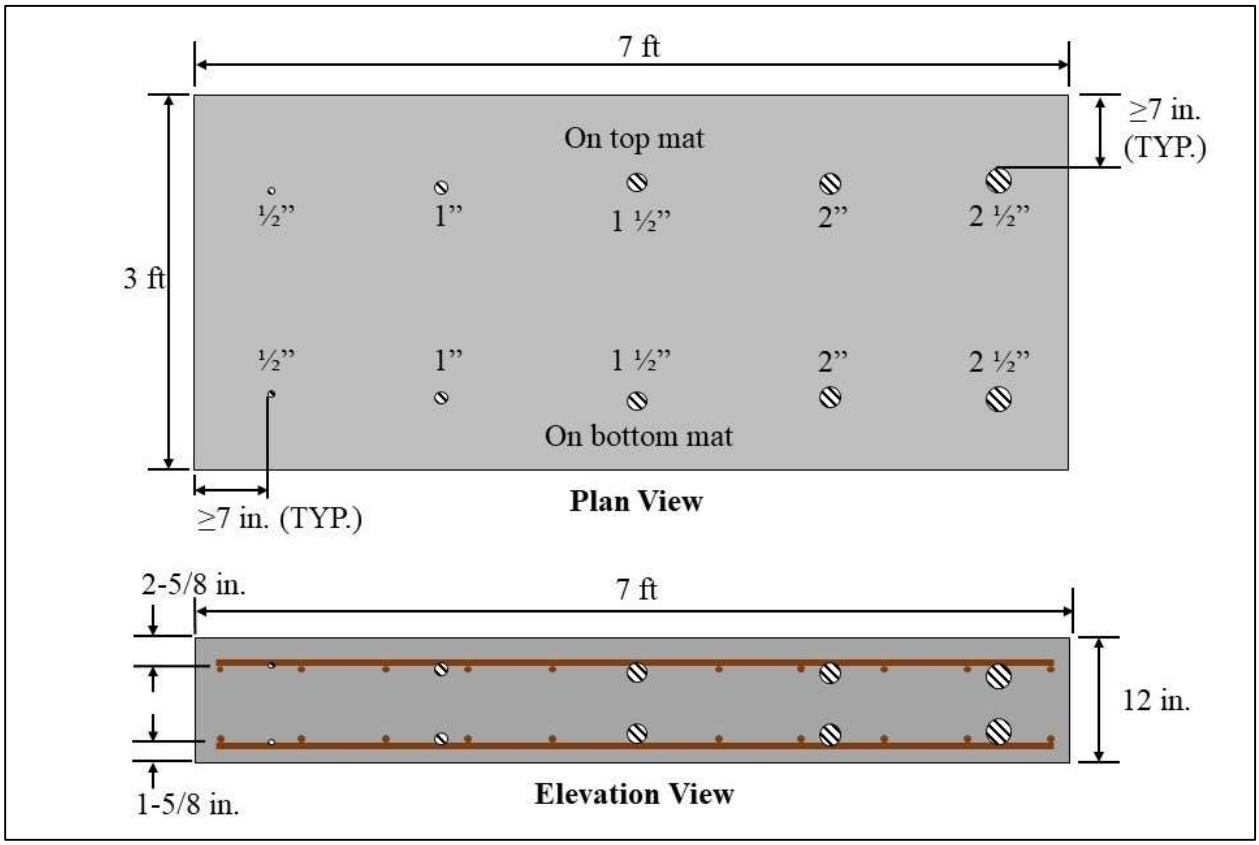

Figure 3-10: Diagram of Specimen V2

Figure 3-11: Specimen V2 prior to concrete placement

3.4.2 Delaminated Specimens

3.4.2.1 Specimen DL1

Specimen DL1 was constructed with the following objectives in mind:

- Determine thinnest detectable shallow delamination, and
- Evaluate performance of plastic relative to foam for delamination simulation.

This slab served to test the detectability of artificial, shallow delaminations and was therefore constructed to be 7.25 in. thick. Delaminations were made from foam sheets or plastic sheets of varying thickness, as shown in Figure 3-12 and Figure 3-13. All delaminations in this specimen measured 8 in. long and 4 in. wide, with rounded edges. In order to properly construct this specimen, concrete was placed into the formwork until the surface of the concrete was at the level of the bottom bars of the top reinforcement mat. All concrete in the formwork was then consolidated, after which the delaminations were placed between the longitudinal and transverse bars of the top reinforcement mat. Additional concrete was then immediately placed above the in-place concrete and consolidated using a vibrator. Care was taken to ensure that vibratory consolidation did not alter the location of the artificial delaminations.

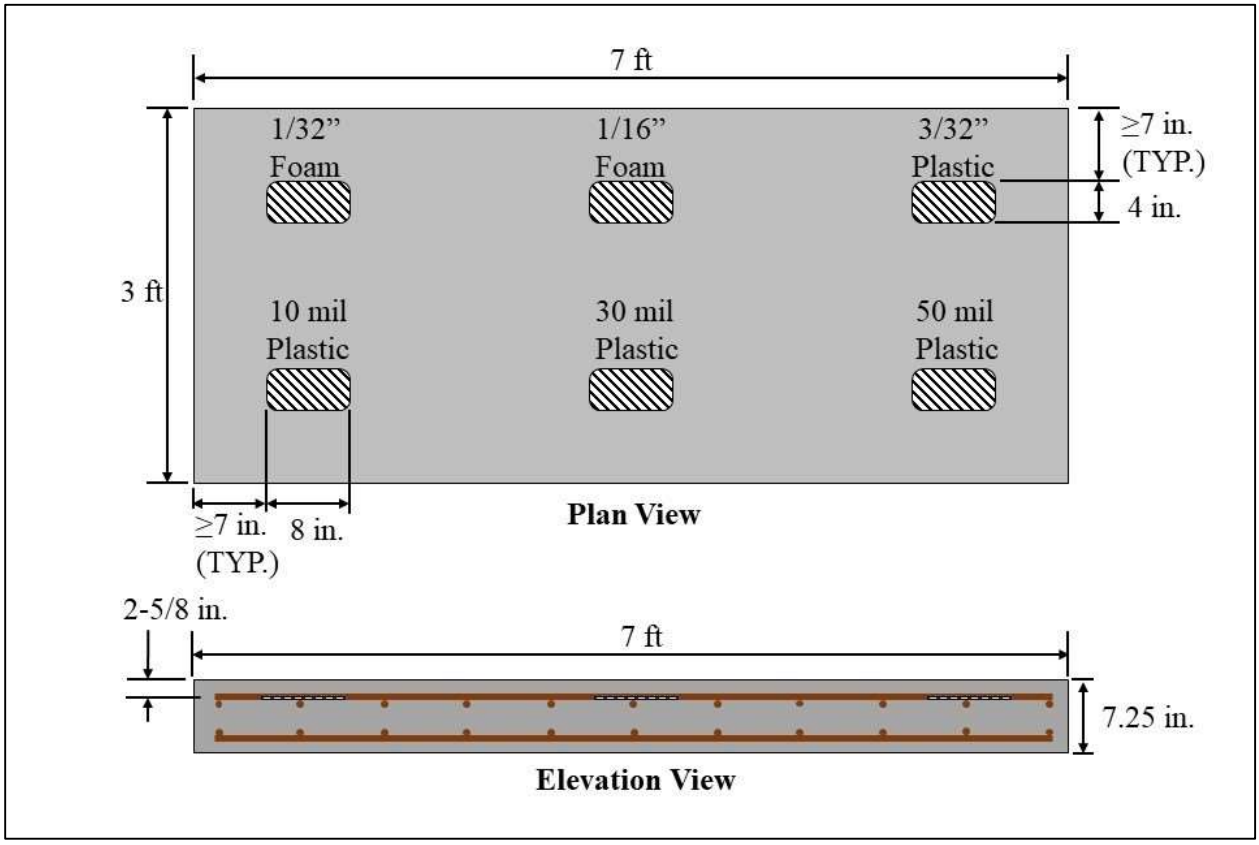

Figure 3-12: Diagram of Specimen DL1

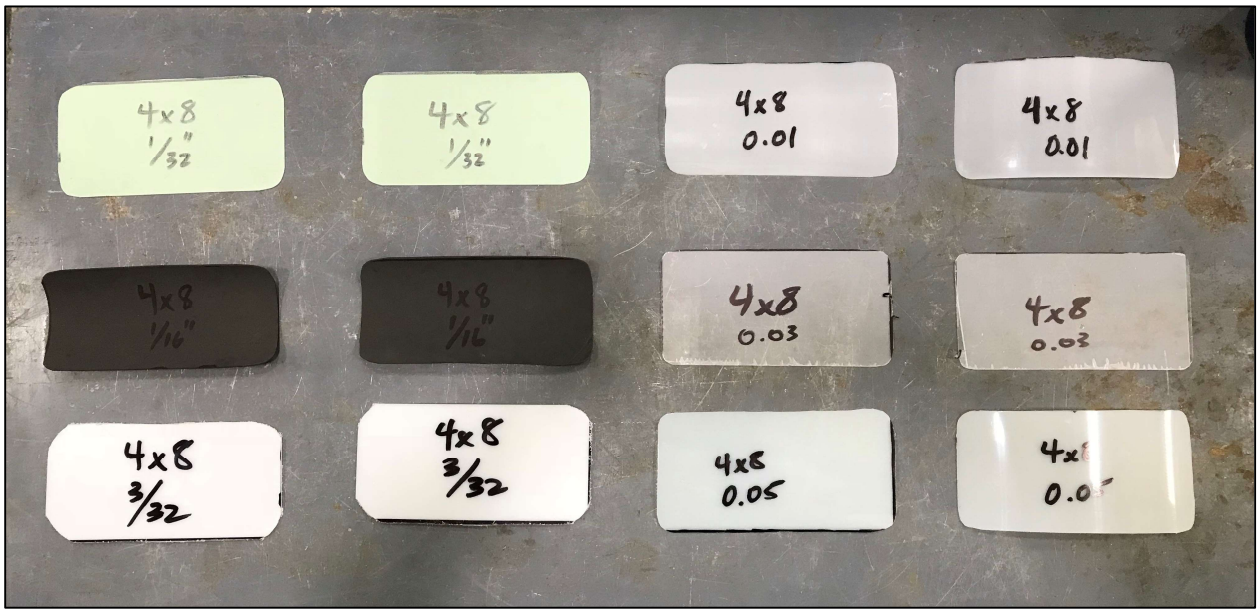

Figure 3-13: Plastic and foam sheets used as delaminations in DL1 and DL2

3.4.2.2 Specimen DL2

Specimen DL2 was constructed with the following objectives in mind:

- Determine thinnest detectable deep delamination,
- Determine effect of delamination depth on detectability, and
- Evaluate performance of plastic relative to foam for delamination simulation.

In order to investigate the detectability of these delaminations at deep locations, this slab was constructed to be 12 in. thick. Similar to Specimen DL1, these delaminations were made from foam sheets or plastic sheets of varying thickness, as shown in Figure 3-13 and Figure 3-14. All delaminations in this specimen measured 8 in. long and 4 in. wide, with rounded edges. In order to properly construct this specimen, concrete was placed into the formwork until the surface of the concrete was at the level of the bottom bars of the bottom reinforcement mat. All concrete in the formwork was then consolidated, after which the delaminations were placed between the longitudinal and transverse bars of the bottom reinforcement mat, as shown in Figure 3-15. Additional concrete was then immediately placed above the in-place concrete and consolidated using a vibrator. Care was taken to ensure that vibratory consolidation did not alter the location of the artificial delaminations.

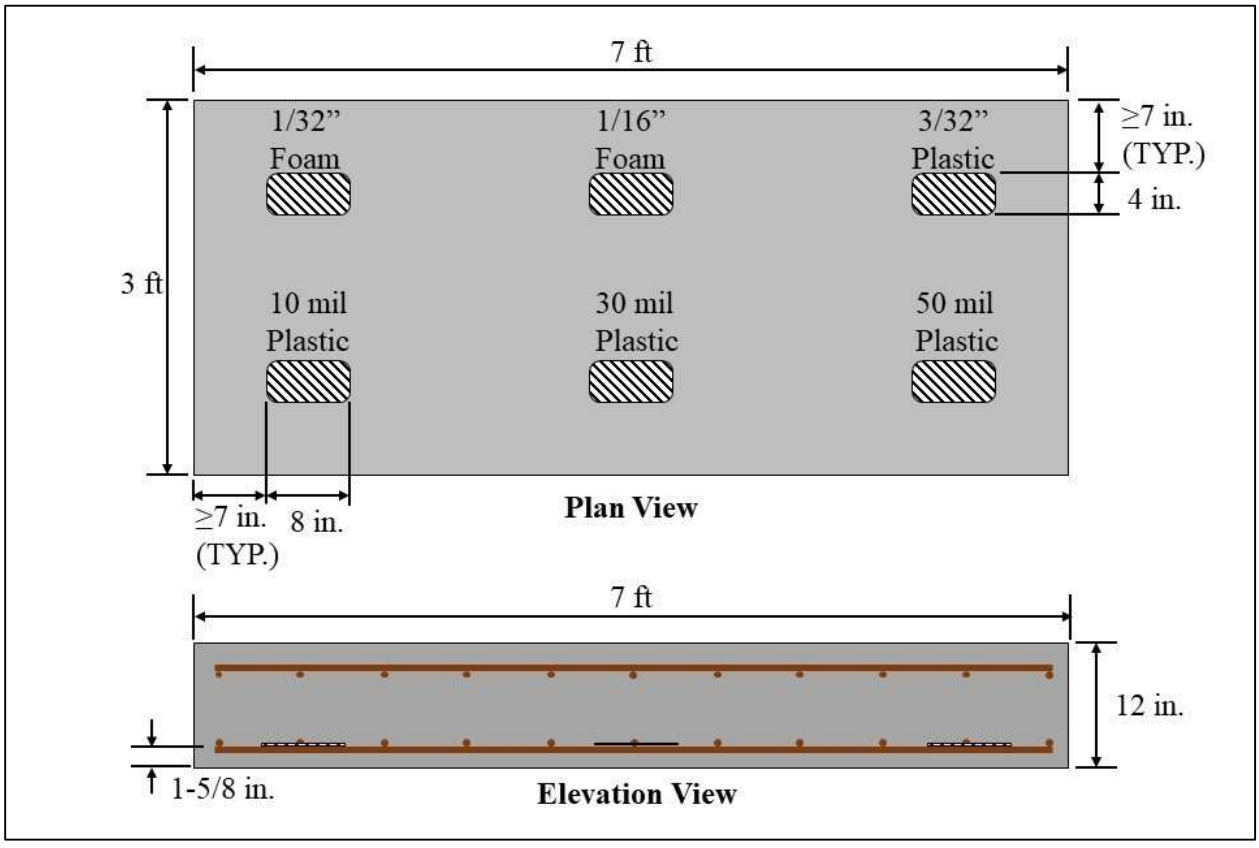

Figure 3-14: Diagram of Specimen DL2

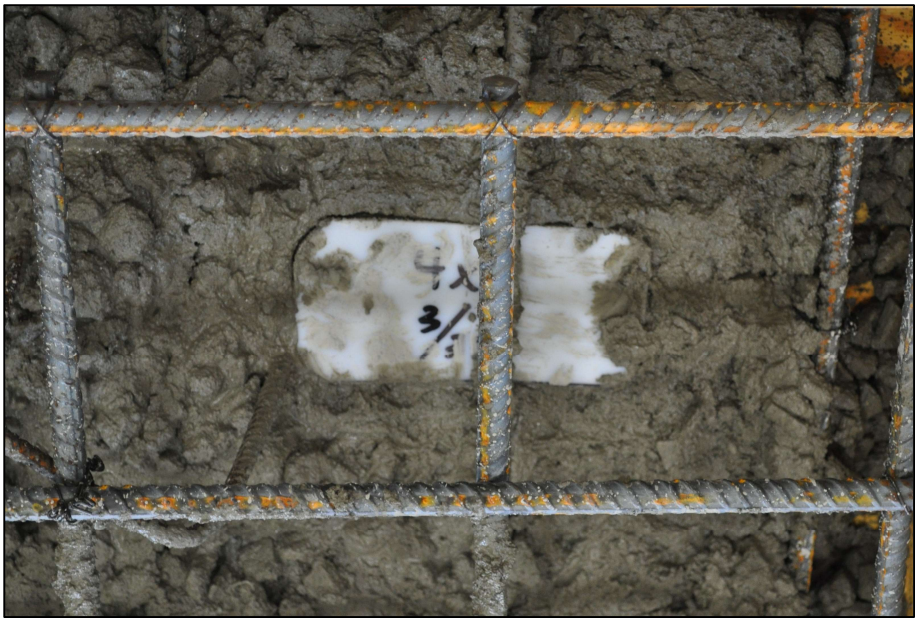

Figure 3-15: Plastic delamination between bars of bottom steel reinforcement

3.4.2.3 Specimen DL3

Specimen DL3 was constructed with the following objectives in mind:

- Evaluate the effectiveness of sand and oil to create delaminations, and
- Determine the effectiveness of creating a real debonded area relative to using plastic or foam inserts to simulate delaminations.

This slab served to test the detectability of artificial, shallow delaminations and was therefore constructed to be 7.25 in. thick. These delaminations were created using areas of sand or oil in an attempt to create a debonded area within the specimen, as shown in Figure 3-16. Both delaminated areas in this specimen measured 1.5 ft in length and spanned the full width of the slab. In order to properly construct this specimen, concrete was placed into the formwork until the surface of the concrete was at the level of the bottom bars of the top reinforcement mat. All concrete in the formwork was then consolidated. The concrete was then allowed to set, after which the strips of sand and oil were placed on the surface, as shown in Figure 3-17. Additional concrete was then placed above the in-place concrete. Care was taken to ensure that vibratory consolidation did not alter the artificial delaminations.

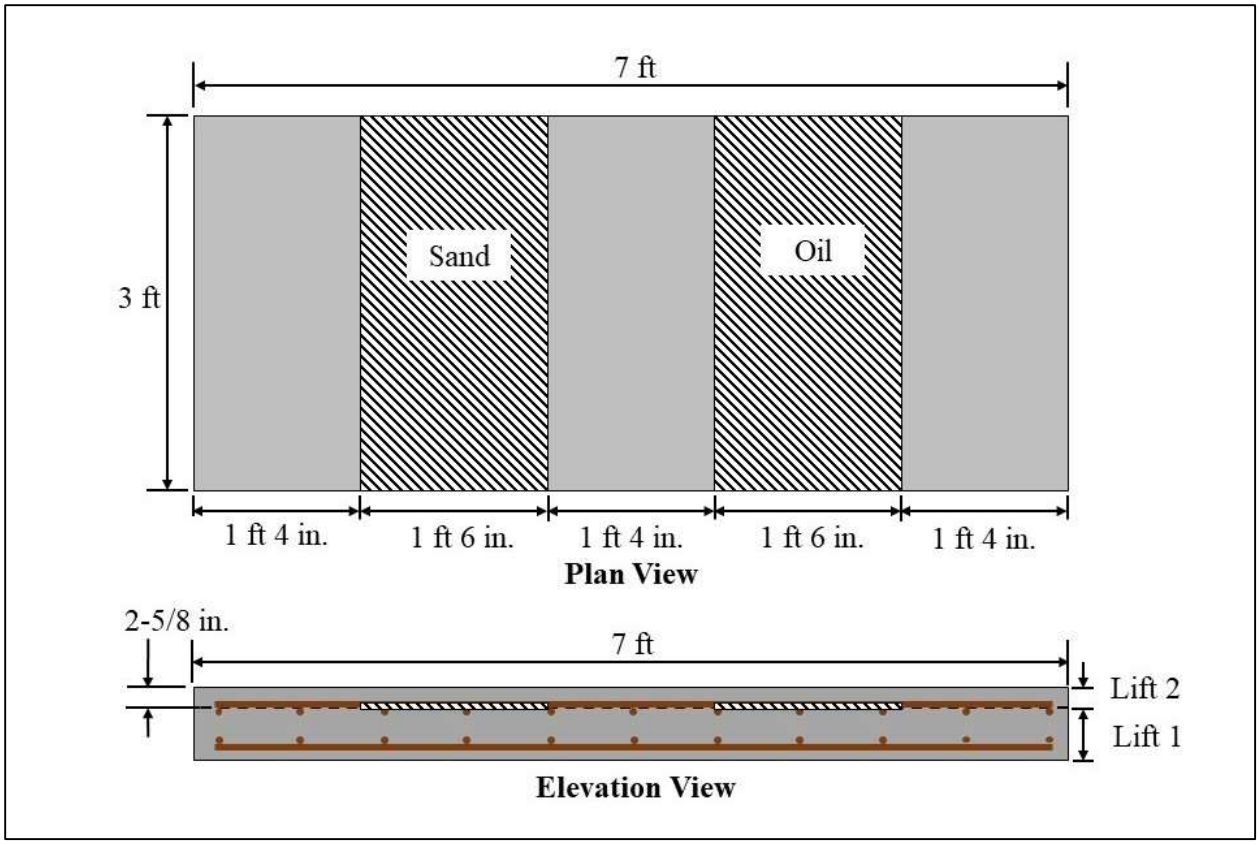

Figure 3-16: Diagram of Specimen DL3

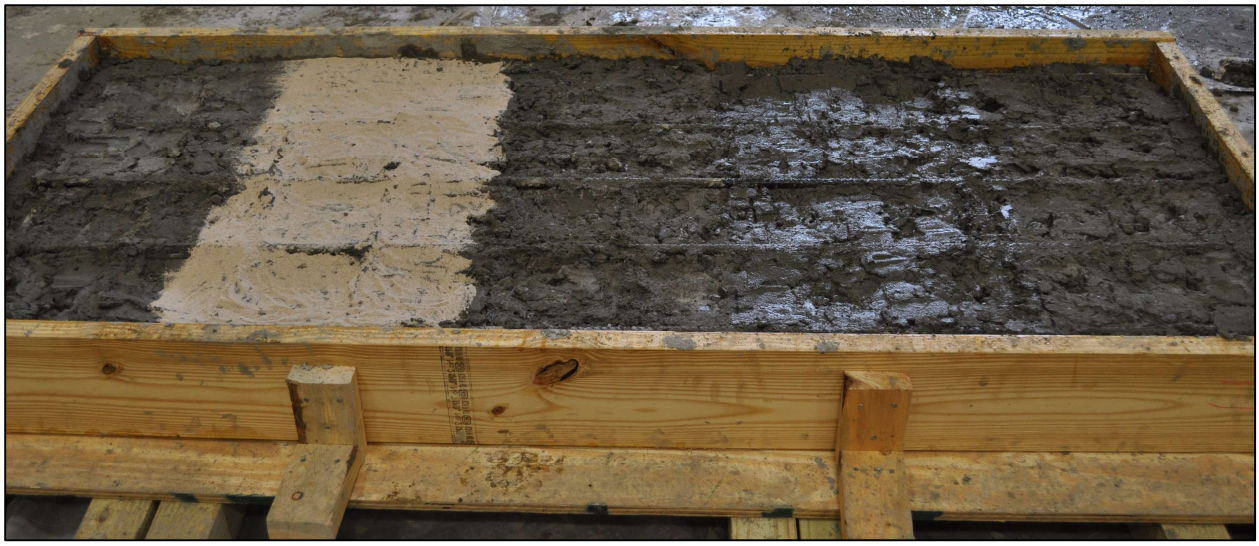

Figure 3-17: Sand and oil at the top layer of reinforcement

3.4.2.4 Specimen DL4

Specimen DL4 was constructed with the following objective in mind:

- Evaluate the effectiveness of sand and oil to create delaminations, and

- Determine the effectiveness of creating a real debonded area at the bottom reinforcement mat relative to using plastic or foam inserts to simulate delaminations.
- Determine the effect of delamination depth on detectability.

In order to investigate the detectability of these delaminations at deep locations, this slab was constructed to be 12 in. thick. Similar to Specimen DL3, these delaminations were created using areas of sand or oil in an attempt to create a debonded area within the specimen, as shown in Figure 3-18. Both delaminated areas in this specimen measured 1.5 ft in length and spanned the full width of the slab. In order to properly construct this specimen, concrete was placed into the formwork until the surface of the concrete was at the level of the bottom bars of the bottom reinforcement mat. All concrete in the formwork was then consolidated. The concrete was then allowed to set, after which the strips of sand and oil were placed on the surface. Additional concrete was then placed above the in-place concrete. Care was taken to ensure that vibratory consolidation did not alter the artificial delaminations.

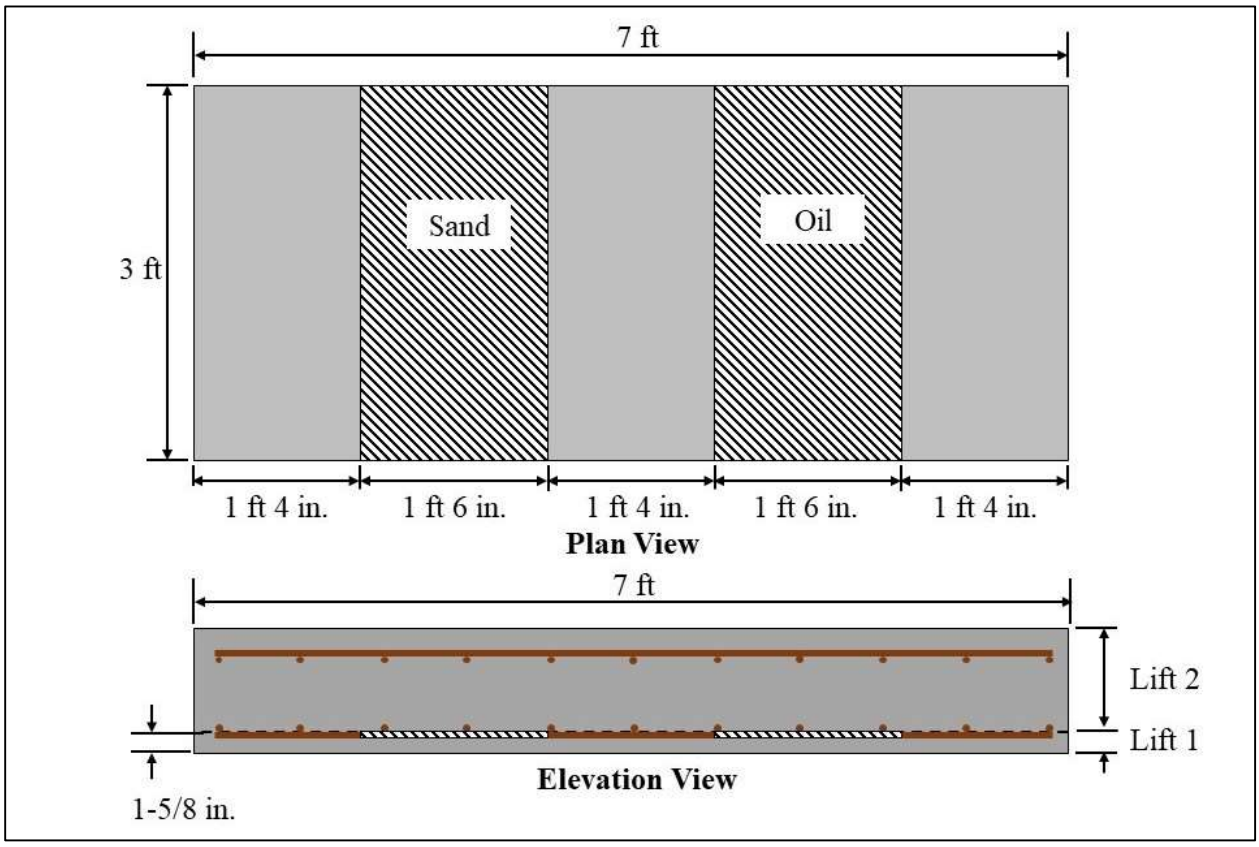

Figure 3-18: Diagram of Specimen DL4

3.4.2.5 Specimen DL5

Specimen DL5 was constructed with the following objective in mind:

- Determine smallest detectable shallow delamination.

This slab served to test the detectability of artificial, shallow delaminations and was therefore constructed to be 7.25 in. thick. Delaminations were made from plastic sheets of varying size and a constant 30 mil thickness, as shown in Figure 3-19. In order to properly construct this specimen, concrete was placed into the formwork until the surface of the concrete was at the level of the bottom bars of the top reinforcement mat. All concrete in the formwork was then consolidated, after which the delaminations were placed between the longitudinal and transverse bars of the top reinforcement mat. Additional concrete was then immediately placed above the in-place concrete and consolidated using a vibrator. Care was taken to ensure that vibratory consolidation did not alter the location of the artificial delaminations.

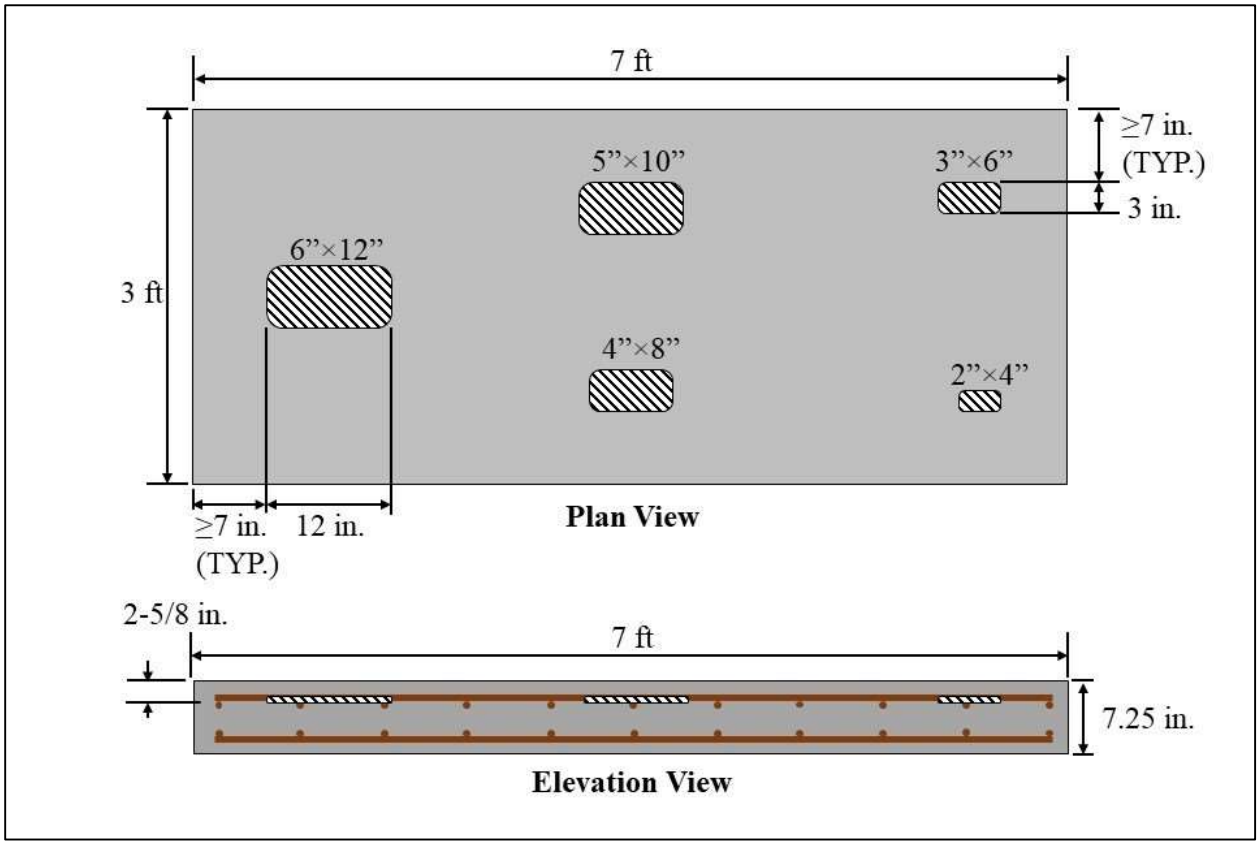

Figure 3-19: Diagram of Specimen DL5

3.4.2.6 Specimen DL6

Specimen DL6 was constructed with the following objectives in mind:

- Determine smallest detectable deep delamination, and
- Determine effect of depth of defect on detectability.

In order to investigate the detectability of these delaminations at deep locations, this slab was constructed to be 12 in. thick. Delaminations were made from plastic sheets of varying plan dimension and a constant 30 mil thickness, as shown in Figure 3-20. In order to properly construct this specimen, concrete was placed into the formwork until the surface of the concrete was at the level of the bottom bars of the bottom reinforcement mat. All concrete in the formwork was then consolidated, after which the delaminations were placed between the longitudinal and transverse bars of the bottom of reinforcement mat. Additional concrete was then immediately placed above the in-place concrete and consolidated using a vibrator. Care was taken to ensure that vibratory consolidation did not alter the location of the artificial delaminations.

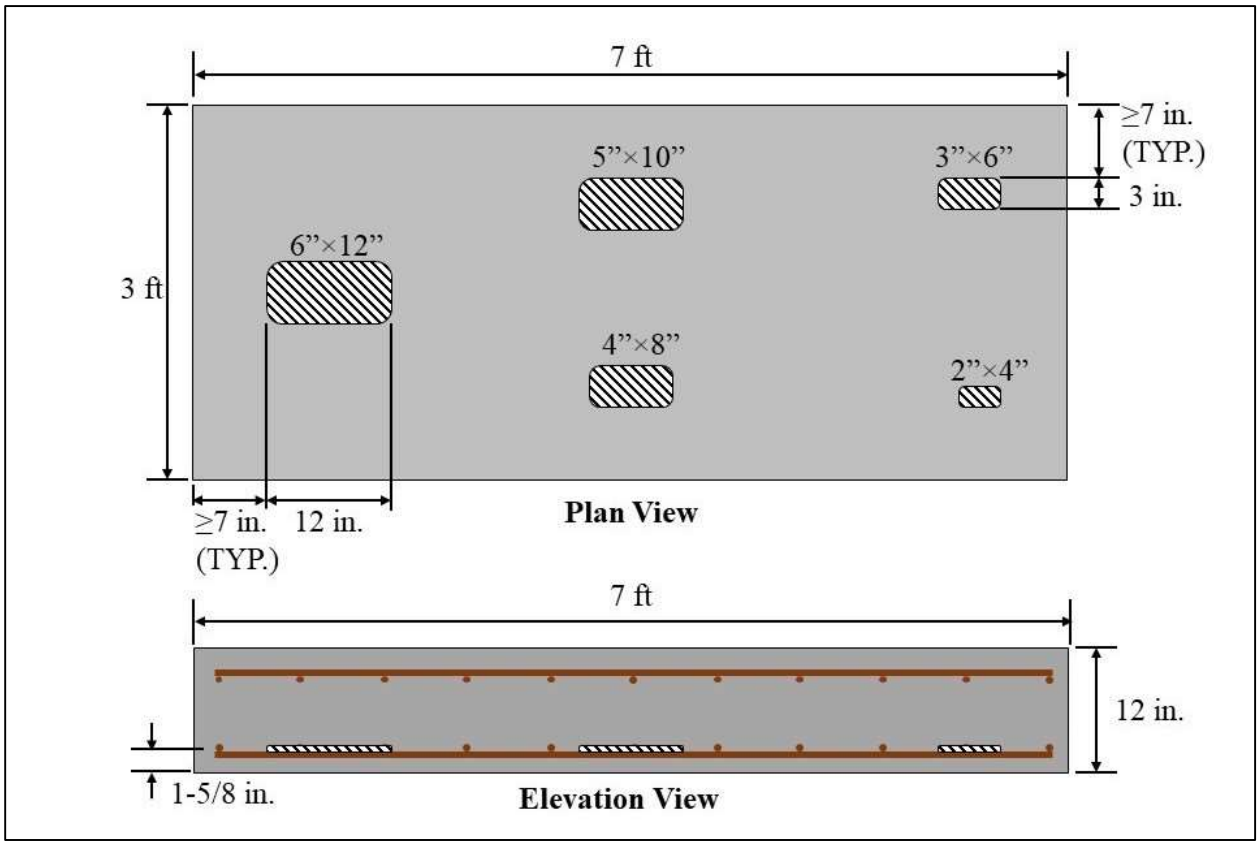

Figure 3-20: Diagram of Specimen DL6

3.4.2.7 Specimen DL7

Specimen DL7 was constructed with the following objectives in mind:

- Determine the effect of partial bond of shallow delaminations, and
- Determine the effect of thickness of partially bonded delaminations.

This slab served to test the detectability of artificial, shallow delaminations and was therefore constructed to be 7.25 in. thick. Delaminations were made from plastic sheets with 10 mil or 30 mil thickness, and a fraction of area removed in a checkerboard fashion, as shown in Figure 3-21 and Figure 3-22. The unbonded fraction, U, represents the percentage of delamination that was not cut out in checkerboard pattern. All delaminations in this specimen measured 8 in. long and 4 in. wide. In order to properly construct this specimen, concrete was placed into the formwork until the surface of the concrete was at the level of the bottom bars of the top reinforcement mat. All concrete in the formwork was then consolidated, after which the delaminations were placed between the longitudinal and transverse bars of the top reinforcement mat, as shown in Figure 3-23. Additional concrete was then immediately placed above the in-place concrete and blended using vibratory consolidation techniques. Care was taken to ensure that vibratory consolidation did not alter the location of the artificial delaminations.

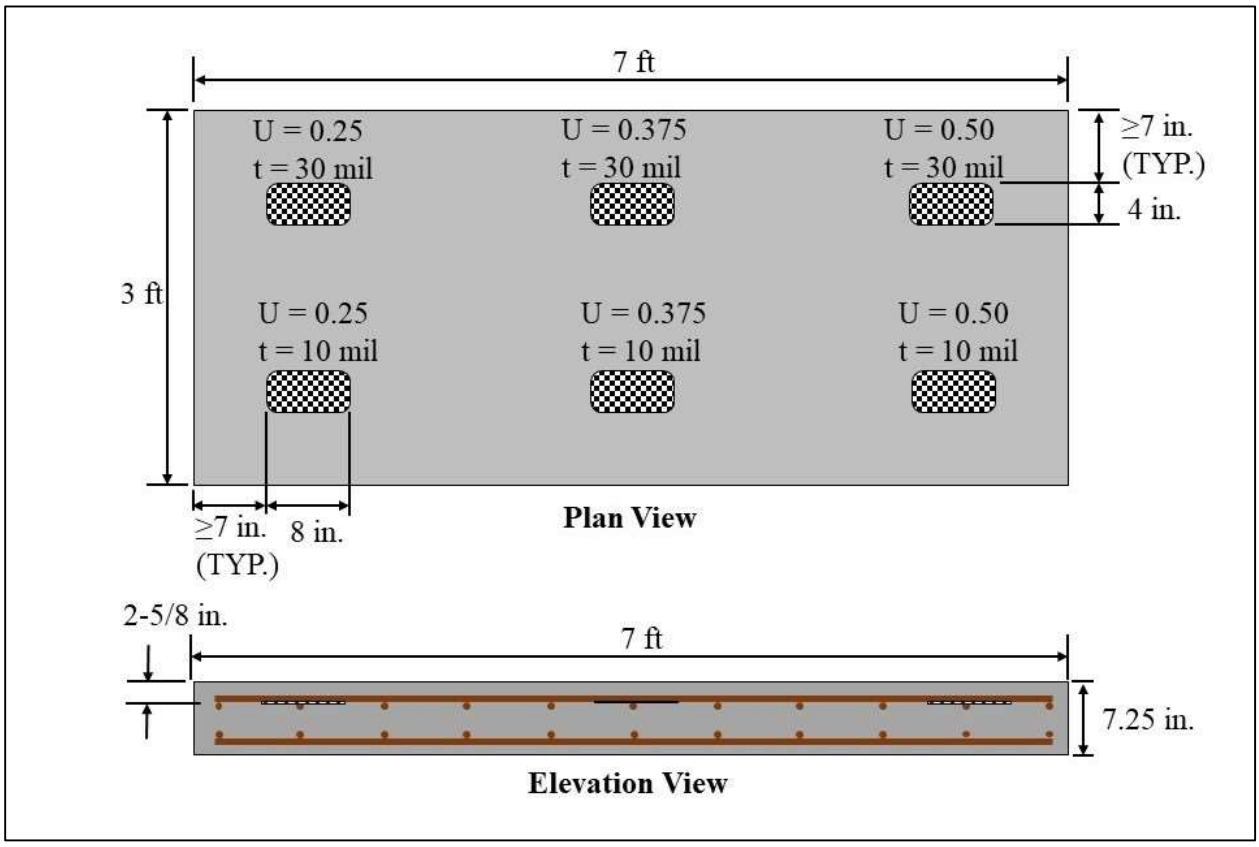

Figure 3-21: Diagram of Specimen DL7

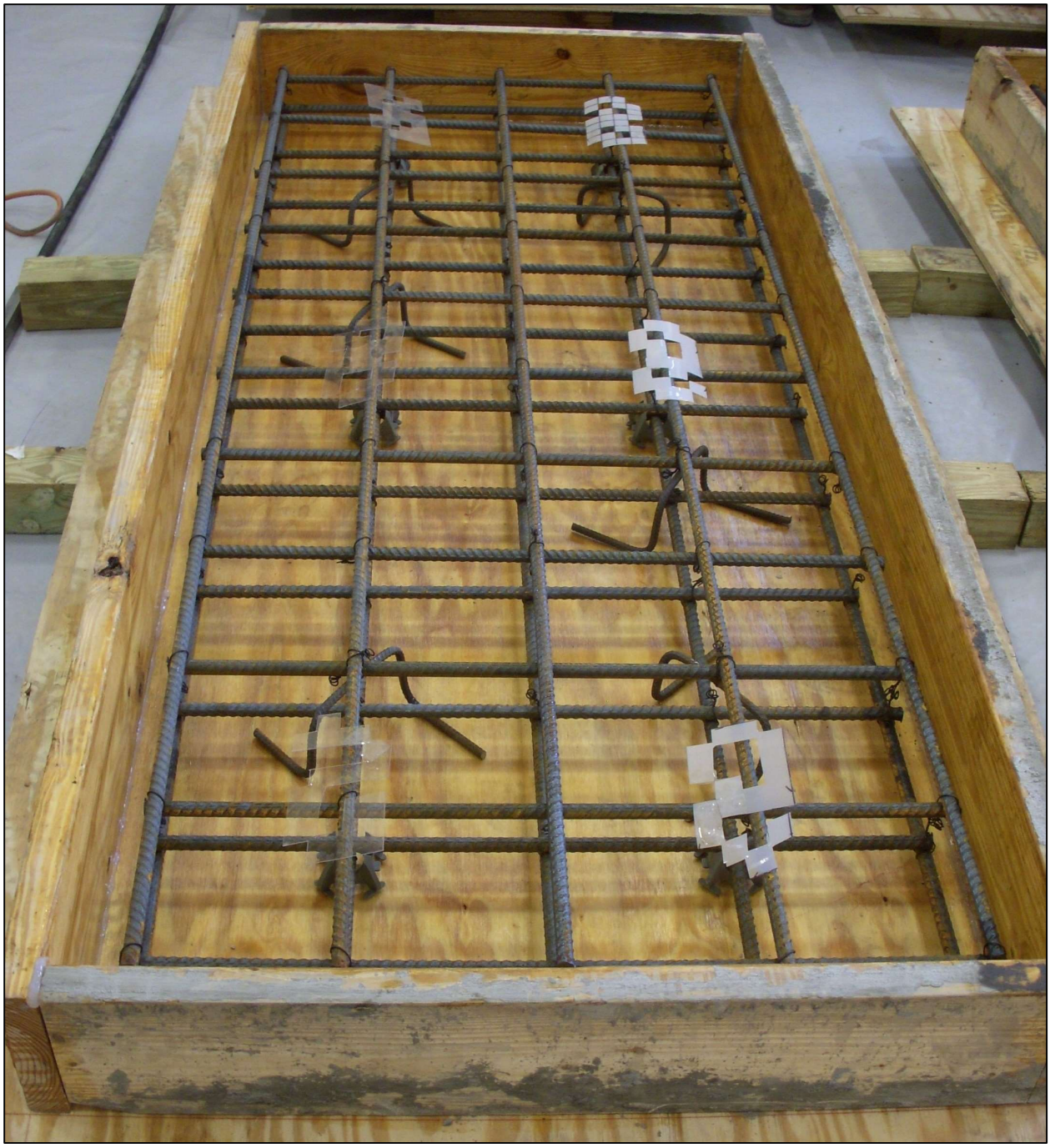

Figure 3-22: Delaminations exhibiting unbonded fractions

Figure 3-23: Unbonded delamination in place

3.4.2.8 Specimen DL8

Specimen DL8 was constructed with the following objectives in mind:

- Determine the effect of partial bond of deep delaminations,
- Determine the effect of thickness of partially bonded delaminations, and
- Determine the effect of defect depth on detectability.

In order to investigate the detectability of these delaminations at deep locations, this slab was constructed to be 12 in. thick. Delaminations were made from plastic sheets with 10 mil or 30 mil thickness, and a fraction of area removed in a checkerboard fashion, as shown in Figure 3-24. The unbonded fraction, U, represents the percentage of delamination that was not cut out in checkerboard pattern. All delaminations in this specimen measured 8 in. long and 4 in. wide. In order to properly construct this specimen, concrete was placed into the formwork until the surface of the concrete was at the level of the bottom bars of the top reinforcement mat. All concrete in the formwork was then consolidated, after which the delaminations were placed between the longitudinal and transverse bars of the top reinforcement mat. Additional concrete

was then immediately placed above the in-place concrete and consolidated using a vibrator. Care was taken to ensure that vibratory consolidation did not alter the location of the artificial delaminations.

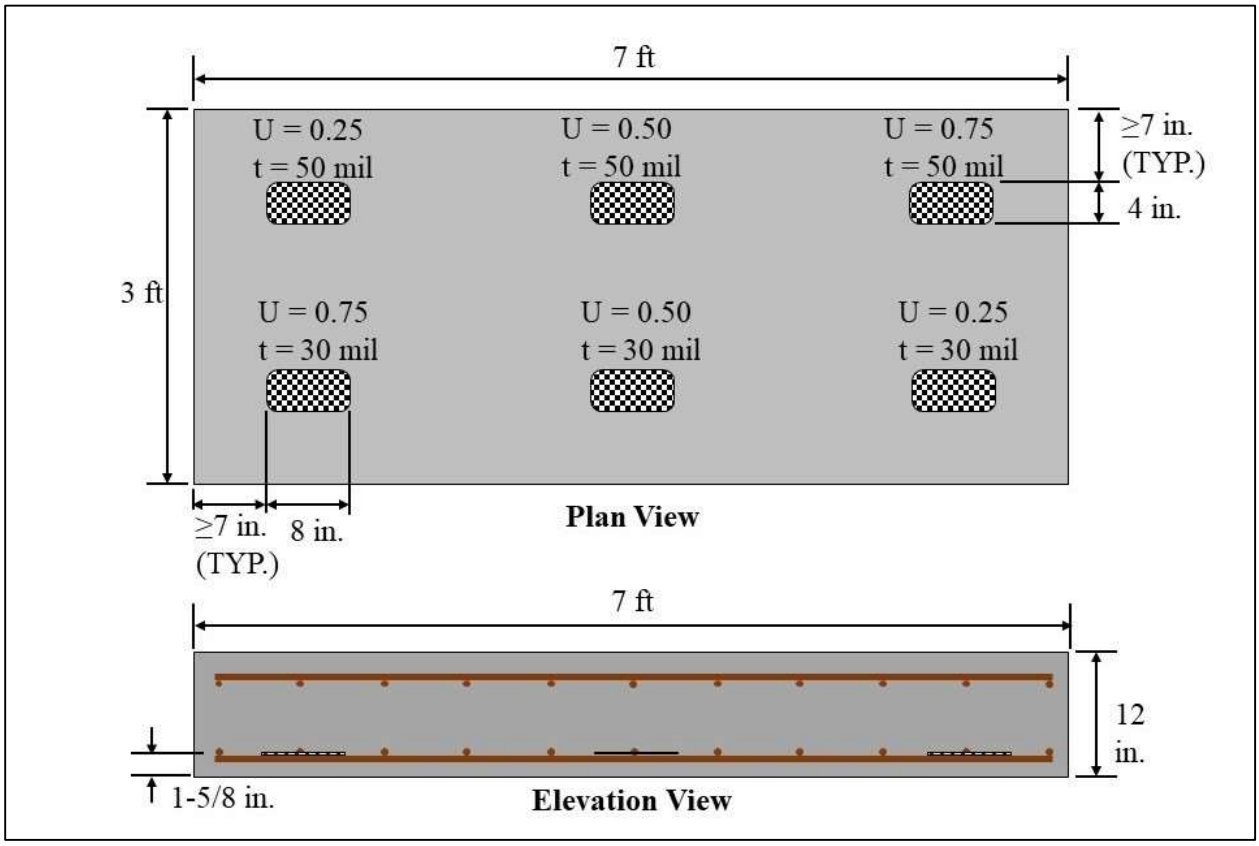

Figure 3-24: Diagram of Specimen DL8

3.4.3 Cracking Specimen

3.4.3.1 Specimen CR1

Specimen CR1 was constructed with the following objectives in mind:

- Test the appearance of the full-depth crack and verify that it forms properly and does not run the full slab thickness, and
- Test the viability of cracks made using plastic sheeting.

This slab served to test the detectability of artificial, shallow cracks and was therefore constructed to be 7.25 in. thick. Vertical cracks were made from plastic sheets of varying thickness and varying depth; one partial-depth crack in the center of the specimen was created using synthetic grease to debond the concrete, as shown in Figure 3-25 and Figure 3-26. Plastic

cracks in this specimen measured 12 in. long. These plastic cracks were held vertically in place using a thin plastic string. In order to construct this specimen, a form bulkhead was placed midway along the longitudinal axis of the specimen. Concrete was placed into the formwork, measuring 3 × 3.5 ft, until the surface of the concrete was level with the top of the formwork. All concrete in the formwork was then consolidated, with care taken to ensure that vibratory consolidation did not adjust the location of the vertically oriented cracks. The concrete was allowed to partially set, after which the formwork bulkhead was removed and grease was applied to the top half of the concrete interface, as shown in Figure 3-27. Formwork was then placed around the uncast portion of the slab, and fresh concrete was subsequently placed there and consolidated, with care being taken to ensure that consolidation did not alter the location of the plastic cracks.

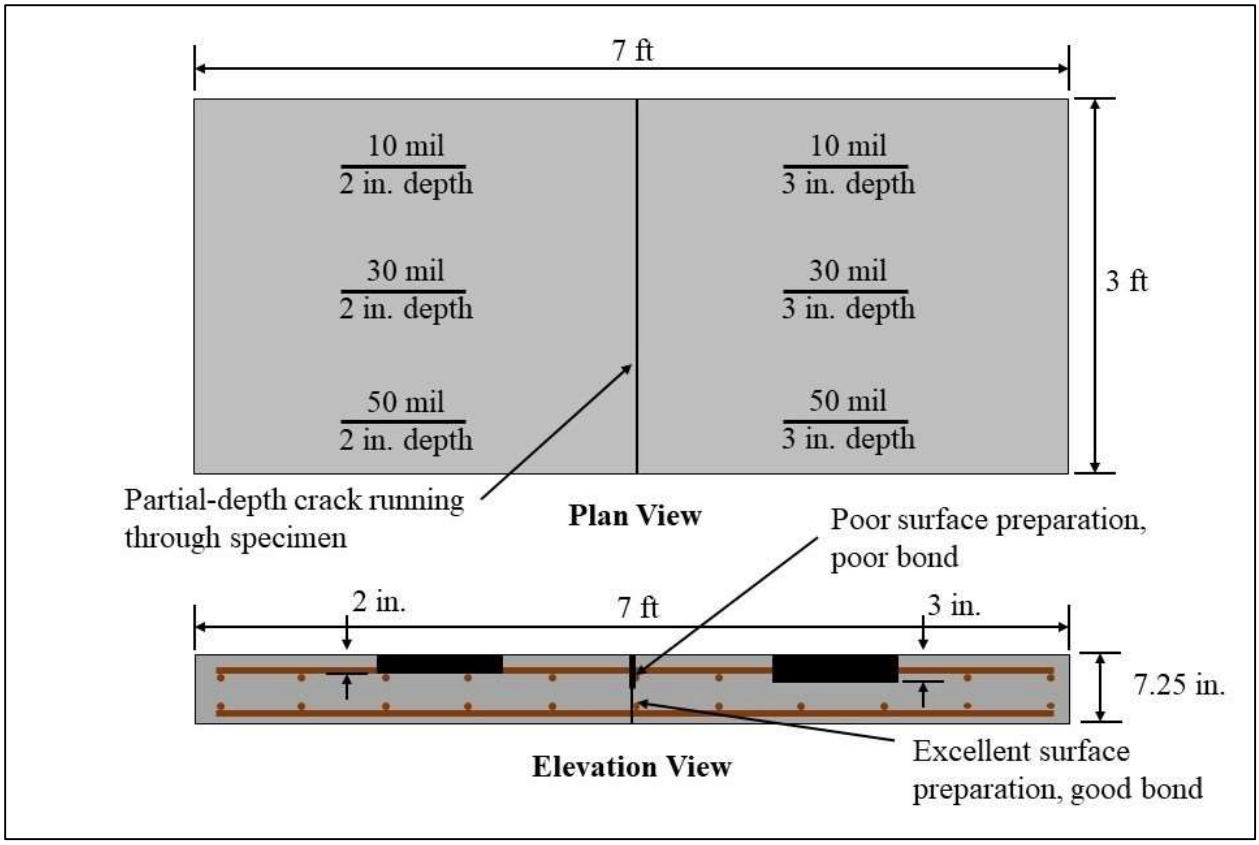

Figure 3-25: Diagram of Specimen CR1

Figure 3-26: Plastic sheets representing vertical cracks

Figure 3-27: Grease used to represent vertical debonding

3.4.4 Corrosion Specimens

3.4.4.1 Specimen C1

Specimen C1 was constructed with the following objective in mind:

- Determine the relation between the duration of current application and the extent of corrosion,

- Determine the detectability of corroded rebar in a specimen with shallow concrete cover, and
- Determine the detectability of corrosion-induced delaminations in a specimen with shallow concrete cover.

This slab, which had a concrete cover of ¾" from the surface of the specimen to the top layer of reinforcing steel, served to test the detectability of corrosion-induced delaminations in the top reinforcement mat and was therefore constructed to be 7.25 in. thick. Corrosion was induced using accelerated corrosion techniques. The top reinforcement mat, which was the target for corrosion activity, was divided into three sections in the longitudinal direction, as shown in Figure 3-28. At the locations of rebar discontinuity, a rubber-based compound was applied to the ends of the reinforcing steel bars to in order to electrically isolate each section. Prior to casting, an insulated wire was attached to each section by a screw placed into a threaded hole in the reinforcing steel. After the specimen was cast and cured, the surface was ponded with a three percent sodium chloride solution for one week prior to the application of current, as shown in Figure 3-29. The ponding reservoir was constructed using 0.375 in. thick acrylic sheets. All joints were sealed and the reservoir was bonded to the concrete using a construction adhesive. To provide current to the system, standard 12 V batteries were connected to both Zone 2 and Zone 3, the former being connected for 7 days and the latter being connected for 14 days. The circuit was connected such that the reinforcing steel was connected to the positive post of the battery, while a stainless steel plate on the concrete surface, submersed in the sodium chloride solution, was connected to the negative post of the battery. Trickle chargers were connected to each battery in order to prevent significant current loss. Ponding was held constant throughout the application of current. Aside from times where the research team tested the specimen to measure corrosion progression, sodium chloride solution and current were continuously applied to the specimen. The research team notated the amount of time where the current source was disconnected and compensated for any time lost in order to ensure a full 7-day or 14-day current application.

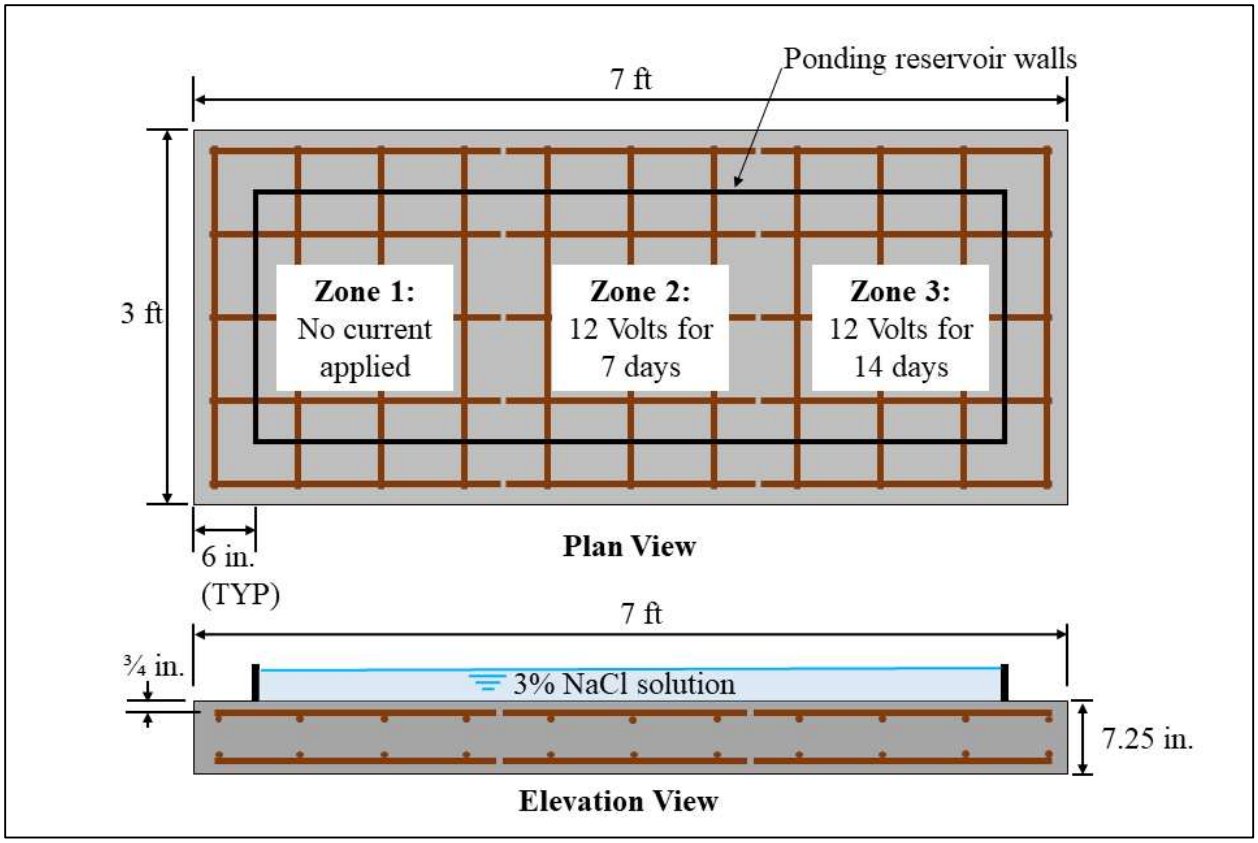

Figure 3-28: Diagram of Specimen C1

Figure 3-29: Corrosion specimens with ponding and current being applied

3.4.4.2 Specimen C2

Specimen C2 was constructed with the following objective in mind:

- Determine the relation between the duration of current application and the extent of corrosion,
- Determine the detectability of corroded rebar in a specimen with shallow concrete cover, and
- Determine the detectability of corrosion-induced delaminations in a specimen with shallow concrete cover.

This slab, which had a concrete cover of 2" from the surface of the specimen to the top layer of reinforcing steel, served to test the detectability of corrosion-induced delaminations in the top reinforcement mat and was therefore constructed to be 7.25 in. thick. Corrosion was induced using accelerated corrosion techniques. The top reinforcement mat, the target for corrosion activity, was divided into three sections in the longitudinal direction, as shown in Figure 3-30. At the locations of rebar discontinuity, a rubber-based compound was applied to the ends of the reinforcing steel bars in order to electrically isolate each section. Prior to casting, an insulated wire was attached to each section by a screw placed into a threaded hole in the reinforcing steel. After the specimen was cast and cured, the surface was ponded with a three percent sodium chloride solution for one week prior to the application of current. The ponding reservoir was constructed using 0.375 in. thick acrylic sheets. All joints were sealed and the reservoir was bonded to the concrete using a construction adhesive. To provide current to the system, standard 12 V batteries were connected to both Zone 2 and Zone 3, the former being connected for 14 days and the latter being connected for 28 days. The circuit was connected such that the reinforcing steel was connected to the positive post of the battery, while a stainless steel plate placed at the concrete surface, submersed in the sodium chloride solution, was connected to the negative post of the battery. Trickle chargers were connected to each battery in order to prevent significant current loss. Ponding was held constant throughout the application of current. Aside from times where the research team tested the specimen to measure corrosion progression, sodium chloride solution and current were continuously applied to the specimen. The research team notated the amount of time where the current source was disconnected and compensated for any time lost in order to ensure a full 14-day or 28-day current application.

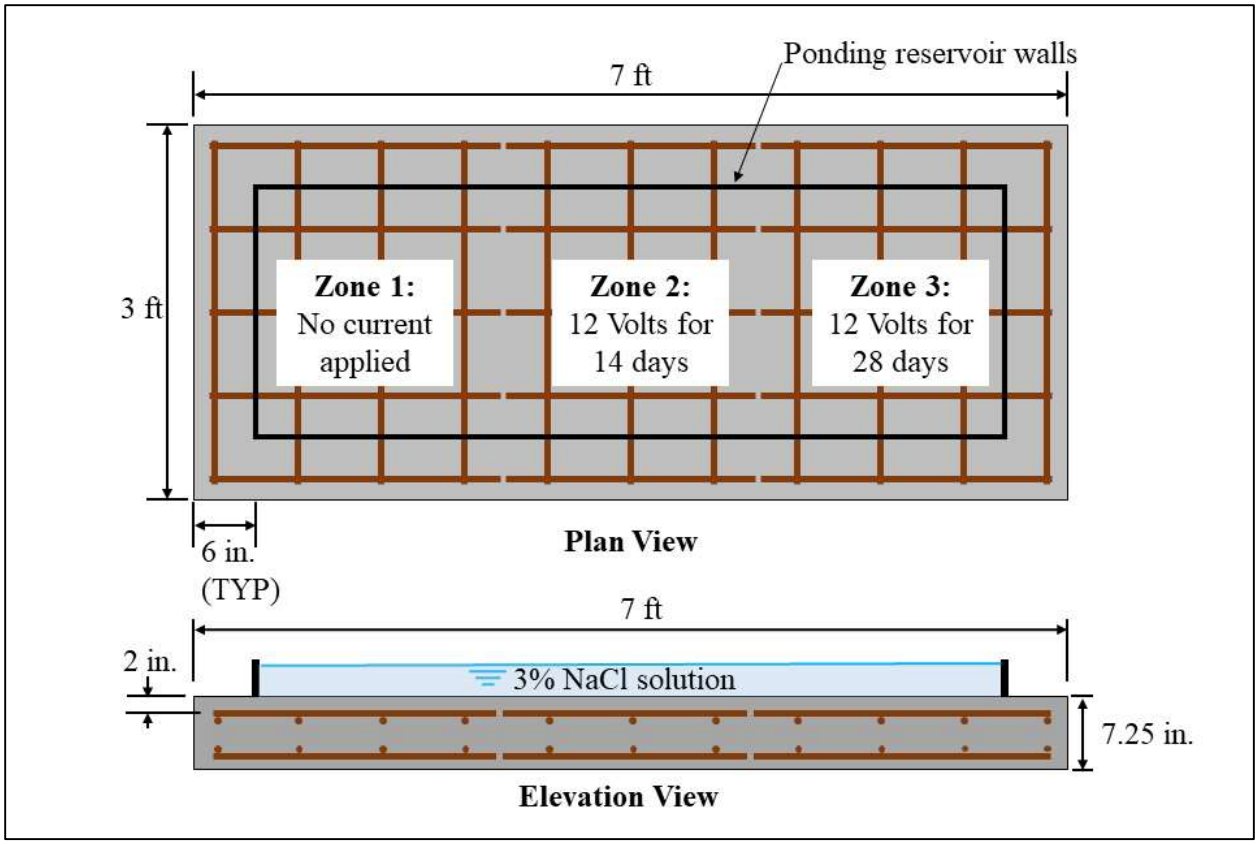

Figure 3-30: Diagram of Specimen C2

3.4.5 Control Specimen

3.4.5.1 Specimen CONTROL

Specimen CONTROL was constructed with the following objective in mind:

- Verify that no cold joint is detectable in a two-stage casting method when using the same concrete mixture.

This slab served to test the detectability of a cold joint in any of the specimens that used a two-phase casting method, and was therefore constructed to be 7.25 in. thick. Constructing this specimen required two separate casting phases. The first phase consisted of casting a small, 4-inch thick specimen, measuring 1 × 5 ft. This smaller specimen was cast using a concrete mixture batched according to the ALDOT bridge deck mixture proportions. The encased specimen concrete mixture proportions for Specimen CONTROL can be found in Table 3-4. In order to keep the reinforcement continuous throughout the entire test slab, the smaller specimen was cast using a two-part form ("the two-part form"), as shown in Figure 3-31. Mixture ingredients were individually batched according to the mixture proportions and mixed in the

laboratory using a concrete mixer powered by an electric motor ("the laboratory mixer"), shown in Figure 3-32. The concrete was then placed into the formwork, consolidated, and raked to provide adequate surface roughness. The small specimen was then moist cured for seven days. The second phase consisted of placing the small specimen, shown in Figure 3-33, into the formwork for the larger 3 × 7 ft test specimens, and adding a top layer of reinforcing steel. The standard ALDOT bridge deck mixture of ready-mixed concrete was then cast around the small specimen, creating an embedded area of distressed concrete as shown in Figure 3-34.

Table 3-4: Encased specimen mixture proportions for Specimen CONTROL

Material	Proportions	
#57 Limestone Coarse Aggregate	1,900	lb/yd^3
Fine Aggregate	1,285	lb/yd^3
Portland Cement	465	lb/yd^3
Class C Fly Ash	155	lb/yd^3
Water	275	lb/yd^3
Air Entraining Admixture	1.5	oz/yd^3
HRWR Admixture	25	oz/yd^3

Figure 3-31: The two-part form used to cast 1 × 5 ft specimens

Figure 3-32: Concrete mixer in the laboratory

Figure 3-33: Encased specimen of control concrete

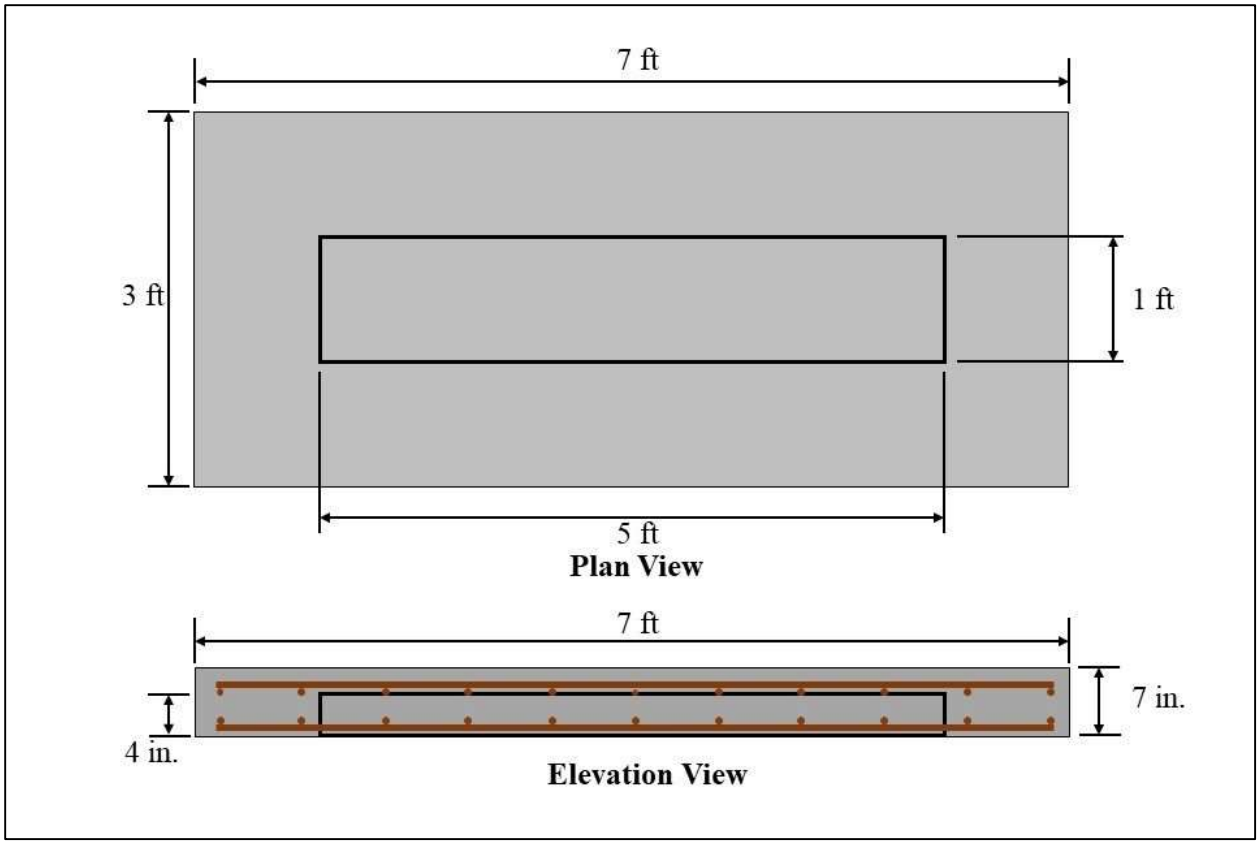

Figure 3-34: Diagram for Specimen CONTROL

3.4.6 Deteriorated Specimens

3.4.6.1 Specimen DE2

Specimen DE2 was constructed with the following objectives in mind:

- Verify that the deterioration is detected as a deteriorated region using NDT equipment, and
- Determine if a concrete mixture with a high entrained air content is suitable for replicating concrete deterioration

This slab served to represent a typical bridge deck in the state of Alabama and was therefore constructed to be 7.25 in. thick. Constructing this specimen required two separate casting phases. The first phase consisted of casting a small, 4-inch thick specimen, measuring 1 × 5 ft. This smaller specimen was cast using a concrete mixture containing a high amount of air-entraining admixture in attempt to increase the air content within the concrete. The encased specimen concrete mixture proportions for Specimen DE2 can be found in Table 3-5. In order to

keep the reinforcement continuous throughout the entire test slab, the smaller specimen was cast using the two-part form. Mixture ingredients were individually batched according to the mixture proportions and mixed in the laboratory using the laboratory mixer. The high air concrete mixture was then placed into the formwork, consolidated, and raked to provide adequate surface roughness. The small specimen was then moist cured for seven days. The second phase consisted of placing the small specimen, shown in Figure 3-32, into the formwork for the larger 3 × 7 ft test specimens, and adding a top layer of reinforcing steel. The standard ALDOT bridge deck mixture of ready-mixed concrete was then cast around the small specimen, creating an embedded area of distressed concrete as shown in Figure 3-36.

Table 3-5: Encased specimen mixture proportions for Specimen DE2

Item	Proportions	
#57 Limestone Coarse Aggregate	1,737	lb/yd^3
Fine Aggregate	1,175	lb/yd^3
Portland Cement	425	lb/yd^3
Class C Fly Ash	142	lb/yd^3
Water	251	lb/yd^3
Air Entraining Admixture	4.5	oz/yd^3
HRWR Admixture	23	oz/yd^3

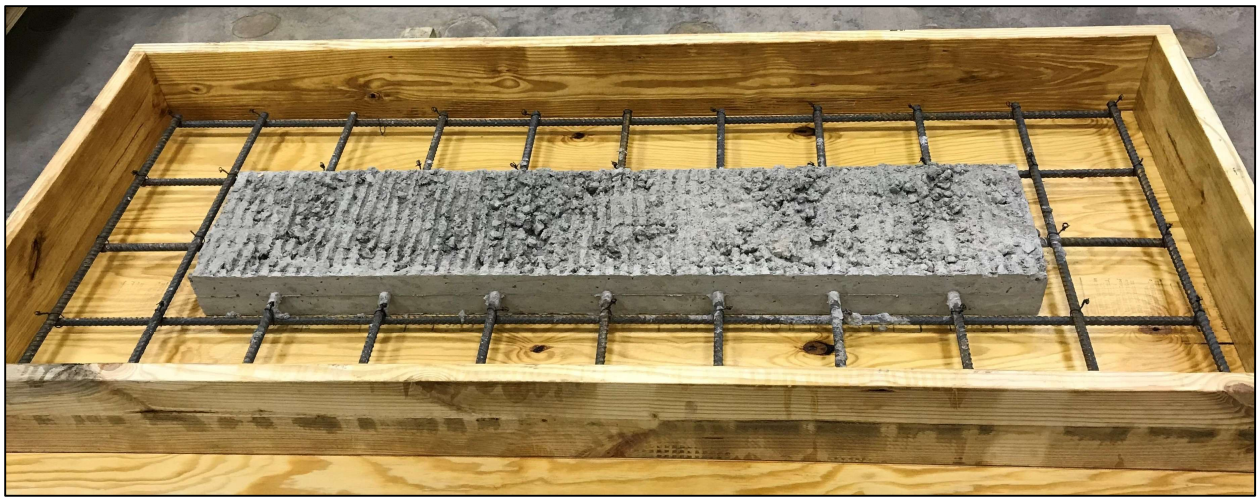

Figure 3-35: Encased specimen with high air content

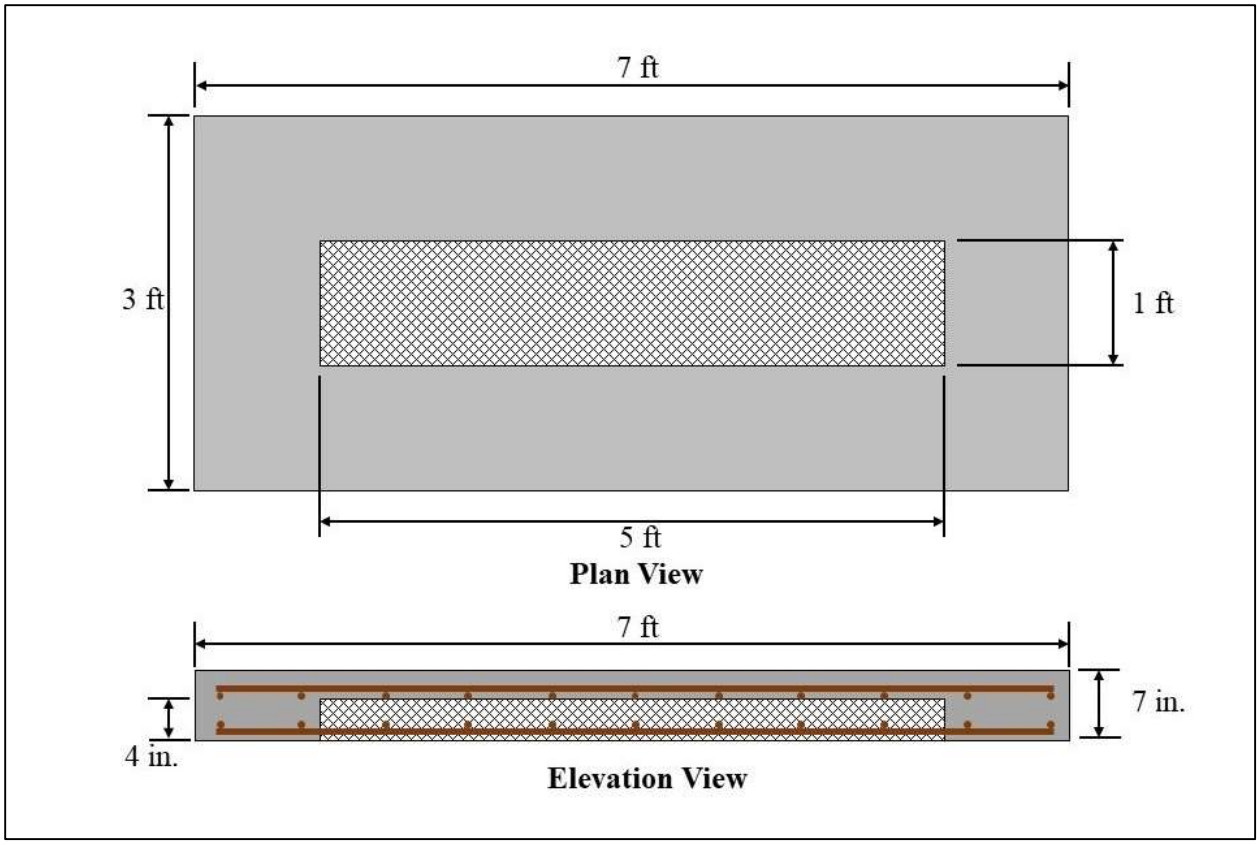

Figure 3-36: Diagram of Specimen DE2

3.4.6.2 Specimen DE3

Specimen DE3 was constructed with the following objectives in mind:

- Verify that the deterioration is detected as a deteriorated region using NDT equipment
- Determine if a concrete mixture with low paste content is suitable for replicating concrete deterioration

This slab served to represent a typical bridge deck in the state of Alabama and was therefore constructed to be 7.25 in. thick. Constructing this specimen required two separate casting phases. The first phase consisted of casting a small, 4-inch thick specimen, measuring 1 × 5 ft. This smaller specimen was cast using a concrete mixture having a low paste content in attempt to promote a honeycombing effect within the concrete. The encased specimen concrete mixture proportions for Specimen DE3 can be found in Table 3-6. In order to keep the reinforcement continuous throughout the entire test slab, the smaller specimen was cast using the two-part form. Mixture ingredients were individually batched according to the mixture

proportions and mixed in the laboratory using the laboratory mixer. The low paste concrete mixture was then placed into the formwork, consolidated, and raked to provide adequate surface roughness. The small specimen was then moist cured for seven days. The second phase consisted of placing the small specimen, shown in Figure 3-37 into the formwork for the larger 3 × 7 ft test specimens, and adding a top layer of reinforcing steel. The standard ALDOT bridge deck mixture of ready-mixed concrete was then cast around the small specimen, creating an embedded area of distressed concrete as shown in Figure 3-38.

Table 3-6: Encased specimen mixture proportions for Specimen DE3

Material	Proportions	
#57 Limestone Coarse Aggregate	2,280	lb/yd^3
Fine Aggregate	1,285	lb/yd^3
Portland Cement	275	lb/yd^3
Class C Fly Ash	92	lb/yd^3
Water	163	lb/yd^3
Air Entraining Admixture	1.5	oz/yd^3
HRWR Admixture	25	oz/yd^3

Figure 3-37: Encased specimen with low paste content

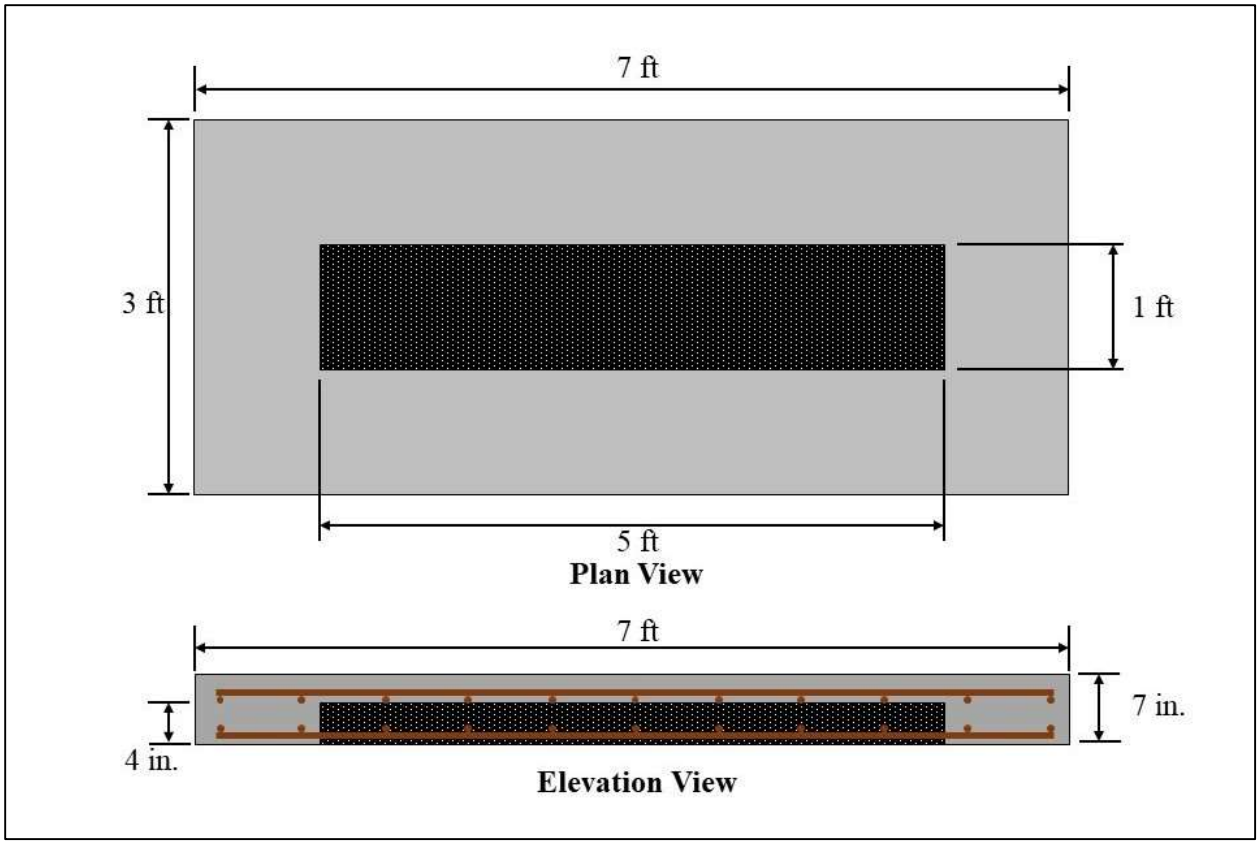

Figure 3-38: Diagram of Specimen DE3

3.4.6.3 Specimen DE4

Specimen DE4 was constructed with the following objectives in mind:

- Verify that the deterioration is detected as a deteriorated region using NDT equipment
- Determine if a concrete mixture with a high dosage of polypropylene fibers is suitable for replicating concrete deterioration

This slab served to represent a typical bridge deck in the state of Alabama and was therefore constructed to be 7.25 in. thick. Constructing this specimen required two separate casting phases. The first phase consisted of casting a small, 4-inch thick specimen, measuring 1 × 5 ft. This smaller specimen was cast using a concrete mixture containing a high amount of polypropylene fibers in attempt to model a severely deteriorated concrete matrix with significant internal cracking. The encased specimen concrete mixture proportions for Specimen DE4 can be found in Table 3-7. In order to keep the reinforcement continuous throughout the entire test slab, the smaller specimen was cast using the two-part form. Mixture ingredients were individually

batched according to the mixture proportions and mixed in the laboratory using the laboratory mixer. The fibrous concrete mixture was then placed into the formwork, consolidated, and raked to provide adequate surface roughness. The small specimen was then moist cured for seven days. The second phase consisted of placing the small specimen, shown in Figure 3-39, into the formwork for the larger 3 × 7 ft test specimens, and adding a top layer of reinforcing steel. The standard ALDOT bridge deck mixture of ready-mixed concrete was then cast around the small specimen, creating an embedded area of distressed concrete as shown in Figure 3-40.

Table 3-7: Encased specimen mixture proportions for Specimen DE4

Material	Proportions	
#57 Limestone Coarse Aggregate	1,900	lb/yd^3
Fine Aggregate	1,285	lb/yd^3
Portland Cement	465	lb/yd^3
Class C Fly Ash	155	lb/yd^3
Water	275	lb/yd^3
Air Entraining Admixture	1.5	oz/yd^3
HRWR Admixture	25	oz/yd^3
Polypropylene Fibers	12	lb/yd^3

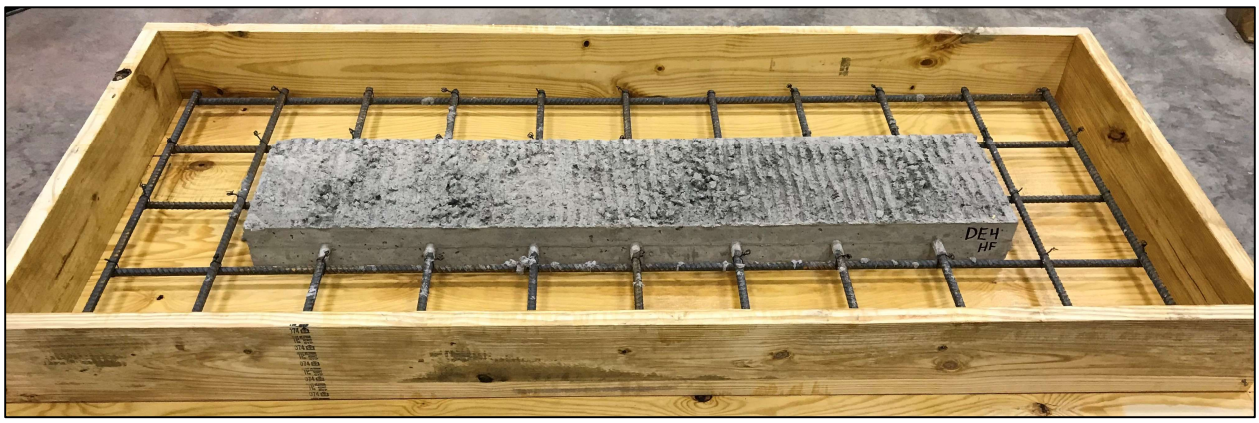

Figure 3-39: Encased specimen with high fiber content

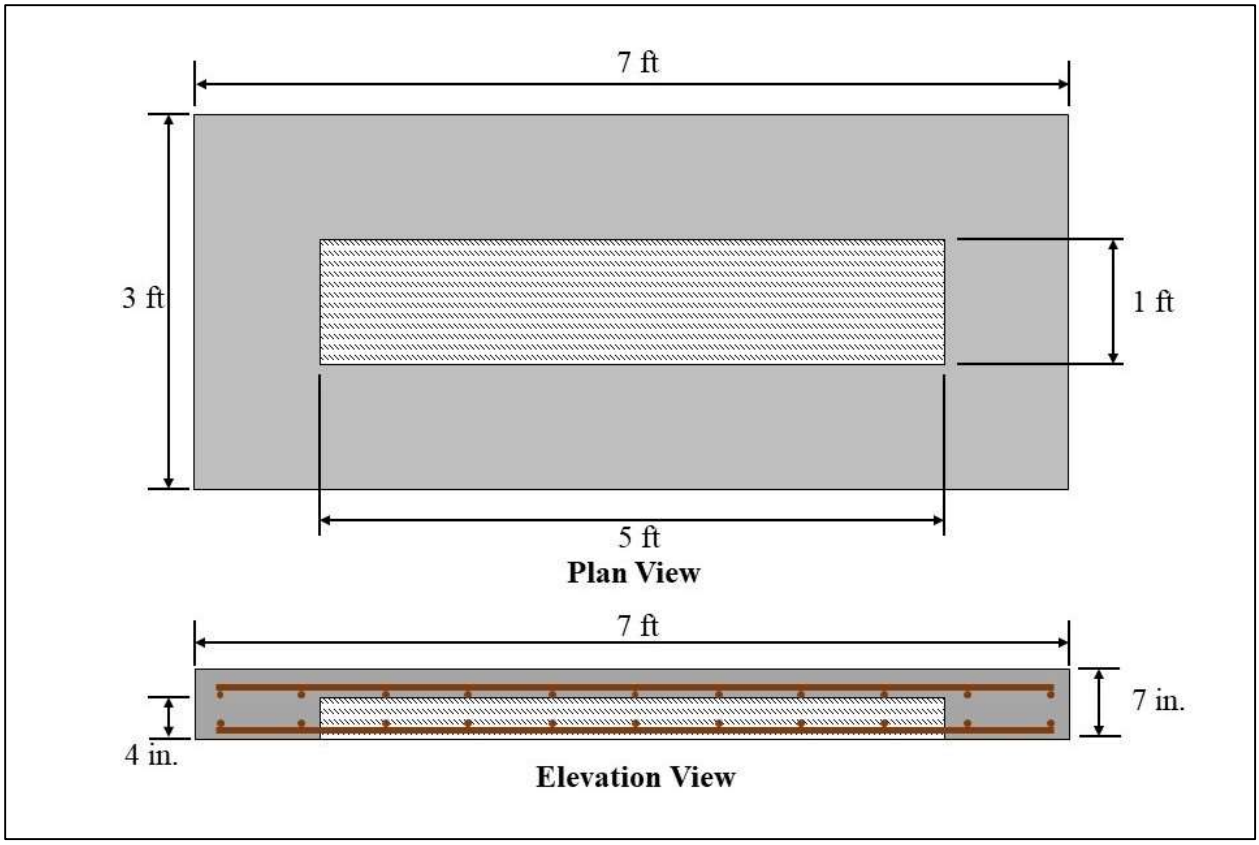

Figure 3-40: Diagram of Specimen DE4

3.4.6.4 Specimen DE5

Specimen DE5 was constructed with the following objectives in mind:

- Verify that the deterioration is detected as a deteriorated region using NDT equipment
- Determine if a concrete mixture with a moderate dosage of anti-cracking fibers is suitable for replicating concrete deterioration

This slab served to represent a typical bridge deck in the state of Alabama and was therefore constructed to be 7.25 in. thick. Constructing this specimen required two separate casting phases. The first phase consisted of casting a small, 4-inch thick specimen, measuring 1 × 5 ft. This smaller specimen was cast using a concrete mixture containing a moderate amount of anti-cracking fibers in attempt to model a mildly deteriorated concrete matrix. The encased specimen concrete mixture proportions for Specimen DE5 can be found in Table 3-8. In order to keep the reinforcement continuous throughout the entire test slab, the smaller specimen was cast using the two-part form. Mixture ingredients were individually batched according to the mixture

proportions and mixed in the laboratory using the laboratory mixer. The fibrous concrete mixture was then placed into the formwork, consolidated, and raked to provide adequate surface roughness. The small specimen was then moist cured for seven days. The second phase consisted of placing the small specimen, shown in Figure 3-41, into the formwork for the larger 3 × 7 ft test specimens, and adding a top layer of reinforcing steel. The standard ALDOT bridge deck mixture of ready-mixed concrete was then cast around the small specimen, creating an embedded area of distressed concrete as shown in Figure 3-42.

Table 3-8: Encased specimen mixture proportions for Specimen DE5

Material	Proportions	
#57 Limestone Coarse Aggregate	1,900	lb/yd^3
Fine Aggregate	1,285	lb/yd^3
Portland Cement	465	lb/yd^3
Class C Fly Ash	155	lb/yd^3
Water	275	lb/yd^3
Air Entraining Admixture	1.5	oz/yd^3
HRWR Admixture	25	oz/yd^3
Polypropylene Fibers	6	lb/yd^3

Figure 3-41: Encased specimen with moderate fiber content

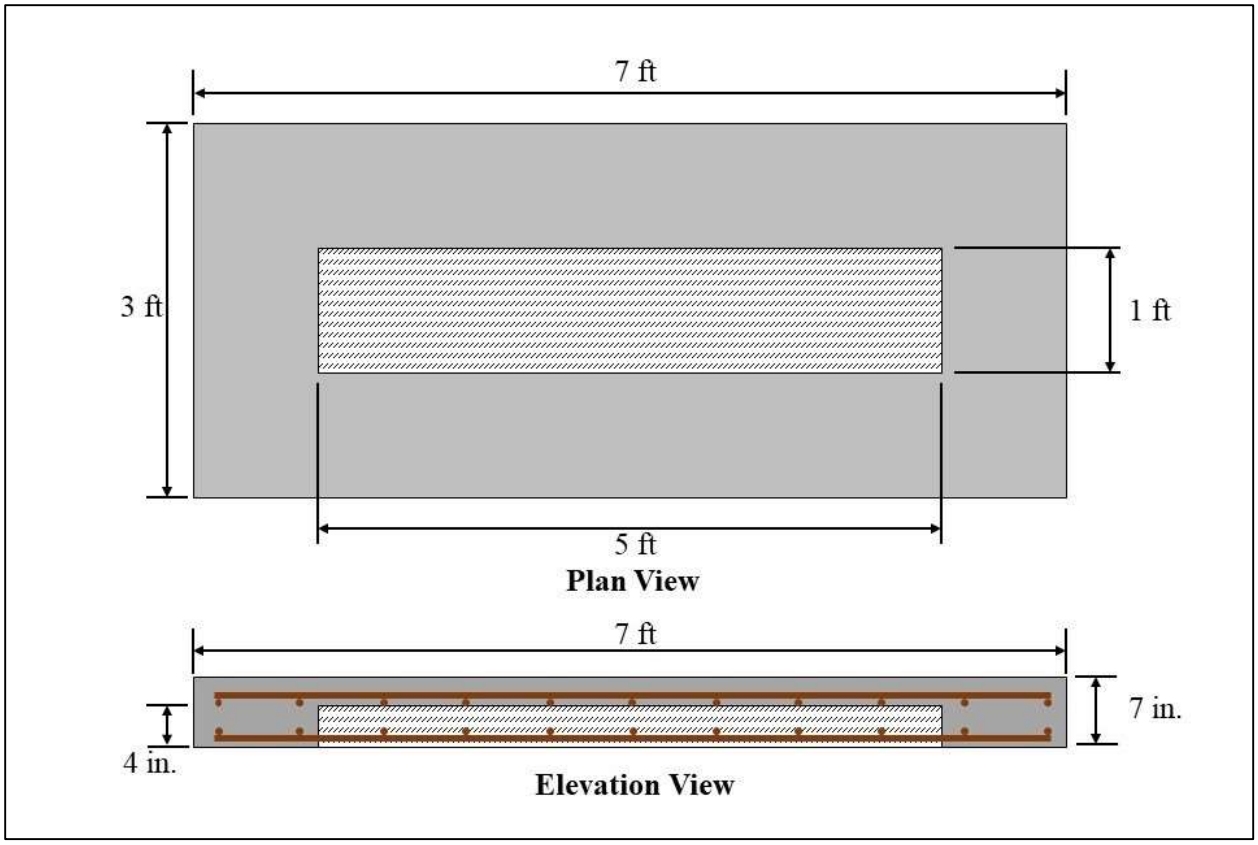

Figure 3-42: Diagram of Specimen DE5

3.4.7 Poor Construction Specimens

3.4.7.1 Specimen PC1

Specimen PC1 was constructed with the following objectives in mind:

- Verify that the deterioration is detected as a deteriorated region using NDT equipment, and
- Determine if a low-strength concrete mixture is suitable for replicating deteriorated concrete.

This slab served to represent a typical bridge deck in the state of Alabama and was therefore constructed to be 7.25 in. thick. Constructing this specimen required two separate casting phases. The first phase consisted of casting a small, 4-inch thick specimen, measuring 1 × 5 ft. This smaller specimen was cast using a concrete mixture with a water-to-cement ratio of 0.6 in an attempt to simulate an area of low strength concrete. The encased specimen concrete mixture proportions for Specimen PC1 can be found in Table 3-9. In order to keep the reinforcement continuous throughout the entire test slab, the smaller specimen was cast using the

two-part form. Mixture ingredients were individually batched according to the mixture proportions and mixed in the laboratory using the laboratory mixer. The low strength concrete was then placed into the formwork, consolidated, and raked to provide adequate surface roughness. The small specimen was then moist cured for seven days. The second phase consisted of placing the small specimen, shown in Figure 3-43, into the formwork for the larger 3 × 7 ft test specimens, and adding a top layer of reinforcing steel. The standard ALDOT bridge deck mixture of ready-mixed concrete was then cast around the small specimen, creating an embedded area of distressed concrete as shown in Figure 3-44.

Table 3-9: Encased specimen mixture proportions for Specimen PC1

Material	Proportions	
#57 Limestone Coarse Aggregate	1,900	lb/yd^3
Fine Aggregate	889	lb/yd^3
Portland Cement	465	lb/yd^3
Class C Fly Ash	155	lb/yd^3
Water	372	lb/yd^3
Air Entraining Admixture	1.5	oz/yd^3
HRWR Admixture	-	oz/yd^3

Figure 3-43: Encased specimen with high water-to-cement ratio

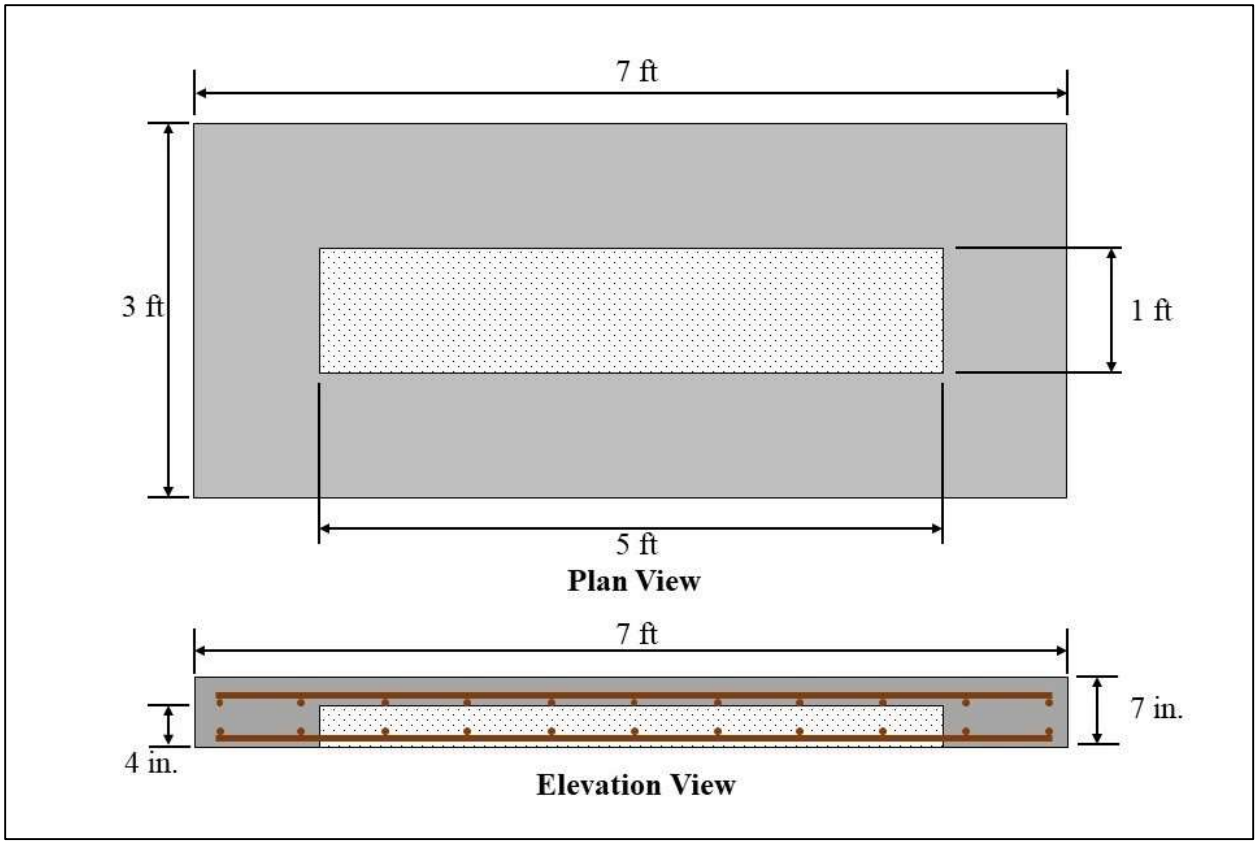

Figure 3-44: Diagram of Specimen PC1

3.4.7.2 Specimen PC2

Specimen PC2 was constructed with the following objectives in mind:

- Verify that the deterioration is detected as a deteriorated region using NDT equipment, and
- Determine if a poorly consolidated concrete mixture with high entrapped air content is suitable for replicating deteriorated concrete.

This slab served to represent a typical bridge deck in the state of Alabama and was therefore constructed to be 7.25 in. thick. Constructing this specimen required two separate casting phases. The first phase consisted of casting a small, 4-inch thick specimen, measuring 1 × 5 ft. This smaller specimen was cast using a concrete mixture batched according to the ALDOT bridge deck mixture proportions. The encased specimen concrete mixture proportions for Specimen PC2 can be found in Table 3-10. In order to keep the reinforcement continuous throughout the entire test slab, the smaller specimen was cast using the two-part form. Mixture ingredients were individually batched according to the mixture proportions and mixed in the

laboratory using the laboratory mixer. The concrete was then placed into the formwork, but was not consolidated, in attempt to mimic poor construction practices. The surface was raked to provide adequate surface roughness. The small specimen was then moist cured for seven days. The second phase consisted of placing the small specimen, shown in Figure 3-45, into the formwork for the larger 3 × 7 ft test specimens, and adding a top layer of reinforcing steel. The standard ALDOT bridge deck mixture of ready-mixed concrete was then cast around the small specimen, creating an embedded area of distressed concrete as shown in Figure 3-46.

Table 3-10: Encased specimen mixture proportions for Specimen PC2

Material	Proportions	
#57 Limestone Coarse Aggregate	1,900	lb/yd^3
Fine Aggregate	1,285	lb/yd^3
Portland Cement	465	lb/yd^3
Class C Fly Ash	155	lb/yd^3
Water	275	lb/yd^3
Air Entraining Admixture	1.5	oz/yd^3
HRWR Admixture	25	oz/yd^3

Figure 3-45: Embedded specimen with poor consolidation

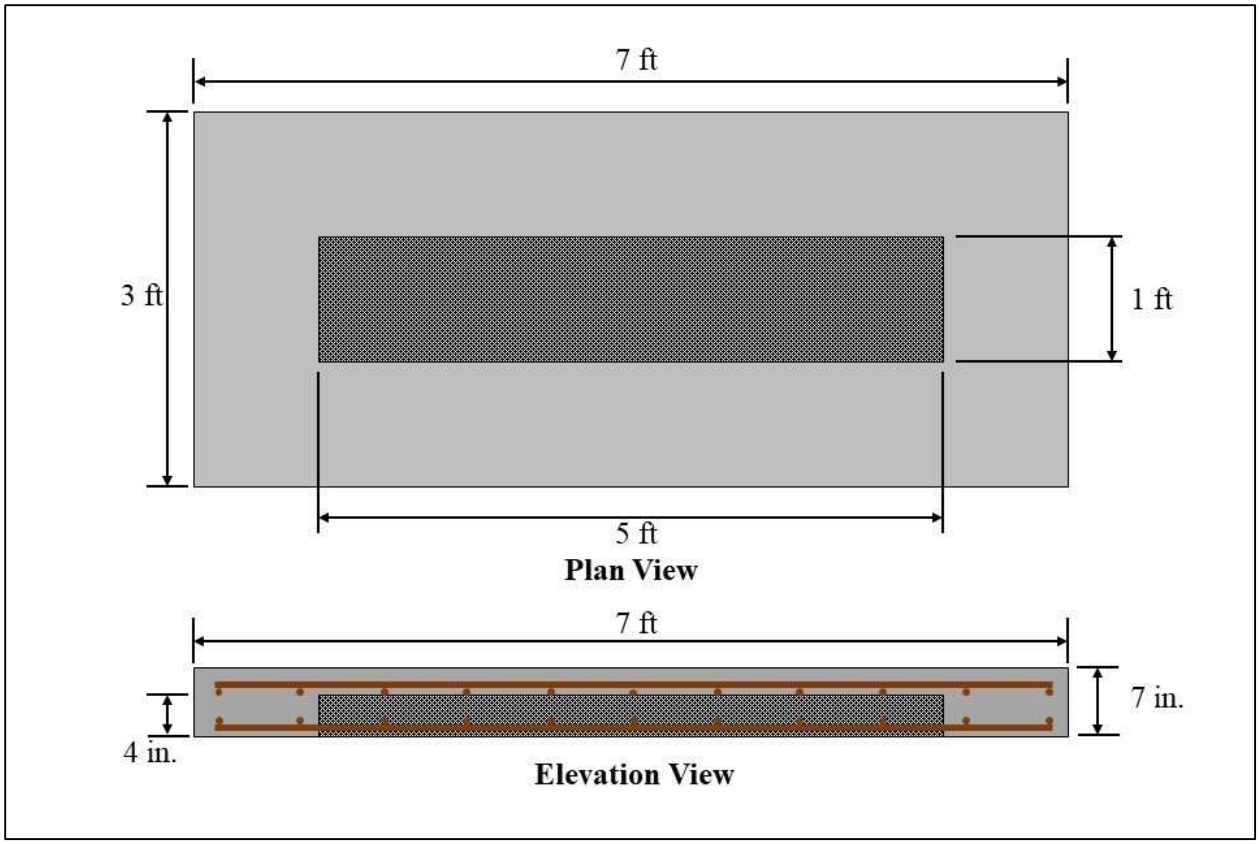

Figure 3-46: Diagram of Specimen PC2

CHAPTER 4

PRESENTATION AND ANALYSIS OF RESULTS

4.1 INTRODUCTION

The laboratory testing results from the evaluation of NDT methods and the subsequent evaluation of artificial defect techniques are discussed in this chapter. A discussion of findings from cores taken from the laboratory specimens is offered in Section 4.2. Results from testing the laboratory specimens are presented in Section 4.3. An evaluation of the methods used to create defects within the laboratory specimens is detailed in Section 4.5. The three NDT methods described in this report are the impact-echo, half-cell potential, and surface resistivity. Evaluation of these three methods for use by the Alabama Department of Transportation is detailed in Section 4.4. Chapter 4 is concluded with a brief summary of results presented in Section 4.6.

4.2 CORE RESULTS

The following subsections present results of cores taken from each specimen in the laboratory and a discussion of the results. The position of each core is presented in terms of its x-coordinate and y-coordinate location, which corresponds to the x- and y-coordinates provided with the results in Section 4.3. The units for the x- and y- coordinates are inches.

4.2.1 Void Specimens

4.2.1.1 Specimen V1

Cores taken from Specimen V1 in the laboratory are shown in Figure 4-1. For Specimen V1, cores were taken at most void locations throughout the specimen. The locations from which each core was extracted are shown in Table 4-1.

Figure 4-1: Cores taken from Specimen V1

Table 4-1: Locations of cores extracted from Specimen V1

Label (from Figure 4-1)	Location	Defect
a	(4,4)	½ in. diameter deep void
b	(36,20)	1½ in. diameter shallow void
c	(52,20)	2 in. diameter shallow void
d	(68,4)	2½ in. diameter deep void

Specimen V1 was created using water-filled balloons to simulate both shallow and deep voids within a concrete slab. Ultimately, one may interpret, from the cores taken, that all simulated voids, both shallow and deep, successfully created a voided area within the specimen, and remained in the approximate plan location they were placed. The vertical location of the voids along the depth of the specimen varied slightly from location of initial placement, likely due to forces present during the concrete casting process.

4.2.1.2 Specimen V2

Cores taken from Specimen V2 in the laboratory are shown in Figure 4-2. For Specimen V2, cores were taken at most void locations throughout the specimen. The locations from which each core was extracted are shown in Table 4-2.

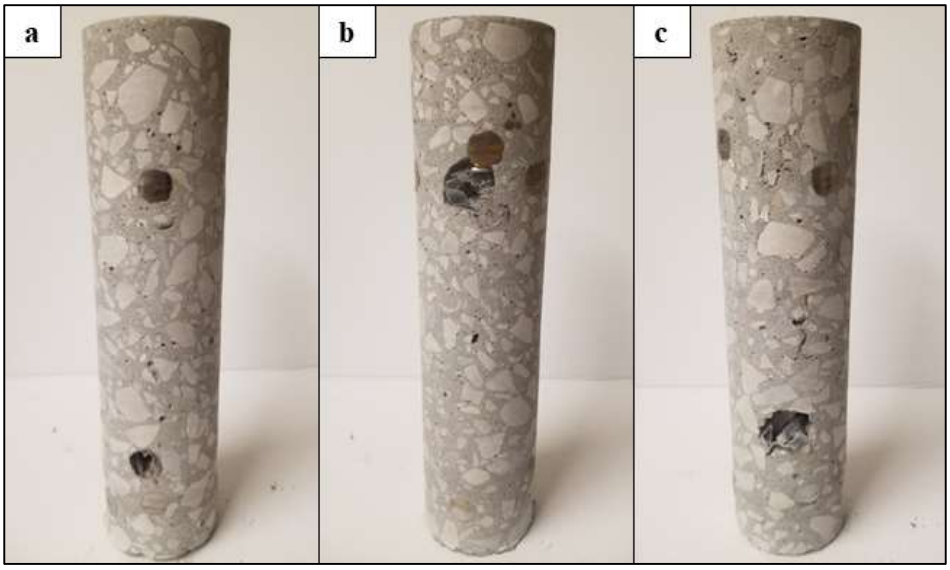

Figure 4-2: Cores taken from Specimen V2

Table 4-2: Locations of cores extracted from Specimen V2

Label (from Figure 4-2)	Location	Defect
a	(4,4)	½ in. diameter deep void
b	(20,20)	1 in. diameter shallow void
c	(52,20)	2 in. diameter shallow void

Specimen V2 was created using clay-filled bags to simulate both shallow and deep voids within a concrete slab. Ultimately, one may interpret, from the cores taken, that all simulated voids, both shallow and deep, successfully created a voided area within the specimen, and remained in the approximate plan location they were placed. The vertical location of the voids along the depth of the specimen varied slightly from location of initial placement, likely due to forces present during the concrete casting process.

4.2.2 Delaminated Specimens

4.2.2.1 Specimen DL1

Cores taken from Specimen DL1 in the laboratory are shown in Figure 4-3. One core was extracted from each of the six delaminated locations within the specimen. The locations from which each core was extracted are shown in Table 4-3.

Figure 4-3: Cores taken from Specimen DL1

Table 4-3: Locations of cores extracted from Specimen DL1

Label (from Figure 4-3)	Location	Defect
a	(4,4)	10 mil plastic delamination
b	(36,4)	30 mil plastic delamination
c	(68,4)	50 mil plastic delamination
d	(4,20)	1/32 in. foam delamination
e	(36,20)	1/16 in. foam delamination
f	(68,20)	3/32 in. plastic delamination

The cores were extracted from Specimen DL1 to evaluate the results of laboratory testing using the impact-echo method. By observing the six cores taken from Specimen DL1 and the impact-echo results, one can see that plastic and foam inserts, as thin as 10 mil and 1/32 in.,

respectively, are suitable for simulating shallow delaminations within a reinforced-concrete bridge deck.

4.2.2.2 Specimen DL2

Cores taken from Specimen DL2 in the laboratory are shown in Figure 4-4. One core was extracted from each of the six delaminated locations within the specimen. The locations from which each core was extracted are shown in Table 4-4.

Figure 4-4: Cores taken from Specimen DL2

Table 4-4: Locations of cores extracted from Specimen DL2

Label (from Figure 4-4)	Location	Defect
a	(4,4)	10 mil plastic delamination
b	(36,4)	30 mil plastic delamination
c	(68,4)	50 mil plastic delamination
d	(4,20)	1/32 in. foam delamination
e	(36,20)	1/16 in. foam delamination
f	(68,20)	3/32 in. plastic delamination

The cores were extracted from Specimen DL2 to evaluate the results of laboratory testing using the impact-echo method. By observing the six cores taken from Specimen DL2 and the secondary frequency impact-echo results, one can see that plastic and foam inserts, as thin as 10 mil and 1/32 in., respectively, are suitable for simulating deep delaminations within a reinforced-concrete bridge deck.

4.2.2.3 Specimen DL3

Cores taken from Specimen DL3 in the laboratory are shown in Figure 4-5. Cores were extracted from each of the delaminated locations within the specimen, as well as where no delaminations were placed. The locations from which each core was extracted are shown in Table 4-5.

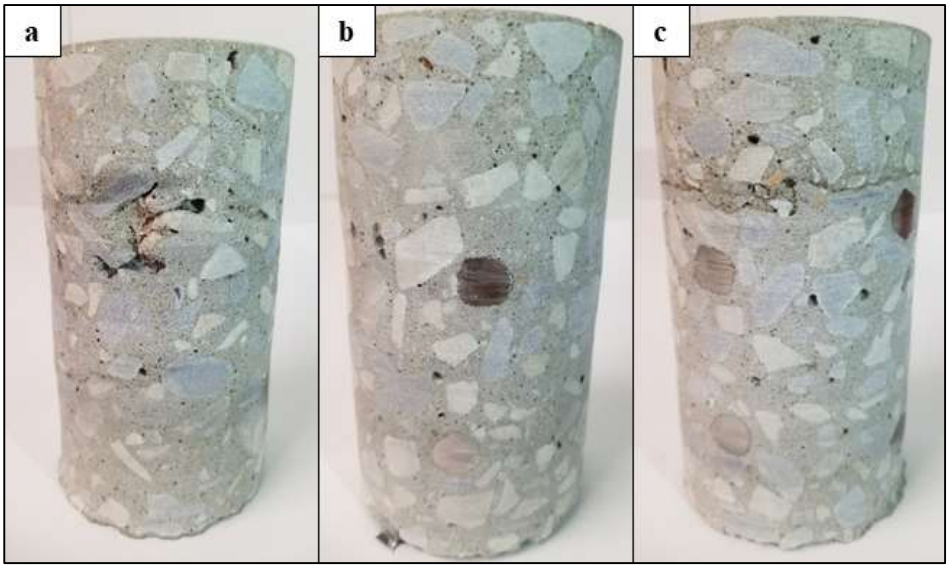

Figure 4-5: Cores taken from Specimen DL3

Table 4-5: Locations of cores extracted from Specimen DL3

Label (from Figure 4-5)	Location	Defect
a	(20,16)	Sand layer
b	(36,8)	No delamination
c	(44,20)	Oil layer

The cores were extracted from Specimen DL3 to evaluate the results of laboratory testing using the impact-echo method. From observing the cores, one can see slight layer of sand in Figure 4-5(a) and an acceptable delamination due to the oil applied in Figure 4-5(c). Neither sand nor oil can be seen in the middle core, which proves that the sand and oil did not shift laterally during concrete placement. These results indicate that a layer of sand or oil works well to simulate a delaminated area within a reinforced-concrete slab, but layers should likely be thicker than what was used in the laboratory specimen.

4.2.2.4 Specimen DL4

Cores taken from Specimen DL4 in the laboratory are shown in Figure 4-6. Cores were extracted from each of the delaminated locations within the specimen. The locations from which each core was extracted are shown in Table 4-6.

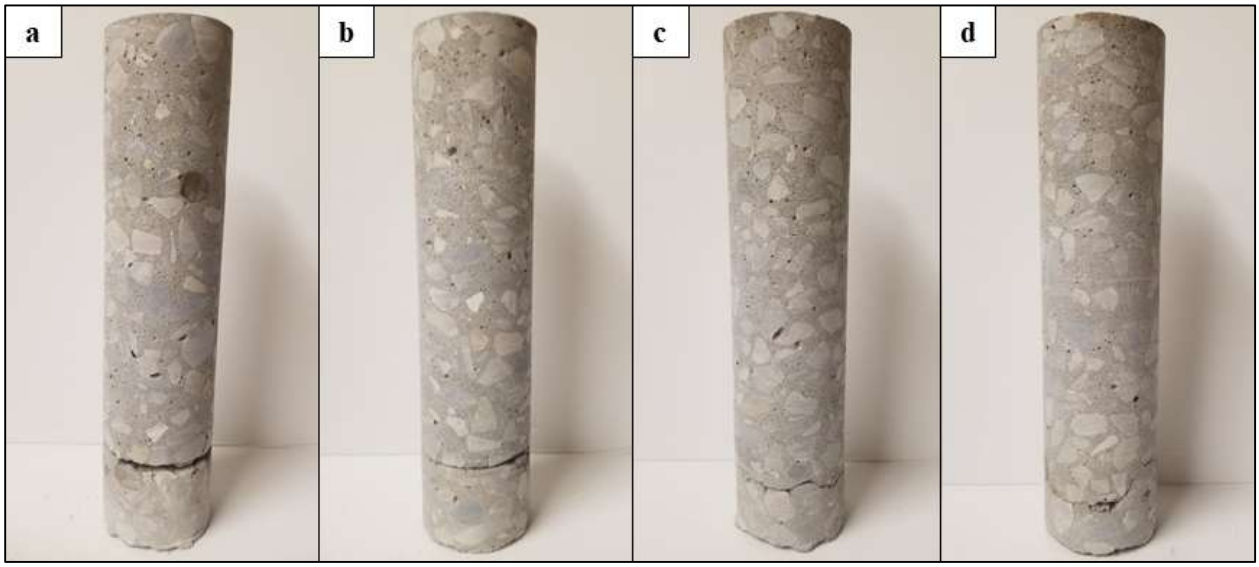

Figure 4-6: Cores taken from Specimen DL4

Table 4-6: Locations of cores extracted from Specimen DL4

Label (from Figure 4-6)	Location	Defect
a	(16,8)	Sand layer
b	(20,16)	Sand layer
c	(48,8)	Oil layer
d	(60,8)	Oil layer

The cores were extracted from Specimen DL4 to evaluate the results of laboratory testing using the impact-echo method. From observing the cores, one can see a slight layer of sand in Figure 4-5(a) and (b), as well as an acceptable delamination due to the oil applied in Figure 4-5(c) and (d). These results indicate that a layer of sand or oil works well to simulate a delaminated area within a reinforced-concrete slab, but layers should likely be thicker than what was used in the laboratory specimen.

4.2.2.5 Specimen DL5

Cores taken from Specimen DL5 in the laboratory are shown in Figure 4-7. A core was extracted from each of the five delaminated locations within the specimen. The locations from which each core was extracted are shown in Table 4-7. Some cores were damaged due to spinning during the coring process. Therefore, only portions of some cores were recovered from some locations.

Figure 4-7: Cores taken from Specimen DL5

Table 4-7: Locations of cores extracted from Specimen DL5

Label (from Figure 4-7)	Location	Defect
a	(8,12)	6 × 12 in. plastic delamination
b	(32,20)	5 × 10 in. plastic delamination
c	(36,4)	4 × 8 in. plastic delamination
d	(68,20)	3 × 6 in. plastic delamination
e	(68,4)	2 × 4 in. plastic delamination

The cores were extracted from Specimen DL5 to evaluate the results of laboratory testing using the impact-echo method. By observing the five cores taken from Specimen DL5 and the impact-echo results, one can see that plastic inserts with plan dimensions as small as 2 × 4 in. are suitable for simulating shallow delaminations within a reinforced-concrete bridge deck, though

smaller delaminations may go undetected when using a test grid spacing larger than the dimensions of the delaminated area.

4.2.2.6 Specimen DL6

Cores taken from Specimen DL6 in the laboratory are shown in Figure 4-8. A core was extracted from each of the five delaminated locations within the specimen. The locations from which each core was extracted are shown in Table 4-8.

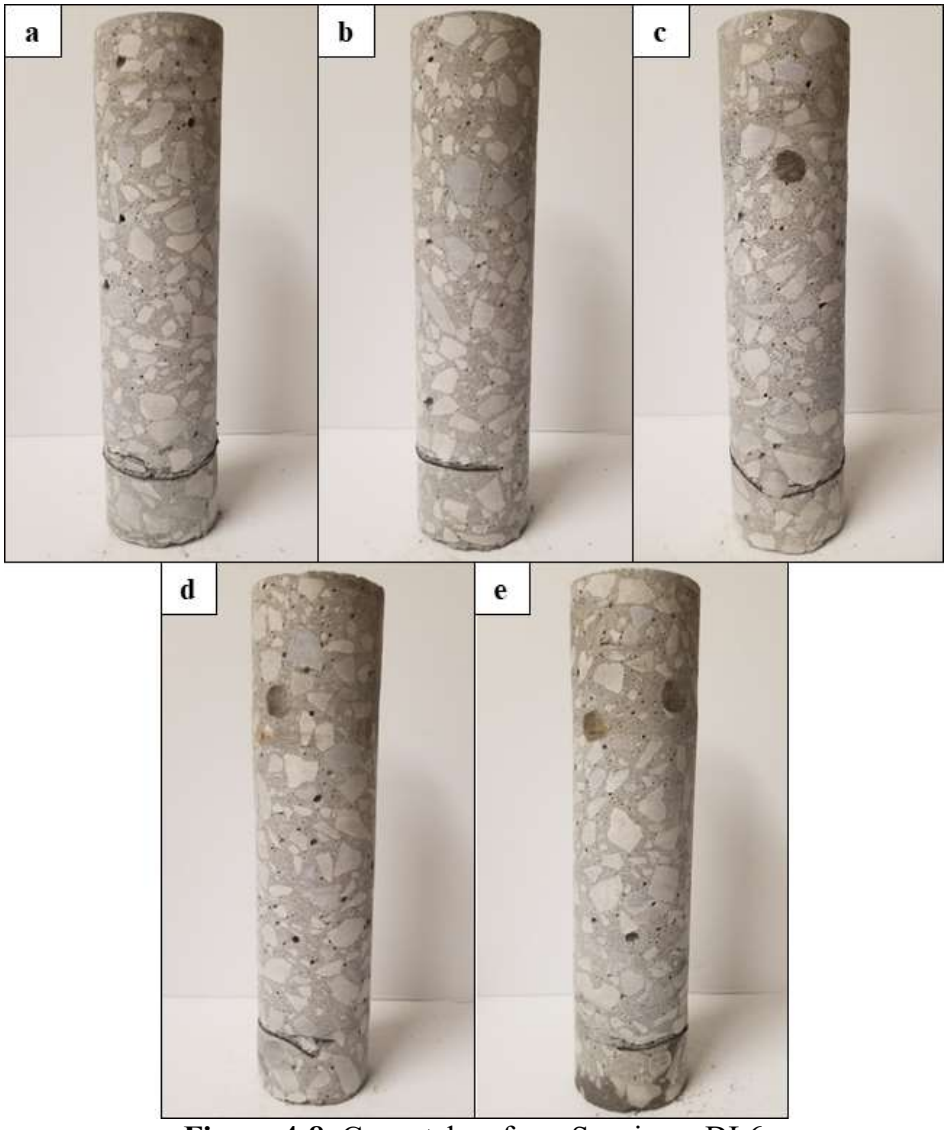

Figure 4-8: Cores taken from Specimen DL6

Table 4-8: Locations of cores extracted from Specimen DL6

Label (from Figure 4-8)	Location	Defect
a	(8,12)	6 × 12 in. plastic delamination
b	(32,20)	5 × 10 in. plastic delamination
c	(36,4)	4 × 8 in. plastic delamination
d	(68,20)	3 × 6 in. plastic delamination
e	(68,4)	2 × 4 in. plastic delamination

Cores were extracted from Specimen DL6 to evaluate the results of laboratory testing using the impact-echo method. By observing the five cores taken from Specimen DL6 and the impact-echo results, one can see that plastic inserts with plan dimensions as small as 2 × 4 in. are suitable for simulating deep delaminations within a reinforced-concrete bridge deck, though smaller delaminations may go undetected when using a test grid spacing larger than the dimensions of the delaminated area.

4.2.2.7 Specimen DL7

Cores taken from Specimen DL7 in the laboratory are shown in Figure 4-9. A core was extracted from each of the six delaminated locations within the specimen, though only two cores are presented in this report. The locations from which the presented cores were extracted are shown in Table 4-9.

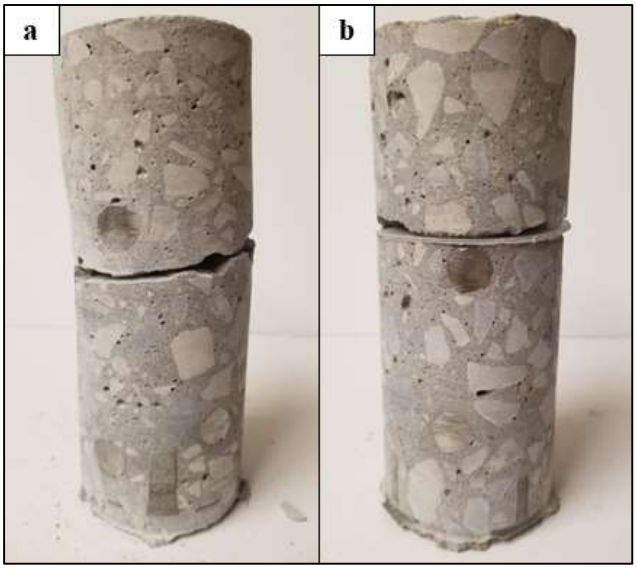

Figure 4-9: Cores taken from Specimen DL7

Table 4-9: Locations of cores extracted from Specimen DL7

Label (from Figure 4-9)	Location	Defect
a	(36,4)	10 mil, 62.5 percent unbonded plastic delamination
b	(36,20)	30 mil, 62.5 percent unbonded plastic delamination

The cores were extracted from Specimen DL7 to evaluate the results of laboratory testing using the impact-echo method. By observing the cores taken from Specimen DL7 and the impact-echo results, one can see that plastic inserts, as thin as 10 mil and as low as 50 percent unbonded, are suitable for simulating shallow delaminations within a reinforced-concrete bridge deck.

4.2.2.8 Specimen DL8

Cores taken from Specimen DL8 in the laboratory are shown in Figure 4-10. A core was extracted from each of the six delaminated locations within the specimen, though only two cores are presented in this report. The locations from which the presented cores were extracted are shown in Table 4-10.

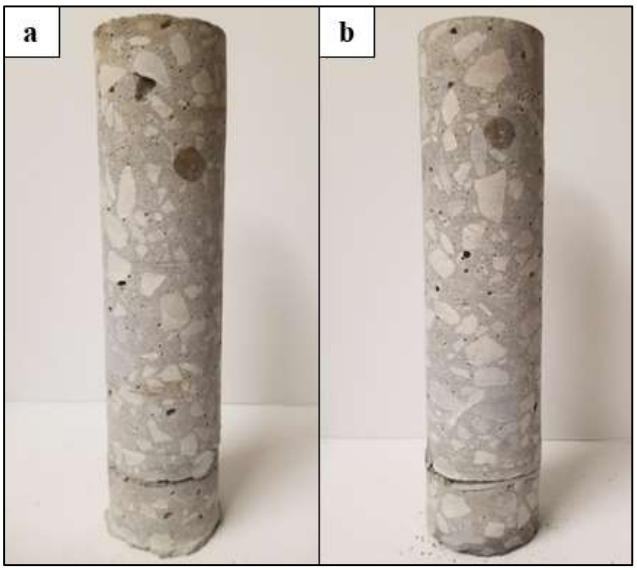

Figure 4-10: Cores taken from Specimen DL8

Table 4-10: Locations of cores extracted from Specimen DL8

Label (from Figure 4-10)	Location	Defect
a	(36,4)	30 mil, 62.5 percent unbonded plastic delamination
b	(36,20)	50 mil, 62.5 percent unbonded plastic delamination

The cores were extracted from Specimen DL8 to evaluate the results of laboratory testing using the impact-echo method. By observing the cores taken from Specimen DL8 and the impact-echo results, one can see that plastic inserts, as thin as 30 mil and as low as 50 percent unbonded, are suitable for simulating deep delaminations within a reinforced-concrete bridge deck.

4.2.3 Cracking Specimen

4.2.3.1 Specimen CR1

No cores were taken from Specimen CR1. Cracks visible from the surface of the specimen allowed the research team to confirm the location of defects.

4.2.4 Corrosion Specimens

4.2.4.1 Specimen C1

Cores taken from Specimen C1 in the laboratory are shown in Figure 4-11. The locations from which the presented cores were extracted are shown in Table 4-11.

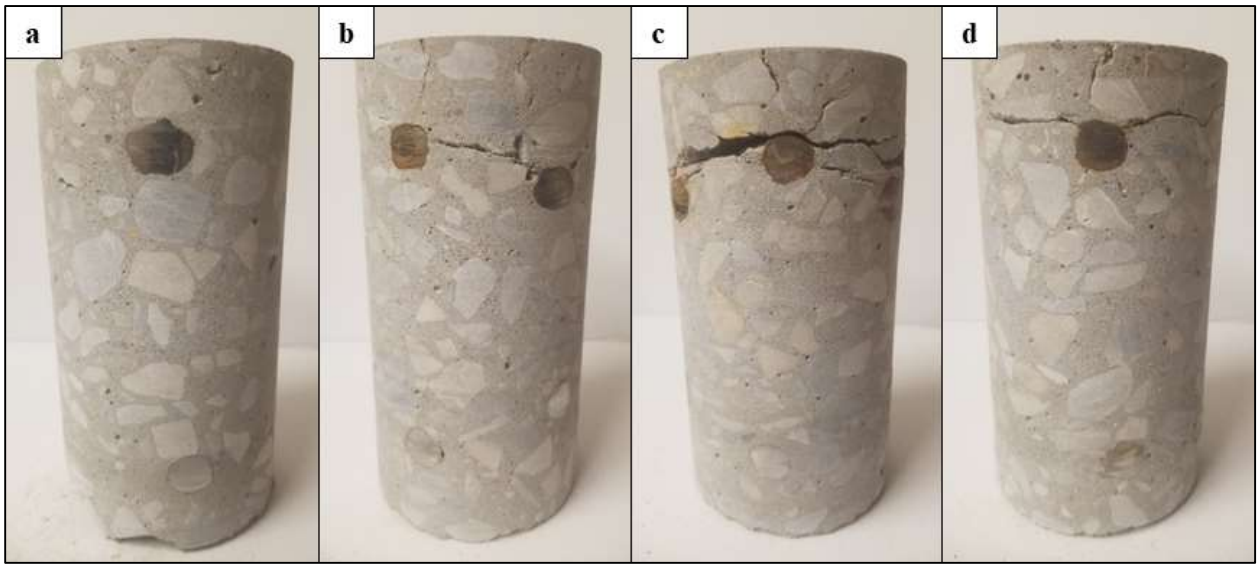

Figure 4-11: Cores taken from Specimen C1

Table 4-11: Locations of cores extracted from Specimen C1

Label (from Figure 4-11)	Location	Defect
a	(16,4)	Zone 1 (no corrosion)
b	(36,12)	Zone 2 (moderate corrosion)
c	(52,4)	Zone 3 (severe corrosion)
d	(60,4)	Zone 3 (severe corrosion)

The cores were extracted from Specimen C1 to evaluate the results of laboratory testing using the impact-echo, half-cell potential, and surface resistivity methods. No corrosion-inducing techniques were used in Zone 1 of Specimen C1, and by looking at the core in Figure 4-11(a), one may infer that no corrosion activity took place within this region. Zone 2 was the region of the specimen to which moderate corrosion-inducing techniques were applied. The delamination and thin vertical crack at the top reinforcement layer in the core shown in Figure 4-11(b) are indicative of some corrosion activity within Zone 2. Zone 3 was the region of the specimen to which severe corrosion-inducing techniques were applied. The severe delaminations and vertical cracking that can be seen in the cores presented in Figure 4-11(c) and Figure 4-11(d), in addition to the rust staining around the top reinforcement layer, indicate a high level of corrosion activity in Zone 3.

4.2.4.2 Specimen C2

Cores taken from Specimen C2 in the laboratory are shown in Figure 4-12. The locations from which the presented cores were extracted are shown in Table 4-12.

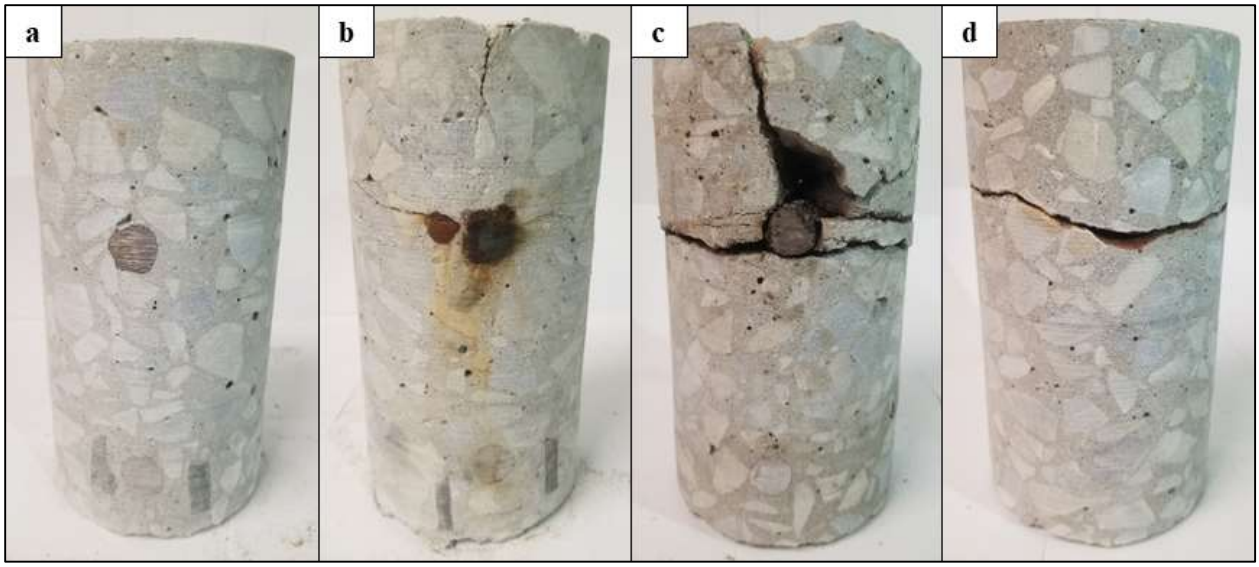

Figure 4-12: Cores taken from Specimen C2

Table 4-12: Locations of cores extracted from Specimen C2

Label (from Figure 4-12)	Location	Defect
a	(8,4)	Zone 1 (no corrosion)
b	(36,20)	Zone 2 (moderate corrosion)
c	(60,20)	Zone 3 (severe corrosion)
d	(64,8)	Zone 3 (severe corrosion)

The cores were extracted from Specimen C2 to evaluate the results of laboratory testing using the impact-echo, half-cell potential, and surface resistivity methods. No corrosion-inducing techniques were used in Zone 1 of Specimen C2, and by looking at the core in Figure 4-12(a), one may infer that no corrosion activity took place within this region. Zone 2 was the region of the specimen to which moderate corrosion-inducing techniques were applied. The mild delamination and vertical crack, coupled with the presence of rust at the top reinforcement layer, in the core shown in Figure 4-12(b) are indicative of some corrosion activity within Zone 2. Zone 3 was the region of the specimen to which severe corrosion-inducing techniques were applied. The extreme delaminations, vertical cracking, and steel section loss that can be seen around the top reinforcement layer of the cores presented in Figure 4-12(c) and Figure 4-12(d) indicate an extreme level of corrosion activity in Zone 3.

4.2.5 Control Specimen

4.2.5.1 Specimen CONTROL

A core taken from Specimen CONTROL in the laboratory is shown in Figure 4-13.

Figure 4-13: Core taken from Specimen CONTROL

Specimen CONTROL contained a cast-in region of concrete that had mixture proportions identical to the surrounding concrete. A core taken from location (12,12) is shown in Figure 4-13. Through visual examination of this core, one might determine that the concrete in the cast-in portion is similar to the surrounding concrete. Results from testing the specimen with the impact-echo method show a difference in the areas containing the encased specimen and the areas with only surrounding concrete. Because of this, cores were taken at locations where no reinforcement was present, cut along the line dividing the encased and surrounding concrete, and subjected to compressive strength testing. Core extraction was performed in accordance with ASTM C42 and compressive strength testing was performed in accordance with ASTM C39. The results of the compressive strength testing are shown in Table 4-13.

Table 4-13: Core compressive strength results for Specimen CONTROL

Location (x,y)	Strength (psi)	
	Surrounding Concrete	Encased Concrete
12,12	7340	~~13460~~
48,8	8130	9070
24,12	7600	9440
48,16	7550	9100
36,8	8060	7760

The high data point for the encased concrete was an outlier and was therefore discarded. A statistical analysis using an f-test and a t-test was performed on the compressive strength data set. Microsoft Excel was used to perform both the f-test and t-test. The results from the f-test indicated that the mean of the compressive strengths for the surrounding concrete had equal variance with the mean of the compressive strengths for the encased concrete. The results from the t-test indicated that the mean of the compressive strengths for the surrounding concrete was different (lower) than the mean of the compressive strengths for the encased concrete. Therefore, one may assume that the surrounding concrete and encased concrete had different strengths.

4.2.6 Deteriorated Specimens

4.2.6.1 Specimen DE2

Specimen DE2 contained a cast-in region of concrete that had a high air content. Cores taken from Specimen DE2 in the laboratory are shown in Figure 4-14.

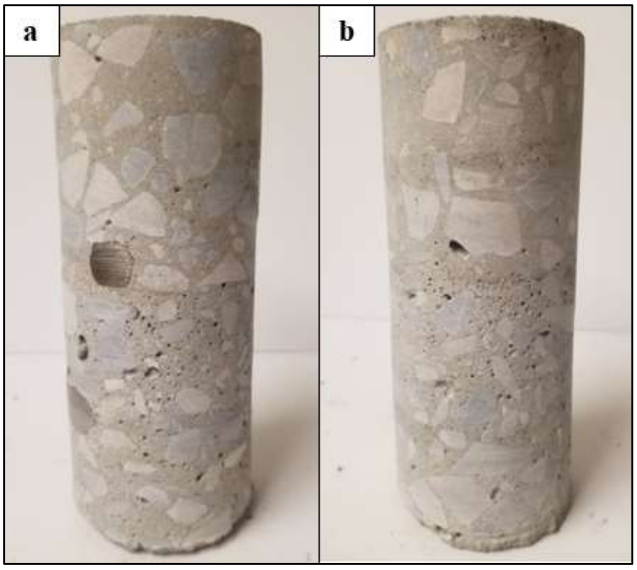

Figure 4-14: Cores taken from Specimen DE2

Cores taken from locations (12,16) and (56,12) are shown in Figure 4-14(a) and Figure 4-14(b), respectively. A visual examination of these cores shows a concrete structure characterized by high air content within the lower 4 in. of the core, which coincides with the depth of the high air concrete specimen. The concrete in the top 3.25 in. of the core is characterized by a uniform, low air content structure.

4.2.6.2 Specimen DE3

Specimen DE3 contained a cast-in region of concrete that had a low paste content. Cores taken from Specimen DE3 in the laboratory are shown in Figure 4-15.

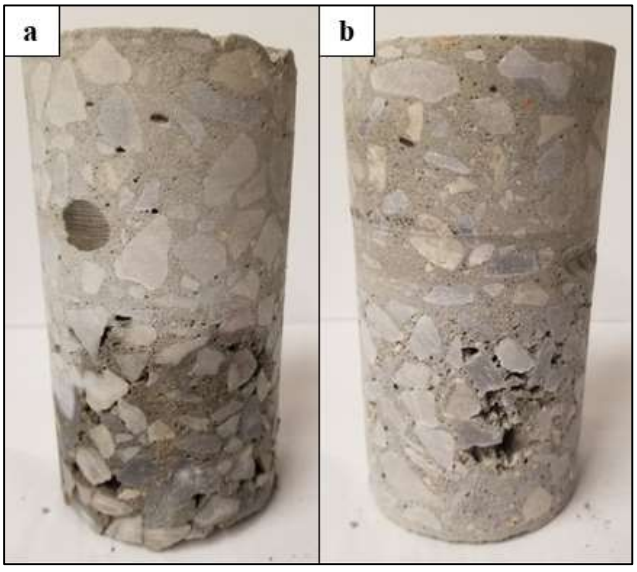

Figure 4-15: Cores taken from Specimen DE3

Cores taken from locations (48,12) and (56,20) are shown in Figure 4-15(a) and Figure 4-15(b), respectively. A visual examination of these cores shows a very porous concrete structure within the lower 4 in. of the core, which coincides with the depth of the high air concrete specimen. The concrete in the top 3.25 in. of the core is characterized by a uniform structure, which is typical of well-consolidated concrete.

4.2.6.3 Specimen DE4

Specimen DE4 contained a cast-in region of concrete that had a high dosage of anti-cracking fibers. Cores taken from Specimen DE4 in the laboratory are shown in Figure 4-16.

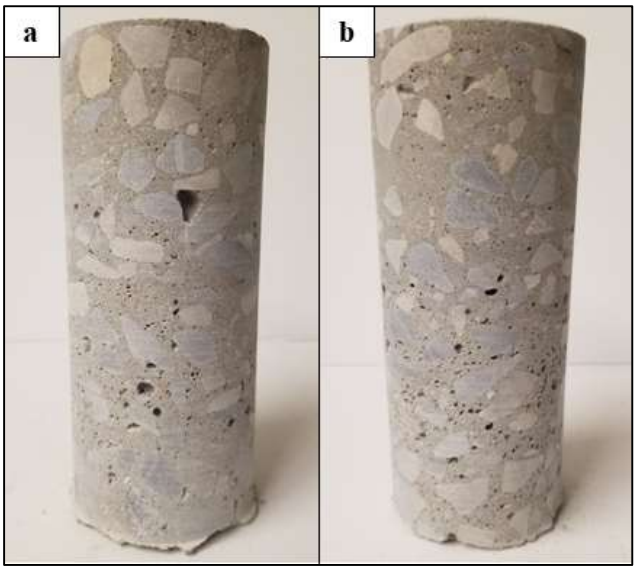

Figure 4-16: Cores taken from Specimen DE4

Cores taken from locations (16,8) and (48,16) are shown in Figure 4-16(a) and Figure 4-16(b), respectively. Through visual examination of the cores, one can see that the concrete in the lower 4 inches of the core, which corresponds to the depth of the cast-in portion of the specimen, contained a significantly higher entrapped air content than the surrounding concrete.

4.2.6.4 Specimen DE5

Specimen DE5 contained a cast-in region of concrete that had a moderate dosage of anti-cracking fibers. Cores taken from Specimen DE5 in the laboratory are shown in Figure 4-17.

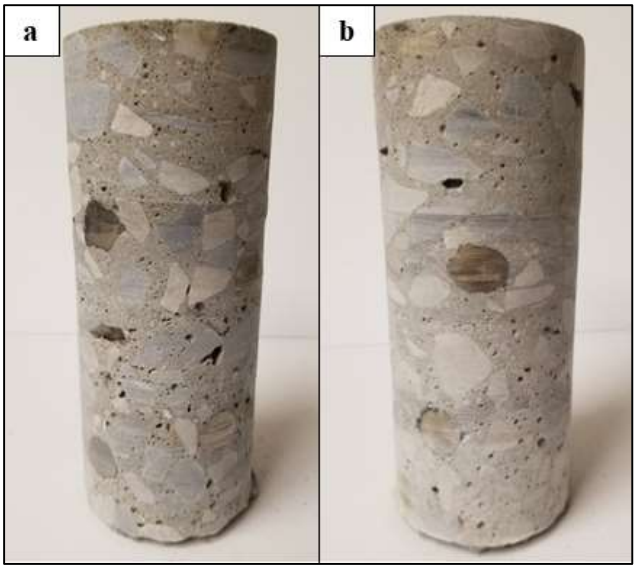

Figure 4-17: Cores taken from Specimen DE5

Cores taken from locations (12,12) and (44,16) are shown in Figure 4-17(a) and Figure 4-17(b), respectively. Through visual examination of the cores, one can see that the concrete in the lower 4 inches of the core, which corresponds to the depth of the cast-in portion of the specimen, contained a slightly higher entrapped air content than the surrounding concrete, similar to the cores taken from Specimen DE4.

4.2.7 Poor Construction Specimens

4.2.7.1 Specimen PC1

Specimen PC1 contained a cast-in region of low strength concrete, which had a high water-to-cement ratio. Cores taken from Specimen PC1 in the laboratory are shown in Figure 4-18.

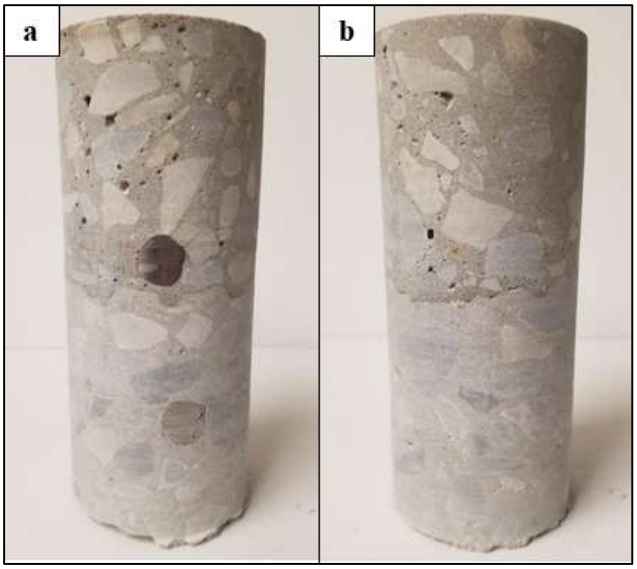

Figure 4-18: Cores taken from Specimen PC1

Cores taken from locations (20,8) and (32,16) are shown in Figure 4-18(a) and Figure 4-18(b), respectively. A visual examination of these cores shows a very smooth, non-porous concrete structure within the lower 4 in. of the core, which coincides with the depth of the low strength, high water-to-cement concrete specimen. The concrete in the top 3.25 in. of the core is characterized by a structure with regions of high entrapped air.

4.2.7.2 Specimen PC2

Specimen PC2 contained a cast-in region of concrete with high entrapped air, which was caused by an intentional lack of vibratory consolidation. Cores taken from Specimen PC2 in the laboratory are shown in Figure 4-19.

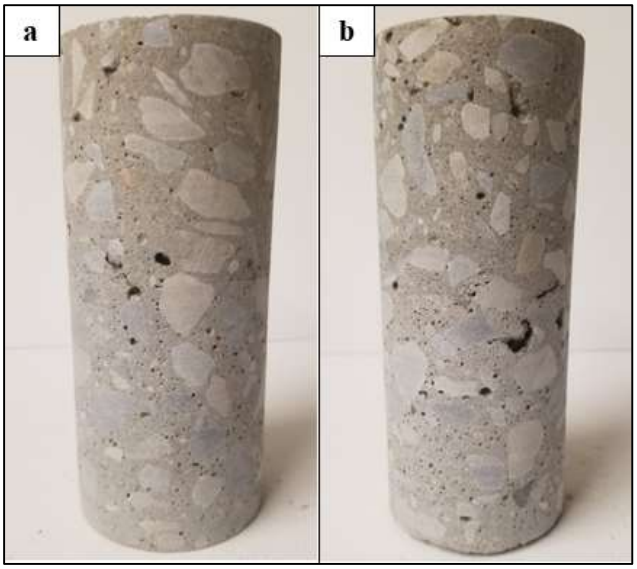

Figure 4-19: Cores taken from Specimen PC2

Cores taken from locations (8,16) and (48,16) are shown in Figure 4-19(a) and Figure 4-19(b), respectively. A visual examination of these cores shows a concrete structure with a significant amount of entrapped air within the lower 4 in. of the core, which coincides with the depth of the concrete with high entrapped air. The concrete in the top 3.25 in. of the core is also seemingly characterized by an elevated amount of entrapped air, though it is less than the amount of entrapped air within the lower portion of the cores.

4.3 RESULTS OF TESTING LABORATORY SPECIMENS

As a secondary objective of this report, methods for creating and manufacturing artificial deterioration and defects within concrete bridge decks were evaluated for the purpose of developing the full-scale testing site. For every specimen tested, a surface contour plot was developed using the DPlot software.

The impact-echo method, which was used to test all laboratory specimens, provided a three-dimensional output at each point scanned: x-coordinate, y-coordinate, and dominant frequency. The half-cell potential method, which was used to test the two corrosion specimens, provided a three-dimensional output at set intervals along each line scan: x-coordinate, y-coordinate, and measured potential. The surface resistivity method, which was used to test the two corrosion specimens, provided a three-dimensional output at each point scanned: x-coordinate, y-coordinate, and measured surface resistance.

For each specimen tested, the resulting surface contour plot was visually compared with the specimen's known defect locations in order to determine the success of the respective defect construction method. Impact-echo test data from deeper specimens that contained deep delaminations were visually inspected for secondary peak waveforms. Secondary peak waveforms are peaks in the frequency-amplitude domain that are pronounced peaks but have a lower amplitude than the dominant peak waveforms. Additionally, receiver operating characteristic (ROC) analysis (Fawcett 2006) was performed on the impact-echo data for each specimen, in order to numerically determine the success of the NDT method, as well as the respective defect construction method used within the specimen. Upper and lower thresholds were set using the Solver tool within Microsoft Excel in order to maximize the accuracy, or the percent agreement between the actual and perceived location of the defects within each specimen. This percent agreement, ranging from 0 to 1, was calculated by the following formula (Fawcett 2006):

$$Accuracy = \frac{TP + TN}{n} \qquad \text{Equation 4.1}$$

where *TP* is the number of true positive results; *TN* is the number of true negative results; *n* is the total number of points tested. A true positive rate, or the sensitivity of the test, ranging from 0 to 1, was used to compare the number of true positives recorded relative to the total number of defective test points present within the specimen; this true positive rate was calculated by the following equation (Fawcett 2006):

$$TPR = \frac{TP}{TP + FN} \qquad \text{Equation 4.2}$$

where *TPR* is the true positive rate; *TP* is the number of true positive results; *FN* is the number of false negative results. Accuracy is important to the characterization of results because it expresses the ability of the candidate NDT method to return true readings in both regions of sound and defective concrete; the closer the accuracy value is to 1, the more likely the candidate NDT method is to return a true reading in sound and defective concrete. TPR is the most important value for determining the success of a particular defect production method, as it expresses the number of points where a defect was successfully located relative to the total number test points within the specimen, which were defected; in other words, TPR numerically

expresses the detectability of each artificial defect. A TPR value approaches a value of 1 signifies a more detectable or successful artificial defect.

The ROC analysis results for the impact-echo data for each specimen is shown in Figure 4-20. The results of ROC analysis performed upon data evaluated for secondary peak waveforms are denoted with an "s" following the specimen identification. ROC analysis results for Specimen CR1 are zero, as no ROC analysis was performed on the data set. The subsections that follow Figure 4-20 present the surface contour plots and the respective defect layout, and results of ROC analysis, as well as a discussion of the results.

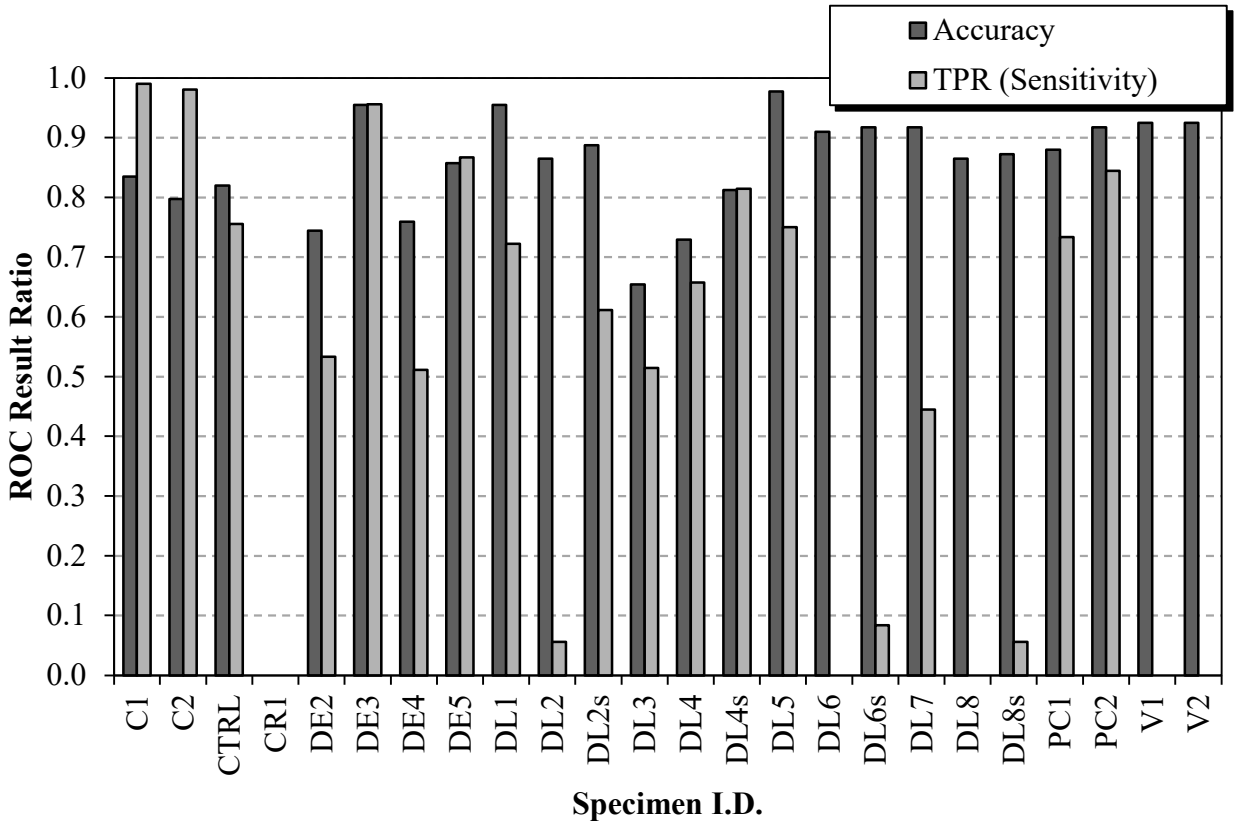

Figure 4-20: ROC analysis of impact-echo results

4.3.1 Void Specimens

4.3.1.1 Specimen V1

A comparison between the known defect locations and the surface contour plot of the impact-echo results for Specimen V1 is shown in Figure 4-21.

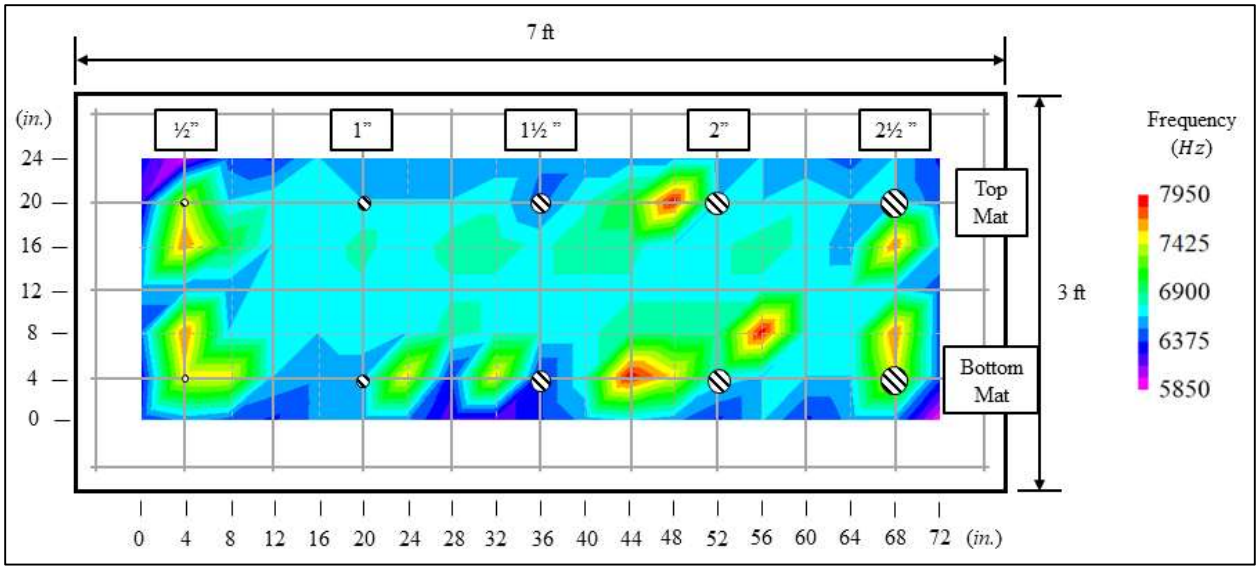

Figure 4-21: Impact-echo results for Specimen V1

By examining impact-echo results for Specimen V1, one can see that the impact-echo method responded to the presence of the full range of water-filled voids (0.5 in. to 2.5 in.) within the specimen. Despite a decent response to void presence, results exhibited relatively poor spatial correlation between apparent and actual location. From the ROC analysis results, one can see that the impact-echo method was very accurate, with an accuracy value of 0.925, but failed to successfully locate any of the ten voids within Specimen V1, which is evident in the TPR value of 0.000. These results indicate that the impact-echo method struggles to discern between sound and defective concrete when testing for both shallow and deep voids simulated by water-filled balloons.

4.3.1.2 Specimen V2

A comparison between the known defect locations and the surface contour plot of the impact-echo results for Specimen V2 is shown in Figure 4-22.

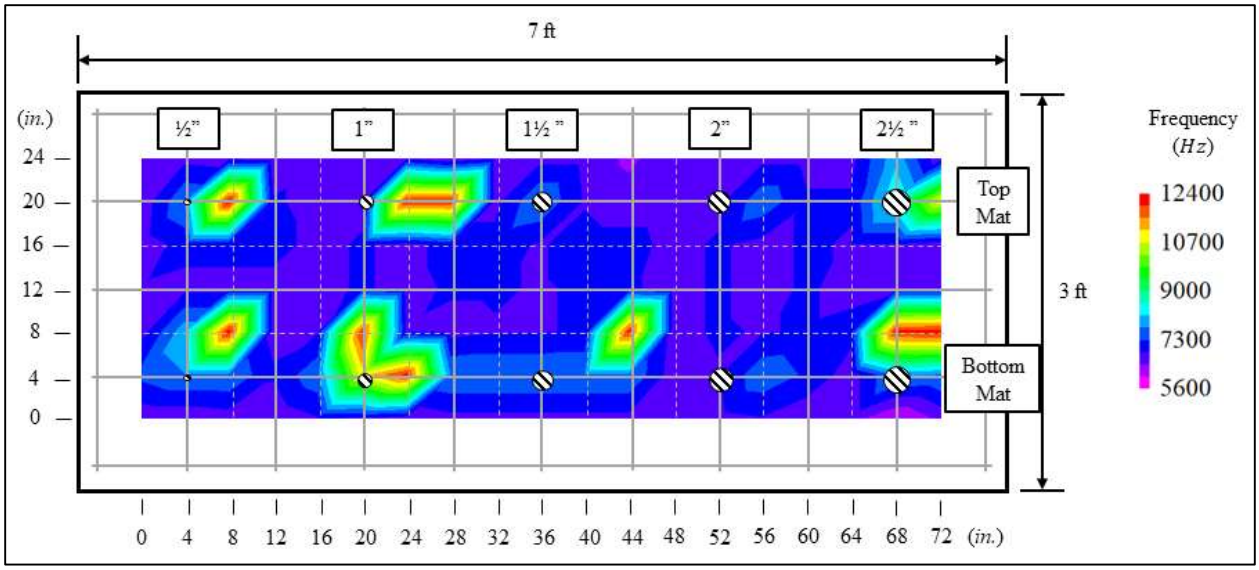

Figure 4-22: Impact-echo results for Specimen V2

By examining impact-echo results for Specimen V2, one can see that the impact-echo method responded to the presence of the full range of clay-filled voids (0.5 in. to 2.5 in.) within the specimen. As with Specimen V1, despite a decent response to void presence, results exhibited relatively poor spatial correlation between apparent and actual location. From the ROC analysis results, one can see that the impact-echo method was very accurate, with an accuracy value of 0.925, but failed to successfully locate any of the ten voids within Specimen V2, which is evident in the TPR value of 0.000. These results indicate that the impact-echo method struggles to discern between sound and defective concrete when testing for both shallow and deep voids simulated by clay-filled balloons.

4.3.2 Delaminated Specimens

4.3.2.1 Specimen DL1

A comparison between the known defect locations and the surface contour plot of the impact-echo results for Specimen DL1 is shown in Figure 4-23.

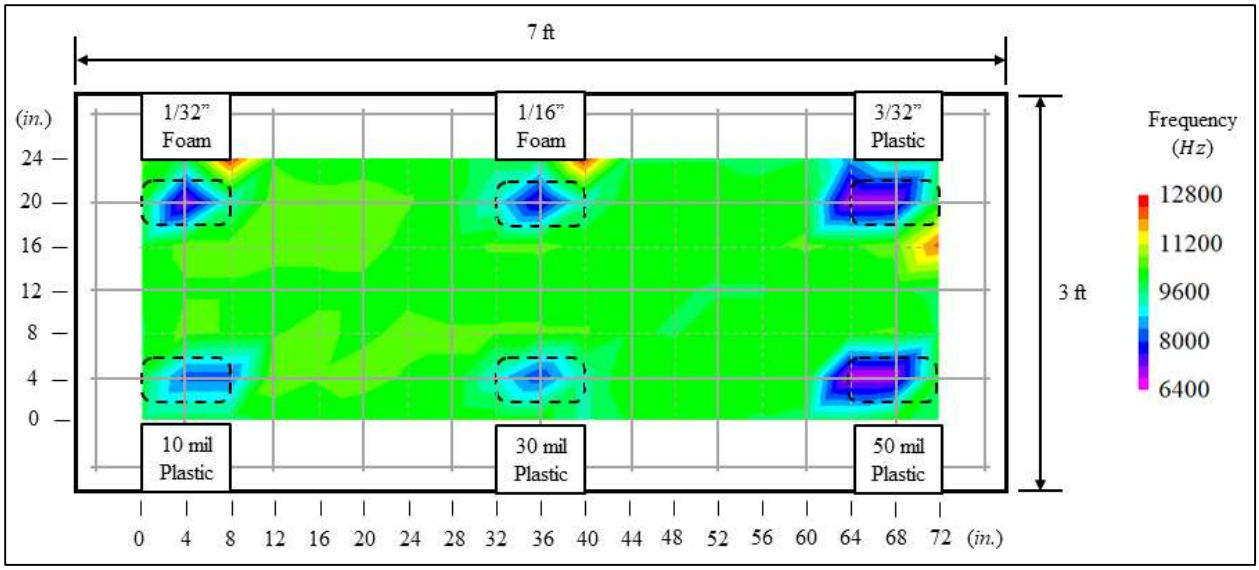

Figure 4-23: Impact-echo results for Specimen DL1

Through observing the impact-echo results for Specimen DL1, one can see that the impact-echo method was able to accurately detect all six artificial delaminations within the specimen, regardless of thickness or material. Responses for all six shallow delaminations were characterized by a shift to a dominant frequency lower than that of the rest of the specimen. This low dominant frequency response to shallow delaminations is consistent with the findings of previous studies (Gucunski, et al. 2013; Cheng and Sansalone 1993). From the ROC analysis results, one can see that the impact-echo method was very accurate, with an accuracy value of 0.955. All six plastic sheets were located, but the impact-echo method struggled to locate the sheets near their edges, which is evident in the TPR value of 0.722 for Specimen DL1. These results indicate that the impact-echo method accurately locates and characterizes plastic sheets of various thicknesses as shallow delaminations within reinforced-concrete slabs.

4.3.2.2 Specimen DL2

A comparison between the known defect locations and the surface contour plot of the impact-echo results for Specimen DL2 is shown in Figure 4-24.

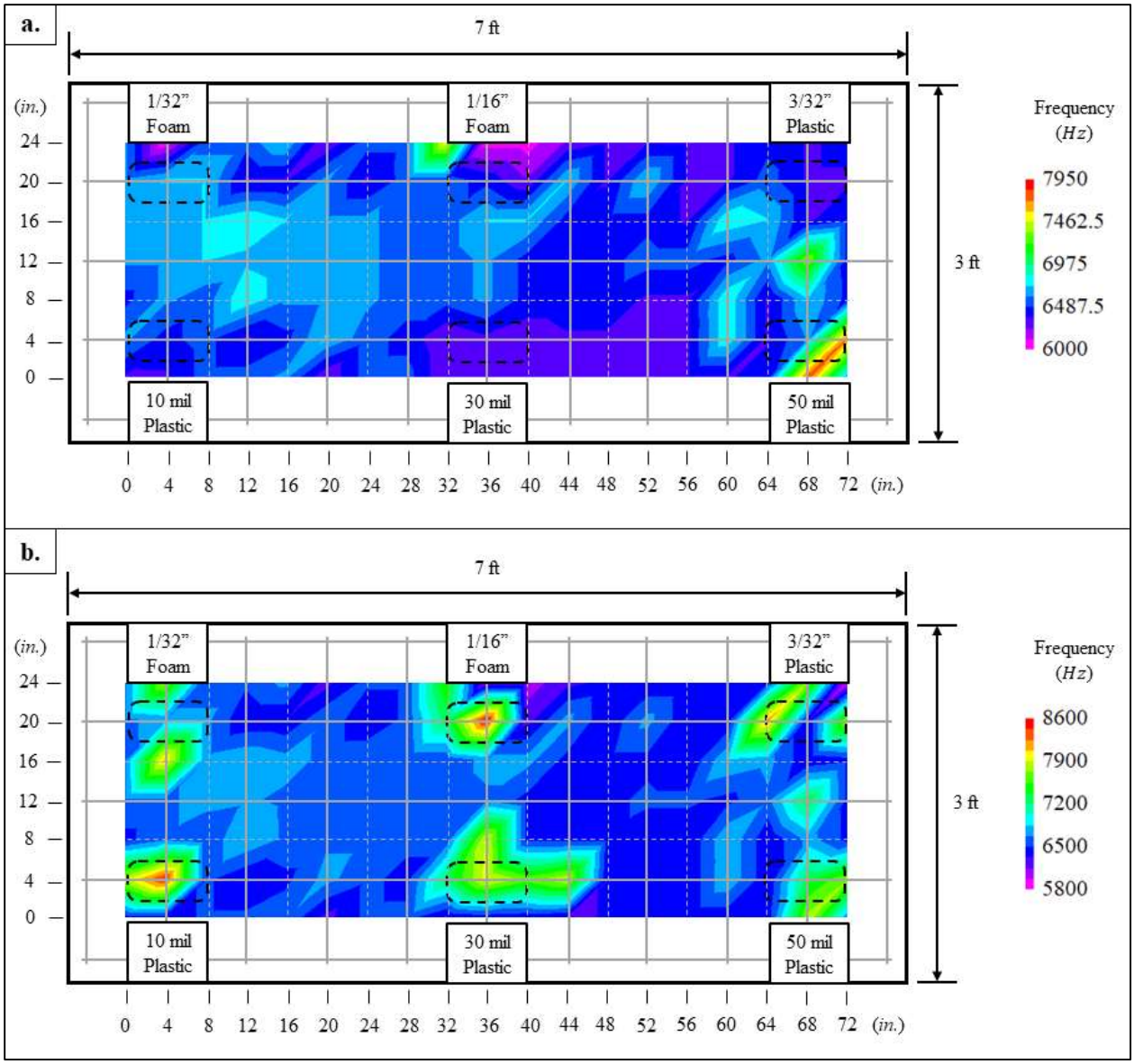

Figure 4-24: Impact-echo results for Specimen DL2; a) dominant frequencies, b) secondary peak frequencies

Through observing the dominant frequency impact-echo results for Specimen DL2 in Figure 4-24(a), one can see that the impact-echo struggled initially to detect any of the delaminations placed within the specimen. Almost none of the dominant return frequencies indicate response to the presence of a delamination. ROC analysis yielded an accuracy of 0.865 and a TPR of 0.056. Upon further visual inspection and analysis into the return waveforms at individual test points, the surface contour plot in Figure 4-24(b) was produced. This surface contour plot includes results of some secondary peak frequencies in the frequency-amplitude domain. From Figure 4-24(b), one can see areas of higher dominant frequency near locations of

the delaminations. These higher dominant frequencies are indicative of waves reflecting off an interface at a depth less than the full depth of the specimen. One can see from the ROC analysis performed on the secondary waveform data that the impact-echo method was more accurate than originally determined from Figure 4-24(a), with an accuracy value of 0.887, and the plastic sheets placed at the bottom layer of steel were able to be detected, with a TPR of 0.611. These results show that the impact-echo method, with added data analysis of the waveforms, was able to detect the presence of all six deep delaminations within Specimen DL2, though the impact-echo method appeared to struggle in characterizing the boundaries of delaminations.

4.3.2.3 Specimen DL3

A comparison between the known defect locations and the surface contour plot of the impact-echo results for Specimen DL3 is shown in Figure 4-25.

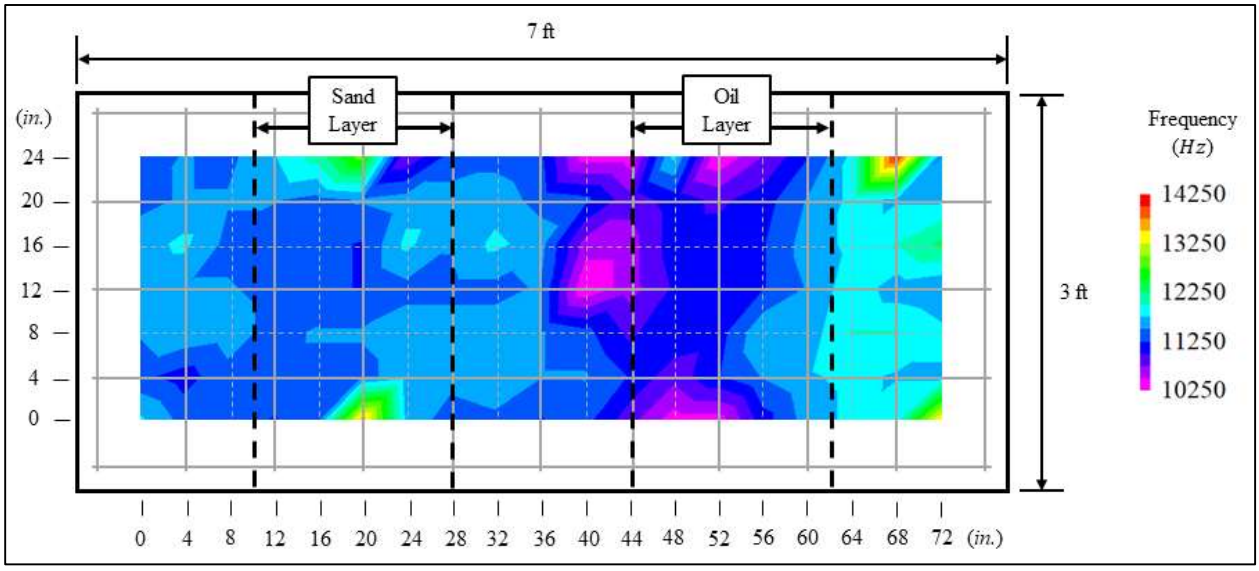

Figure 4-25: Impact-echo results for Specimen DL3

Through observing the impact-echo results for Specimen DL3, one can see that the impact-echo method responded well to the presence of the section delaminated with oil, but was largely unable to detect the area delaminated with sand. The response to the oil delaminated section was characterized by a shift in the dominant frequency to a value lower than that of the rest of the specimen, though the response lacked spatial correlation between the actual and apparent location of the delamination. This low dominant frequency response to a shallow delamination is consistent with the findings of previous studies (Gucunski, et al. 2013; Cheng and Sansalone 1993). From the ROC analysis results, it was determined that the impact-echo

method exhibited an accuracy of 0.654. The TPR value for Specimen DL3 was 0.514, which means that just over half of the total defective points were located. The lack of response to the sand delamination could be due to an inadequate thickness of the sand layer, or due to an inability of the impact-echo method to detect such a delamination. Further research will have to be done in order to determine the reason why the sand delamination elicited no response from the impact-echo method.

4.3.2.4 Specimen DL4

A comparison between the known defect locations and the surface contour plot of the impact-echo results for Specimen DL4 is shown in Figure 4-26.

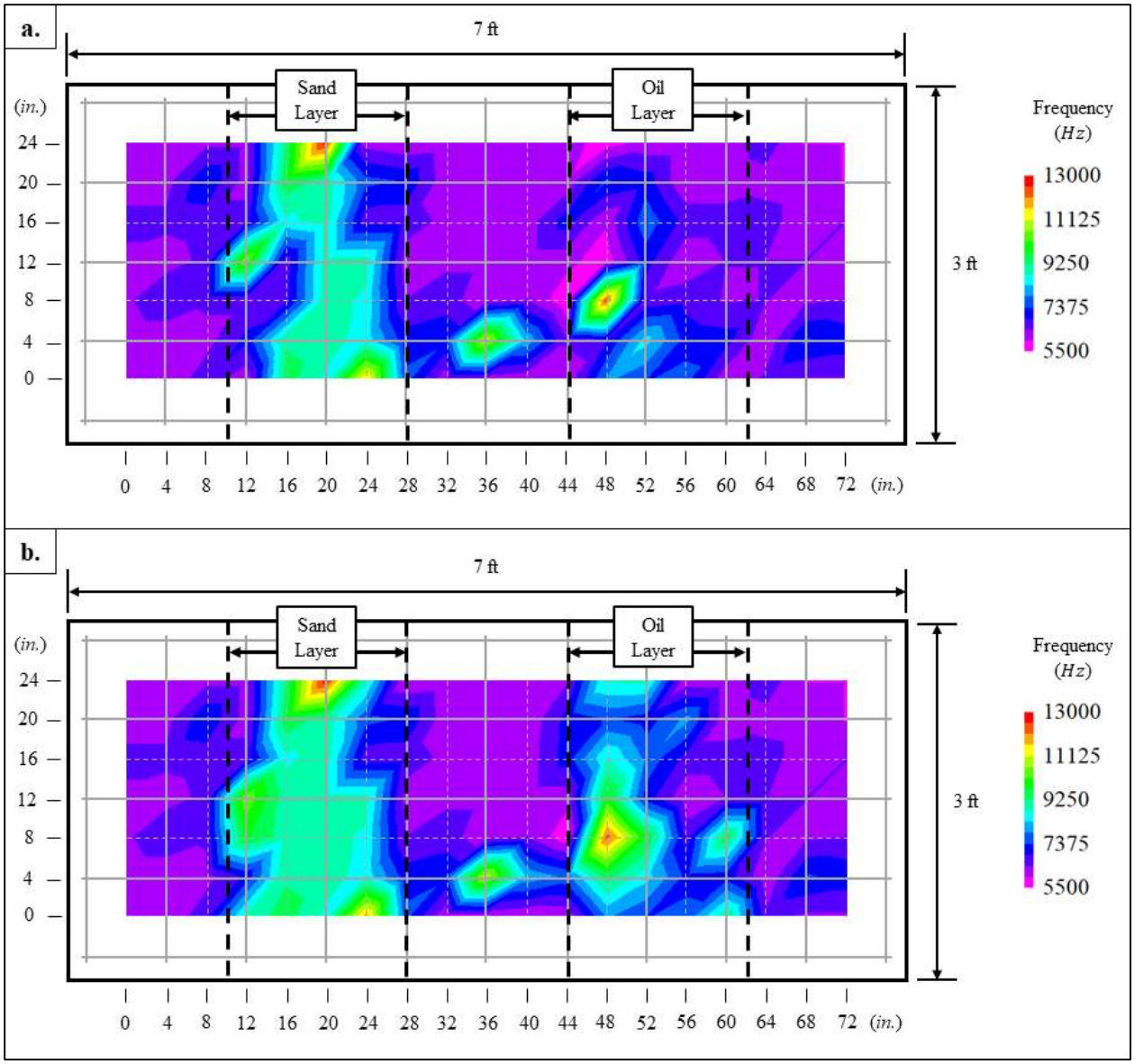

Figure 4-26: Impact-echo results for Specimen DL4; a) dominant frequencies, b) secondary peak frequencies

Through observing the dominant frequency impact-echo results for Specimen DL4 in Figure 4-26(a), one can see that the impact-echo method responded fairly well to the presence of the section delaminated with sand, but showed less of a response to the section delaminated with oil. ROC analysis provided an accuracy of 0.729 and a TPR value of 0.657. Upon further visual inspection and analysis into the return waveforms at individual test points, the surface contour plot in Figure 4-26(b) was produced. This surface contour plot includes results of some secondary peak frequencies in the frequency-amplitude domain. From Figure 4-26(b), one can see a greater number of areas of higher frequency correlate with the locations of the debonded

layers. These higher dominant frequencies are indicative of waves reflecting off an interface at a depth less than the full depth of the specimen. ROC analysis of the impact-echo results secondary peak frequencies yielded a greater accuracy of 0.812 and a TPR value of 0.814, which is indicative of a larger percentage of the delaminated areas being located. These results show that the impact-echo method, with added data analysis of the waveforms, was able to detect and locate both sand and oil debonded deep delaminations within Specimen DL4.

4.3.2.5 Specimen DL5

A comparison between the known defect locations and the surface contour plot of the impact-echo results for Specimen DL5 is shown in Figure 4-27.

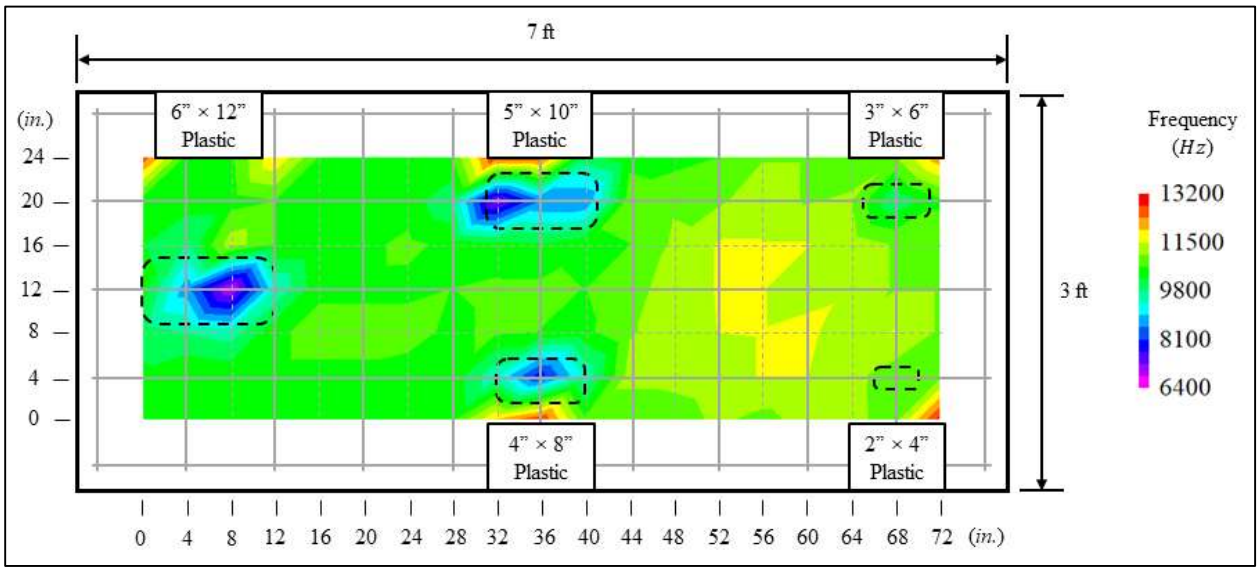

Figure 4-27: Impact-echo results for Specimen DL5

Through observing the impact-echo results for Specimen DL5, one can see that the impact-echo method was able to clearly detect and locate the largest three plastic, shallow delaminations. Responses for the detected shallow delaminations were characterized by a shift to a dominant frequency relatively lower than that of the rest of the specimen. This low frequency response to shallow delaminations is consistent with the findings of previous studies (Gucunski, et al. 2013; Cheng and Sansalone 1993). From the ROC analysis results, one can see that the impact-echo method was very accurate, with an accuracy value of 0.977. Only the largest three of the five plastic sheets were able to be located, which is reflected by the TPR value of 0.722 for Specimen DL5. A very mild response was noted at the location of the 3 × 6 in. plastic delamination, whereas no response was observed for the 2 × 4 in. delamination. This may be a

result of the grid spacing used to test the specimen, as the dimensions of the delaminated portions not detected were less than or equal to the space between test points.

4.3.2.6 Specimen DL6

A comparison between the known defect locations and the surface contour plot of the impact-echo results for Specimen DL6 is shown in Figure 4-28.

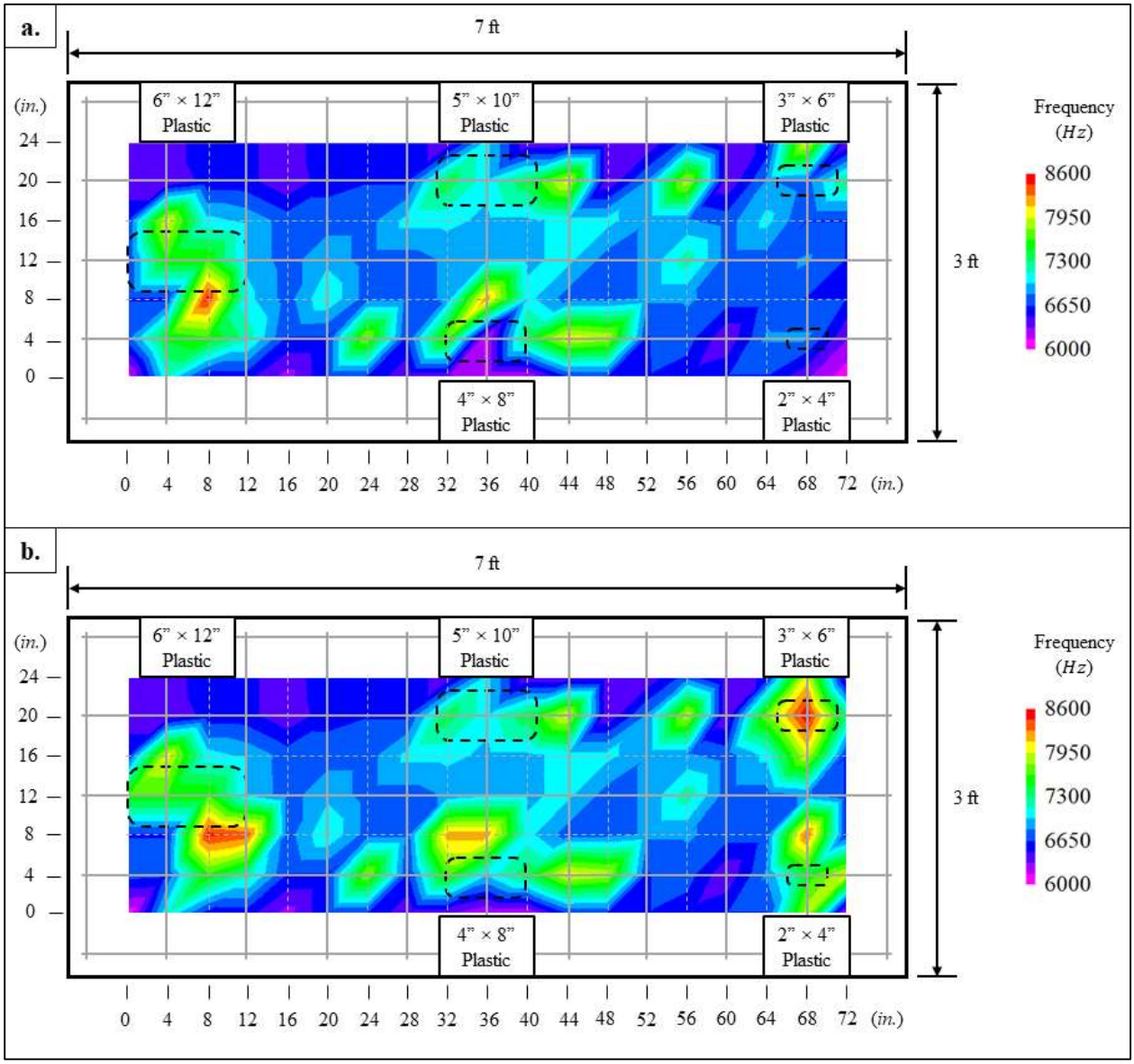

Figure 4-28: Impact-echo results for Specimen DL6; a) dominant frequencies, b) secondary peak frequencies

Through observing the dominant frequency impact-echo results for Specimen DL6 in Figure 4-28(a), one can see that the impact-echo method exhibited a response at or near the

location of all five deep plastic delaminations, with an accuracy of 0.910. Despite the response to delamination presence, the dominant frequency results exhibited poor spatial correlation between the actual and perceived locations of the delaminations, which is evident in the TPR value of 0.000. Upon further visual inspection and analysis into the return waveforms at individual test points, the surface contour plot in Figure 4-28(b) was produced. This surface contour plot includes results of some secondary peak frequencies in the frequency-amplitude domain. From Figure 4-28(b), one can see a greater number of areas of higher frequency correlate with the locations of the plastic delaminations, with an accuracy of 0.917 and a TPR value of 0.083. For both the dominant and secondary frequency surface contour plots, the higher return frequencies indicate wave reflection off an interface shallower than the full depth of the specimen. These results show that the impact-echo method, with added data analysis of the waveforms, was able to detect the presence of all plastic, deep delaminations within Specimen DL6, but showed poor ability in accurately locating the delaminations.

4.3.2.7 Specimen DL7

A comparison between the known defect locations and the surface contour plot of the impact-echo results for Specimen DL7 is shown in Figure 4-29.

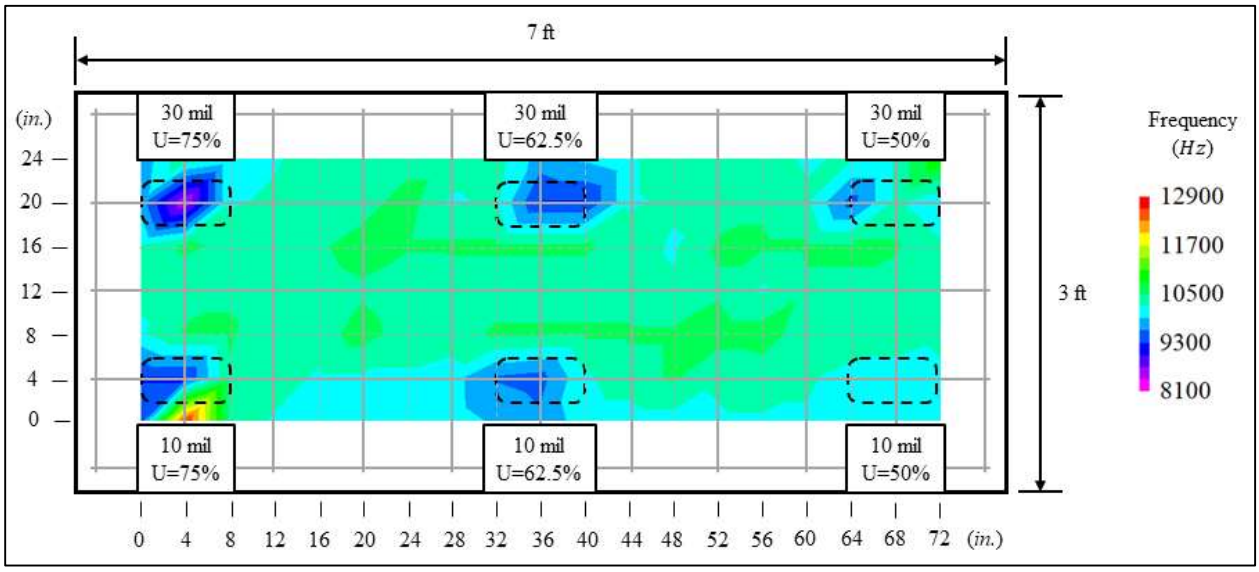

Figure 4-29: Impact-echo results for Specimen DL7

Through observing the impact-echo results for Specimen DL7, one can see that the impact-echo method responded well to the presence of the unbonded delaminations within the specimen. Response to the unbonded delaminations was characterized by a shift to a lower

dominant return frequency at the locations of the delaminations within the specimen, which is consistent with the findings of previous research (Gucunski, et al. 2013; Cheng and Sansalone 1993). The impact-echo method was able to detect and locate all three of the 30 mil plastic inserts, with detectability increasing with unbonded fraction. Regarding the 10 mil plastic inserts, the impact-echo method only displayed a strong response at the location of the 75 percent unbonded and 62.5 percent unbonded delaminations. A slight drop in frequency may be observed near the location of the 10 mil, 50 percent unbonded delamination, but one could attribute that to operator bias. From the ROC analysis results, one can see that the impact-echo method was very accurate, with an accuracy value of 0.917. Five of the six plastic sheets were located, but the impact-echo method struggled to locate the sheets at points near their edges, which is evident in the TPR value of 0.444 for Specimen DL7.

4.3.2.8 Specimen DL8

A comparison between the known defect locations and the surface contour plot of the impact-echo results for Specimen DL8 is shown in Figure 4-30.

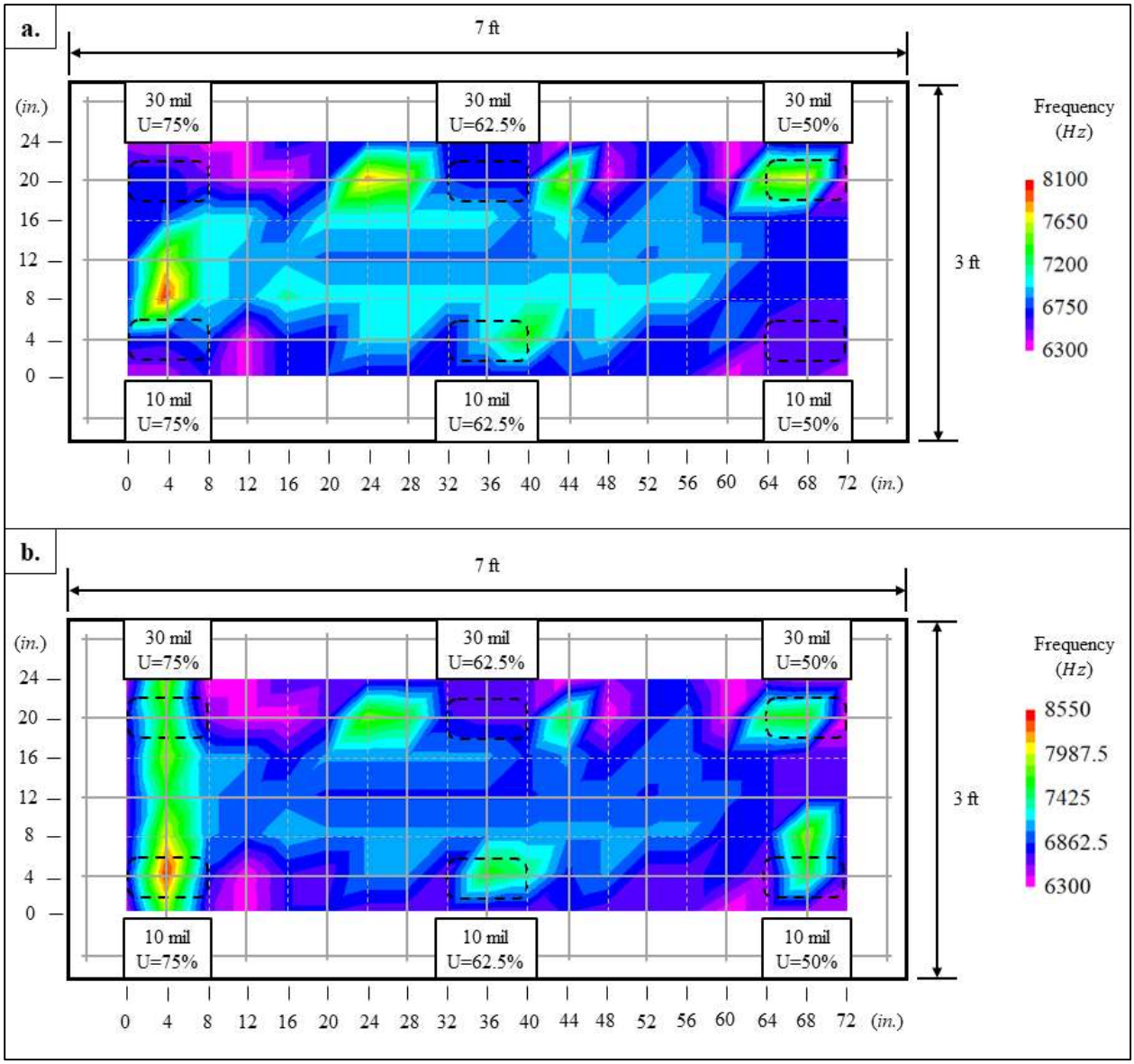

Figure 4-30: Impact-echo results for Specimen DL8; a) dominant frequencies, b) secondary peak frequencies

Through observing the dominant frequency impact-echo results for Specimen DL8 in Figure 4-30(a), one can see that the impact-echo method was much less successful in detecting and locating the deep, unbonded delaminations than it was in locating the shallow, unbonded delaminations in Specimen DL7. From the ROC analysis results of the peak dominant frequencies, one can see that the impact-echo method displayed an accuracy of 0.865, but an ROC value of 0.000. Upon further visual inspection and analysis into the return waveforms at individual test points, the surface contour plot in Figure 4-30(b) was produced. This surface contour plot includes results of some secondary peak frequencies in the frequency-amplitude

domain. From Figure 4-30(b), one can see a greater number of areas of higher frequency correlate with the locations of the debonded layers. These higher dominant frequencies are indicative of waves reflecting off an interface at a depth less than the full depth of the specimen. From these results, one can see that the impact-echo method was able to detect the presence of all plastic inserts within the specimen, and ROC analysis showed an accuracy of 0.872. Poor spatial correlation between the actual and perceived location of some delaminations within the specimen can be noted, especially at the 50 mil, 62.5 percent unbonded delamination, which is evidenced by the TPR value of 0.056. It appears that, for the range of values used within this specimen, neither unbonded fraction nor defect thickness has a significant effect on detectability of deep delaminations.

4.3.3 Cracking Specimen

4.3.3.1 Specimen CR1

A comparison between the known defect locations and the surface contour plot of the impact-echo results for Specimen CR1 is shown in Figure 4-31.

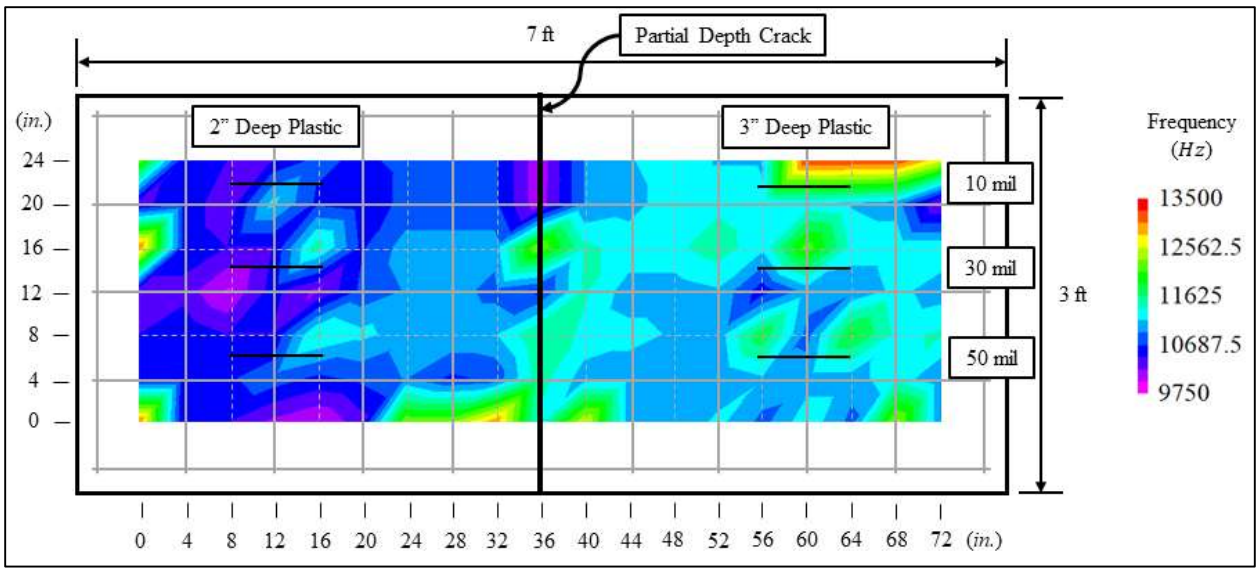

Figure 4-31: Impact-echo results for Specimen CR1

Through observing the impact-echo results for Specimen CR1, one can see that the impact-echo method was unable to detect any of the vertical cracks created in the specimen. No strong shifts in frequency are noted near the locations of the artificial cracks. ROC analysis was not performed on Specimen CR1. Further research will have to be done in order to determine if the impact-echo method is suitable for detection of vertical cracks, or if the artificial defect

methods used, including plastic inserts and a partially debonded cold joint, fail to accurately resemble naturally occurring vertical cracks.

4.3.4 Corrosion Specimens

4.3.4.1 Specimen C1

4.3.4.1.1 Impact-Echo Test Results

A comparison between the known defect locations and the surface contour plot of the impact-echo results for Specimen C1, the corrosion specimen with 3/4 in. cover to the top layer of reinforcing steel, is shown in Figure 4-32.

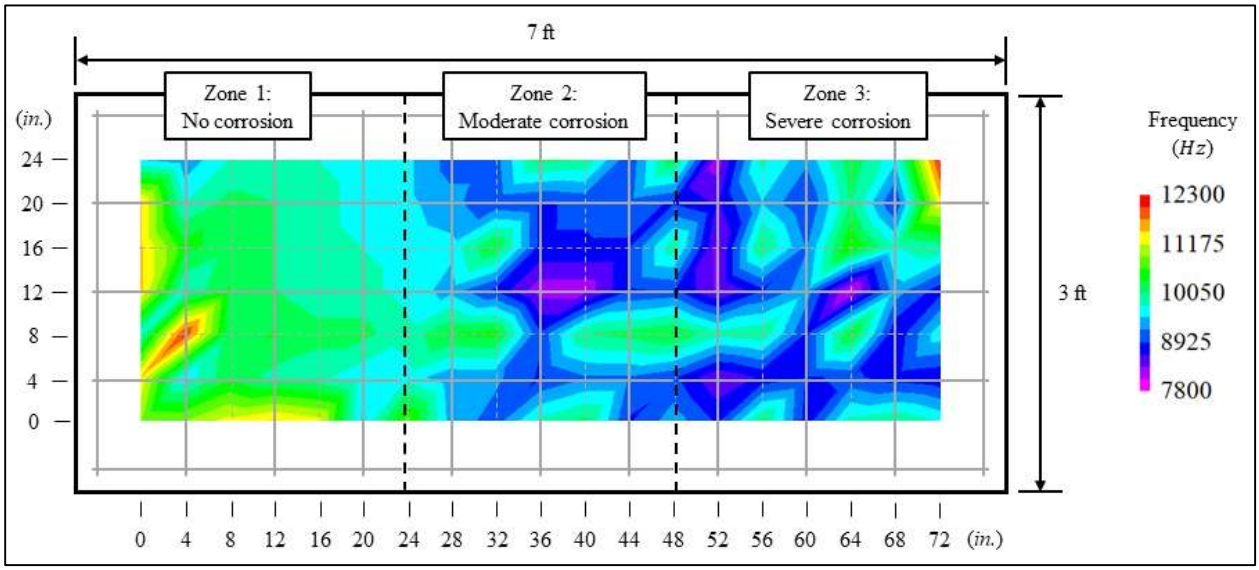

Figure 4-32: Impact-echo results for Specimen C1

Through observing the impact-echo results for specimen C1, one can see that the impact-echo method was able to detect delaminations resulting from corrosion activity within the specimen. The response to these shallow delaminated areas within the specimen is characterized by a shift to a lower dominant return frequency at expected locations of corrosion-induced delaminations. This response is consistent with the findings of previous studies (Gucunski, et al. 2013; Cheng and Sansalone 1993). From the ROC analysis results, one can see that the impact-echo method was accurate, with an accuracy value of 0.835. Specimen C1's TPR value of 0.990 was the highest such value of all specimens. Within Specimen C1, both Zones 2 and 3 appear to be severely deteriorated. Contrary to expectation, there appears to be a similar amount of corrosion-induced delaminations in Zones 2 and 3. This is possibly explained by the fact that

Specimen C1 exhibited a severe amount of vertical cracking throughout its corroded regions. As described in Section 4.3.3.1, the data collected from Specimen CR1 is inconclusive concerning the suitability of the impact-echo method to discern between varying extents of vertical cracking.

4.3.4.1.2 Half-Cell Potential Test Results

A comparison between the known defect locations and the surface contour plot of the half-cell potential results for Specimen C1 is shown in Figure 4-33.

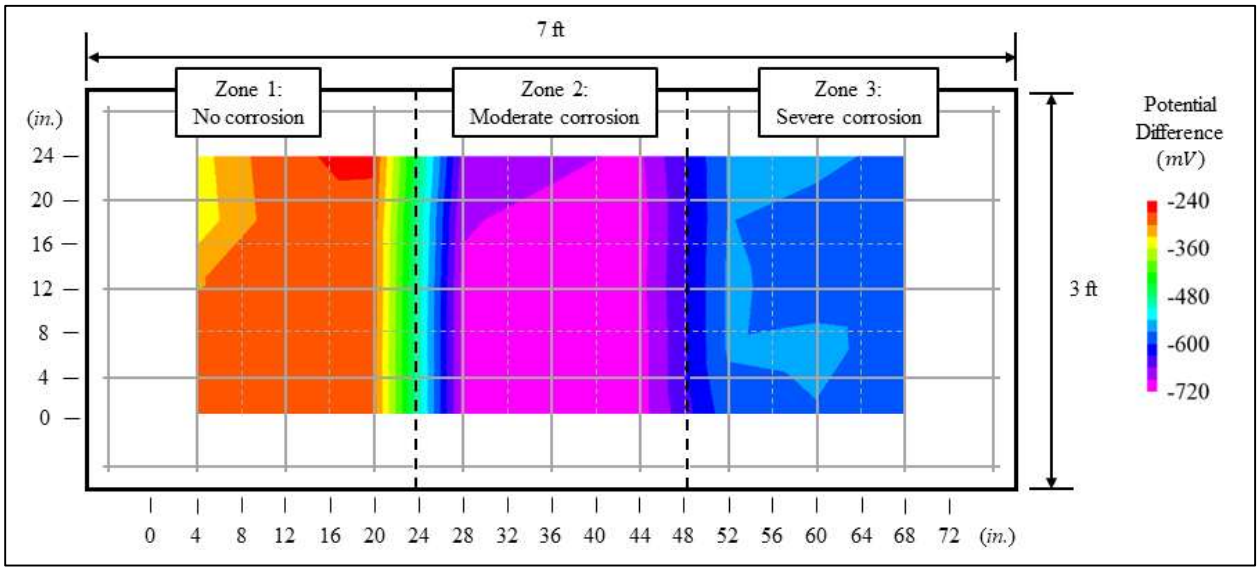

Figure 4-33: Half-cell potential results for Specimen C1

Through observing the half-cell potential results for Specimen C1, one can see that the half-cell potential method was able to accurately detect and locate corrosion activity within the specimen. According to Table 2-1, adapted from ASTM C876 (2015), a test point with a measured potential at or below -350 mV corresponds to a 90 percent or greater probability of corrosion activity at that location. The measured potentials in Zones 2 and 3 are approximately -700 mV and -600 mV, respectively. No reasonable conclusion was drawn as to why the potential difference for Zone 2 was more negative than that of Zone 3. These values are far beyond the -350 mV threshold, signifying a very high probability of corrosion within Zones 2 and 3. The measured potential in Zone 1 is approximately -300 mV, signifying an uncertain probability of corrosion activity.

4.3.4.1.3 Surface Resistivity Test Results

A comparison between the known defect locations and the surface contour plot of the surface resistivity results for Specimen C1 is shown in Figure 4-34.

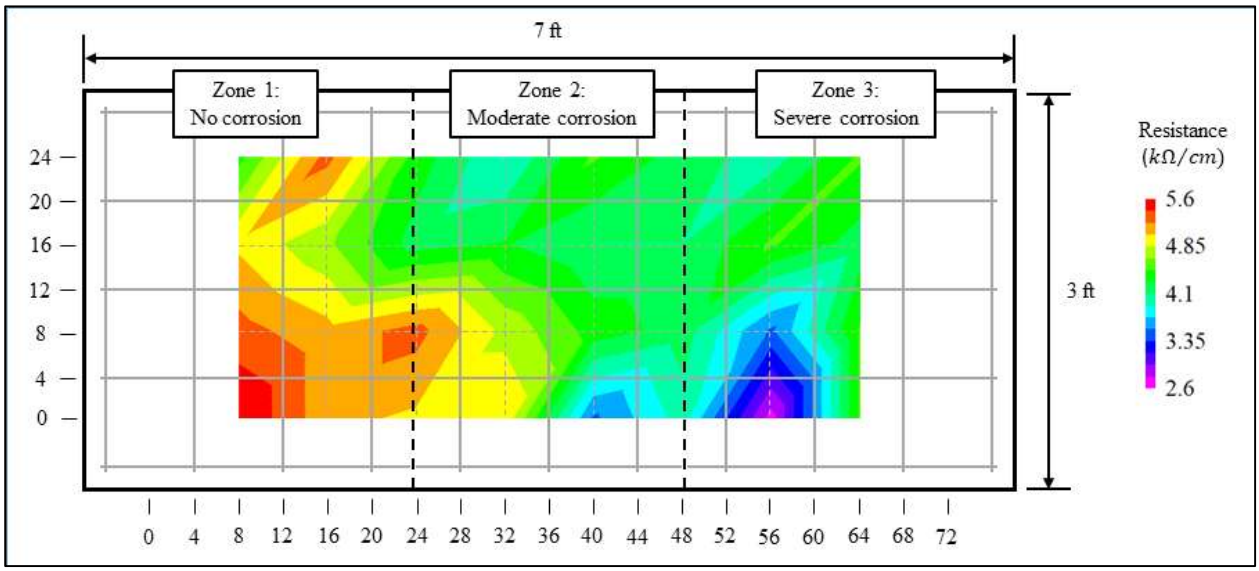

Figure 4-34: Surface resistivity results for Specimen C1

According to Table 2-2, adapted from Gucunski et al (2013), a measured resistivity below 5 kΩ-cm is indicative of a very high corrosion rate, and a measured resistivity between 5 and 10 kΩ-cm is indicative of a high corrosion rate. By examining the surface resistivity test results, one can see that the surface resistivity method indicated a high to very high corrosion rate for all three zones within Specimen C1, despite only Zones 2 and 3 being corroded. This can be explained by the fact that the concrete was saturated with sodium chloride solution as a part of the accelerated corrosion process. Zone 1 exhibited a slightly greater resistance compared to that of Zones 2 and 3, which is likely due to the internal cracking that resulted from corrosion activity within Zones 2 and 3. From these results, one can see that the surface resistivity method struggles to locate definitively areas of concrete in which corrosion activity is occurring, at least when areas of both sound and defective concrete have each been exposed to the presence of sodium chloride. The surface resistivity method tests for concrete conditions conducive to corrosion activity, and not for corrosion activity itself.

4.3.4.2 Specimen C2

4.3.4.2.1 Impact-Echo Test Results

A comparison between the known defect locations and the surface contour plot of the impact-echo results for Specimen C2, the corrosion specimen with 2 in. cover to the top layer of reinforcing steel, is shown in Figure 4-35.

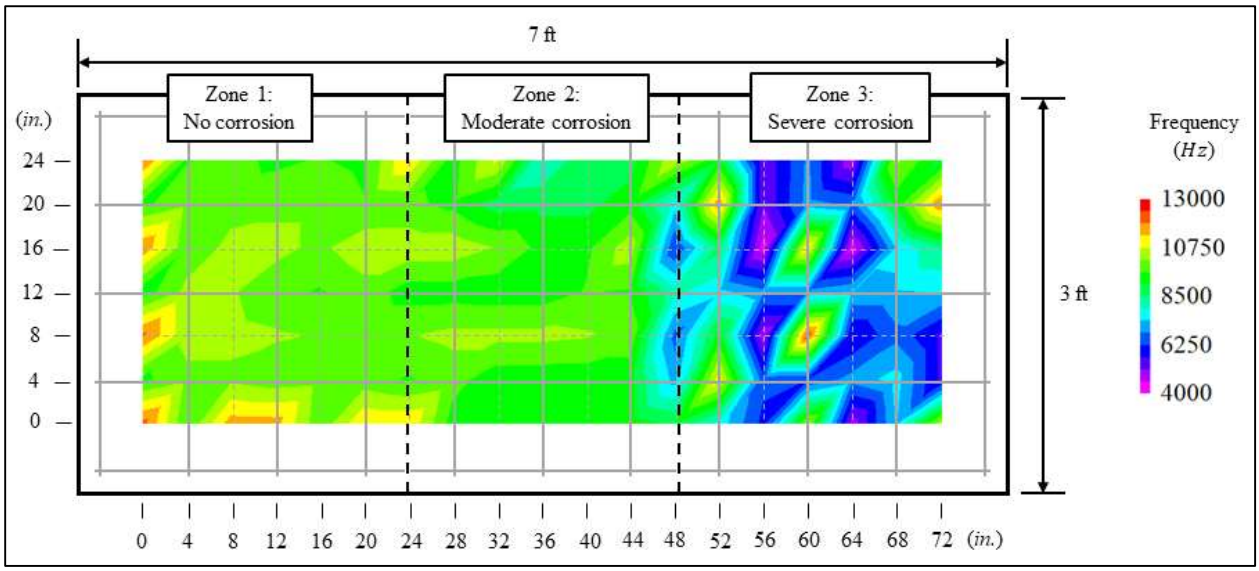

Figure 4-35: Impact-echo results for Specimen C2

Through observing the impact-echo results for specimen C2, one can see that the impact-echo method was able to detect delaminations resulting from corrosion activity within the specimen. The response to these shallow delaminated areas within the specimen is characterized by a shift to a lower dominant return frequency at expected locations of corrosion-induced delaminations. This response is consistent with the findings of previous studies (Gucunski, et al. 2013; Cheng and Sansalone 1993). From the ROC analysis results, one can see that the impact-echo method was accurate, with an accuracy value of 0.797. Specimen C2's TPR value of 0.980 was the second highest such value of all specimens, behind only Specimen C1. Within Specimen C2, Zone 2 appears to be mildly delaminated, as frequency values are slightly greater in Zone 2 than in Zone 1, while Zone 3 appears to have severe delaminations.

4.3.4.2.2 Half-Cell Potential Test Results

A comparison between the known defect locations and the surface contour plot of the half-cell potential results for Specimen C2 is shown in Figure 4-36.

Figure 4-36: Half-cell potential results for Specimen C2

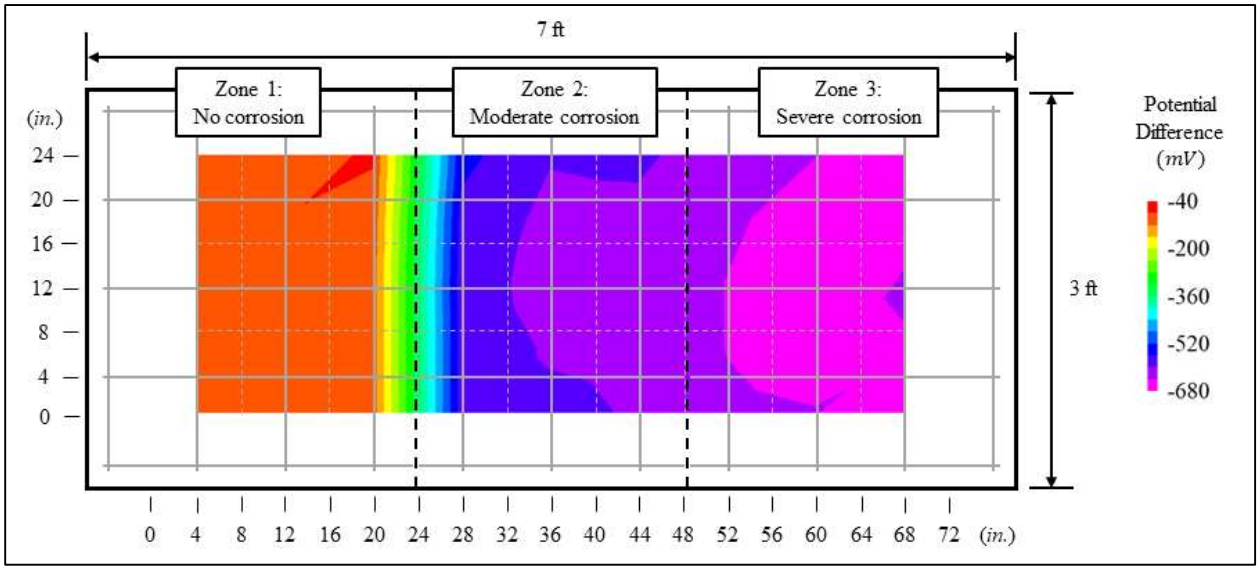

Through observing the half-cell potential results for Specimen C2, one can see that the half-cell potential method was able to accurately detect and locate corrosion activity within the specimen. According to Table 2-1, adapted from ASTM C876 (2015), a test point with a measured potential at or below -350 mV corresponds to a 90 percent or greater probability of corrosion activity at that location. The measured potential for both Zones 2 and 3 fall between -500 mV and -680 mV. These values are far beyond the -350 mV threshold, signifying a very high probability of corrosion within Zones 2 and 3. The measured potential in Zone 1 is approximately -100 mV. This value is greater than the -200 mV threshold, denoting a less than 10 percent probability of corrosion activity.

4.3.4.2.3 Surface Resistivity Test Results

A comparison between the known defect locations and the surface contour plot of the surface resistivity results for Specimen C2 is shown in Figure 4-37.

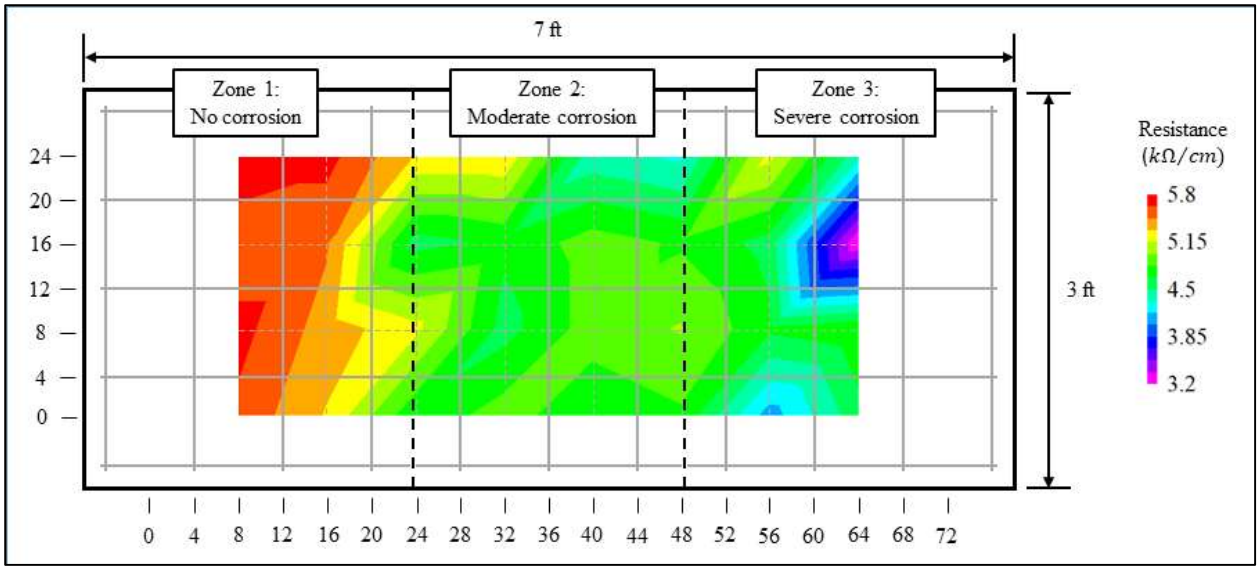

Figure 4-37: Surface resistivity results for Specimen C2

According to Table 2-2, adapted from Gucunski et al (2013), a measured resistivity below 5 kΩ-cm is indicative of a very high corrosion rate, and a measured resistivity between 5 and 10 kΩ-cm is indicative of a high corrosion rate. By examining the surface resistivity test results, one can see that the surface resistivity method indicated a high to very high corrosion rate for all three zones within Specimen C2, despite only Zones 2 and 3 being corroded. Zones 2 and 3 did have a lower surface resistivity than Zone 1, though all three zones were indicative of a high to very high corrosion rate. This can be explained by the fact that the concrete was saturated with sodium chloride solution as a part of the accelerated corrosion process. From these results, one can see that the surface resistivity method struggles to locate areas of concrete in which severe corrosion activity is occurring, as it tests for concrete conditions conducive to corrosion activity, and not for corrosion activity itself.

4.3.5 Control Specimen

4.3.5.1 Specimen CONTROL

A comparison between the known defect locations and the surface contour plot of the impact-echo results for Specimen CONTROL is shown in Figure 4-38.

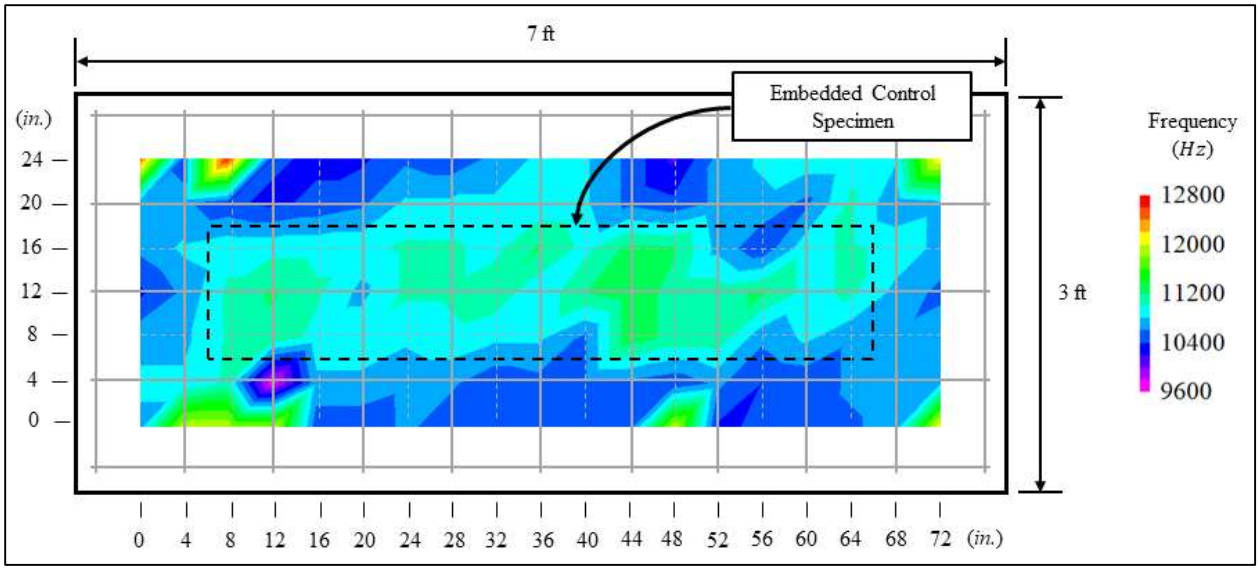

Figure 4-38: Impact-echo results for Specimen CONTROL

Through observing the impact-echo results for Specimen CONTROL, one can see that the impact-echo method did locate the control concrete within the specimen. The response to the control concrete is characterized by a shift to a higher dominant return frequency at the location of the deteriorated concrete within the specimen. The small specimen within Specimen CONTROL was cast with a concrete having the same mixture proportions as the rest of the slab, yet these results show that the impact-echo method was able to locate the cast-in specimen. An explanation for this can be found in Section 4.2.5.1, where core results proved the cast-in concrete to be significantly stronger than the surrounding concrete. Because the strength of the cast-in concrete was found to be stronger than the surrounding concrete, the area of the cast-in specimen was regarded as deteriorated during ROC analysis. From ROC analysis, one can see that the impact-echo method had an accuracy of 0.820 and a TPR value of 0.756, showing that the cast-in specimen was 75.6 percent detectable by impact-echo surveying.

4.3.6 Deteriorated Specimens

4.3.6.1 Specimen DE2

A comparison between the known defect locations and the surface contour plot of the impact-echo results for Specimen DE2 is shown in Figure 4-39.

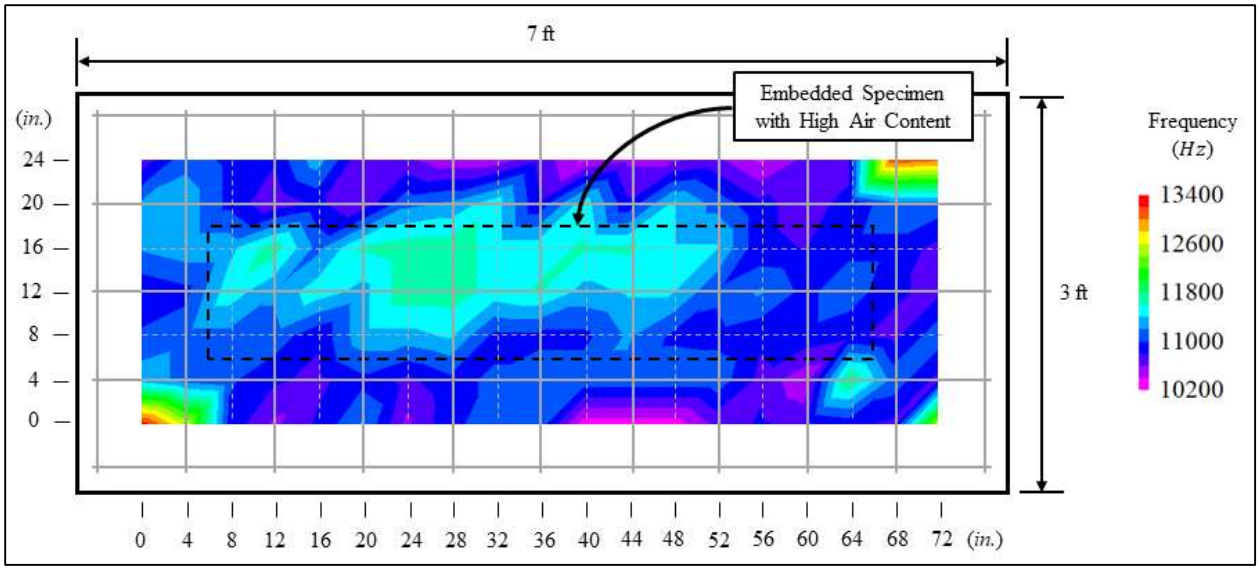

Figure 4-39: Impact-echo results for Specimen DE2

Through observing the impact-echo results for Specimen DE2, one can see that the impact-echo method was able to detect a significant portion of the deteriorated concrete. This response to the deteriorated concrete is characterized by a shift to a higher dominant return frequency at the location of the deteriorated concrete within the specimen. The deteriorated concrete for Specimen DE2 was created using a concrete mixture having a high entrained air content. From ROC analysis, one can see that the impact-echo method had an accuracy of 0.744 and a TPR value of 0.533, showing that the cast-in specimen was 53.3 percent detectable by impact-echo surveying. Therefore, one may draw the conclusion that the impact-echo method is able to detect and locate some regions of concrete that have a greater entrained air content than the surrounding concrete.

4.3.6.2 Specimen DE3

A comparison between the known defect locations and the surface contour plot of the impact-echo results for Specimen DE3 is shown in Figure 4-40.

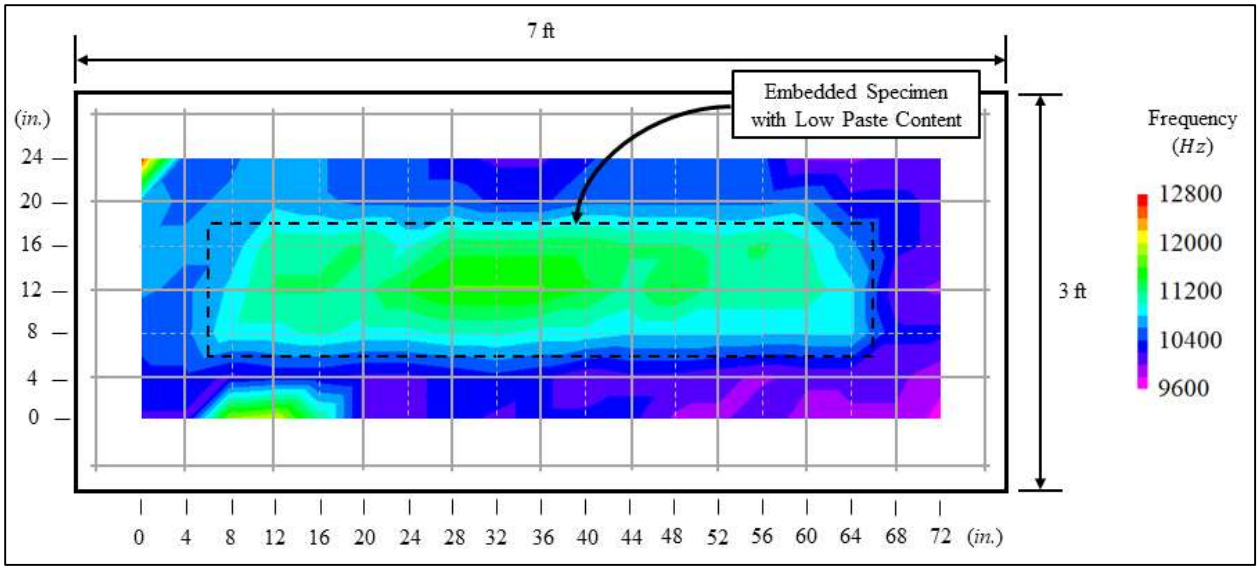

Figure 4-40: Impact-echo results for Specimen DE3

Through observing the impact-echo results for Specimen DE3, one can see that the impact-echo method provided a significant response and strong spatial correlation to the deteriorated concrete. This response to the deteriorated concrete is characterized by a shift to a higher dominant return frequency at the location of the deteriorated concrete within the specimen. The deteriorated concrete for Specimen DE3 was created using a concrete mixture having low paste content. From ROC analysis, one can see that the impact-echo method had an accuracy of 0.955 and a TPR value of 0.956, showing that the cast-in specimen was 95.6 percent detectable by impact-echo surveying. Therefore, one may draw the conclusion that the impact-echo method is very successful at detecting and locating regions of concrete characterized by low paste content and a voided makeup.

4.3.6.3 Specimen DE4

A comparison between the known defect locations and the surface contour plot of the impact-echo results for Specimen DE4 is shown in Figure 4-41.

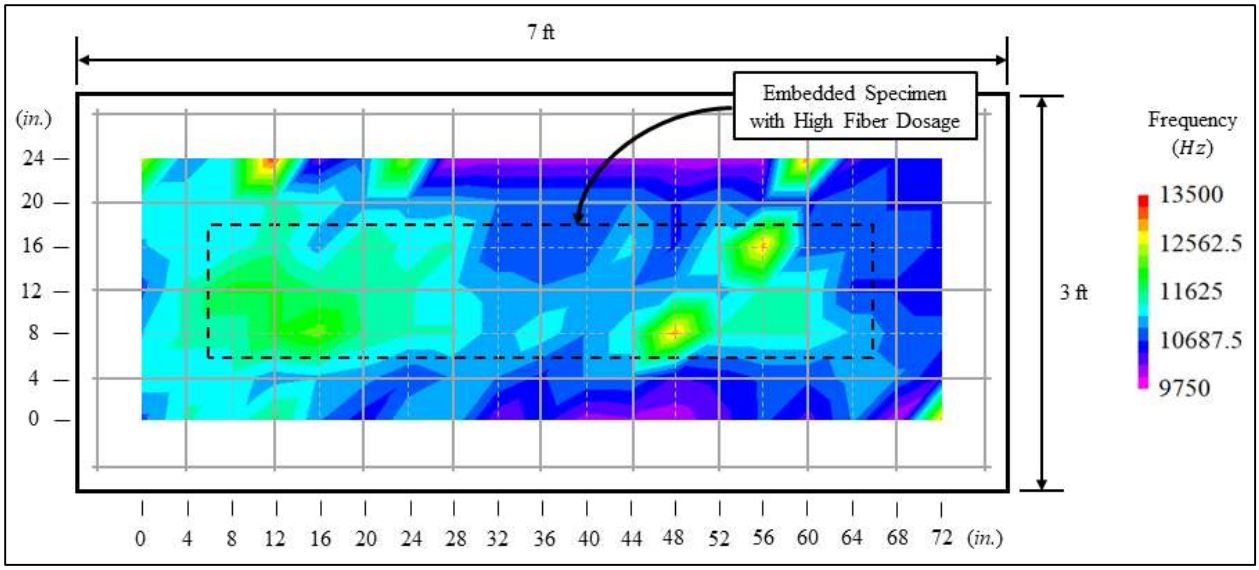

Figure 4-41: Impact-echo results for Specimen DE4

Through observing the impact-echo results for Specimen DE4, one can see that the impact-echo method responded to some of the deteriorated area within the specimen. This response to the deteriorated concrete is characterized by a shift to a higher dominant return frequency near the location of the deteriorated concrete within the specimen. The deteriorated concrete for Specimen DE4 was created using a concrete mixture containing a high dosage of polypropylene fibers. The impact-echo method was able to locate approximately half of the deteriorated region of concrete, but also returned some false-positive results at the left of the specimen, between x-coordinates 0 and 24 inches. From ROC analysis, one can see that the impact-echo method had an accuracy of 0.759 and a TPR value of 0.533, showing that the cast-in specimen was 53.3 percent detectable by impact-echo surveying. From these results, coupled with the cores taken from Specimen DE4, it is reasonable to infer that the impact-echo method detected the air trapped within the concrete and not the fibers themselves. Therefore, one may conclude, from these results, that a high dosage of polypropylene fibers is somewhat suitable for replicating deteriorated concrete, at least in regards to impact-echo testing.

4.3.6.4 Specimen DE5

A comparison between the known defect locations and the surface contour plot of the impact-echo results for Specimen DE5 is shown in Figure 4-42.

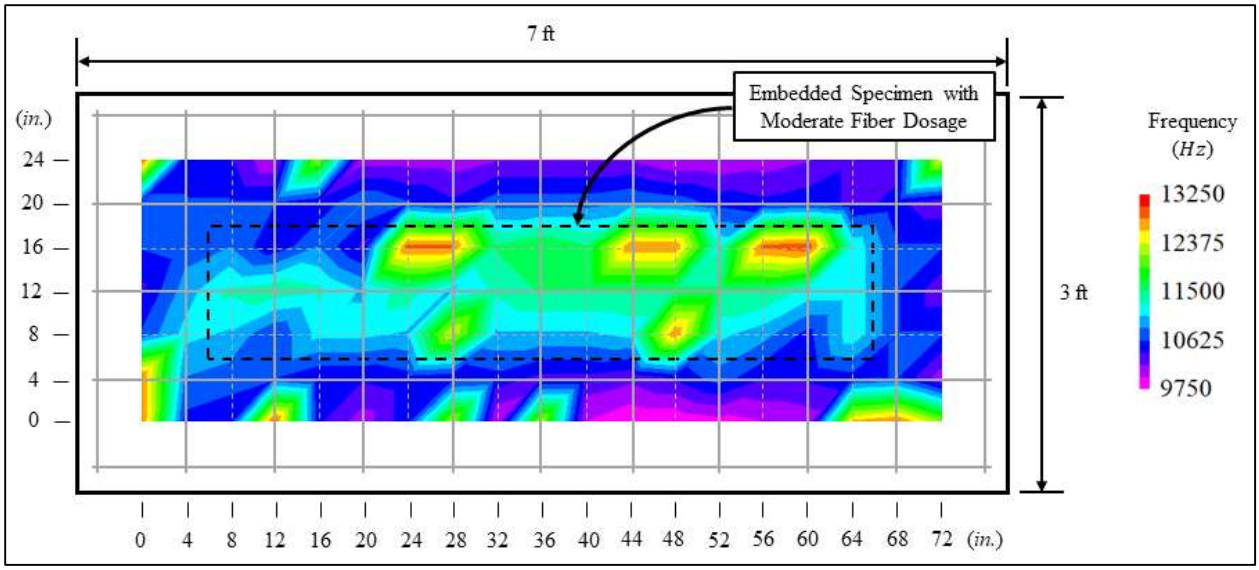

Figure 4-42: Impact-echo results for Specimen DE5

Through observing the impact-echo results for Specimen DE5, one can see that the impact-echo method responded to some of the deteriorated area within the specimen. This response to the deteriorated concrete is characterized by a shift to a higher dominant return frequency near the location of the deteriorated concrete within the specimen. The deteriorated concrete for Specimen DE5 was created using a concrete mixture containing a moderate dosage of polypropylene fibers. Ironically, the impact-echo was able locate more of the deteriorated region of Specimen DE5 than Specimen DE4, which had a greater dosage of polypropylene fibers to simulate deterioration. From ROC analysis, one can see that the impact-echo method had an accuracy of 0.857 and a TPR value of 0.867, showing that the cast-in specimen was 86.7 percent detectable by impact-echo surveying, with almost no false-positives occurring, aside from points potentially influenced by edge effects. These results, coupled with the cores taken from Specimen DE5, it is reasonable to infer that the impact-echo method detected the air trapped within the concrete and not the fibers themselves. Therefore, one may conclude that a moderate dosage of polypropylene fibers is somewhat suitable for replicating deteriorated concrete, at least in regards to impact-echo testing.

4.3.7 Poor Construction Specimens

4.3.7.1 Specimen PC1

A comparison between the known defect locations and the surface contour plot of the impact-echo results for Specimen PC1 is shown in Figure 4-43.

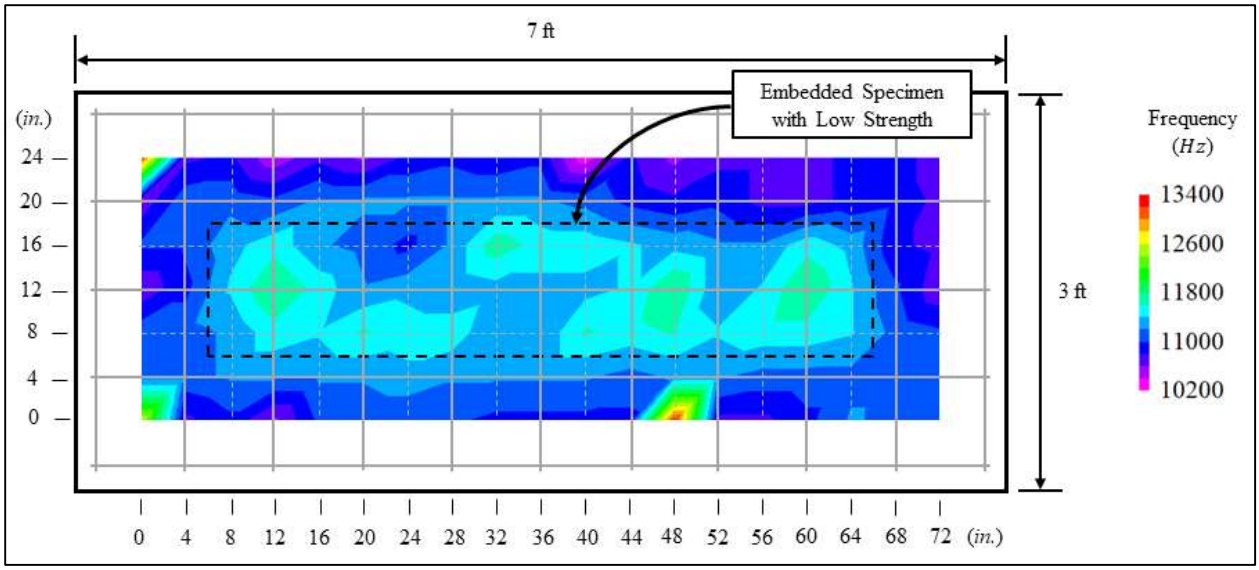

Figure 4-43: Impact-echo results for Specimen PC1

Through observing the impact-echo results for Specimen PC1, one can see that the impact-echo method responded to most of the poorly constructed area within the specimen. This response to the poorly constructed concrete is characterized by a shift to a higher dominant return frequency near the location of the deteriorated concrete within the specimen. The deteriorated concrete for Specimen PC1 was created using a low-strength concrete mixture. From ROC analysis, one can see that the impact-echo method had an accuracy of 0.880 and a TPR value of 0.733, showing that the cast-in specimen was 73.3 percent detectable by impact-echo surveying, with only a few false-positives occurring, aside from points potentially influenced by edge effects. From these results, one may conclude that low-strength concrete encased in regular strength concrete is detectable with impact-echo testing.

4.3.7.2 Specimen PC2

A comparison between the known defect locations and the surface contour plot of the impact-echo results for Specimen PC2 is shown in Figure 4-44.

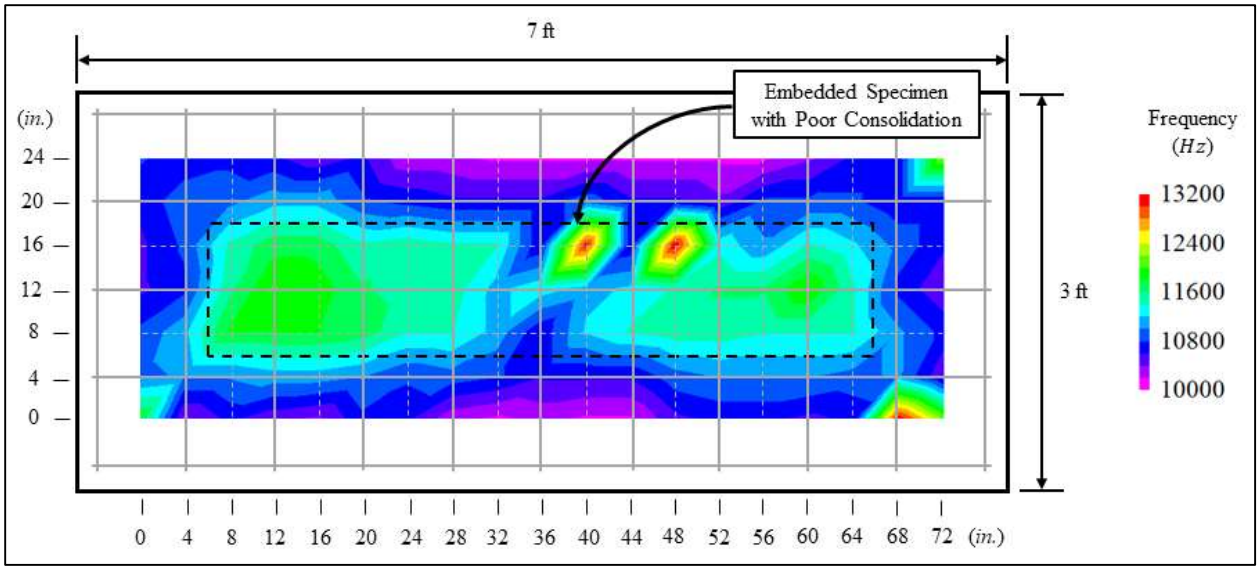

Figure 4-44: Impact-echo results for Specimen PC2

Through observing the impact-echo results for Specimen PC2, one can see that the impact-echo method responded well to the poorly constructed area within the specimen. This response to the poorly constructed concrete is characterized by a shift to a higher dominant return frequency at the location of the deteriorated concrete within the specimen. The deteriorated concrete for Specimen PC2 was created using a poorly consolidated concrete mixture. From ROC analysis, one can see that the impact-echo method had an accuracy of 0.917 and a TPR value of 0.844, showing that the cast-in specimen was 84.4 percent detectable by impact-echo surveying, with only a few false-positives occurring, aside from points potentially influenced by edge effects. From these results, one may conclude that poorly consolidated concrete encased in regular strength concrete is detectable with impact-echo testing.

4.4 EVALUATION OF NDT METHODS USED

As a secondary objective of this research, the three NDT methods outlined in this report were evaluated, with advantages and disadvantages being determined. Of the three NDT methods evaluated in this report, the impact-echo method is the only method designed to assess all types of defects occurring within concrete bridge decks. Therefore, it was the only method of the three used to test all types of defects. The half-cell potential method and surface resistivity method were designed to detect corrosion activity and therefore were only used to survey the two corrosion specimens. This prohibited direct comparison of each method's ability to detect all

types of defects. Therefore, the three methods were individually evaluated, but were not ranked in comparison with the others.

Five performance measures were used to assess the technologies: accuracy, precision, ease of use, speed of testing, and cost of testing. These performance measures, presented in Gucunski, et al. (2013) were selected because they encompass the main concerns of the selection of a NDT method or technology for the condition assessment of bridge decks.

4.4.1 Impact Echo Method

Through research of the impact-echo method and use of the Olson Instruments Impact-Echo Head, the following advantages and disadvantages were determined, as summarized in Table 4-14.

Table 4-14: Advantages and disadvantages of the impact echo method

Impact Echo Method	
Advantages	**Disadvantages**
Effective for detecting delaminations, as well as honeycombs and voids; moderately effective at detecting cracks and deterioration	Cannot detect corrosion activity, only damage resulting from corrosion
Accuracy: • Able to detect localized delaminations and defects • Able to detect early delaminations	**Ease of use**: • Moderate to high experience needed for both data collection and analysis
Precision: • Method and results are repeatable in different environments and with different operators	**Cost**: • Traffic control required • Expensive equipment
Speed (For Olson Sonic Surface Scanner): • Able to scan at a rate up to 20,000 points per hour	**Speed** (For Olson IE Head): • Able to scan between 50-200 points per hour, depending on user experience

Based on the findings of this project, the impact-echo method was the most effective NDT method of those evaluated. The impact-echo method proved to be very accurate in locating delaminated areas, as well as deteriorated and poorly constructed regions. Defective regions were accurately differentiated and extremities of the defective regions were able to be found. Additionally, the impact-echo method results are repeatable in different environments and with different operators; quantitative thickness results may change if the environmental fluctuations cause a change in wave speed within the concrete, but comparison of frequency results, as

performed in this report, still allow for the detection and location of defects. Additionally, as supported by research documented in the literature review, the impact-echo method is not affected by the presence of reinforcing steel within the concrete.

Unfortunately, the impact-echo method does not detect early-age corrosion activity within concrete, but only damage resulting from corrosion activity (i.e. delaminations). At a minimum, moderate experience is necessary for both data collection and analysis. Additionally, the accuracy and precision of the impact-echo method make it be quite costly. Traffic control is required for testing and the equipment is rather expensive. Also, testing of Specimens DL5 and DL6 proved that delaminations with dimensions smaller than the testing spacing between testing points may go undetected using the impact-echo method. Additionally, the impact-echo method does not perform well on rough concrete surfaces. For most accurate results, the test surface should be relatively smooth and free of debris so that a solid impact is generated at the concrete surface, and the receiver is adequately coupled to the concrete.

The speed at which the impact-echo method can be performed depends on the equipment used when testing. The IE Head from Olson Instruments, which was used by the research team in the laboratory, is able to scan between 50 and 200 points per hour, depending on user experience. Conversely, the Sonic Surface Scanner, another option for impact-echo testing from Olson Engineering, is able to scan at a rate up to 20,000 points per hour (Olson Engineering n.d.). Equipment that allows the user to scan at a higher rate is typically more expensive, though this extra expense might be justified, considering the cost of traffic control.

4.4.2 Half-Cell Potential Method

Through research of the half-cell potential method and use of the Proceq Profometer corrosion wheel electrode, the following advantages and disadvantages were determined, as summarized in Table 4-15.

Table 4-15: Advantages and disadvantages of the half-cell potential method

Half-Cell Potential Method	
Advantages	**Disadvantages**
Highly effective for detecting corrosion activity	Cannot detect delaminations, voids, cracks or deterioration
Accuracy: • Able to detect localized regions of corrosion • Able to detect early corrosion activity • Able to quantify different levels of corrosion activity	**Ease of use**: • Moderate experience needed for both data collection and analysis • Requires solid connection to reinforcing steel
Precision: • Method and results are repeatable in some different environments and with different operators	**Cost**: • Traffic control required • Expensive equipment
Speed (For Proceq Corrosion Wheel): • Able to collect and analyze data at a favorable rate	**Speed** (For traditional method): Rate of data collection and analysis is not favorable

The half-cell potential method allows for the detection of corrosion activity within reinforced-concrete. It is able to detect localized regions of corrosion and is able to measure or quantify different levels of corrosion. The half-cell potential method provides results that are repeatable between different operators, though tests in different environments may vary as ambient temperature, concrete moisture content, and resistivity vary.

Because the half-cell potential method was developed to electrochemically test corrosion activity within reinforced-concrete, it cannot detect delaminations, voids, cracks, nor deteriorated regions. Moderate experience is needed for both data collection and analysis. Additionally, connection to the reinforcing steel is required, which makes the half-cell potential method more difficult and costly. Traffic control is required for half-cell potential testing of a bridge deck, and advanced testing equipment is expensive.

By using the Proceq Corrosion Wheel, which was used by the research team in the laboratory, data is able to be collected and analyzed at a favorable rate. The traditional method of half-cell potential testing, which utilizes a voltmeter and a copper-copper sulfate half-cell probe, is cheaper than rapid testing equipment but is limited to point-by-point scanning and therefore is very time-inefficient. Proceq also offers a four-wheel electrode for half-cell potential

testing, which would allow the operator to scan at a rate four times greater than the single-wheel unit.

4.4.3 Surface Resistivity Method

Through research of the surface resistivity method and use of the Proceq Resipod, the following advantages and disadvantages were determined, as summarized in Table 4-16.

Table 4-16: Advantages and disadvantages of the surface resistivity method

Surface Resistivity Method	
Advantages	**Disadvantages**
Effective for detecting the rate of corrosion activity	Cannot detect delaminations, voids, cracks or deterioration; only detects probability of corrosion based on corrosion rate
Accuracy: • Able to detect localized regions of corrosion • Able to detect early corrosion activity	**Ease of use**: • Moderate experience needed for both data collection and analysis • Not recommended for testing over reinforcement (need to know steel locations)
Precision: • Method and results are repeatable in some different environments and with different operators	**Cost**: • Moderately priced equipment • Requires traffic control
	Speed: • Data collection at a rate around 150 points per hour

The surface resistivity method is effective at detecting the rate of corrosion activity within reinforced-concrete. It is able to detect localized regions of corrosion, as well as early corrosion activity. Results are repeatable between different operators. Environmental conditions, such as temperature and concrete moisture content can affect testing results, but effects of aforementioned conditions have been explored by other researchers and are well documented.

The surface resistivity method is unable to detect delaminations, voids, cracks, or deterioration; the method is only useful for detecting the probability of corrosion activity by measuring the rate at which corrosion could occur. Moderate experience is needed for both data collection and analysis. Testing should not be performed over reinforcing steel, which means

that the precise location of reinforcing steel within the bridge deck must be known. Testing equipment is moderately priced, but testing of a bridge deck requires traffic control. The speed at which the half-cell potential method can be performed may vary between operators, but the research team found data collection to occur at a rate of approximately 150 points per hour.

4.5 EVALUATION OF METHODS USED TO CREATE DEFECTS IN LABORATORY SPECIMENS

As a secondary objective of this research project, the various methods for constructing defects (e.g. voids, delaminations, cracks, corrosion, and deterioration) in a controlled manner were evaluated with consideration being given to both detectability and ability to replicate the defect in a full-scale testing site. The following subsections offer a discussion of successful methods used to create defects.

4.5.1 Void Specimens

To create voids in the laboratory specimens, water-filled and clay-filled balloons ranging from ½ in. to 2½ in. in diameter were placed within the specimens at both the top and bottom mats of reinforcing steel. The impact-echo method did not respond well to the presence of the voids, as it struggled to accurately determine the location both the water-filled and clay-filled balloons. Cores taken from the void specimens showed that both water-filled and clay filled balloons successfully created voids within the reinforced-concrete slabs. Therefore, the research team concluded that larger water-filled and clay-filled balloons would be used to simulate voids in the full-scale testing site.

4.5.2 Delaminated Specimens

To create delaminations in the laboratory specimens, plastic and foam sheets of varying thickness, plan dimension and unbonded fraction, as well as layers of sand and oil, were placed within the specimens at both the top and bottom mats of reinforcing steel. The impact-echo method successfully located plastic and foam sheets as thin as 10 mil and with plan dimensions as small as 4 × 8 in., with a potential to locate sheets with smaller plan dimensions using a smaller spacing between test points. Additionally, plastic sheets with unbonded fractions as low as 50 percent were detectable with the impact-echo method. The impact-echo method also detected the presence of sand and oil layers within the specimens, though the layers placed in

laboratory specimens proved to be too thin in some locations. Therefore, the research team concluded that thin plastic sheets with large plan areas, as well as thicker layers of sand and oil, should be used to simulate delaminated areas in the full-scale testing site.

4.5.3 Cracking Specimen

To create vertical cracks in the laboratory specimens, plastic sheets, which had varying thickness and depth, and a vertical grease layer were placed within a specimen. The impact-echo method was unsuccessful at locating or characterizing any of the "cracks" placed within the specimen. Further research is necessary to determine if the methods used are accurate or inadequate representation of actual cracking under inspection of other NDT methods. Therefore, the research team concluded that no simulated vertical cracks were to be used in the full-scale testing site.

4.5.4 Corrosion Specimens

To induce corrosion and corrosion related deterioration within the laboratory specimens, accelerated corrosion techniques were implemented on the slabs. Accelerated corrosion techniques consisted of ponding the specimens with 3 percent sodium chloride solution and applying current to the reinforcing steel by way of a 12 V battery. Batteries were used because these techniques would later be used to induce corrosion at the full-scale testing site. The impact-echo method, as well as the half-cell potential method and the surface resistivity method, successfully located regions of corrosion and corrosion-induced delaminations within the regions to which accelerated corrosion techniques were applied. Cores taken from the two corrosion specimens show a moderate amount of corrosion activity and corrosion induced delaminations within "Zone 2" of each specimen, and a severe amount of corrosion activity and deterioration within "Zone 3" of each specimen. Therefore, the research team concluded that ponding with 3 percent sodium chloride solution and applying current to reinforcing steel would be used to accelerate corrosion and to produce corrosion-induced delaminations and deterioration at the full-scale testing site.

4.5.5 Deteriorated Specimens

To create deterioration within the laboratory specimens, smaller specimens were cast into the full specimens. These small specimens were cast using concrete mixtures having high

entrained air content, low paste content, and varied dosages of polypropylene anti-cracking fibers. The impact-echo method successfully located the regions of high entrained air content and low paste content, but struggled to accurately characterize the regions containing anti-cracking fibers. Therefore, the research team concluded that small, cast-in specimens of high entrained air content and low paste content would be used to simulate deteriorated regions in the full-scale testing site.

4.5.6 Poor Construction

To mimic poor construction practices within the laboratory specimens, smaller specimens were cast into the full specimens. These small specimens were cast using concrete mixtures having low strength and high entrapped air content. The impact-echo method successfully located both the regions of low strength and high entrapped air content. Therefore, the research team concluded that small, cast-in specimens of low strength concrete as well as high entrapped air concrete would be used to simulate regions of poor construction in the full-scale testing site.

4.6 SUMMARY OF RESULTS

After analysis and inspection of all nondestructive testing results and cores taken from the laboratory specimens, the following table, Table 4-17, was created to summarize the most effective methods for replicating each type of defect within a reinforced-concrete bridge deck.

Table 4-17: Effective methods for creating defects in reinforced-concrete bridge decks

Defect Type	Effective Method(s) for Replication
Voids	• Balloons filled with clay or water
Delaminations	• Plastic or foam sheets, as thin as 10 mil • Sand and/or oil layer at a cold joint
Corrosion	• Current applied to electrically isolated bars ponded in sodium chloride solution
Cracking	• No conclusion
Deterioration	• Cast-in specimen with a high air content, created by adding a high volume of air entraining admixture during the mixing process
Poor Construction	• Cast-in, honeycombed specimen, created by using mixture proportions with low paste content • Cast-in, low strength specimen, created by using a concrete mixture with a high water-to-cement ratio

CHAPTER 5

DESIGN AND CONSTRUCTION OF FULL-SCALE BRIDGE DECK NDT SITE

5.1 INTRODUCTION

After consideration of the results obtained from laboratory testing and evaluation of methods used to create artificial defects, as outlined in the previous chapter, a full-scale bridge deck NDT site was designed and constructed in order to accomplish the primary objective of the work documented in this thesis. The design of the full-scale bridge deck NDT site ("the NDT bridge") is detailed in Section 5.2. After design of the bridge was completed, construction was performed by the research team, as outlined in Section 5.3. Chapter 5 concludes with Section 5.4, where an as-built layout of the bridge deck NDT site is presented, which summarizes the location and type of all defects built into the bridge deck.

5.2 DESIGN OF FULL-SCALE BRIDGE DECK NDT SITE

Upon the completion of laboratory testing and consideration of the effective methods for replicating defects within reinforced-concrete bridge decks, the research team began designing the NDT bridge. It was preliminarily concluded that the NDT bridge should have a bridge deck with 15 × 30 ft of clear area on the slab surface for placement of defects and for subsequent NDT testing. It was also decided that the NDT bridge should be able to be accessed from one side by pickup truck so that ALDOT personnel could test the effectiveness of trailer-mounted NDT equipment. With these criteria in mind, the design of the NDT bridge took place as described in the following subsections.

5.2.1 Site Selection

The site selected for construction of the NDT bridge was the Spring Villa National Geotechnical Experimentation Site (NGES), which is a tract of land adjacent to the National Center for Asphalt Technology in Opelika, AL. The location of the selected site is shown in Figure 5-1. A map of the Spring Villa NGES Test Site is shown in Figure 5-2.

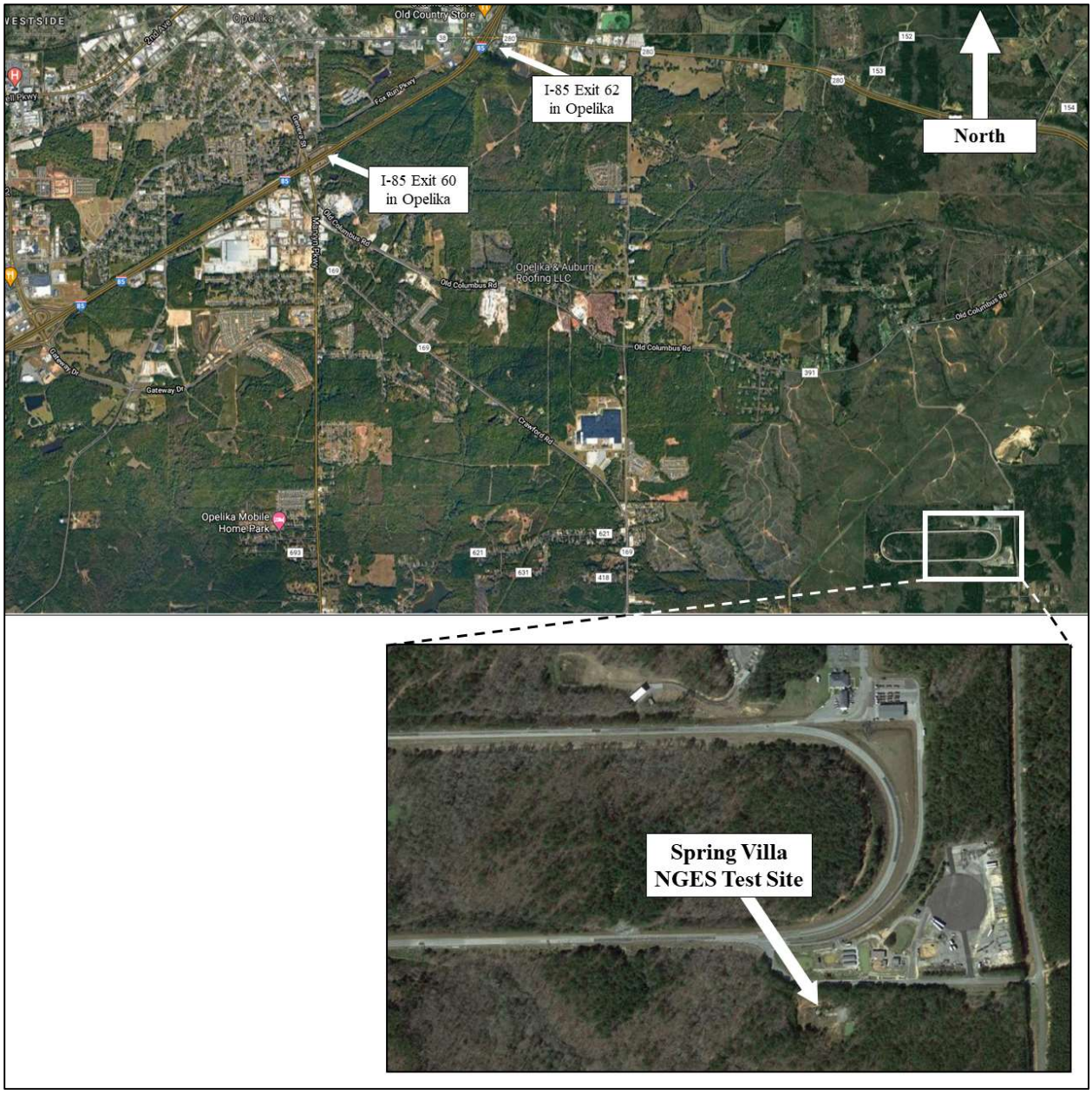

Figure 5-1: Map showing location of selected site (Google Maps 2021)

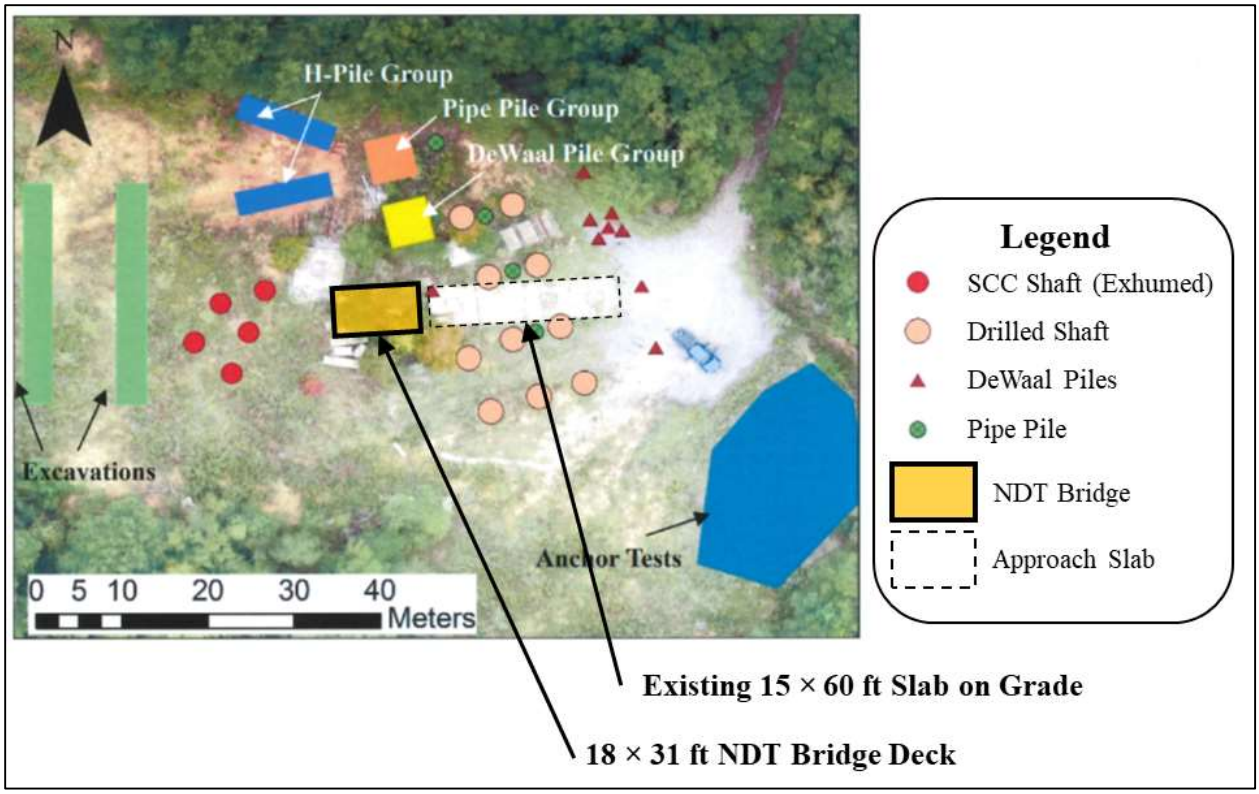

Figure 5-2: Map of Spring Villa NGES, including proposed location of the NDT bridge

The Spring Villa NGES Test Site was selected because it provided a location accessible to Auburn University employees, as well as ALDOT personnel, and had ample space for the construction of the NDT bridge. The location of the NDT bridge, which is notated in Figure 5-2, was selected because it provided a slightly sloped topography with minimal interference from existing research structures at the site. Since parts of the deck were to contain defective concrete, it was also a criteria that the deck not be accessible to any public or truck traffic. Additionally, the existing 15 × 60 ft slab on grade, which is also notated in Figure 5-2, provided an access drive to the proposed NDT bridge. The NDT bridge was designed and constructed spanning east to west. For the purposes of this report, the easternmost side of the bridge will be referred to as the "East end" and the westernmost end of the bridge will be referred to as the "West end".

5.2.2 Design of Structural Elements

After the site was selected and the location of the NDT bridge was finalized, the research team began the structural design of the bridge components. To provide adequate bridge deck area for defect placement and testing, it was determined that the overall plan dimensions of the

bridge deck would be 18 × 31 ft. For construction simplicity, and because span length was moderate, the NDT bridge was designed as a single span structure. Four girders, spaced at 5 ft 8 in. on center, supported the bridge deck. The structure was designed such that the bridge deck surface was sloped at one percent grade in order to promote shedding of water. The following subsections detail the design process. All reinforced-concrete elements were designed according to AASHTO LRFD and ACI 318-14, Building Code Requirements for Structural Concrete. All reinforced-concrete elements were designed to contain ASTM Grade 60 reinforcing steel.

5.2.2.1 Foundation Design

With the selected site being a National Geotechnical Experimentation Site, a report on the site characterization of the Spring Villa NGES Test Site was available to the research team (Vinson and Brown 1997). This report described the in-situ soil as residual soils ranging from sand silt to silty sand (Vinson and Brown 1997). Relevant soil characteristics are shown in Table 5-1.

Table 5-1: Soil characteristics for the Spring Villa NGES Test Site (Adapted from Vinson and Brown 1997)

Internal Shear Strength	φ	31°
Cohesion Value	c	355.1
Average Wet Unit Weight of Soil Under Footing	γ_{wet}	117.2 pcf
Average Dry Unit Weight of Soil Under Footing	γ_{dry}	85.6 pcf

With the above soil characteristics, and with geometric constraints of the preliminary design, the research team decided to use 2 ft thick, 22 × 4 ft cast-in-place spread footings, with a specified design strength of 4000 psi, to support the girders at each end of the NDT bridge. Allowable bearing capacity of the in-situ soil was determined using Meyerhoff bearing capacity equations. Using the final design loads, which were determined at the end of the design process and checked against the initial footing geometry, the factors of safety with respect to the applied bearing stress for the East and West footings were 21.1 and 22.3, respectively.

Shear strength and flexural strength, both in elevation and section view, were considered during the reinforced-concrete design of the footings. It was determined that 6 No. 7 steel bars, placed at both the top and bottom of the footing, would provide flexural reinforcement along the full width of the NDT bridge, while No. 7 closed rectangular "stirrups", spaced at 7 in. on center, would provide flexural reinforcement in the 4 ft dimension of the footings. Design drawings of the footing reinforcement can be found in Appendix B.

The research team also designed a retaining wall to be constructed on the easternmost side of the East footing to allow for backfill and construction of an approach slab connecting the existing slab to the NDT bridge. This retaining wall, which measured 22 ft long, 1 ft thick, and 2 ft 8.25 in. tall, was designed with reinforcement anchorage into the footing. Design loads on the retaining wall consisted of active earth pressure resulting from backfill soil, approach slab, and pickup truck weight. The water table was well below the level of the footing and therefore was not considered. Using ACI 318-14, the research team determined that the retaining wall would have flexural reinforcement consisting of No. 5 steel bars spaced at 7 in. on center, with straight No. 5 steel bars for shrinkage and temperature control. Design drawings of the retaining wall reinforcement can be found in Appendix B.

5.2.2.2 Bridge Girder Design

After considering constructability, it was decided that the girders for the NDT bridge would be reinforced-concrete girders, cast with a concrete mixture having a specified design strength of 4000 psi. Girders were sized at 12 in. wide by 24 in. deep. When designing the girders for the NDT bridge, a live load of 9000 lb was applied to the bridge. This 9000 lb load served to represent the weight of a pickup truck and trailer used by ALDOT personnel in testing trailer-mounted equipment. A factor of 1.2 was applied to the dead load of the structure, and a factor of 1.6 was applied to the pickup truck live load, in accordance with ACI 318-14 Equation 5.3.1b. Structural analysis of the girders yielded the design loads shown in Table 5-2. Torsion at the exterior girders was considered in the design process but was able to be neglected.

Table 5-2: Factored loads for design of the NDT bridge girders

Factored Moment	M_u	221.5	kip-ft
Factored Shear	V_u	22.3	kips

Considering the applied loading, it was determined that all four girders would have flexural reinforcement consisting of three No. 9 steel bars at the bottom of the girder and shear reinforcement consisting of No. 3 rectangular closed stirrups, spaced at 10 in. on center. The superstructure of the NDT bridge was designed as a non-composite structure, and therefore vertical girder reinforcing steel was not designed to be anchored into the bridge deck. Design drawings of the NDT bridge girders and reinforcement can be found in Appendix B.

5.2.2.3 Bridge Deck Design

The bridge deck was designed as a one-way slab spanning between the bridge girders. Chapter 9 of the AASHTO LRFD Bridge Design Specifications, as well as other bridge deck designs of ALDOT bridges, were used as a design guide for the bridge deck. The bridge deck was designed to be 7¼ in. thick. This value was selected because it is greater than the minimum required thickness prescribed by AASHTO, and is equal to the nominal width of 2×8 in. standard dimensional lumber. The U.S. Highway 331 bridge deck, which was researched by Schindler, et al. (2010), had a thickness of 7 in. with girders spaced at 5 ft 8 in. clear. Because the girder spacing in the NDT bridge was 4 ft 8 in., clear, it was determined that a 7¼ in. thick bridge deck was structurally adequate for the application.

Four layers of reinforcement were provided and were located as close to the outer surfaces as permitted by concrete cover requirements, as specified in Section 9.7.2.5 of AASHTO LRFD. No. 5, Grade 60 reinforcing steel bars, spaced at 8 in. center-to-center, were selected in the design of the bridge deck in order to meet requirements set forth by AASHTO LRFD. Additionally, this reinforcement spacing provided the NDT bridge with a greater ratio of reinforcing steel throughout the bridge deck cross section than the U.S. Highway 331 bridge, further ensuring its structural adequacy.

5.2.2.4 Safety Barrier System Design

The research team decided that a barrier system should be designed and constructed around the edge of the NDT bridge. This barrier would provide safety against falling from the bridge for any personnel testing the bridge deck, and would also prevent any light vehicles from driving off of the sides of the bridge. A steel cable barrier system was chosen over traditional concrete barrier system for ease of construction. ASCE 7-10 Section 4.5.3 gives the design loads

for a vehicle barrier system, a single 6000 lb horizontal load applied to the barrier system at a height between 1 ft 6 in. and 2 ft 3 in. above the deck surface to produce the maximum load effect (American Society of Civil Engineers 2010). Additionally, a document from the Florida Department of Transportation describes that AASHTO specifications require a standard pedestrian railing height be at least 42 in. and that the barrier system shall reject the passage of a 6 in. diameter sphere (Florida Department of Transportation 2013). Using the AISC 15 Steel Design Manual, the research team designed a barrier system comprised of HSS steel posts anchored to the bridge deck with holes spaced at 6 in. along the height of the post to allow steel cable to pass through the posts. Design drawings of the safety barrier system can be found in Appendix B.

5.2.3 Design and Location of Defects

Using the results found and conclusions drawn from the laboratory experimental program, which are summarized in Section 4.6, the research team designed a plan for the placement of defects within the full-scale bridge deck NDT site. It was determined that, in order to group defects and control crack propagation, the bridge deck would be divided into three sections by providing two expansion joints. The section nearest the approach end of the slab ("the East section"), measuring approximately 8 ft along the length of the bridge, would contain corrosion defects. The middle section ("the middle section"), measuring approximately 14 ft along the length of the bridge, would contain delaminations and voids. The furthest section from the approach end of the slab ("the West section"), measuring approximately 9 ft, would contain cast-in specimens simulating deteriorated concrete and poor construction practices. The preliminary outline of the defects that were placed within the bridge deck are shown in Figure 5-3. Table 5-3 contains the coordinate locations of the southeastern-most corner of each defect section, with the southeastern-most corner of the bridge deck taken as the coordinate origin, the x-axis along the transverse dimension of the bridge, and the y-coordinate along the longitudinal dimension of the bridge.

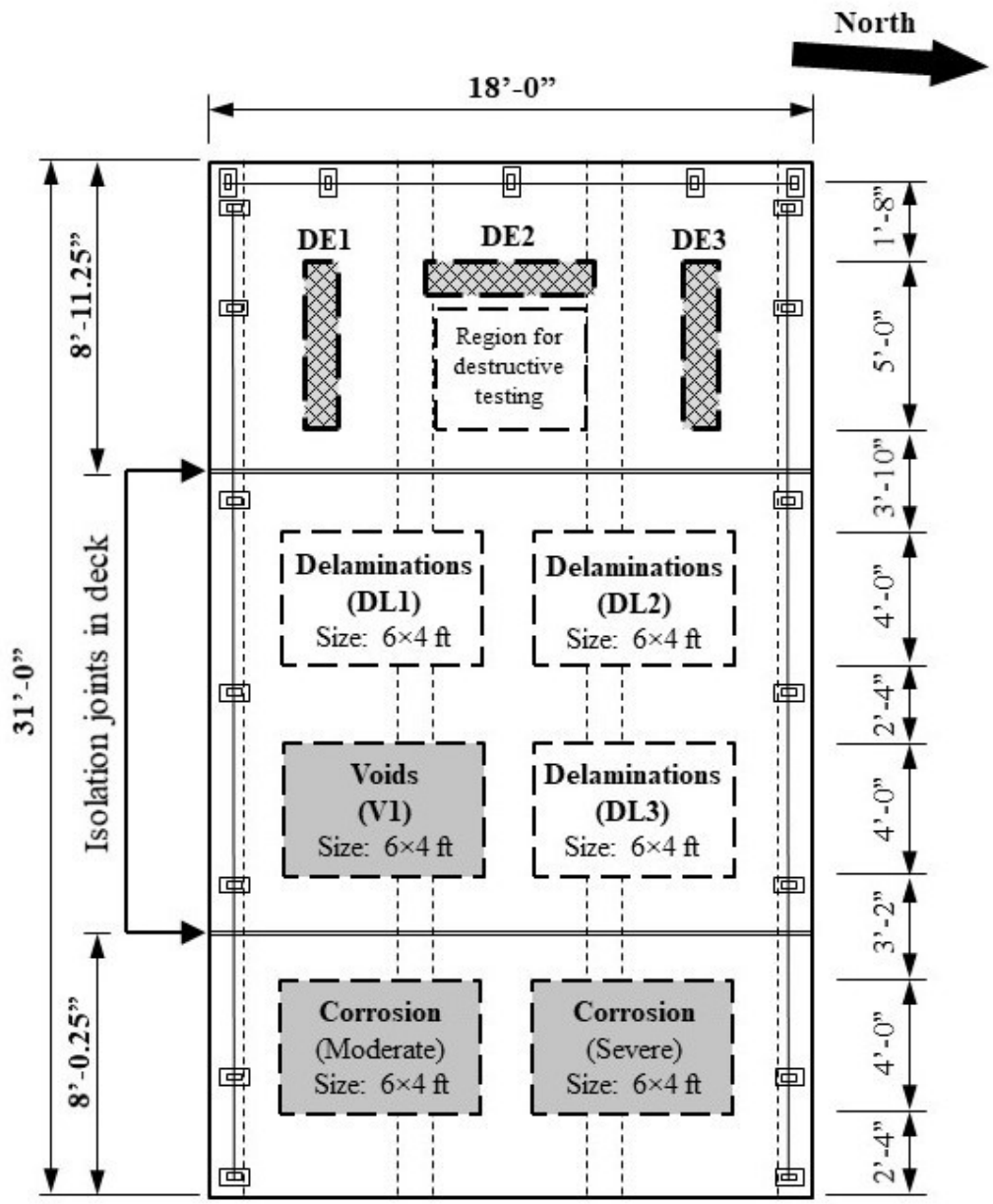

Figure 5-3: Preliminary design of defect layout for the NDT bridge (not to scale)

Table 5-3: Preliminary locations of defects in the NDT bridge deck

Defect Zone	Coordinate Location (x,y)
Corrosion - Moderate	(2 ft 4 in., 2 ft 4 in.)
Corrosion - Severe	(9 ft 8 in., 2 ft 4 in.)
V1	(2 ft 0 in., 9 ft 6-1/2 in.)
DL1	(2 ft 0 in., 15 ft 10-1/2 in.)
DL2	(10 ft 0 in., 15 ft 10-1/2 in.)
DL3	(10 ft 0 in., 9 ft 6-1/2 in.)
DE1	(3 ft 6 in., 23 ft 8-1/2 in.)
DE2	(6 ft 10 in., 24 ft 8-1/2 in.)
DE3	(13 ft 6 in., 23 ft 8-1/2 in.)

5.2.3.1 Voids

Following the conclusions drawn from the results of laboratory testing, the research team designed water-filled and clay-filled balloons to simulate voids within the NDT bridge. It was determined that 1 in., 2 in., and 3 in. diameter water-filled and clay-filled balloons would be placed at both the top and bottom mats of reinforcing steel within Zone V1 of the bridge deck, for a total of 12 voids. A layout of the voids within Zone V1, which lies within the middle section of the NDT bridge deck, can be found below in Figure 5-4.

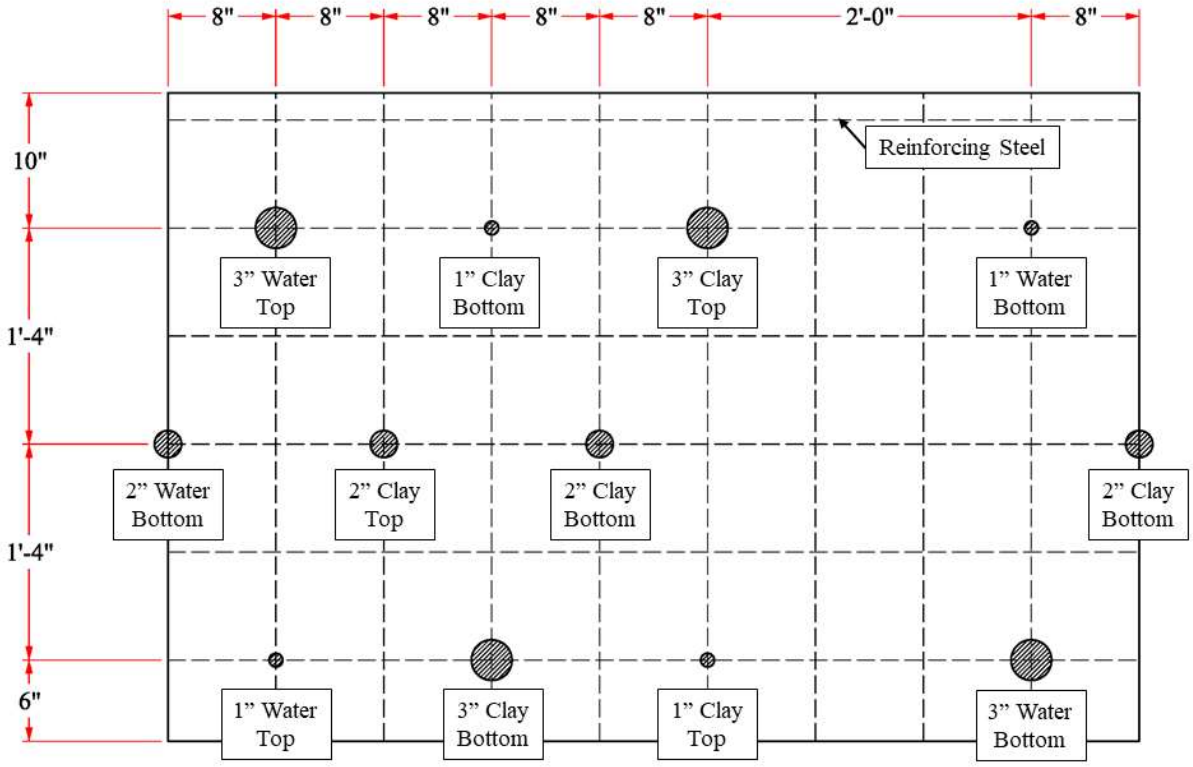

Figure 5-4: Layout of voids within Zone V1

5.2.3.2 Delaminations

Following the conclusions drawn from the results of laboratory testing, the research team designed artificial delaminations for use within the NDT bridge. The regions containing delaminations were divided into three zones within the middle section of the NDT bridge deck: DL1, DL2, and DL3. Zone DL1 contained four 10 mil plastic sheets with plan dimensions of 12 × 24 in., two placed at the top mat of reinforcement and two placed at the bottom reinforcement mat. Zone DL2 consisted of two 1 × 5 ft miniature specimens, similar to those cast in the laboratory specimens. The small slabs, which measured 4 in. thick, would be cast with a ¼ in. indention on the surface. This indention would serve to hold sand on one specimen and a combination of sand and oil on another specimen, allowing a uniform delamination layer to be created at the top of both specimens. The small slabs in Zone DL2 were designed to have the same concrete mixture proportions as the surrounding bridge deck. Zone DL3 contained four 30 mil plastic sheets with plan dimensions of 12 × 24 in., two placed at the top mat of reinforcement and two placed at the bottom reinforcement mat. Diagrams of Zones DL1, DL2 and DL3 can be found below in Figure 5-5, Figure 5-6, and Figure 5-7, respectively.

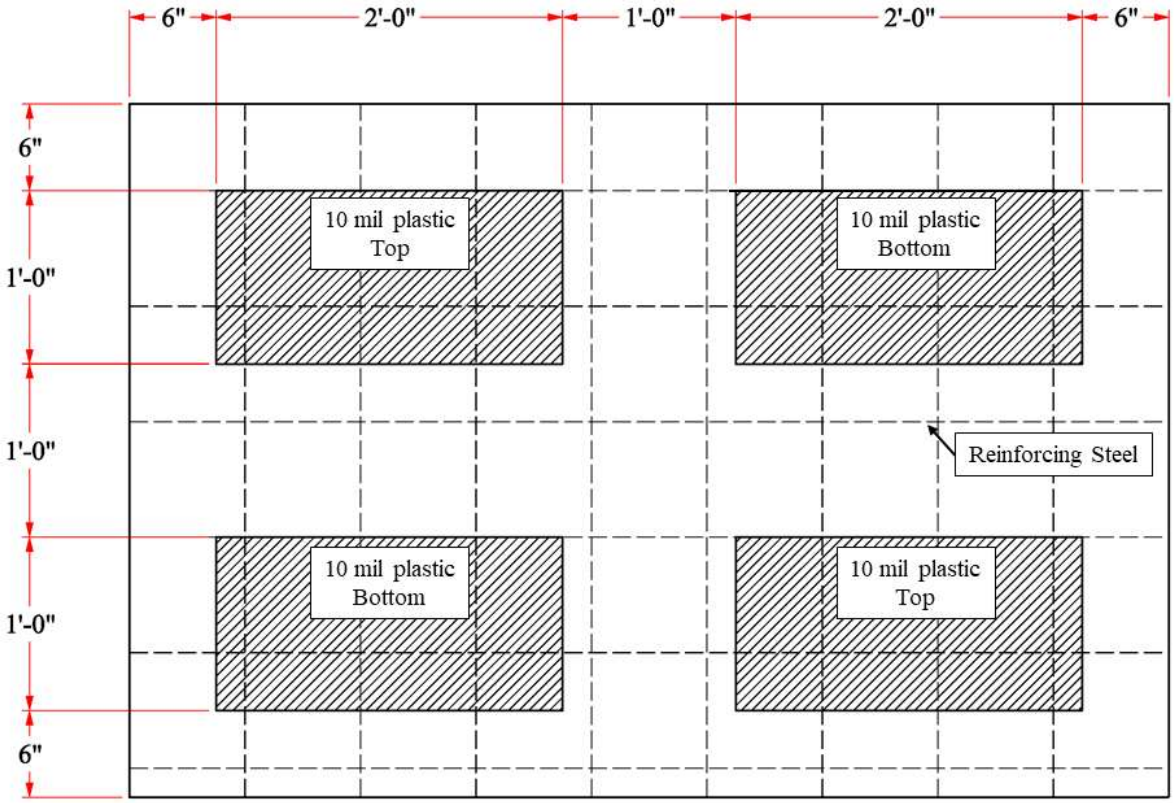

Figure 5-5: Layout of delaminations within Zone DL1

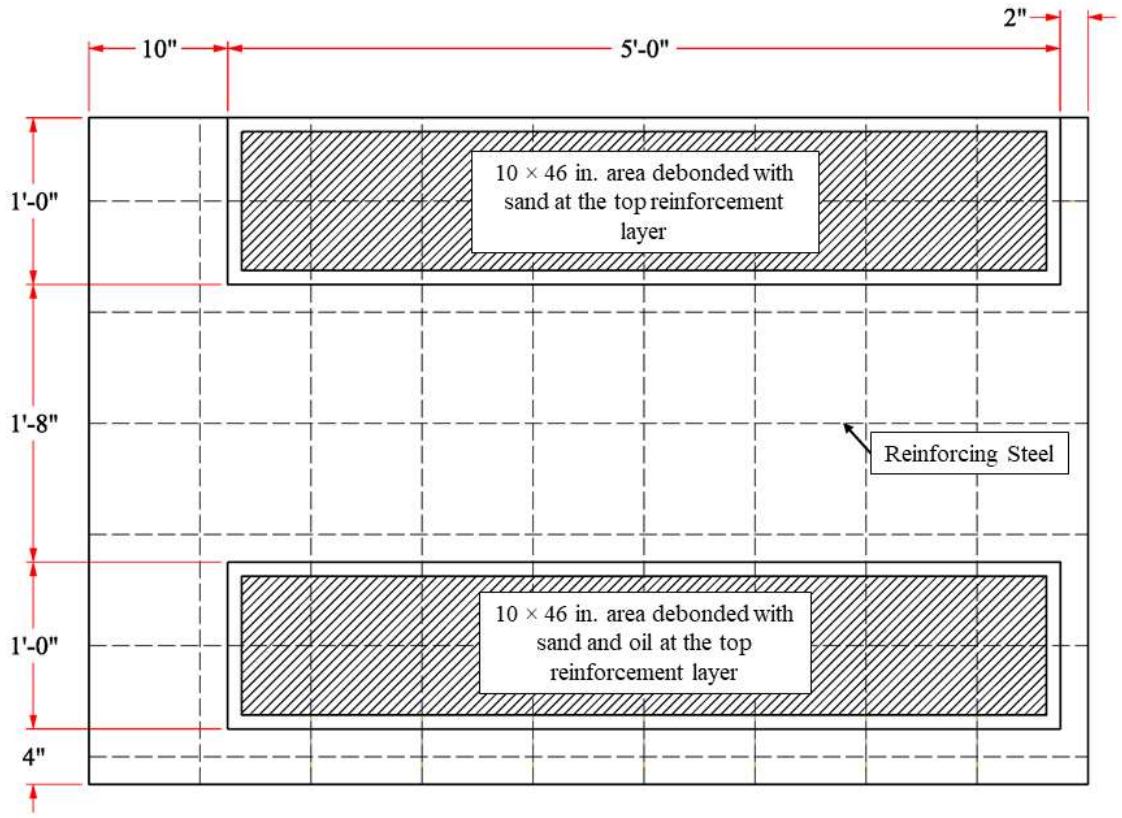

Figure 5-6: Layout of delaminations within Zone DL2

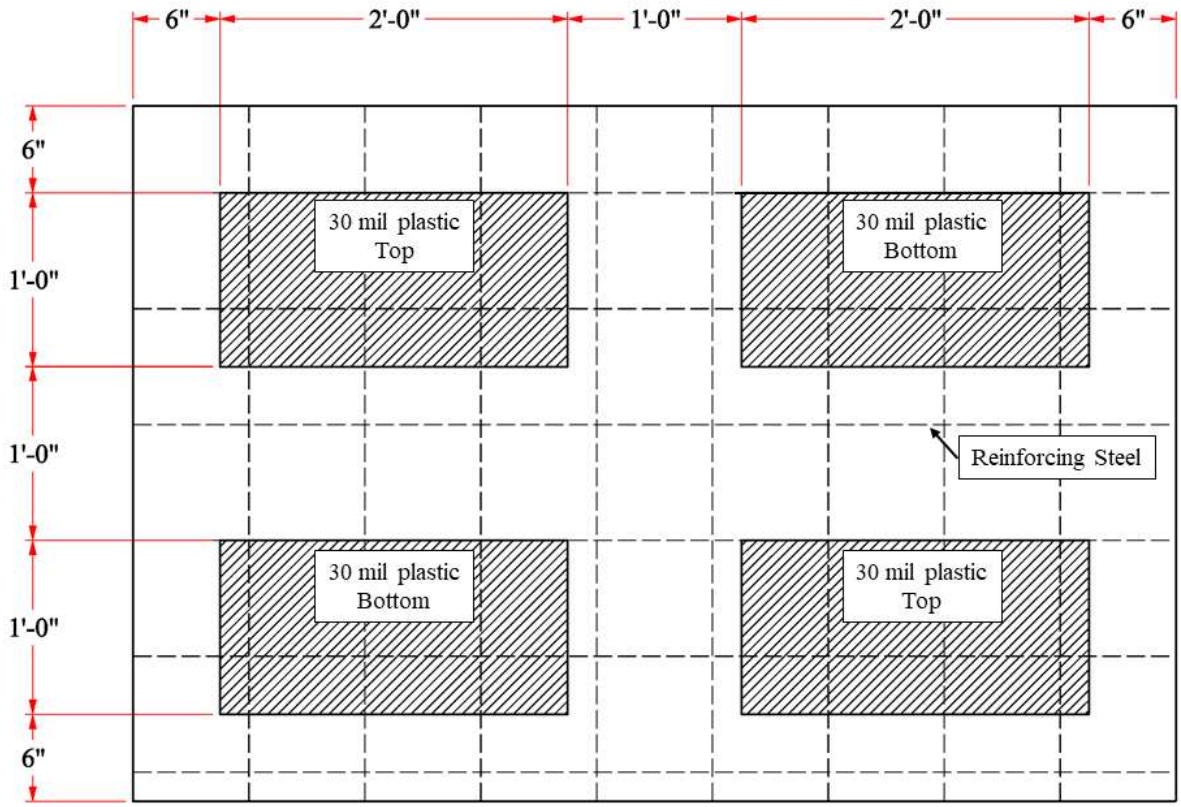

Figure 5-7: Layout of delaminations within Zone DL3

5.2.3.3 Corrosion

Following the conclusions drawn from the results of laboratory testing, the research team formulated a plan to induce corrosion within the NDT bridge. It was determined to induce corrosion into two separate, electrically isolated areas within the East section of the NDT bridge deck, as previously shown in Figure 5-3. Each area would measure 6 × 4 ft in plan dimension. The southernmost area was to have experienced a moderate amount of corrosion activity, while the northernmost area was to have undergone a severe amount of corrosion activity.

5.2.3.4 Deterioration and Poor Construction

Following the conclusions drawn from the results of laboratory testing, the research team designed a layout for simulated deterioration and poor construction methods within the NDT bridge. These regions of deterioration and poor construction were placed within the West section of the NDT bridge deck. Similar to the laboratory specimens, the regions of deterioration and poor construction were characterized by small, cast-in specimens of poor concrete,

measuring 1 × 5 ft in the plan dimension and having a thickness of 4 in., surrounded by regular bridge deck concrete. The layout of simulated these miniature specimens can be found above in Figure 5-3. The miniature specimen located at Zone DE1 was designed to have a concrete mixture with a very high dosage of air-entraining admixture in order to simulate a deteriorated concrete matrix. The miniature specimen located at Zone DE2 was designed to have a concrete mixture with a low paste content in order to simulate honeycombed concrete. The miniature specimen located at Zone DE3 was designed to have a concrete mixture with a high water-to-cement ratio in order to simulate a deteriorated concrete matrix (i.e. low strength). The mixture proportions for the concrete in Zones DE1, DE2, and DE3 can be found below in Table 5-4.

Table 5-4: Mixture proportions for Zones DE1, DE2, and DE3

Material	Proportions			
	Zone DE1	**Zone DE2**	**Zone DE3**	
#57 Limestone Coarse Aggregate	1,760	2,185	1,800	lb/yd^3
Fine Aggregate	1,192	1,285	1,183	lb/yd^3
Portland Cement	430	284	423	lb/yd^3
Class C Fly Ash	144	95	141	lb/yd^3
Water	254	168	367	lb/yd^3
Air Entraining Admixture	6.0	1.5	2	oz/yd^3
HRWR Admixture	25	25	-	oz/yd^3

5.3 CONSTRUCTION OF FULL-SCALE BRIDGE DECK NDT SITE

Once the design of the NDT bridge was complete, the research team was able to begin construction at the NGES Test Site. For cost efficiency and custom nature of this site, it was decided that construction of bridge components would be performed in-house, either in the laboratory or on-site at the Spring Villa National Geotechnical Experimentation Site (NGES). The following subsections describe the full construction process.

5.3.1 Site Preparation

The first step in the construction of the NDT bridge was to clear and prepare the selected location at the Spring Villa NGES test site. Vegetation at the site was very thick, as shown in

Figure 5-9. A compact excavator and a compact wheel loader, which are shown in Figure 5-8, were used to clear the vegetation debris from the site.

Figure 5-8: Equipment; a) compact excavator, b) compact wheel loader

Figure 5-9: Looking westward at the Spring Villa NGES test site prior to clearing

In addition to clearing vegetation, the research team also needed to remove existing structures that were in the selected footprint of the NDT bridge. These existing structures consisted of various lengths of 42 in. diameter extruded drilled shafts, in addition to a 15 × 15 ft slab on grade. A compact excavator and a compact wheel loader were also used to remove the existing structures from the site. The cleared property prior to commencement of construction is shown in Figure 5-10.

Figure 5-10: Standing alongside the existing approach slab, looking west-northwest at the cleared test site

After the property was cleared, the research team used tape measures and string line to lay out the locations of the bridge foundations. Soil was excavated from the locations of the bridge foundations with the compact excavator, and a laser level was used to determine the final grade for the cut.

5.3.2 Construction of Bridge Structure

After the construction site was fully prepped for foundation construction, the research team began constructing the structural elements for the NDT bridge. All formwork was designed and constructed using standard dimensional lumber and plywood sheets. Sabel Steel in Montgomery, AL supplied all reinforcing steel used in construction of the NDT bridge. Each time concrete was placed, a certified ACI technician tested the slump, air content and unit weight of the concrete mixture. Nine standard 6 in. diameter by 12 in. tall cylinders were cast for each

mixture and placement. All concrete was moist cured with wet burlap covered by plastic sheets for 7 days following casting. Compressive strength cylinders were moist cured until testing their compressive strength. The fresh properties of each placement, as well as the average 28-day strength of each placement, are presented with the construction process of their respective structural element, which are described in the following subsections.

5.3.2.1 Foundation Construction

In order to construct the foundations for the NDT bridge, the research team first fabricated the formwork for the foundations, using standard 2×6 in. dimensional lumber and ¾ in. plywood sheets. The plywood sheets were coated with polyurethane in order to prevent absorption of water during the concrete casting and curing process. Construction of the foundation formwork took place in the laboratory, as this provided a controlled environment for work to take place.

The reinforcing steel cages for the footings, as well as the retaining wall, were assembled and tied in the laboratory while hanging from wooden frames, as shown in Figure 5-11. Once assembly of formwork and reinforcing steel cages for the foundations were complete, the aforementioned elements were transported to the Spring Villa NGES test site with a pickup truck and trailer, as shown in Figure 5-12.

Figure 5-11: Tied reinforcing steel cage for the West-end footing

Figure 5-12: East-end footing and reinforcing steel cage loaded on the trailer

Once the foundation forms and reinforcing steel cages were transported to the construction site, the forms were placed at their respective locations with the compact excavator.

Tape measures were used to verify the accuracy of the formwork locations, and the laser level was used to verify the top of foundation grade. Then, whalers made of 2 × 4 in. dimensional lumber were attached to the sides of the formwork, after which pencil rod ties were placed through the formwork at 42 in. intervals. Once the pencil rod ties were secure, stakes and lateral braces cut from standard 2 × 4 in. dimensional lumber were attached to the formwork in order to secure the location of the formwork during concrete placement. Next, the reinforcing steel cages were placed into the formwork with the compact excavator and properly spaced from both the ground and the form walls using 3 in. plastic chairs. The foundation formwork and reinforcing steel in place can be seen in Figure 5-13 and Figure 5-14.

Figure 5-13: Foundation formwork and reinforcing steel in place

Figure 5-14: East-end foundation formwork and reinforcing steel

The concrete used to cast the NDT bridge foundations was delivered to the Spring Villa NGES test site via ready-mixed truck. The fresh concrete was discharged directly from the mixer's chute into the formwork. The placed concrete was then consolidated using vibratory consolidation techniques and leveled using a section of 2×4 in. dimensional lumber in a screeding process. Once the placed concrete had begun to set, the surface was finished smooth using steel hand trowels. An image of the foundations once casting was complete can be seen in Figure 5-15. The fresh properties of the foundation concrete can be found in Table 5-5. The concrete had an average 28-day compressive strength of 4300 psi for the East-end foundation and 4720 psi for the West end foundation. All strength data for the foundation concrete can be found in Appendix A.

Figure 5-15: Both foundations after casting was complete

Table 5-5: Fresh properties of the foundation concrete

	East-End Foundation	West-End Foundation
Slump (in.)	6.75	5.5
Air Content (%)	3.5	3.2
Unit Weight (pcf)	143.0	143.7
Temperature (ºF)	84	86

Once the moist-curing of the foundations was complete and formwork was removed from the West-end foundation, construction of the retaining wall began. Formwork construction for the retaining wall was performed on-site, using lumber from the casting of the West-end foundation. The formwork was modified for the additional height of the retaining wall, then set into place using the compact excavator. Location and final elevation grade of the retaining wall formwork were checked, after which that formwork was anchored to the in-place, East-end formwork. Braces cut from 2×4 in. dimensional lumber were put into place to secure lateral movement of the formwork, and whalers, also made of 2×4 in. dimensional lumber, were fastened to the sides of the formwork. Pencil rod ties were placed through the formwork at 42 in. intervals along the 22 ft dimension of the wall and secured to the whalers.

The concrete used to cast the retaining wall for the NDT bridge was also delivered to the Spring Villa NGES test site via ready mixed truck. The fresh concrete was discharged directly from the mixer's chute into the formwork. The placed concrete was then consolidated using vibratory consolidation techniques and leveled using section of 2×4 in. dimensional lumber in a screeding process. Once the placed concrete had begun to set, the surface was finished smooth using steel hand trowels. An image of the retaining wall once casting was complete can be seen in Figure 5-16. The fresh properties of the retaining wall concrete can be found in Table 5-6. The concrete had an average 28-day compressive strength of 3250 psi. All strength data for the retaining wall concrete can be found in Appendix A.

Figure 5-16: Retaining wall once casting was complete

Table 5-6: Fresh properties of the retaining wall concrete

Slump (in.)	7.0
Air Content (%)	1.9
Unit Weight (pcf)	144.12
Temperature (ºF)	78

5.3.2.2 Bridge Girder Construction

The full girder construction and casting process took place in the laboratory under controlled conditions. The construction and casting process took place in two phases, each phase consisting of two girders. The same formwork was used to cast both sets of girders.

In order to construct the girders for the NDT bridge, the research team first fabricated the formwork for the girders, using standard 2×6 in. dimensional lumber and ¾ in. plywood sheets. The plywood sheets were coated with polyurethane in order to prevent absorption of water during the concrete casting and curing process. The form walls were attached to a double layer of plywood sheets laid along the laboratory floor to create a flat, removable bottom to the formwork.

Once the girder formwork was constructed, the reinforcing steel cages for the girders were assembled and tied while hanging from wooden frames The fully tied reinforcing steel cages were then lifted using the overhead crane in the laboratory, and set into the formwork. Two inch plastic chairs were placed between the reinforcing steel and the formwork in order to provide adequate concrete cover. One and a quarter inch diameter, Schedule 40 steel pipes were cast into the width of the girders every 5 ft for later use in supporting the bridge deck formwork. One and an eighth inch diameter holes were drilled through the girder formwork at the intended location of each pipe insert, and 1-1/8 in. threaded rods inserted through the holes in order to secure the pipes in place. These threaded rods, combined with nuts and washers, also acted as ties that prevented the form walls from displacing laterally. Lifting anchors, shown in Figure 5-17, were cast into the top of the girders every 6.2 ft. These anchors, which each had a standard working load of 7,500 lb, served to allow the research team to safely lift the girders, both in the lab and at the NGES test site. Images of the girder formwork and reinforcing steel, as well as the lifting anchors, can be found in Figure 5-17 and Figure 5-18.

Figure 5-17: One concrete lifting anchor in place and ready for casting

Figure 5-18: Girder formwork and reinforcing steel prior to casting

The concrete used to cast the NDT bridge girders was delivered to the laboratory via ready-mixed truck. The fresh concrete was dispensed from the mixer's chute into a concrete

placement bucket, where it was then able be moved to the casting location in the laboratory by an overhead crane. The placed concrete was then consolidated using vibratory consolidation techniques and leveled using a section of 2×4 in. dimensional lumber in a screeding process. Once the placed concrete had begun to set, the surface was roughened using a concrete rake, in order to promote bonding to the bridge deck during its casting. Casting of the first pair of girders took place on August 14, 2020, while casting of the second pair of girders took place on August 21, 2020. An image of the girders on August 14 once casting was complete can be seen in Figure 5-19. The fresh properties of the girder concrete can be found in Table 5-7. The concrete had an average 28-day compressive strength of 5810 psi for the girders cast on August 14 and 5400 psi for the girders cast on August 21. All strength data for the foundation concrete can be found in Appendix A.

Figure 5-19: Two girders once casting was complete, prior to surface roughening

Table 5-7: Fresh properties of the girder concrete

	August 14 Casting	**August 21 Casting**
Slump (in.)	5.25	6.0
Air Content (%)	2.8	2.6
Unit Weight (pcf)	152.0	162.5
Temperature (ºF)	89	87

Three days after the girders were cast, they were removed from the formwork. All mechanisms that held the form walls together were released, and the girders were lifted out of the formwork by overhead crane in the laboratory. A W10×30 steel beam was used as a spreader beam to minimize flexural loads in the girder during the lifting process.

The girders were moved to the NGES test site once all forms were removed from the foundation and retaining wall. The research team individually hauled the girders to the site using a Class 4 gross vehicle weight rating (GVWR) truck and 32 ft gooseneck trailer. The overhead crane was used to load the girders onto the trailer and an off-road telescopic forklift, shown in Figure 5-20, was used to unload the girders at the site. An image of the research team unloading the girders at the construction site is shown in Figure 5-21.

Figure 5-20: The off-road telescopic forklift used by the research team

Figure 5-21: The research team unloading a girder at the NGES test site

The research team selected 70 durometer, 12 × 12 × 1 in. neoprene pads to serve as the bearing pads for the NDT bridge girders. After the bearing pads were placed, the research team

used the off-road telescopic forklift to set the girders in place, as shown in Figure 5-22. Special care was taken to ensure that the location of each girder was as close to its designed location as possible. Tape measures were used to verify the location of each girder. Images of all four girders set in place can be seen in Figure 5-23 and Figure 5-24.

Figure 5-22: Positioning a girder to set in place

Figure 5-23: Facing north, an elevation view of all girders set in place

Figure 5-24: Facing east-northeast, a view of all four girders set in place

5.3.2.3 Bridge Deck Construction

After setting the girders, the research team began constructing the bridge deck. The bridge deck was cast in two phases; the first phase consisted of the East and West sections of the bridge deck, while the second phase consisted of the middle section of the bridge deck.

The first step in constructing the bridge deck for the NDT bridge was to construct the formwork. In order to prevent extra, non-reinforcing steel in the bridge deck, 1-1/8 in. steel threaded rods, which were placed through the sleeves cast into the girders, were used to support the formwork system. Six 32 ft support beams, constructed by pairing 2×8 in. standard dimensional lumber boards, were placed on the threaded rods at the sides of each girder, excluding the two outside girder faces. Small, 3 in. sections of steel pipe were placed around the threaded rod at each bearing section to prevent the threads from cutting into the support beams. Nuts and washers were placed on each threaded rod to hold the support beams in place, as shown in Figure 5-25.

Figure 5-25: Paired 2×8 support beams bearing on the threaded rod unit

Next, joists, which were comprised of 2×6 in. standard dimensional lumber boards, were installed at 19.2 in. center-to-center spacing. These joists were secured at each end by Simpson Strong-Tie LUS26 joist hangers. Once the supporting framework was constructed, ¾ in. plywood sheets, coated with polyurethane, were placed on top of the framework, creating a

smooth finish on the underside of the bridge deck. The supporting framework and the plywood sheathing are shown in Figure 5-26 and Figure 5-27, respectively.

Figure 5-26: Framework of the bridge deck formwork

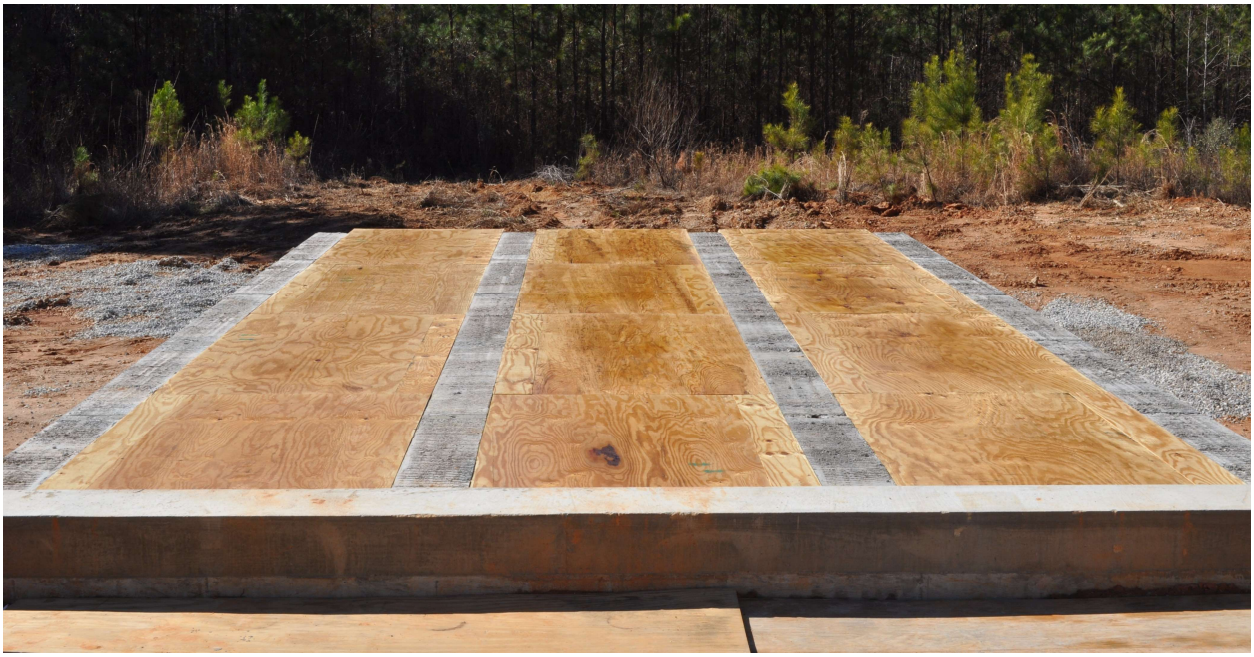

Figure 5-27: Bridge deck formwork with plywood sheathing installed

The sidewalls of the bridge deck formwork were constructed using standard 2×8 in. dimensional lumber. The walls were supported by built-up frames, which rested on the threaded rods. Triangular braces were installed at each supporting frame, as well as along the West-end of

the formwork, in order to hold the walls at an angle perpendicular to that of the slab plan dimension. Braces comprised of standard 2×4 in. dimensional lumber were also placed along the sides of the formwork to prevent lateral displacement between supports. Two bulkhead walls were installed in the transverse direction of the bridge in order to provide a smooth cold joint between the sections of the bridge. These bulkhead walls were in place for the casting of the East-end and West-end sections of the bridge deck and were removed prior to the casting of the middle section.

Reinforcing steel mats for the bridge deck were laid out and tied in place. Precast sections, where applicable, were positioned first, after which the remaining pieces of reinforcing steel were put into place and tied at their final location. Plastic chairs were used to support the both the top and bottom reinforcing steel mats and to ensure adequate cover for each. An image of the NDT bridge prior to the casting of the East-end and West-end sections can be found in Figure 5-28. An image of the NDT bridge prior to the casting of the middle section can be found in Figure 5-29.

Figure 5-28: Facing southwest, the NDT bridge prior to the casting of the East-end and West-end bridge deck sections

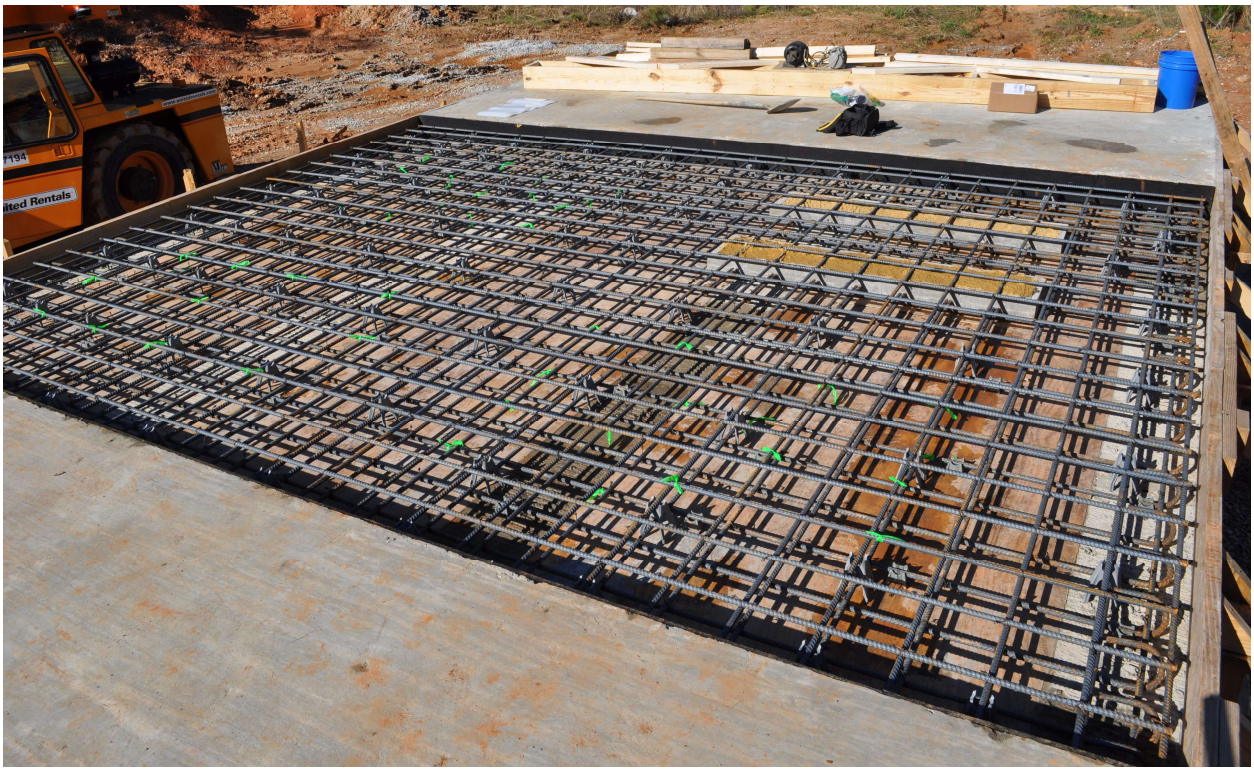

Figure 5-29: Facing west-southwest, the NDT bridge prior to the casting of the middle section

The bridge deck was cast on two different days. The East and West sections of the bridge deck were cast on March 9, 2021, and the middle section of the bridge deck was cast on March 29, 2021. The same process was used to cast all three sections. The concrete used to cast the NDT bridge deck was delivered to the NGES test site via ready-mixed truck. The fresh concrete was dispensed from the mixer's chute into a concrete placement bucket, where it was then able be moved to the casting location in the around the casting area by a 20 ton carry-deck crane. The concrete was placed into the formwork using the placement bucket, where the concrete was then consolidated using immersion vibrators. When casting the East and West sections, the research team used a 2×6 in. dimensional lumber board as a screed to level the surface of the concrete. When casting the middle section, which had a larger longitudinal dimension than the other sections, the research team constructed a vibratory screed, shown in Figure 5-30, to level the concrete surface. This vibratory screed, constructed with 2×8 in. dimensional lumber and an unbalanced electric motor, simultaneously consolidated and smoothed the concrete at the surface, allowing it to be moved more easily and creating a more consistent finish.

Figure 5-30: Vibratory screed used to level the middle section of the NDT bridge deck

Once the placed concrete had begun to set, the surface was finished smooth using steel hand trowels and a bull float. An image of the bridge deck, once casting of the middle section was complete, can be seen in Figure 5-31. The fresh properties of the bridge deck concrete can be found in

Table **5-8**. The concrete had an average 28-day compressive strength of 6610 psi for the East and West sections and 5960 psi for the middle section. All strength data for the bridge deck concrete can be found in Appendix A.

Figure 5-31: The NDT bridge deck after the middle section was cast

Table 5-8: Fresh properties of the bridge deck concrete

	West- and East-End Sections	Middle Section
Slump (in.)	3.75	8.5
Air Content (%)	3.5	4.0
Unit Weight (pcf)	Not recorded	Not recorded
Temperature (ºF)	76	66

Following the completion of the moist curing process, all formwork was removed from the NDT bridge. An image of the NDT bridge once all formwork was removed is shown in Figure 5-32.

Figure 5-32: The NDT bridge once the slab formwork was removed; plastic is covering the corrosion ponds

5.3.2.4 Safety Barrier System Construction

Davis Machine Works in Opelika, AL fabricated the steel barrier posts for the safety barrier system. The steel barrier posts were delivered to the laboratory, where they were stored until construction of the NDT bridge deck was complete. It was decided to postpone the

placement of the barrier rail system until an initial NDT survey of the bridge deck was completed, which will be completed after the submission of this report.

5.3.2.5 Approach Slab Construction

The approach slab was designed and constructed as a slab-on-grade. Construction of the approach slab that connects the existing slab to the NDT bridge deck took place after the construction of the NDT bridge was completed. First, 2×8 in. standard dimensional lumber was used to create side formwork for the approach slab, and stakes were used to secure the form boards in place. Next, reinforcing steel was tied into a reinforcement mat, with No. 5 bars spaced at 8 in. on center. The reinforcing steel mat was then placed into the formwork and set on 4 in. plastic chairs. Casting of the approach slab was postponed until corrosion of the NDT bridge deck was completed. Casting of the approach slab will occur after the submission of this report

5.3.3 Construction and Placement of Defects

The following subsections present and detail the construction of defects for use in the NDT bridge deck, as well as the placement of the defects within the bridge deck. These defects were constructed and placed prior to the casting of the bridge deck, though this section describing their construction and placement follows the section describing the bridge deck construction.

5.3.3.1 Voids

Voids were constructed using regular balloons filled with either water or clay. In order to fill the balloons with clay, the research team placed the opening of each balloon over a funnel, and slowly poured a clayey soil through the funnel and into the balloon until the balloon reached the desired diameter, which was measured with a tape measure. In order to fill the balloons with water, the research team placed the opening of each balloon over the end of a nozzle that was connected to a water hose. Water was injected into the balloon until the balloon reached the desired diameter, which was measured with a tape measure.

During the casting process of the middle section of the bridge deck, the voids were placed into their respective locations in the bridge deck. Fresh concrete was added in Zone V1 until it reached the middle of the bottom mat of reinforcing steel. Then, concrete was removed from

locations were voids were to be placed. Voids were inserted underneath the bottom and top reinforcing steel mats, where applicable, as shown in Figure 5-33, and secured to the reinforcing steel with steel wire, after which fresh concrete was packed around the voids by hand. After all voids were placed and positioned correctly, the remainder of the fresh concrete was carefully placed into the region in and round Zone V1. Care was taken to ensure that voids were not moved or damaged during the vibratory consolidation process.

Figure 5-33: Clay void in place below the top reinforcing steel mat

5.3.3.2 Delaminations

Delaminations in the NDT bridge were divided into three different zones: DL1, DL2, and DL3.

5.3.3.2.1 Zone DL1

Zone DL1 contained 10 mil plastic sheets that simulated delaminations. The research team cut four 12 × 24 in. sections, with 1 in. radius arcs in the corners, from a large sheet of 10 mil plastic, as shown in Figure 5-34.

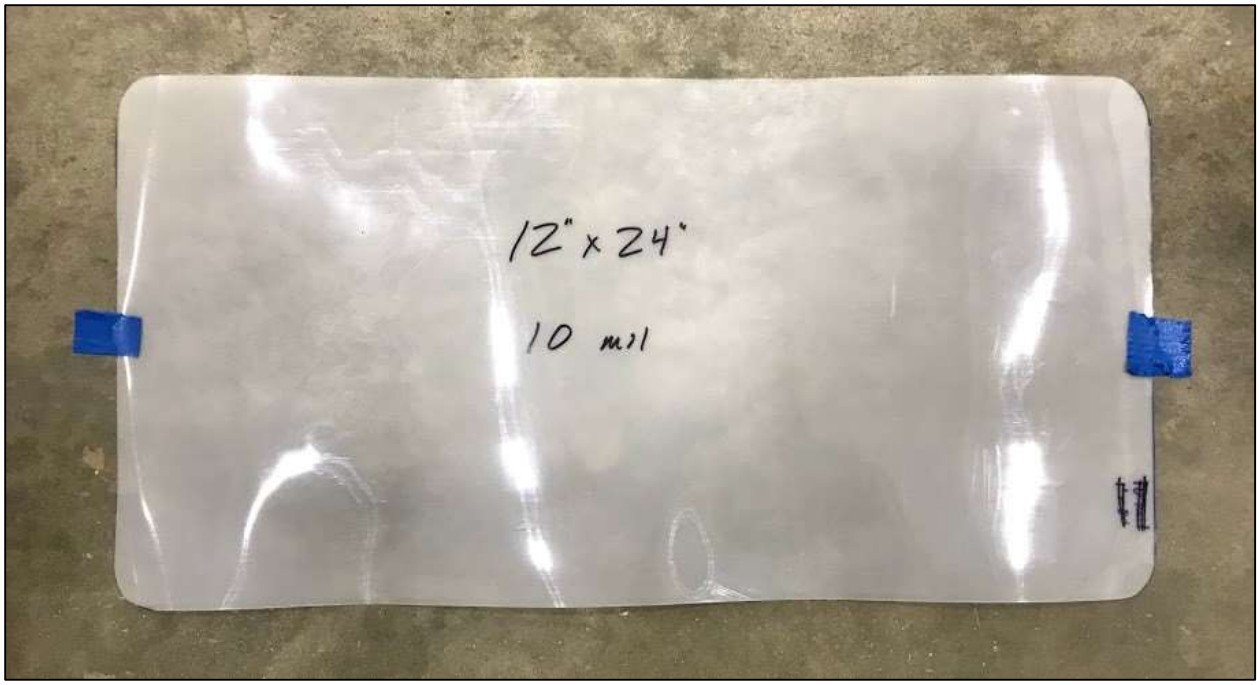

Figure 5-34: 10 mil, 12 × 24 in. plastic sheet

These sheets were placed into the middle section of the NDT bridge deck during the casting process. Fresh concrete was placed in Zone DL1 until it reached the middle of the bottom reinforcing steel mat. Two 10 mil plastic sheets were then placed in between the longitudinal and transverse steel bars that made up the bottom reinforcement mat. Fresh concrete was carefully placed above the plastic sheets and distributed throughout Zone DL1 until it reached the middle of the top reinforcing steel mat. Then, two additional 10 mil plastic sheets were placed in between the longitudinal and transverse steel bars that made up the top reinforcement mat. Once all four sheets were in place, the remainder of the fresh concrete was placed at and around Zone DL1. Care was taken to ensure that vibratory consolidation techniques did not cause damage or a change of location to the plastic sheets. An image of the a 10 mil plastic sheet being placed in Zone DL1 can be found in Figure 5-35.

Figure 5-35: Placing a 10 mil plastic sheet between the top reinforcing bars in Zone DL1

5.3.3.2.2 Zone DL2

Zone DL2 contained a sand layer, as well as a sand mixed with oil layer, to simulate delaminations. The first step in constructing the delaminations in Zone DL2 was to cast two 4 in. thick, 1 × 5 ft miniature slabs with reinforcing steel continuous through both slabs. The two-part forms used to cast the miniature slabs for the laboratory test specimens were used to cast these miniature slabs for the NDT bridge deck. These miniature slabs were cast with a concrete mixture that had mixture proportions identical to the mixture proportions for the NDT bridge deck. The encased concrete mixture proportions can be found in Table 5-9.

Table 5-9: Encased specimen mixture proportions for Zone DL2

Item	Proportions	
#57 Limestone Coarse Aggregate	1,900	lb/yd^3
Fine Aggregate	1,285	lb/yd^3
Portland Cement	465	lb/yd^3
Class C Fly Ash	155	lb/yd^3
Water	275	lb/yd^3
Air Entraining Admixture	1.5	oz/yd^3
HRWR Admixture	25	oz/yd^3

Mixture ingredients were individually batched according to the mixture proportions and mixed in the laboratory using the laboratory mixer. The concrete was then placed into the

formwork and consolidated. The fresh properties of the concrete mixtures used to cast the two specimens are shown in Table 5-10.

Table 5-10: Fresh concrete properties of encased specimen in Zone DL2

Slump (in.)	6.75
Air Content (%)	3.1
Unit Weight (pcf)	150.4
Temperature (ºF)	68

A 10 × 46 in. piece of ¼ in. plywood was pressed into the surface of the fresh concrete in order to create an indentation that would later hold sand during the bridge deck casting. The miniature specimens were moist cured for 7 days. The concrete used to cast the miniature slabs had an average 28-day compressive strength of 6140 psi. All strength data for the concrete in Zone DL2 can be found in Appendix A.

Once the bridge deck formwork was constructed, and the East-end and West-end sections were cast, the miniature slabs that made up Zone DL2 were positioned in their final location. After all reinforcing steel was put into place and prior to any concrete being placed into the middle section bridge deck formwork, both indentations in the miniature slabs were filled with a layer of sand. One layer of sand was moistened with form oil, in accordance with the design for Zone DL2. The layers of sand prior to the placement of fresh concrete are shown in Figure 5-36. Fresh concrete was placed into the region in and around Zone DL2. When the level of the concrete reached the top of the miniature slabs, the remainder of the concrete was placed into the region, and care was taken to ensure that the layer of sand was not disturbed by the placement or consolidation of the fresh concrete.

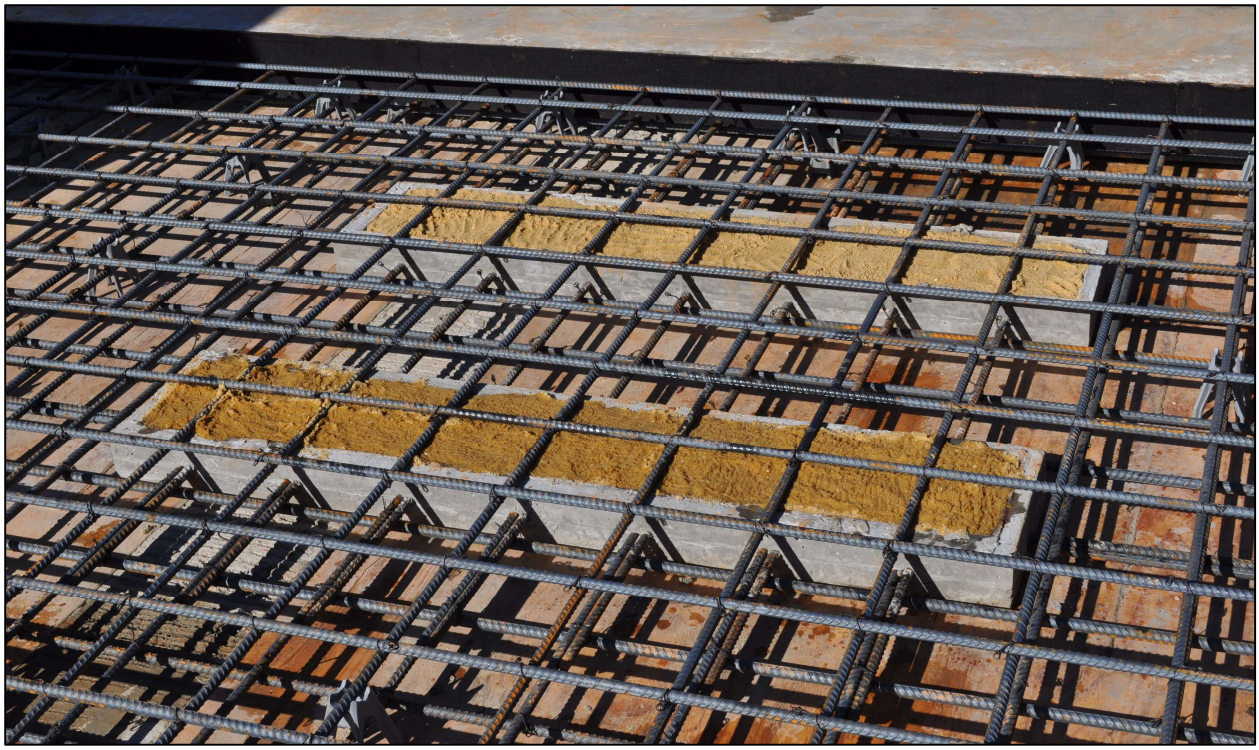

Figure 5-36: Sand layers in Zone DL2; sand with oil in foreground, sand in background

5.3.3.2.3 Zone DL3

Zone DL3 contained 30 mil plastic sheets that simulated delaminations. The research team cut four 12 × 24 in. sections, with 1 in. radius arcs in the corners, from a large sheet of 30 mil plastic, as shown in Figure 5-37.

Figure 5-37: 30 mil, 12 × 24 in. plastic sheet

These sheets were placed into the middle section of the NDT bridge deck during the casting process. Fresh concrete was placed in Zone DL3 until it reached the middle of the bottom reinforcing steel mat. Two 30 mil plastic sheets were then placed in between the longitudinal and transverse steel bars that made up the bottom reinforcement mat. Fresh concrete was carefully placed above the plastic sheets and distributed throughout Zone DL3 until it reached the middle of the top reinforcing steel mat. Then, two additional 30 mil plastic sheets were placed in between the longitudinal and transverse steel bars that made up the top reinforcement mat. Once all four sheets were in place, the remainder of the fresh concrete was placed at and around Zone DL3. Care was taken to ensure that vibratory consolidation techniques did not cause damage or a change of location of the plastic sheets. An image of the a 30 mil plastic sheet being placed in Zone DL3 can be found in Figure 5-38.

Figure 5-38: Placing a 30 mil plastic sheet between the bottom reinforcing bars in Zone DL3

5.3.3.3 Corrosion

The corrosion sections of the NDT bridge were constructed similarly to the laboratory test specimens. Two 4 × 6 ft sections of reinforcing steel mat were made discontinuous from the remainder of the top reinforcement mat in the East-end section, in accordance to the design of the corrosion sections. A ¼ in. gap was created between the steel bars of the 4 × 6 ft sections and the surrounding bars. A rubber-based compound was applied to the ends of all discontinuous steel bars in order to electrically isolate the sections from the remainder of the reinforcement mat, as shown in Figure 5-39.

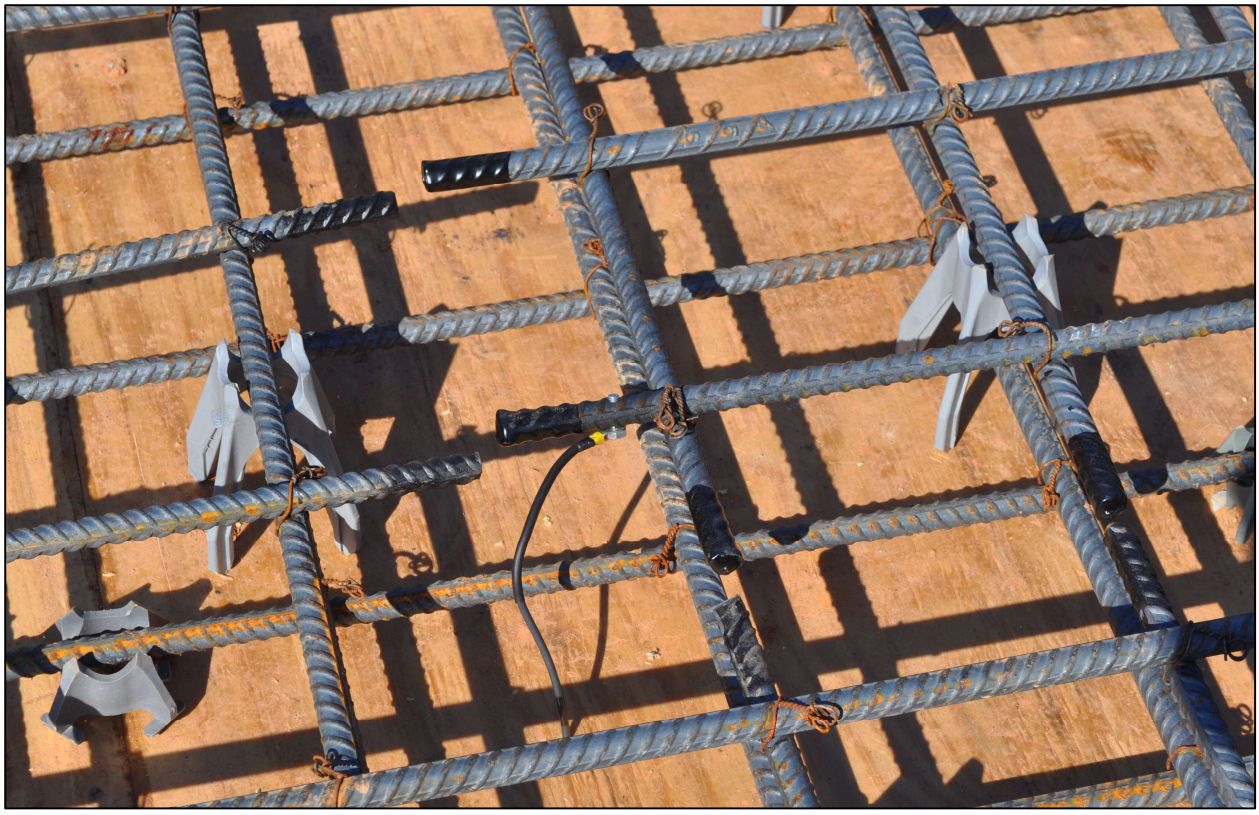

Figure 5-39: Discontinuous and electrically isolated rebar in the moderate corrosion section

Once the East section was cast and moist curing was complete, the research team ponded the surface with a three percent sodium chloride solution. Two 4 × 6 ft ponding reservoirs were constructed from 0.375 in. thick acrylic sheets. The joints of the ponding reservoirs were sealed with a silicone material and the reservoirs were bonded to the concrete surface with a construction adhesive. In order to provide current to the system, the research team connected two 12 V batteries in series to each corrosion section; this provided 24 V to each corrosion section. The circuit was connected such that each reinforcing steel section was connected to the positive posts of a 24 V battery system, while a stainless steel plate submersed in each sodium chloride solution was connected to the negative post of each 24 V battery system. A pond with the submerged stainless steel plate is shown in Figure 5-40.

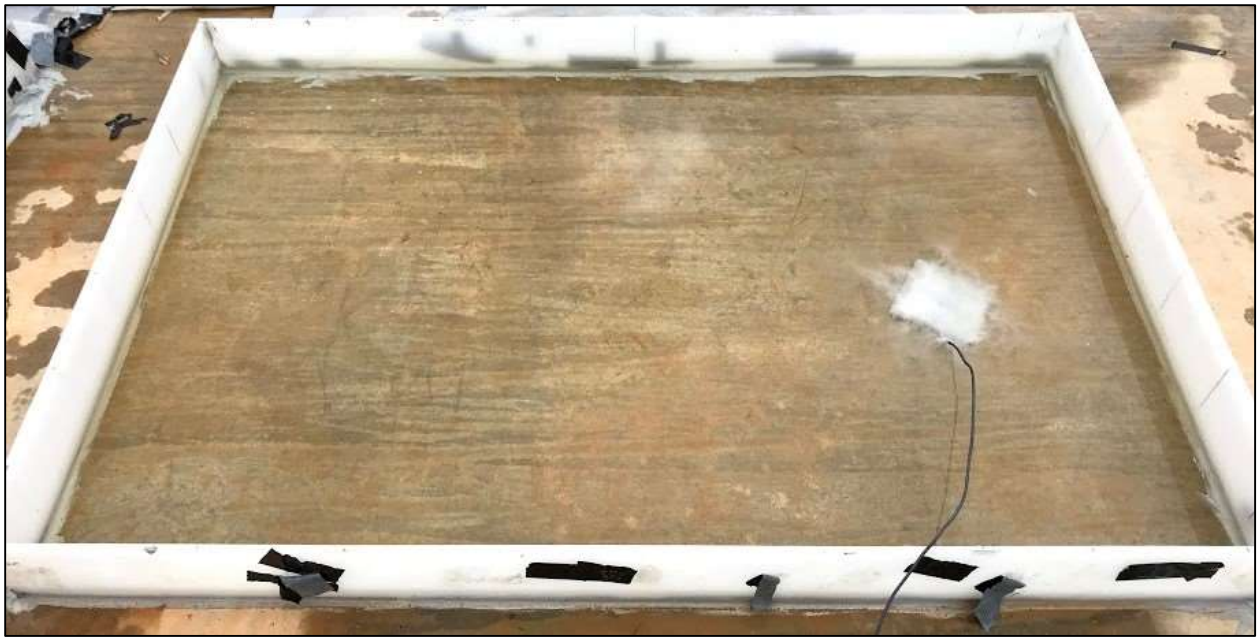

Figure 5-40: Pond walls filled with sodium chloride solution; submerged stainless steel plate

A solar panel was connected to each of the 24 V battery systems in order to sustain a charge on the batteries. Weekly, the research team drained each pond, tested the sections with the half-cell potential method, and re-ponded with a fresh sodium chloride solution. Aside from times when the research team was testing the sections to measure corrosion progression, sodium chloride solution and current were continuously applied to the bridge deck. Current was applied to the moderate section for a total of 70 days, when mild corrosion damage was noticeable at the surface, as shown in Figure 5-41. Some localized rust deposits had risen to the surface, and slight localized cracking had occurred around the area of rust staining.

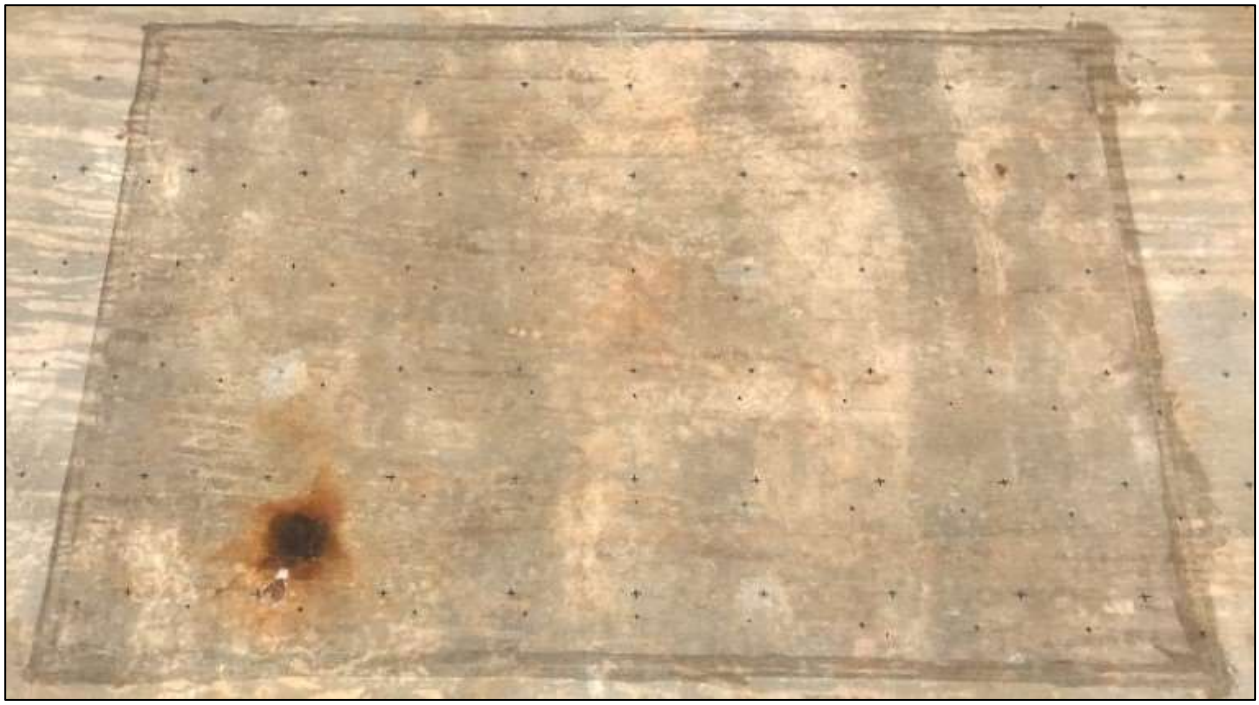

Figure 5-41: Zone C1, once the induced corrosion process was complete

The 24 V battery system was used to induce current into the severe section for 56 days. At that point, it was determined to increase the voltage of the circuit in the severe system from 24 V to 48 V in order to expedite the corrosion process. This was accomplished by connecting four 12 V batteries in series and utilizing a 48 V battery charger to sustain a charge on the batteries. The severe corrosion section was connected to this 48 V system for an additional 42 days, at which point severe corrosion damage was evident at the surface, as shown in Figure 5-42. No rust deposits were visible at the surface, but severe surface cracking was present throughout the region.

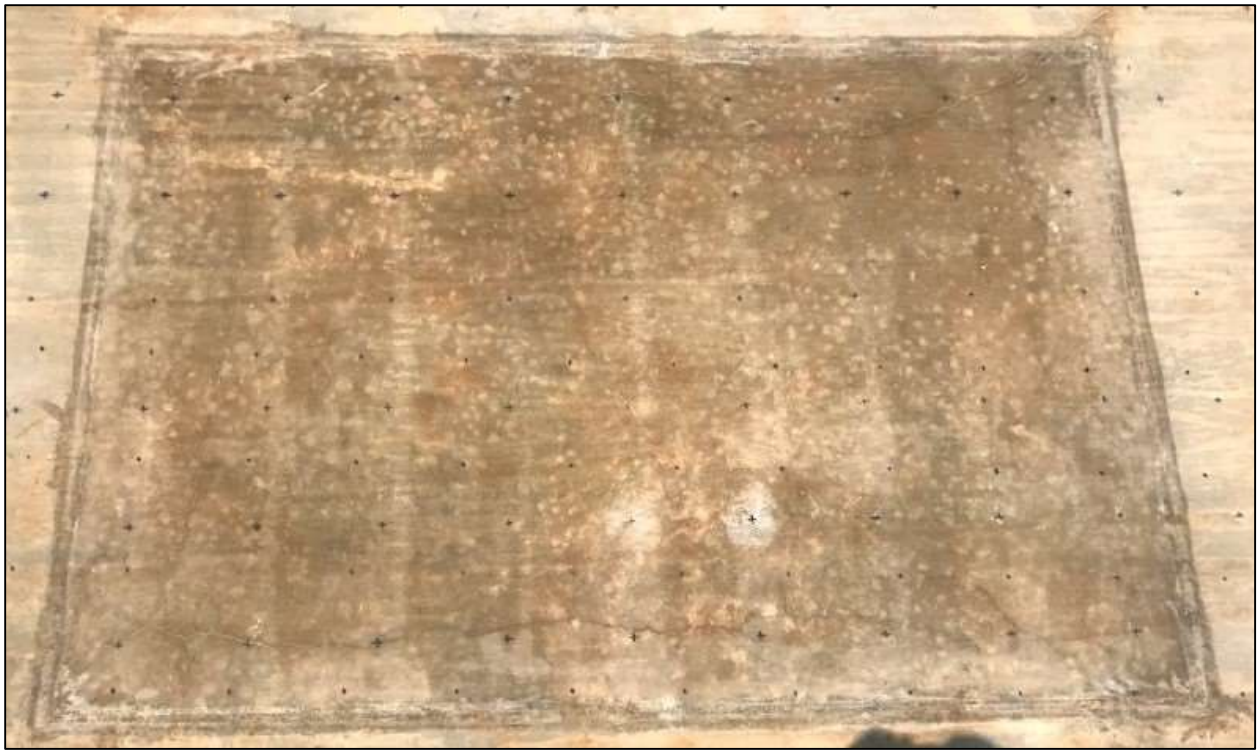

Figure 5-42: Zone C2, once the induced corrosion process was complete

5.3.3.4 Deterioration and Poor Construction

Deterioration and poor construction areas in the NDT bridge were divided into three different zones within the West section: DE1, DE2, and DE3. In each zone, deterioration or poor construction was simulated by a 4 in. thick, 1 × 5 ft slab of precast concrete. Zone DE1 was created using a concrete mixture that had a very high dosage of air-entraining admixture, simulating a deteriorated concrete matrix. Zone DE2 was created using a concrete mixture that had a low paste content, simulating honeycombed concrete. Zone DE3 was created using a concrete mixture that had a high water-to-cement ratio, simulating a deteriorated concrete matrix with low strength.

The three miniature slabs were cast in the laboratory prior to construction of the NDT bridge deck. The specimens were cast using the two-part forms used to cast the miniature slabs that were placed in the laboratory test specimens. The two-part forms allowed for an adequate lap splice length of reinforcing steel to pass beyond the face of the miniature slab. In casting each miniature slab, mixture ingredients were individually batched according to its respective mixture proportions outlined in Table 5-4 and mixed using the laboratory mixer. The concrete for the miniature specimen was then placed in the formwork. The concrete mixtures used to cast

the miniature specimens in Zones DE1 and DE3 were consolidated after placement into the formwork, but the concrete mixture used to cast the miniature specimen in Zone DE2 was not consolidated, in order to maximize the honeycombing effect. The surfaces of all three specimens were raked in order to provide adequate surface roughness. The fresh properties of the concrete mixtures used to cast the three specimens are shown in Table 5-11.

Table 5-11: Fresh concrete properties of encased specimens in the West-end section

	Zone DE1	**Zone DE2**	**Zone DE3**
Slump (in.)	8.5	0.0	10.0
Air Content (%)	13.0	4.5	0.3
Unit Weight (pcf)	130.4	148.8	147.2
Temperature (ºF)	68	68	68

Each specimen was moist cured for seven days following casting. The average 28-day compressive strength of the concrete used to cast the miniature slabs is presented in Table 5-12. All strength data for the concrete in Zones DE1, DE2, and DE3 can be found in Appendix A.

Table 5-12: Average 28-day strength of encased specimens in the West-end section

	Zone DE1	**Zone DE2**	**Zone DE3**
Average 28-day strength (psi)	2580	2910	3090

Once the bridge deck formwork was constructed, the miniature slabs that made up Zones DE1, DE2, and DE3 were positioned in their final locations, as shown in Figure 5-43, Figure 5-44, and Figure 5-45.

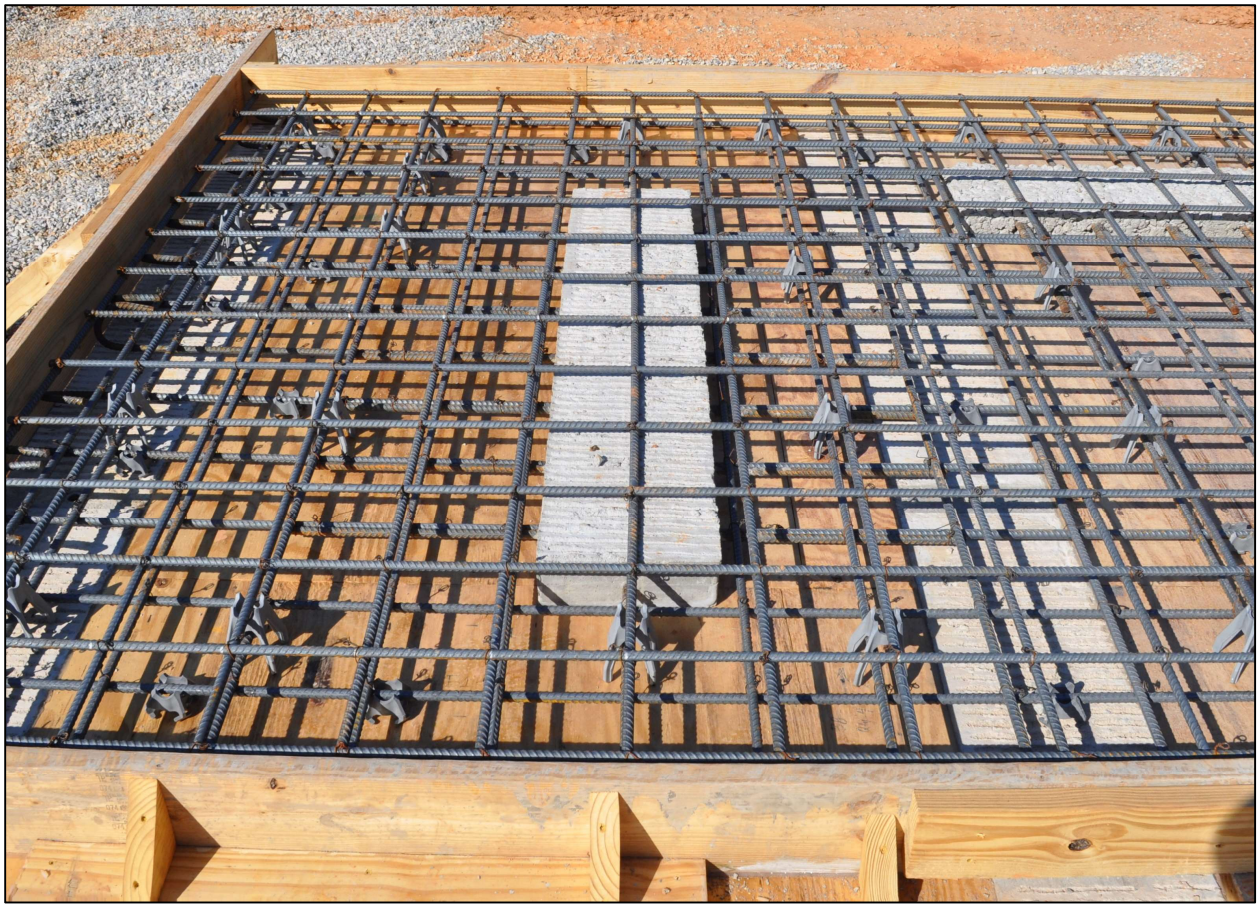

Figure 5-43: High air specimen in place at Zone DE1

Figure 5-44: Honeycombed specimen in place at Zone DE2

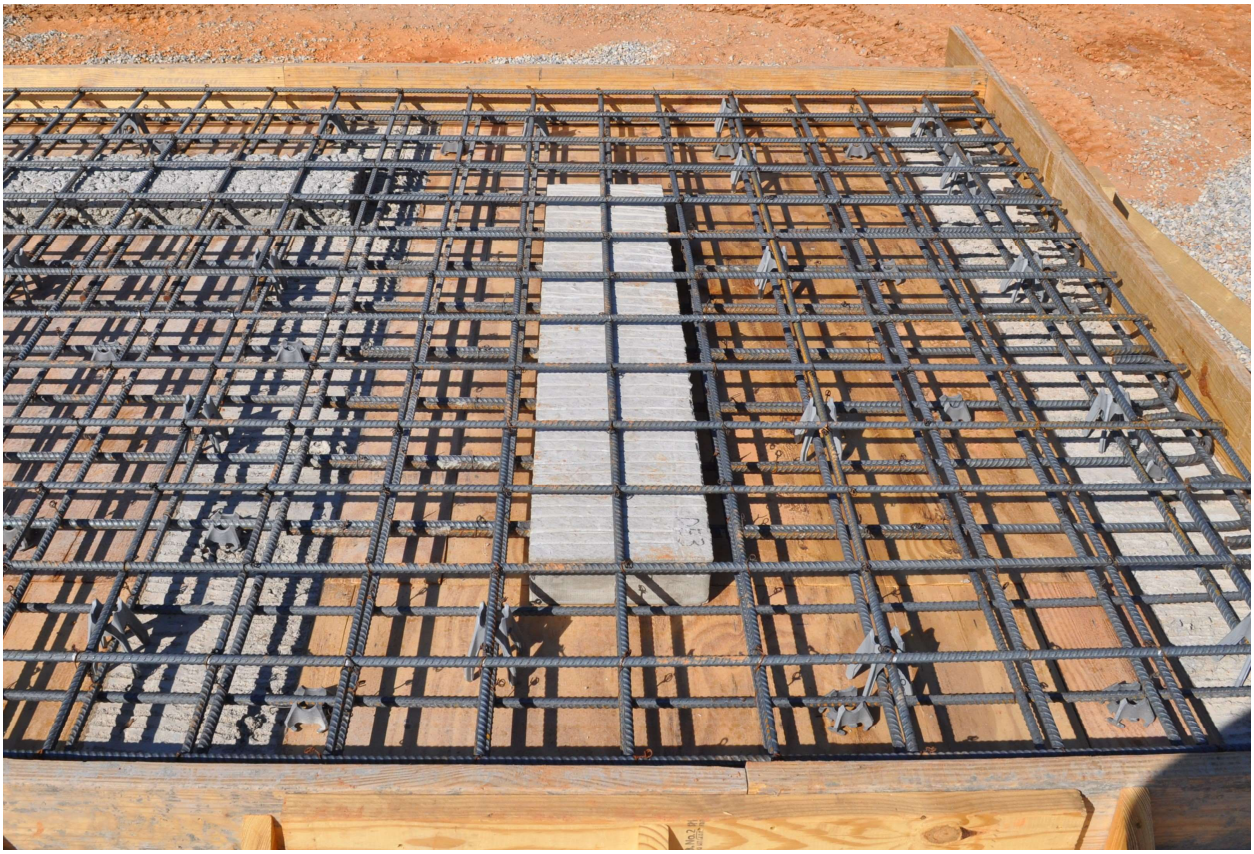

Figure 5-45: Low strength specimen in place at Zone DE3

Immediately before casting of the West section of the bridge deck began, each slab was moistened with water in order to prevent water in the fresh concrete from being absorbed by the surfaces of the miniature slabs, which would create a weaker bridge deck concrete at the surface of the miniature specimens. After the slabs were moistened with water, concrete was placed in the West section of the NDT bridge deck, encasing the miniature specimens.

5.4 AS-BUILT LAYOUT OF DEFECTS IN BRIDGE DECK NDT SITE

Construction and placement of the defects within the NDT bridge deck closely followed the design drawings presented in Section 5.2.3. A summary of the defects placed into the NDT bridge deck can be found in Figure 5-46. A to-scale detail of defects placed into the NDT bridge deck is located in Appendix B.

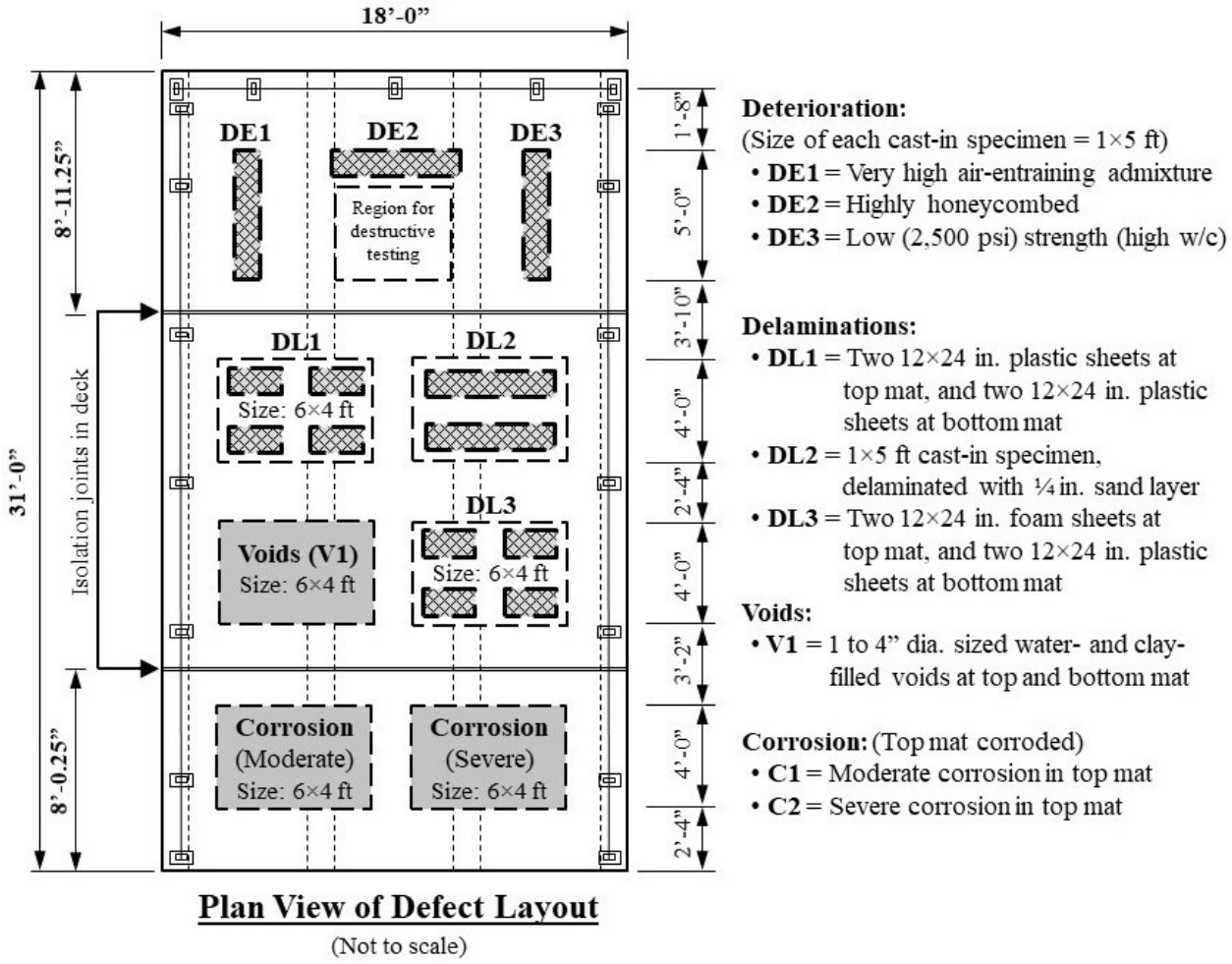

Figure 5-46: NDT bridge deck defect layout

CHAPTER 6

SUMMARY, CONCLUSIONS, AND RECOMMENDATIONS

6.1 SUMMARY OF WORK PERFORMED

Aging infrastructure is an increasing problem in the United States. Bridges are a critical part of the transportation infrastructure system, as they simplify interstate highway traffic and connect roads over terrain that would otherwise be impassable. Throughout their lifespans, reinforced-concrete bridge decks experience deterioration and distresses due to a number of causes, including both human causes (i.e. regular traffic wear, collisions, and use of deicing salts) and natural causes (i.e. freeze-thaw cycles and exposure to marine environments). Resulting deterioration and distresses in reinforced-concrete bridge decks occur in the form of corrosion of reinforcing steel, delaminations, vertical cracking, honeycombing, and concrete degradation. If not monitored and addressed, these distresses can result in loss of a bridge's structural integrity. Nondestructive testing (NDT) offers methods for monitoring reinforced-concrete bridge decks in a manner that does not cause damage to the structure, allowing departments of transportation to track deterioration in bridge decks and perform needed maintenance before they pose a threat to a bridge's integrity. Technologically advanced NDT methods provide departments of transportation with accurate, time-efficient, and cost-efficient ways to inspect and track the condition of their bridges, allowing those departments to better allocate maintenance spending to bridges that need rehabilitation, repair, or replacement the most.

The research documented in this report was primarily performed to provide the Alabama Department of Transportation (ALDOT) with a full-scale bridge deck NDT site where ALDOT personnel can conduct NDT training, calibrate equipment, and evaluate new NDT methods. In order to accomplish this task, twenty small-scale bridge deck specimens were created in the laboratory at Auburn University's Department of Civil and Environmental Engineering. These specimens were constructed using studied methods for replicating defects within reinforced-concrete bridge decks. All specimens were tested using various NDT methods, and spatial contour plots were created in order to compare testing results with defects placed into the

specimens. Defect replication methods that successfully represented defects in the laboratory experimental phase were used in creating the full-scale bridge deck NDT site.

Five NDT methods were assessed in this project for use by ALDOT: impact-echo, ground penetrating radar (GPR), half-cell potential, surface resistivity, and infrared thermography. These five candidate methods were used to survey and identify the defects in the laboratory test specimens. The NDT methods were evaluated for strengths and limitations with regards to accuracy, precision, speed, cost, and ease of use. Methods that successfully detected and characterized the in-place condition of the test specimens were identified.

After all laboratory work was performed, the full-scale bridge deck NDT site was constructed at the National Geotechnical Experimentation Site (NGES) in Opelika, Alabama. A summary of defects placed into the full-scale bridge deck NDT site, as well as an image of the completed bridge structure are shown below in Figure 6-1 and Figure 6-2.

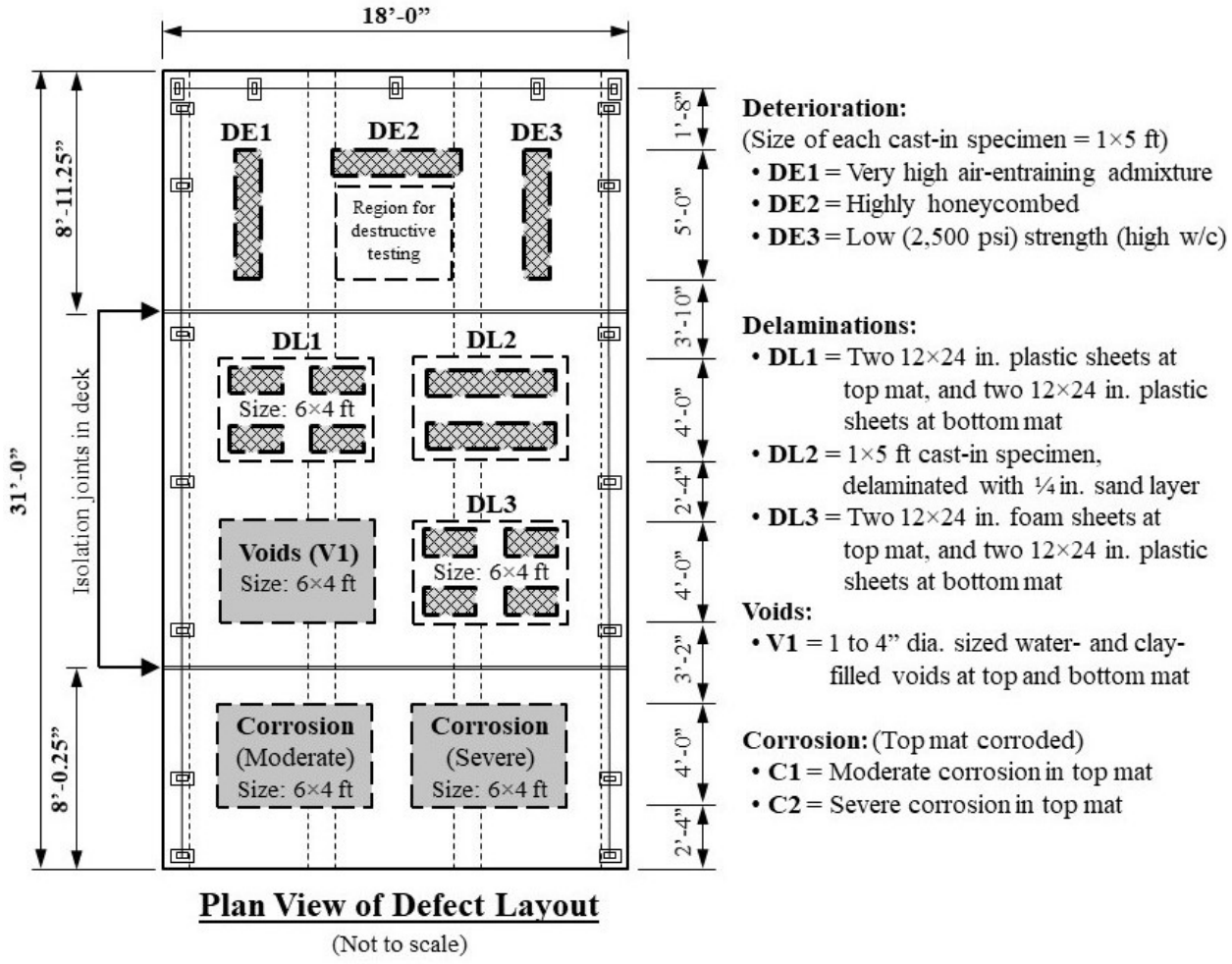

Figure 6-1: Summary of defects placed in the full-scale bridge deck NDT site

Figure 6-2: The NDT bridge at the time of submission of this report

6.2 RESEARCH CONCLUSIONS

The following conclusions are offered based upon the work performed throughout this research project:

- The impact-echo method was determined to be the most effective NDT method tested throughout the course of the research documented in this report, and was determined to be the most suitable for use by the ALDOT. It proved to be the most precise, accurate, and time-efficient test method during the laboratory testing phase.
- The half-cell potential method and the surface resistivity method, in conjunction, work well to characterize corrosion activity within reinforced-concrete, but are only able to identify corrosion activity in the test specimen, not deterioration related to corrosion.
- Thin plastic sheets placed at a level of reinforcement provide excellent representation of horizontal delaminations among reinforcing steel.
- A successful method to induce corrosion in reinforced-concrete is to expose the element to a sodium chloride solution while simultaneously applying current in the form of a direct current power supply (i.e. 12V or greater batteries). The positive post of the power source should be connected to the reinforcing steel where corrosion is desired, and the negative post should be connected to a stainless steel plate submerged in the sodium chloride solution.

- Regions of concrete constructed with poor concrete mixtures (i.e. high air-entraining admixture, low paste content, or high water-to-cement ratio) encased in good concrete are excellent representatives of deteriorated concrete and concrete cast using poor construction practices.
- Casting water- or clay-filled balloons into a reinforced-concrete specimen works well to create voids within concrete elements.

6.3 RECOMMENDATIONS FOR FUTURE WORK

The following future work items are recommended after the completion of the research work documented throughout this report:

- Periodic NDT evaluations should be conducted on the full-scale test bridge site to track and document the development of any further deterioration that may develop in the exposed bridge deck.
- A study involving the selected NDT methods and comparison of their results on actual defective bridges should be conducted throughout the state of Alabama, in order to provide a more accurate conclusion as to the best NDT method for use by ALDOT.
- NDT equipment manufacturers offer equipment that allows for faster operator-controlled NDT surveying. Olson Instruments offers a Sonic Surface Scanner, which is designed for testing bridge decks using the impact-echo method. Further research should be performed investigating the accuracy, precision, and speed of testing of this NDT method, and its suitability for use by ALDOT.
- A study should be conducted that involves an in-depth investigation of the infrared thermography method for surveying the condition of reinforced-concrete bridge decks.
- Automated and trailer-mounted NDT surveying of bridge decks provides a safer alternative to state department personnel and testing operators manually performing bridge deck testing and surveying. Research should be performed that provides insight into the most effective methods for creating trailer-mounted NDT equipment, as well as the most effective automated NDT equipment available to departments of transportation.

REFERENCES

AASHTO. 2020. *LRFD Bridge Design Specifications.* American Association of State Highway and Transportation Officials.

AASHTO. 2019. *T 358: Standard Method of Test for Surface Resistivity Indication of Concrete's Ability to Resist Chloride Ion Penetration.* American Association of State Highway and Transportation Officials.

ACI 222. 2019. *Guide to Protection of Reinforcing Steel in Concrete against Corrosion (ACI 222R-19).* Farmington Hills: American Concrete Institute.

ACI 228. 2013. *Report on Nondestructive Test Methods for Evaluation of Concrete in Structures (ACI 228.2R-13).* Farmington Hills, MI: American Concrete Institute.

ACI 318. 2014. *Building Code Requirements for Structural Concrete (ACI 318-14).* American Concrete Institute.

ACI 364. 2017. *Section Loss Determination of Damaged or Corroded Reinforcing Steel Bars (ACI 364.14T-17).* Farmington Hills: American Concrete Institute.

Afshinnia, K. 2020. "Degradation of Concrete Structures from Influence of Agressive Chemicals." *Roads & Bridges.* Accessed 2020. https://www.roadsbridges.com/degradation-concrete-structures-influence-aggressive-chemicals.

ALDOT Bridge Bureau. 2019. "Structural Design Manual." Alabama Department of Transportation.

Almusallam, A.A., A.S. Al-Gahtani, A. Rauf Aziz, F.H. Dakhil, and Rasheeduzzafar. 1996. "Effect of Reinforcement Corrosion on Flexural Behavior of Concrete Slabs." *Journal of Materials in Civil Engineering* 123-127.

American Concrete Institute. 2018. *CT-18 ACI Concrete Terminology.* Farmington Hills: American Concrete Institute.

American Institute of Steel Construction. 2017. *Steel Construction Manual - 15th Edition.* American Institute of Steel Construction.

American Society of Civil Engineers. 2010. "ASCE 7-10: Minimum Design Loads for Buildings and Other Structures."

ASCE. 2017. *2017 Infrastructure Report Card.* Reston, VA: American Society of Civil Engineers.

ASTM C1383. 2015. *Standard Test Method for Measuring the P-Wave Speed and the Thickness of Concrete Plates Using the Impact-Echo Method.* ASTM International.

ASTM C39. 2020. *Standard Test Method for Compressive Strength of Cylindrical Concrete Specimens.* ASTM International.

ASTM C42. 2020. *Standard Test Method for Obtaining and Testing Drilled Cores and Sawed Beams of Concrete.* ASTM International.

ASTM C876. 2015. *Standard Test Method for Corrosion Potentials of Uncoated Reinforcing Steel in Concrete .* ASTM International.

ASTM D4580. 2018. *Standard Practice for Measuring Delaminations in Concrete Bridge Decks by Sounding.* ASTM International.

ASTM D4788. 2013. *Standard Test Method for Detecting Delaminations in Bridge Decks Using Infrared Thermography .* ASTM International.

ASTM D6087. 2015. *Standard Test Method for Evaluating Asphalt-Covered Concrete Bridge Decks Using Ground Penetrating Radar .* ASTM International.

BAM Division 8.2. 2018. "Honeycombs Reference Specimen." Federal Institute for Materials Research and Testing .

BAM Division 8.2. 2018. "Material degradation at rebars – Corrosion Reference Specimen." Federal Institute for Materials Research and Testing.

Cheng, C., and M. Sansalone. 1993. "The impact-echo response of concrete plates containing delaminations; numerical, experimental and field studies." *Materials and Structures* 26: 274-285.

Cotič, P., D. Kolarič, V.B. Bosiljkov, V. Bosiljkov, and Z. Jagličić. 2015. "Determination of the applicability and limits of void and delamination detection in concrete structures using infrared thermography." *NDT&E International* 74: 87-93.

Emmons, P. H. 1994. *Concrete Repair and Maintenance Illustrated.* Kingston, MA: R.S. Means Company, Inc.

Fawcett, Tom. 2006. "An Introduction to ROC Analysis." *Pattern Recognition Letters* 861-874.

Florida Department of Transportation. 2013. "Instructions for Design Standards Index 852: Steel Pedestrian/Bicycle Railing."

2021. *Google Maps.* Accessed May 2021. https://www.google.com/maps/.

Gucunski, N., A. Imani, F. Romero, S. Nazarian, D. Yuan, H. Wiggenhauser, P. Shokouhi, A. Taffe, and D. Kutrubes. 2013. *Nondestructive Testing to Identify Concrete Bridge Deck Deterioration.* The Second Strategic Highway Research Program, Transportation Research Board, National Academy of Science.

Guo, A., H. Li, X. Ba, X. Guan, and H. Li. 2015. "Experimental investigation on the cyclic performance of reinforced concrete piers with chloride-induced corrosion in marine environment." *Engineering Structures* 105: 1-11.

Ham, S., H. Song, M.L. Oelze, and J.S. Popovics. 2016. "A contactless ultrasonic surface wave approach to characterize distributed cracking damage in concrete." *Ultrasonics* (Elsevier) 75: 46-57.

International Atomic Energy Agency. 2002. "Guidebook on non-destructive testing of concrete structures." Vienna.

Jayaprakash, J., E. Pournasiri, and F. De'nan. 2012. "Effect of bond strength on fiber reinforced polymer enveloped concrete cylinders with rebars exposed to corrosion activity ." *Journal of Reinforced Plastics and Composites* (SAGE) 31: 845-854.

Lim, M. K., and C. Honggang. 2011. "Combining multiple NDT methods to improve testing effectiveness." *Construction and Building Materials* 1310-1315.

Lin, J.M., and M. Sansalone. 1996. "Impact-Echo Studies of Interfacial Bond Quality in Concrete: Part I—Effects of Unbonded Fraction of Area." *ACI Materials Journal* (American Concrete Institute) 93 (3): 223-231.

Lin, J.M., M. Sansalone, and R. Poston. 1996. "Impact-Echo Studies of Interfacial Bond Quality in Concrete: Part II—Effects of Bond Tensile Strength." *ACI Materials Journal* (American Concrete Institute) 93 (4): 318-325.

Lin, S., D. Meng, H. Choi, S. Shams, and H. Azari. 2018. "Laboratory assessment of nine methods for nondestructive evaluation of concrete bridge decks with overlays." *Construction and Building Materials* 966-982.

Maierhofer, C. 2003. "Nondestructive Evaluation of Concrete Infrastructure with Ground Penetrating Radar." *Journal of Materials in Civil Engineering* (American Society of Civil Engineers) 6 (3): 287-297.

Mishra, G. n.d. *Honeycombs in Concrete – Their Causes and Remedies.* https://theconstructor.org/practical-guide/honeycombs-in-concrete-and-remedies/6889/.

Moore, M., B. Phares, B. Graybeal, D. Rolander, and G. Washer. 2001. *Reliability of Visual Inspection for Highway Bridges, Volume I: Final Report.* Technical Report, Federal Highway Administration.

Olson Engineering. n.d. *Impact Echo Bridge Deck Scanning.* Accessed April 2021. https://olsonengineering.com/methods/structural-pavement-tunnel-methods/impact-echo-bridge-deck-scanning/.

Proceq. 2017. *Operating Instructions: Concrete Durability Testing.* Proceq SA.

Sansalone, M., and N.J. Carino. 1989. "Detecting Delaminations in Concrete Slabs with and without Overlays Using the Impact-Echo Method." *ACI Materials Journal* 86: 175-184.

Sansalone, M.J., and W.B. Streett. 1996. "Impact Echo Condition Assessment of Structures." *Structural Engineering International* 6 (4): 282-284.

Schindler, A. K., M. L. Hughes, R. W. Barnes, and B. E. Byard. 2010. *Evaluation of cracking of the US 331 bridge deck.* Highway Research Center at Auburn University.

Taylor, H.F.W., C. Famy, and K.L. Scrivener. 2000. "Delayed ettringite formation." *Cement and Concrete Research*, 683-693.

Vaghefi, K., T.M. Ahlborn, D.K. Harris, and C.N. Brooks. 2015. "Combined Imaging Technologies for Concrete Bridge Deck Condition Assessment." *Journal of Performance of Constructed Facilities* (ASCE) 29 (4).

Vinson, J. L., and D. A. Brown. 1997. "Site Characterization of the Spring Villa Geotechnical Test Site and A Comparison of Strength and Stiffness Parameters for a Piedmont Residual Soil."

APPENDIX A: RAW CONCRETE SAMPLING DATA

A.1 FRESH PROPERTIES OF CONCRETE CAST DURING LABORATORY EXPERIMENTATION

Table A-1 and Table A-2 contains the fresh concrete properties of all encased specimens cast throughout the laboratory experimental process. The fresh properties recorded include slump, air content, unit weight, and temperature.

Table A-1: Fresh properties of encased concrete for DE2 though DE5 specimens

	DE2	**DE3**	**DE4**	**DE5**
Slump (in.)	8.25	0.25	6.50	4.00
Air Content (%)	13.0	5.2	6.8	6.6
Unit Weight (pcf)	135.4	148.7	143.48	147.76
Temperature (ºF)	68	63	67	64

Table A-2: Fresh properties of encased concrete for PC1, PC2, and CONTROL specimens

	PC1	**PC2**	**CONTROL**
Slump (in.)	10.50	9.50	8.75
Air Content (%)	0.4	5.6	6.4
Unit Weight (pcf)	Not recorded	Not recorded	141.2
Temperature (ºF)	67	68	66

A.2 RAW COMPRESSIVE STRENGTH DATA OF NDT BRIDGE ELEMENTS

Table A-3 through Table A-10 contain the raw compressive strength data of all NDT bridge elements. This includes structural elements, as well as miniature specimens cast into the bridge deck.

Table A-3: Concrete compressive strength data for the NDT bridge girders

	Girder Compressive Strength (psi)					
	August 14, 2020 Casting			August 21, 2020 Casting		
	3 day	28 day	91 day	3 day	28 day	91 day
Cylinder 1	3490	5830	7210	2650	5420	6930
Cylinder 2	3530	5860	7140	2660	5400	6730
Cylinder 3	3600	5730	7120	2720	5380	6880
Average	3540	5810	7160	2680	5400	6850

Table A-4: Concrete compressive strength data for the NDT bridge footings

	Footing Compressive Strength (psi)					
	East-End Foundation			West-End Foundation		
	7 day	28 day	91 day	7 day	28 day	91 day
Cylinder 1	3210	4340	5650	3500	4810	6020
Cylinder 2	3130	4240	5520	3760	4610	5940
Cylinder 3	3160	4320	5600	3630	4750	5860
Average	3170	4300	5590	3630	4720	5940

Table A-5: Concrete compressive strength data for the NDT bridge retaining wall

	Retaining Wall Compressive Strength (psi)		
	7 day	28 day	91 day
Cylinder 1	2190	3180	4070
Cylinder 2	2130	3290	4150
Cylinder 3	2170	3270	4070
Average	2160	3250	4100

Table A-6: Concrete compressive strength data for the NDT bridge deck

	Bridge Deck Compressive Strength (psi)					
	East-End and West-End Sections			Middle Section		
	7 day	28 day	91 day	7 day	28 day	91 day
Cylinder 1	4460	6610	7670	4220	5930	7090
Cylinder 2	4430	6500	8200	4250	5960	6930
Cylinder 3	4500	6730	7530	4210	5980	6960
Average	4460	6610	7800	4230	5960	6990

Table A-7: Concrete compressive strength data for the NDT bridge Zone DL2

	Zone DL2 Compressive Strength (psi)		
	7 day	28 day	91 day
Cylinder 1	4180	6120	7680
Cylinder 2	4330	6200	7340
Cylinder 3	4260	6100	7510
Average	4260	6140	7510

Table A-8: Concrete compressive strength data for the NDT bridge Zone DE1

	Zone DE1 Compressive Strength (psi)		
	7 day	28 day	91 day
Cylinder 1	1670	2560	3280
Cylinder 2	1800	2690	3300
Cylinder 3	1880	2480	3420
Average	1780	2580	3330

Table A-9: Concrete compressive strength data for the NDT bridge Zone DE2

	Zone DE2 Compressive Strength (psi)		
	7 day	**28 day**	**91 day**
Cylinder 1	3280	2040	5180
Cylinder 2	3730	2490	4660
Cylinder 3	2730	4190	6170
Average	3250	2910	5340

Table A-10: Concrete compressive strength data for the NDT bridge Zone DE3

	Zone DE3 Compressive Strength (psi)		
	7 day	**28 day**	**91 day**
Cylinder 1	2130	3240	3910
Cylinder 2	1680	2960	4270
Cylinder 3	2070	3080	4090
Average	1960	3090	4090

APPENDIX B: DESIGN DRAWINGS OF NDT BRIDGE ELEMENTS

This appendix, in Figure B-1 through Figure B-13, contains design drawings of NDT bridge elements. These drawings include the full NDT bridge design, foundation, retaining wall, girder, bridge deck, defect layout, safety barrier, and approach slab detail drawings.

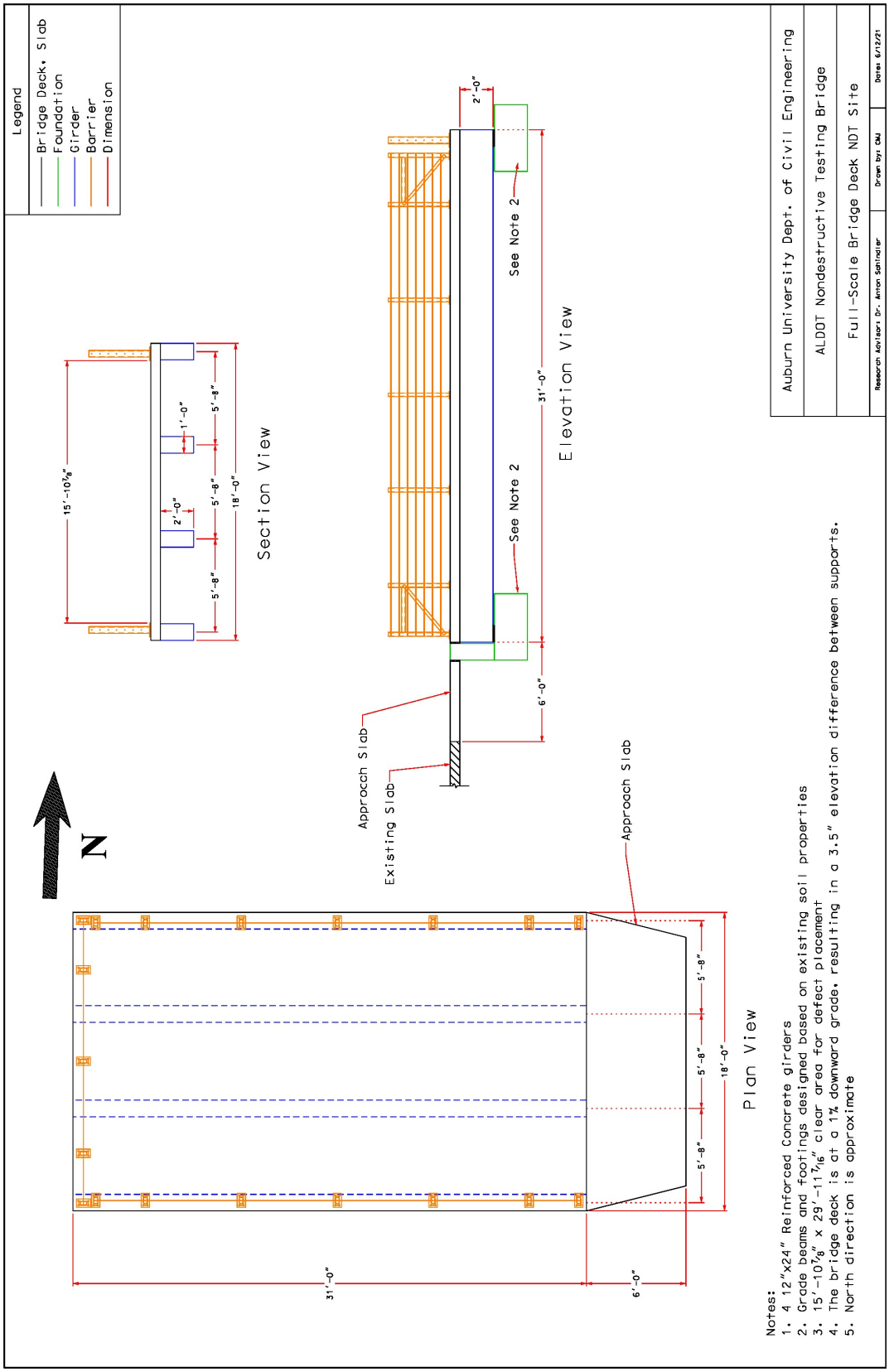

Figure B-1: Full-scale bridge deck NDT site design drawing

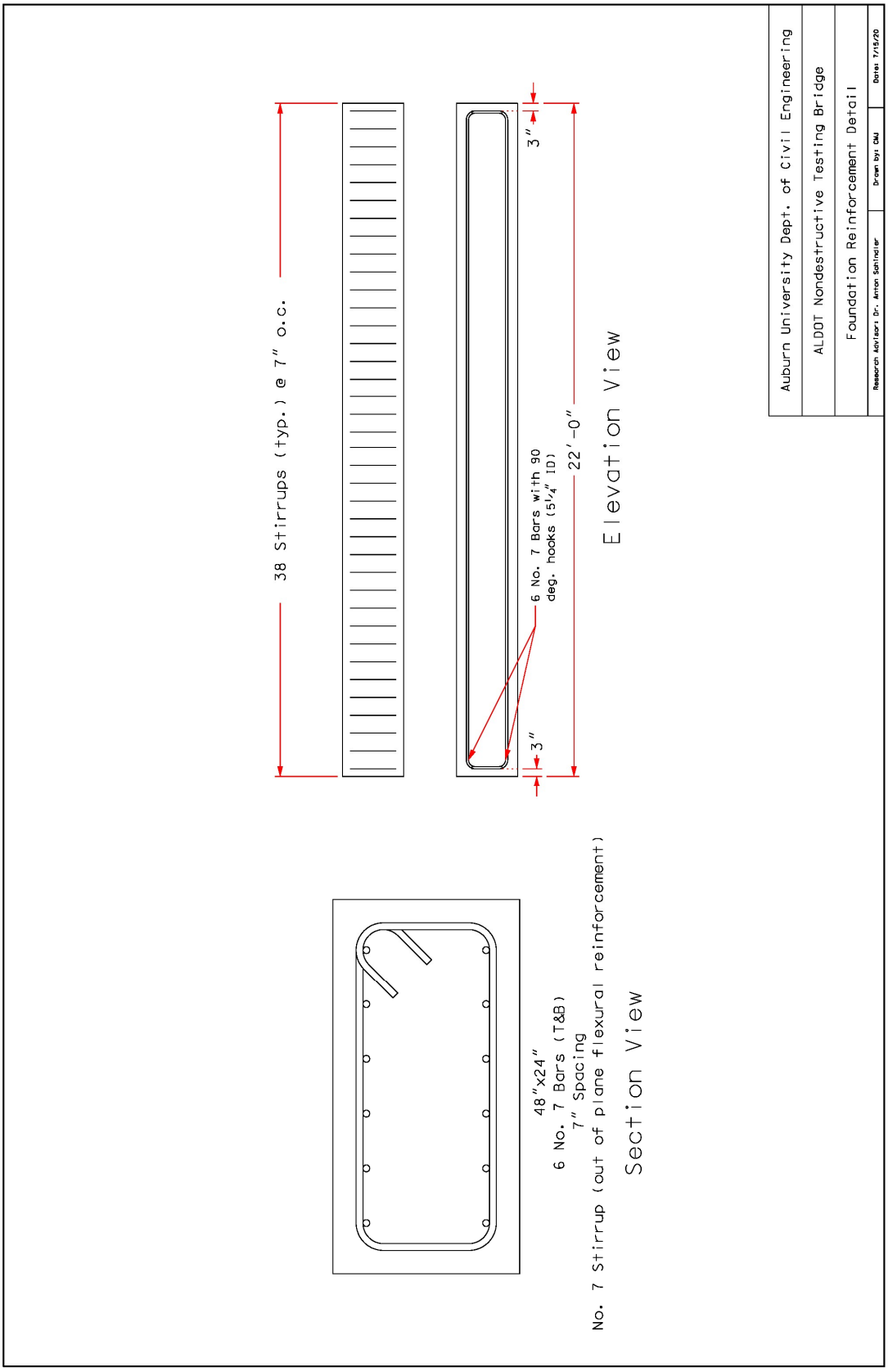

Figure B-2: Foundation reinforcement detail drawing

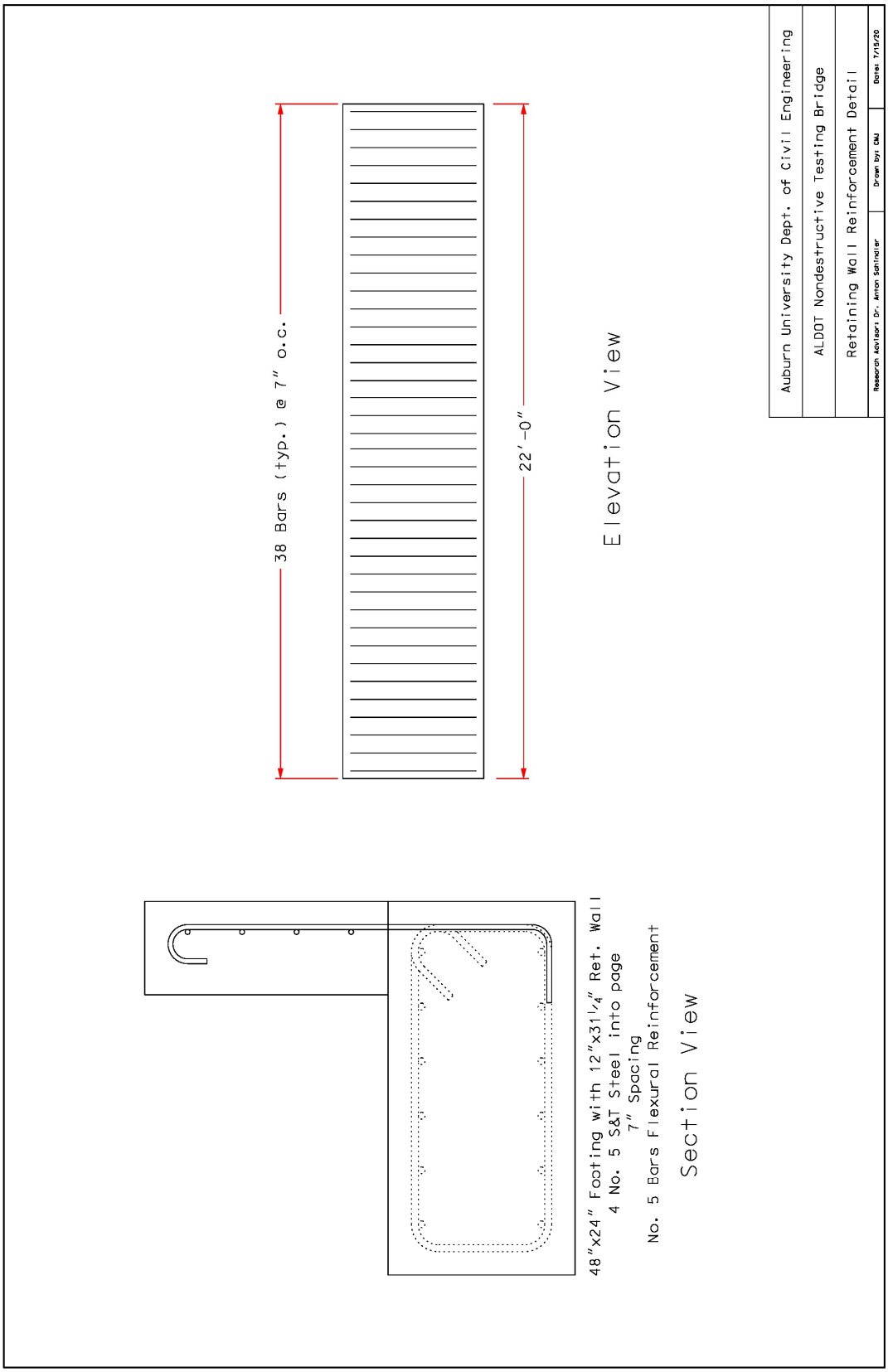

Figure B-3: Retaining wall reinforcement detail drawing

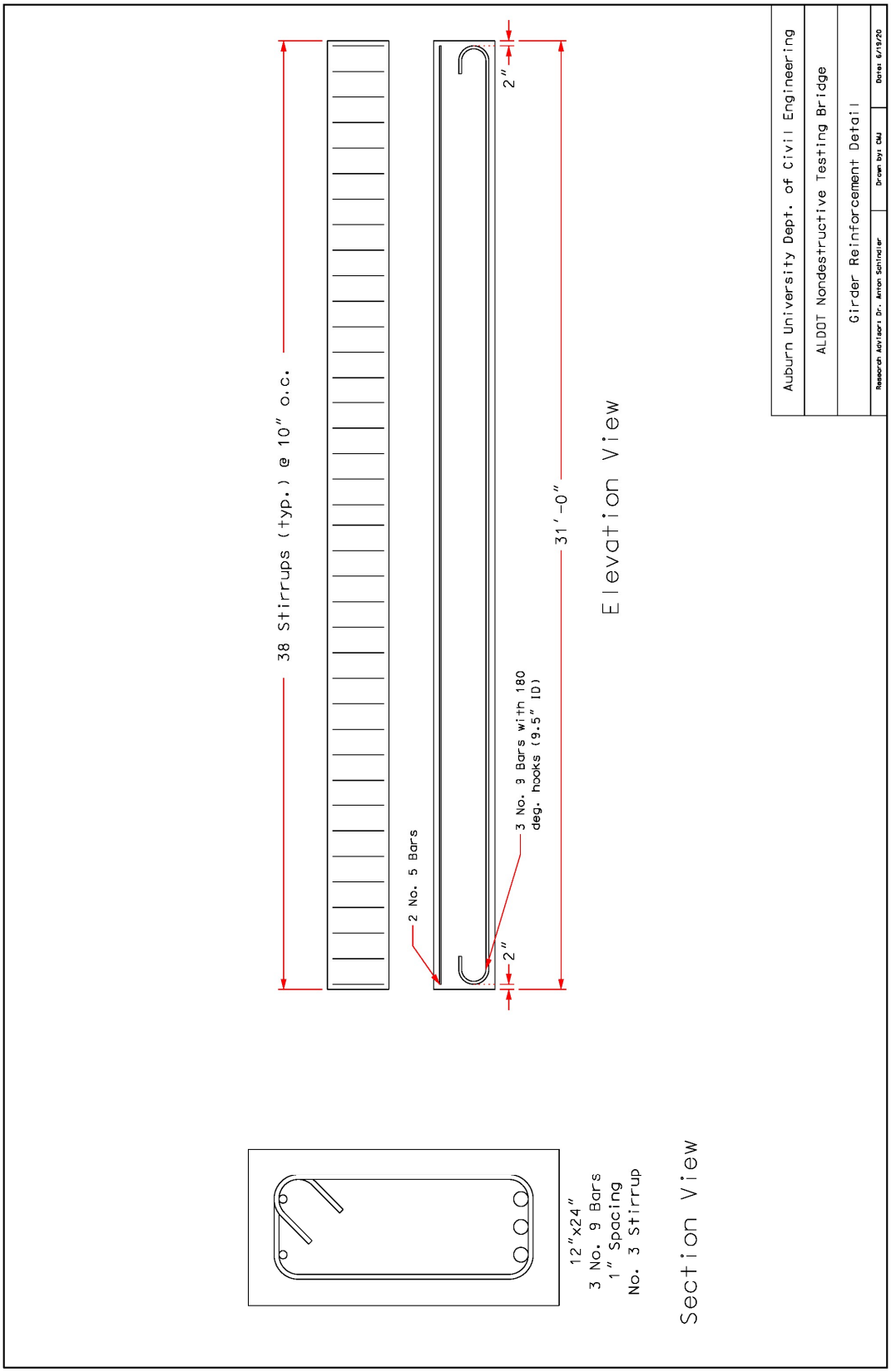

Figure B-4: Girder reinforcement detail drawing

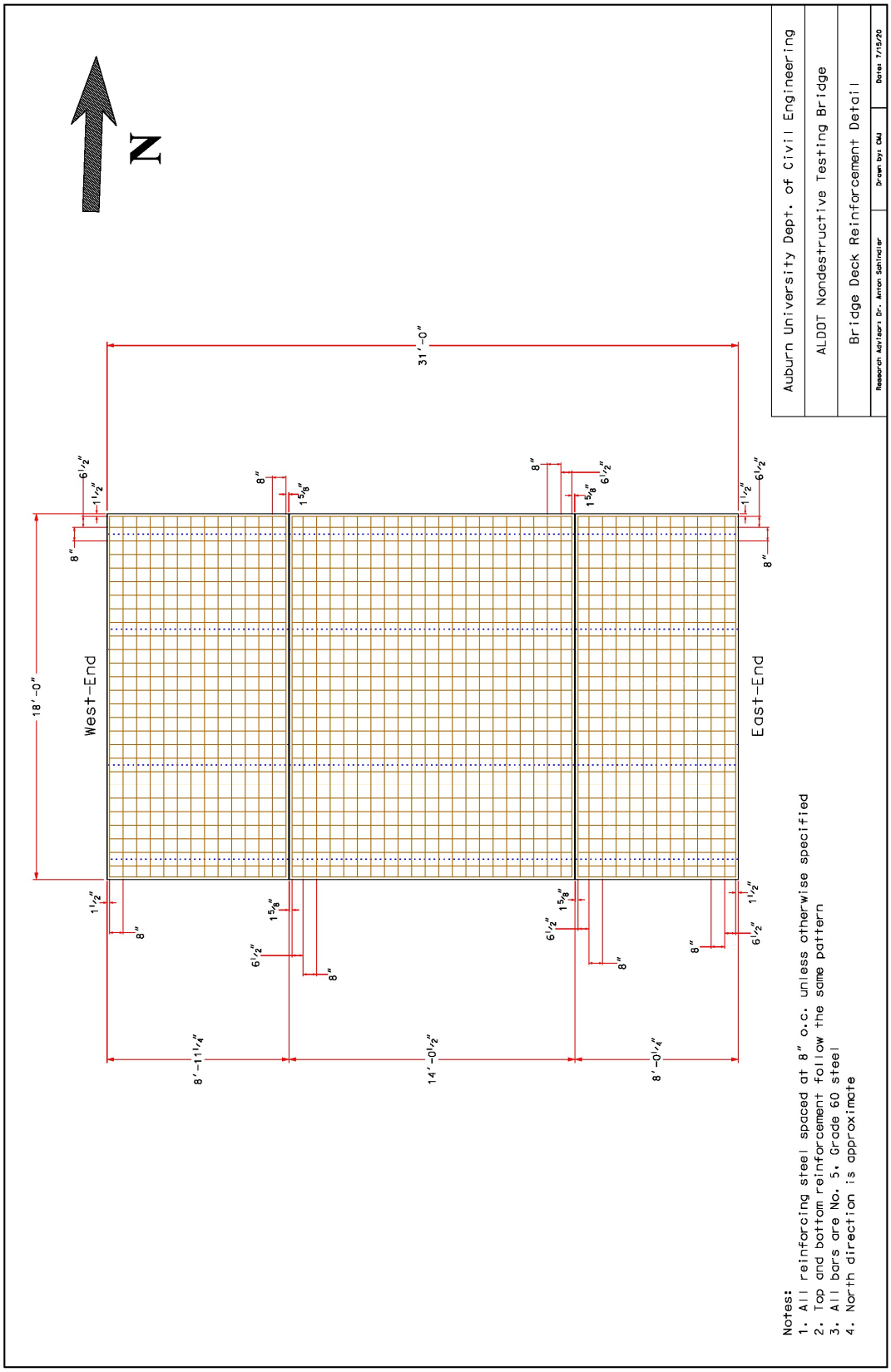

Figure B-5: Bridge deck reinforcement detail drawing

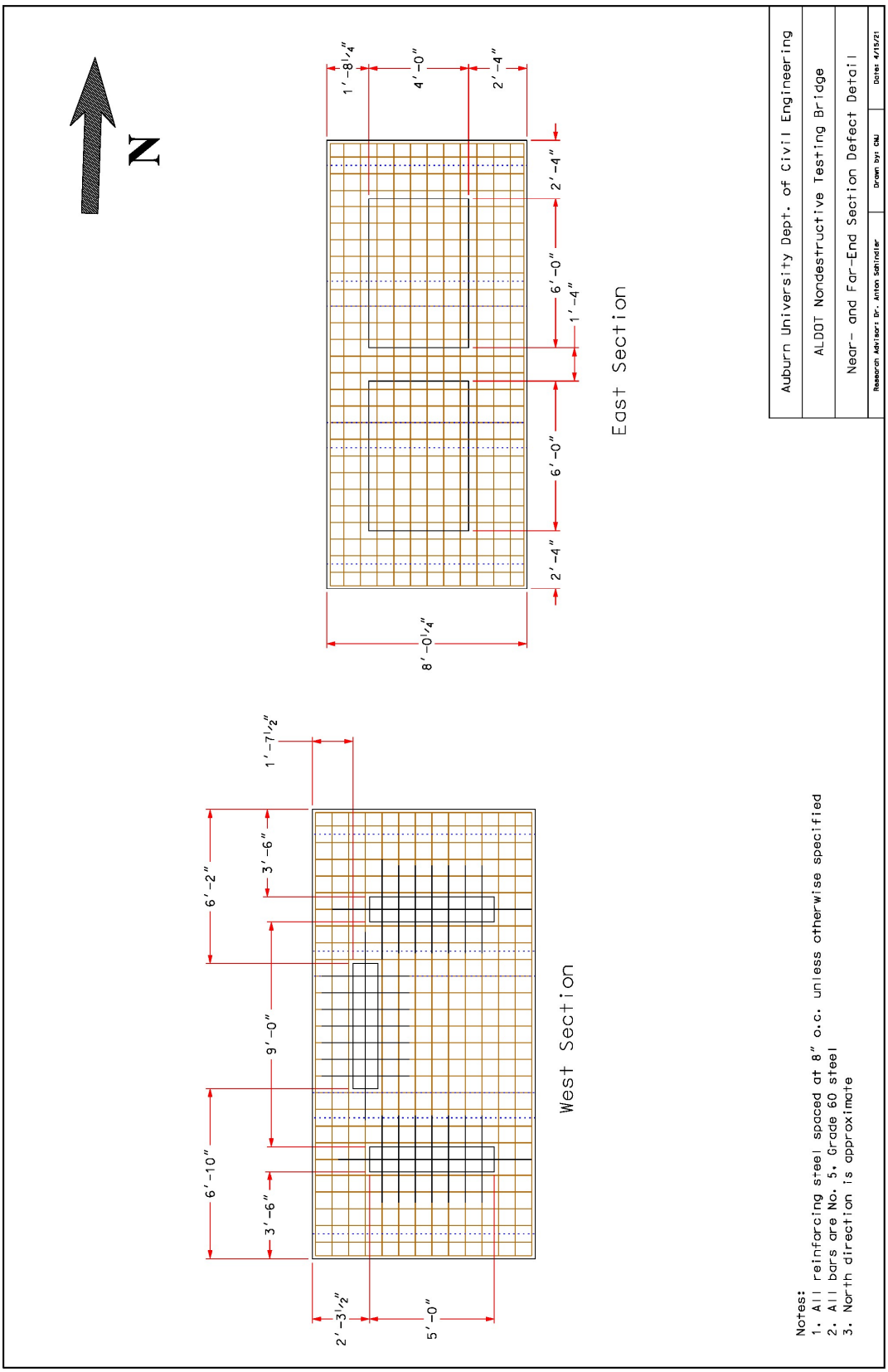

Figure B-6: East- and West-end section defect layout and dimensions

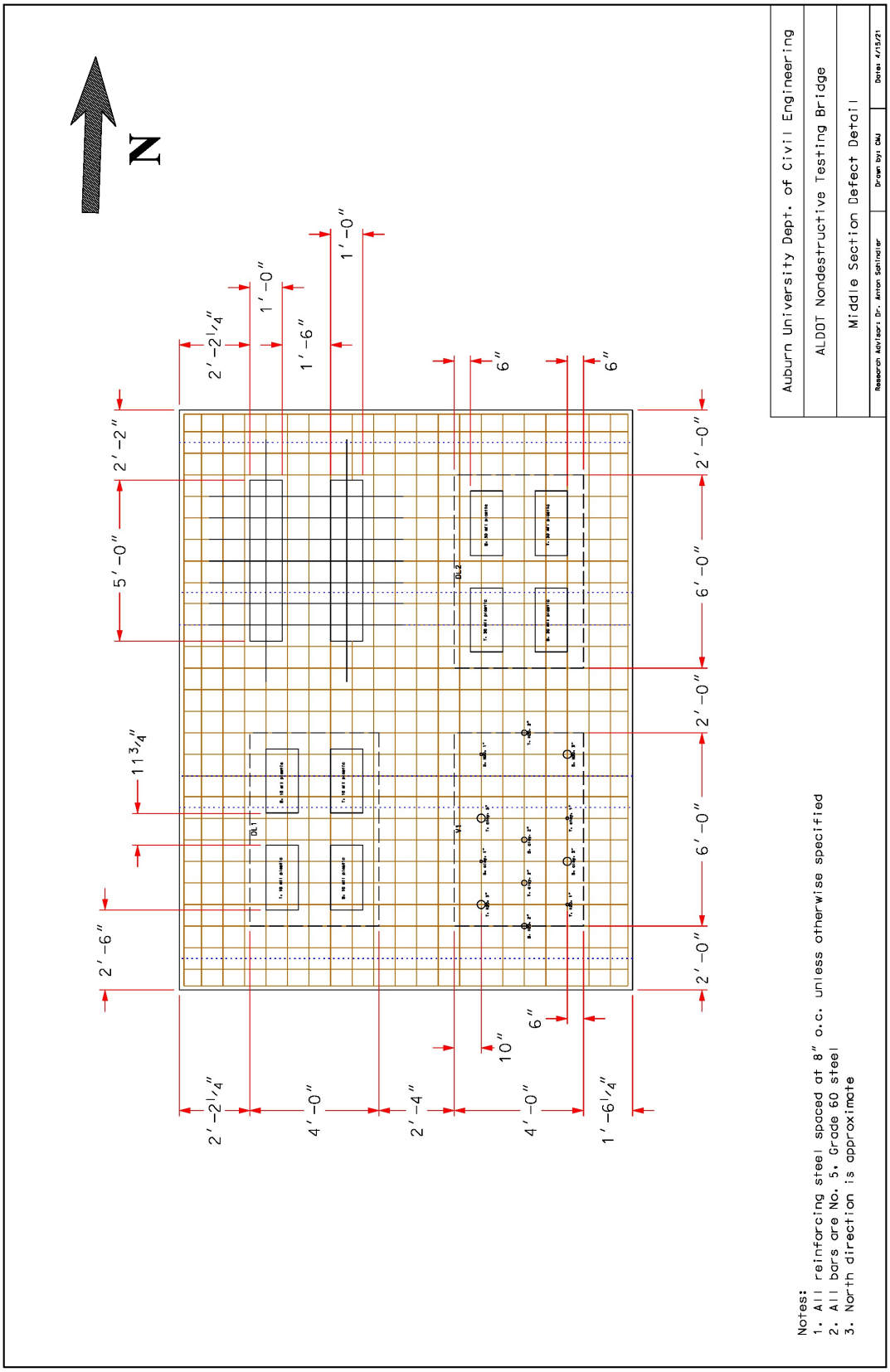

Figure B-7: Middle section defect layout and dimensions

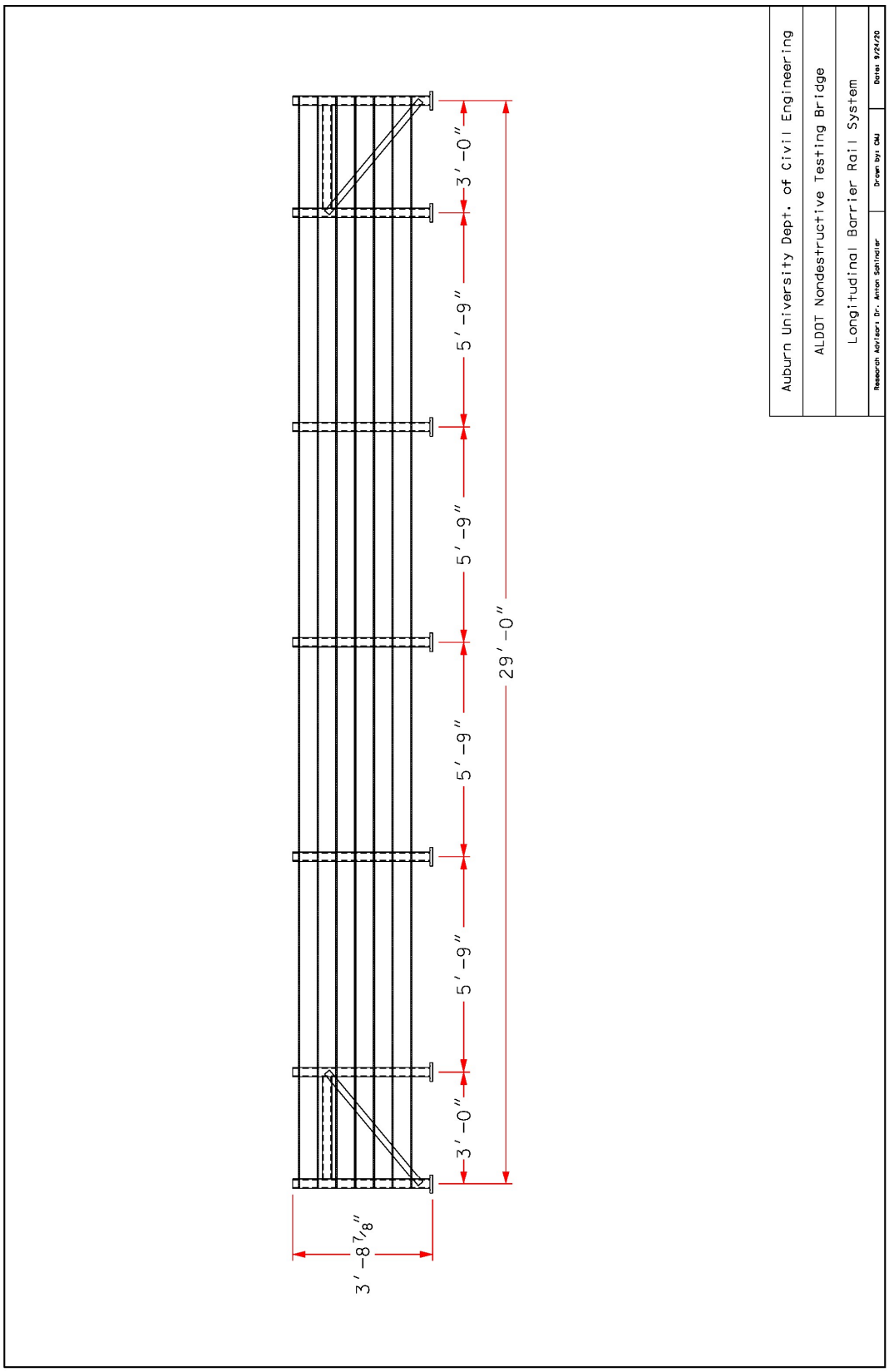

Figure B-8: Longitudinal barrier rail system

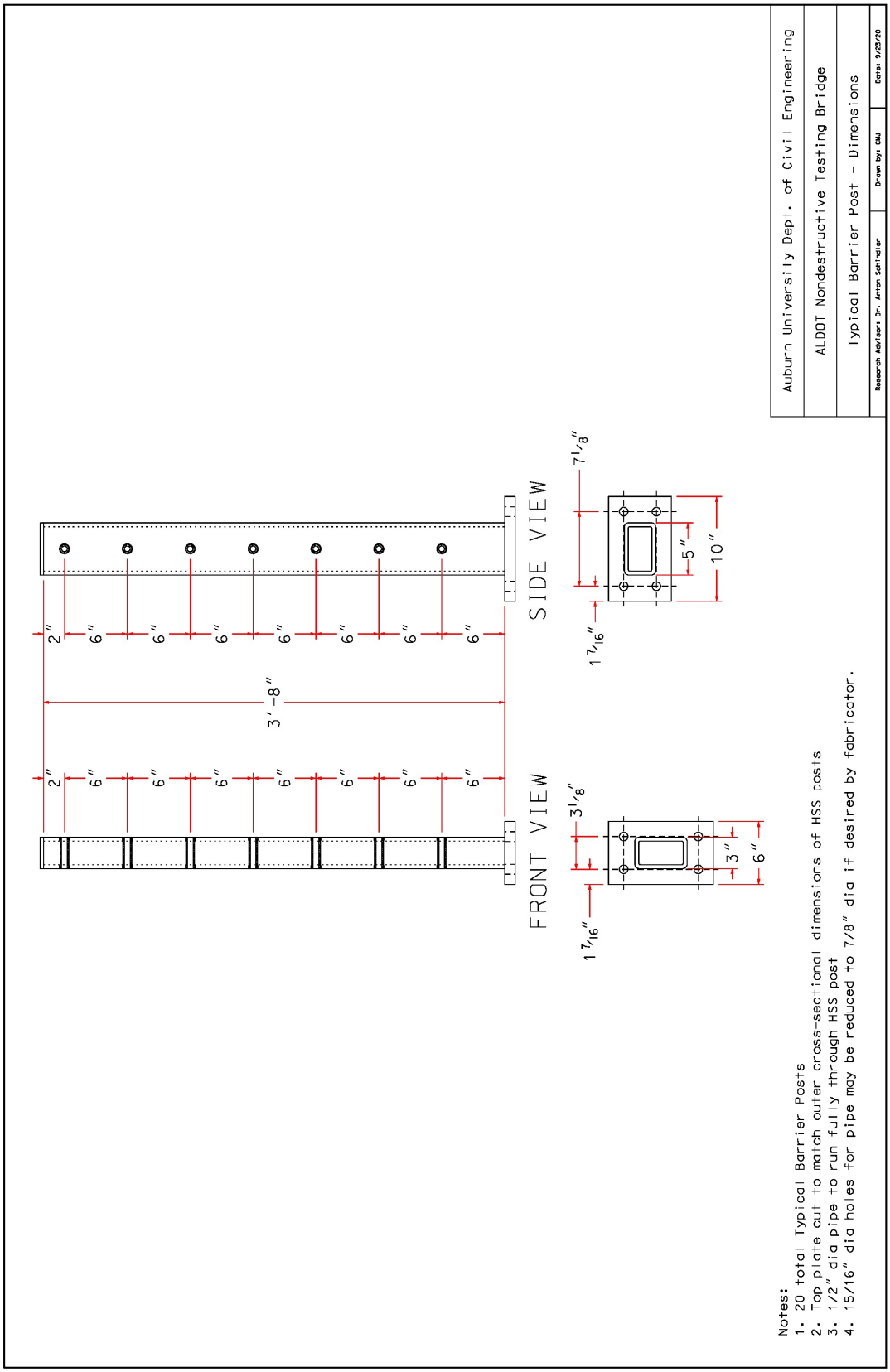

Figure B-9: Typical barrier post dimensions

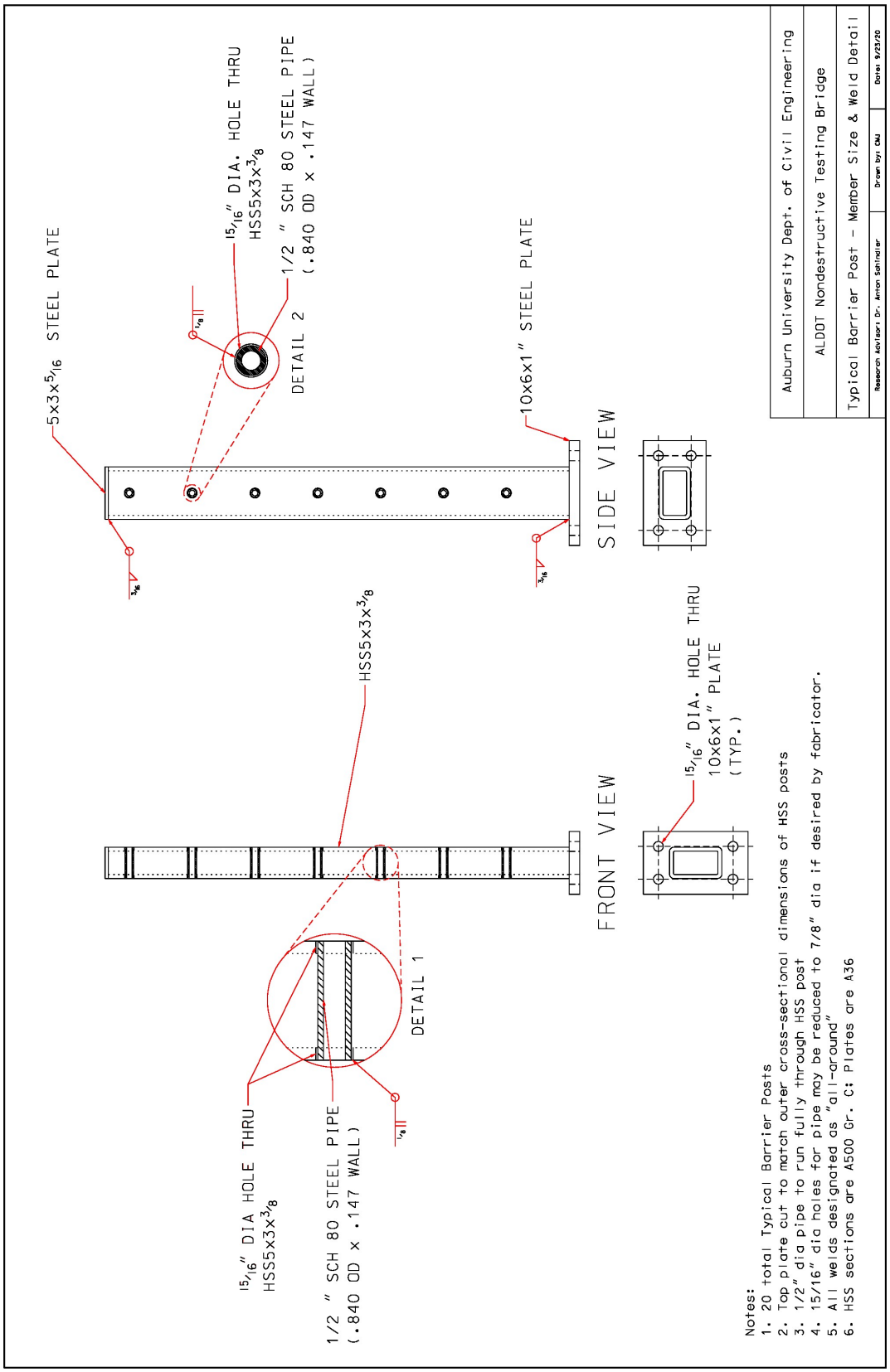

Figure B-10: Typical barrier post detail

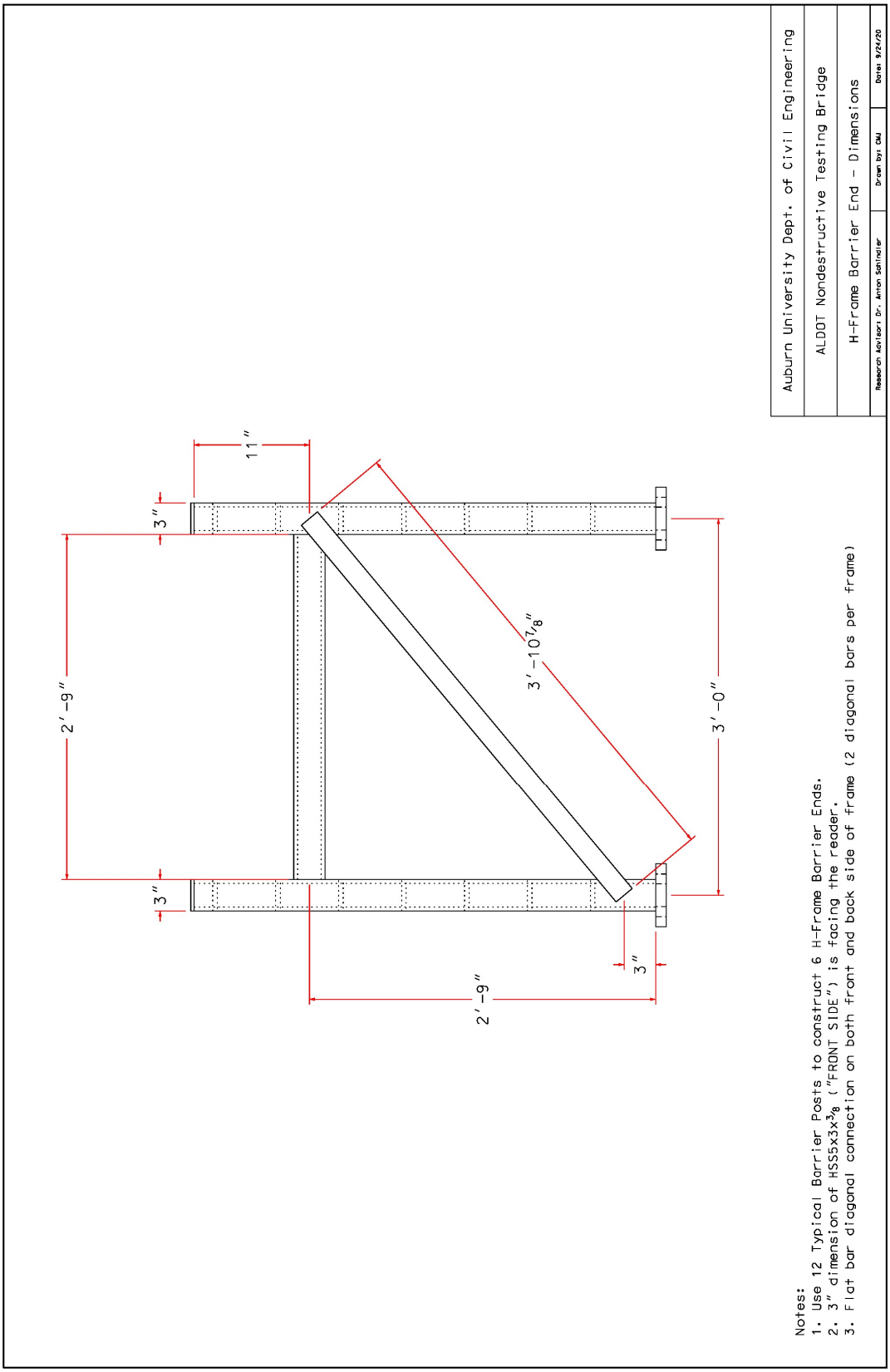

Figure B-11: Typical H-frame barrier end dimensions

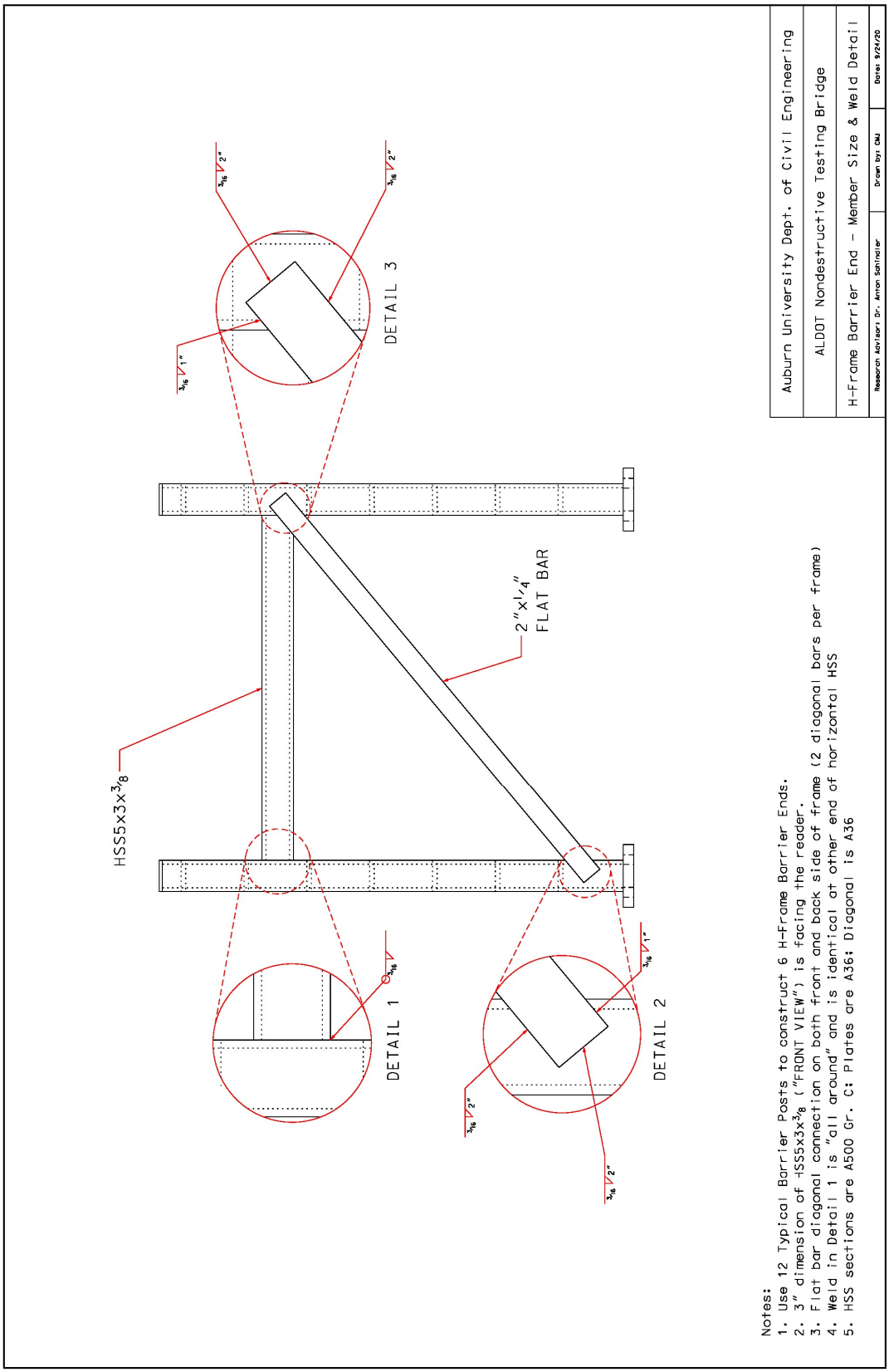

Figure B-12: Typical H-frame barrier end detail

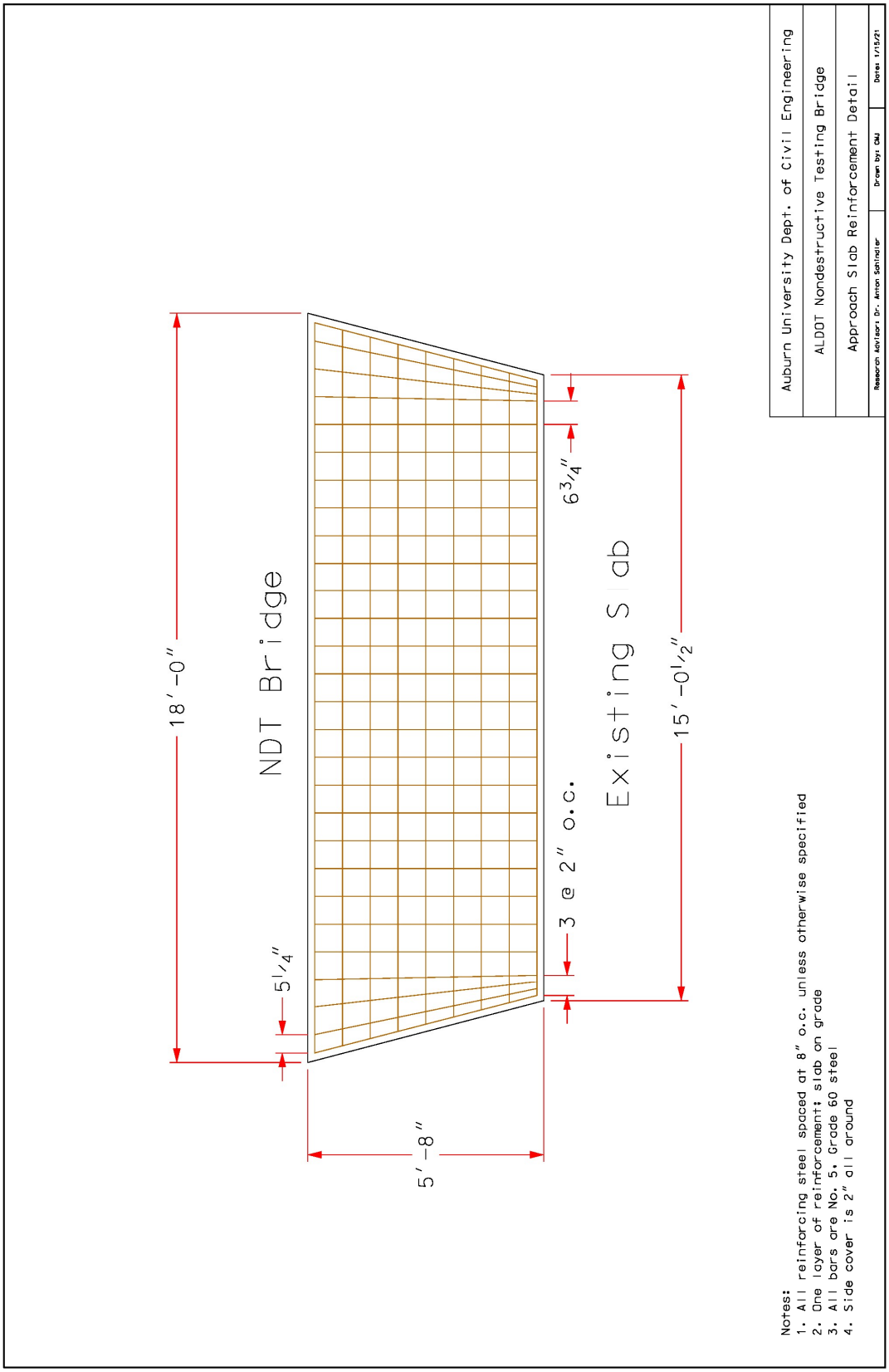

Figure B-13: Approach slab reinforcement detail drawing